Electrical characterizing of superconducting power cable consisted of Second-Generation High-temperature superconducting tapes

Zhang, Zhenyu

Award date:
2016

Awarding institution:
University of Bath

Electrical characterizing of superconducting power cable consisted of Second-Generation High-temperature superconducting tapes

A thesis submitted by Zhenyu Zhang
for the degree of Doctor of Philosophy
Department of Electrical and Electronic Engineering
University of Bath

2016

Signature_____ Date_____

Acknowledge

There are a number of people who have contributed to the work presented in this thesis and I am extremely thankful for your delegated contributions, even you are not personally mentioned here.

Firstly, I would like to express my utmost gratitude to my supervisor, Dr. Weijia Yuan, for his advice, guidance and support throughout the duration of my research. He taught me the skills required for independent research and allowed me the freedom to explore my own ideas. More importantly, with his support, I have achieved a number of accomplishments in the Applied Superconductivity Lab at the University of Bath since the beginning of the lab was setup. Special thanks to Dr. Min Zhang for her generous and invaluable help during my study.

I would also like to thank Dr. Sastry Pamidi, Dr. Chul Han Kim, Dr. Jozef Kvitkovic and Dr. Jin-Geun Kim from the Central for Advance Power System, Florida State University. Thank you all for your help with the superconducting cable experimental tests. My appreciations also go to Dr. Jiahui Zhu from China Electric Power Research Institute and Dr. WenjiangYang from Beihang University, China. Thank you for your helpful advice throughout the project.

I could not finish this dissertation without the help from my colleagues at the University of Bath. I would like to thank my laboratory colleagues, in no particular order, Dr. Huiming Zhang, Fei Liang, Jianwei Li, Qixing Sun, Dong Xing, Sriharsha Venuturumilli and Jay Patel. I must also thank Andy Matthews for his greatly helpful support on lab equipment.

Last but definitely not least, the biggest thanks go to my parents who always love me unconditionally, and to all my family members who always support me. My girlfriend, Nuo Cheng, has supported me wholeheartedly, and without her help and encouragement, I would not have achieved all that I have thus far. The emotional support required to complete a Ph.D. is often underestimate

Abstract

With the continuous decline in the price of second-generation (2G) high temperature superconducting (HTS) tapes, the 2G HTS cables are a promising candidate to significantly improve the electrical power transmission capacity and efficiency. In order to make the HTS cable competitive to its counterparts in the power market, much ongoing research work have made considerable contributions to the HTS cable design. In this thesis, the challenges of electrical issues of superconducting power cable using 2G HTS tapes have been addressed. The specific contributions of the thesis include: the influence of anisotropic characteristics of 2G HTS is investigated in order to increase critical current of HTS cable; For improvement of transmission efficiency and safety, the homogenization of HTS cable current distribution is achieved considering the influence of contact resistances and HTS layer inductances; AC loss of HTS cable is obtained through experimental measurement for cooling system design; and the impact of HTS cable on power grids is analysed for safe integration of HTS cable into grids.

This thesis starts with a literature review of superconductivity and developments of 2G HTS cable. Following the literature review is the critical current investigation of HTS cable considering the anisotropy of 2G HTS tape. 2G HTS tapes were placed in a highly uniform electromagnetic field and the in-field critical currents were measured with various magnitudes and orientations of the magnetic field. The anisotropic characteristics of 2G HTS tape were determined by non-linear curve fitting using measured in-field critical currents and further implemented into the HTS cable finite element method (FEM) modelling. The modelling results indicate that the gap distances among the tapes in the HTS cable affect the critical current of the HTS cable due to the anisotropic characteristics. In order to investigate the critical current of HTS cable with respect to gap distances, an HTS cable circuit model with adjustable gap distances among the parallel placed HTS tapes was designed and built. Extensive experimental and FEM modelling were performed and the results indicate that the minimized gap distance among the neighboring HTS tapes can be beneficial to increase the overall cable critical current.

With DC transporting current, the homogenization of current distribution of HTS cable is achieved by controlling the contact resistances. A 1.5 m long prototype HTS

cable consisted of two HTS layers was fabricated and tested as a further investigation of the HTS cable circuit model. The magnitude of the contact resistance related to each HTS layer was measured to quantitatively calculate the current distribution. It is found that only a few micro-ohms difference of contract resistances can still cause severe imbalanced current distribution. The FEM modelling work was carried out to obtain the balanced current distribution by varying the contact resistances. With AC transporting current, the inductances of HTS layers in the cable also pose a significant influence on current distribution issues. An optimal algorithm was developed to achieve homogeneous current distribution by optimal design of the cable diameter, pitch angle and winding direction. Another short prototype cable wound with two HTS layers was built according to the optimal design and the current distribution was experimentally measured between the two layers. It is found out that the optimal algorithm is effective to homogenize the AC current distribution.

A reliable AC loss measurement was carried out on the 1.5 m long prototype HTS cable in order to quantify the AC loss of the HTS cable for cooling system design. The experimental measurement method is based on the electrical four probe method adopting a compensation coil to cancel the large inductive component of the cable. The HTS cable with long geometry is easily influenced by the surrounding electromagnetic field so that the measured AC loss signal can be influenced. In order to overcome this problem, a symmetrical current return path was utilized in order to eliminate the electromagnetic interface surrounding the HTS cable. The AC loss measurement results are stable and low-noise for a set of AC frequencies, which proves the accuracy of the measurement technique.

Finally, a new superconductor component in PSCAD/EMTDC (Power System Computer Aided Design/Electromagnetic Transients including DC) was developed in order to investigate the impact of the HTS cable integrated into the meshed power network. The superconductor component developed in PSCAS/EMTDC takes into account the heat exchange with the HTS cable cryogenic envelope and the detailed configuration of YBCO HTS tape so that HTS cable model is able to accurately predict the power flow, fault current level and grid losses of the power grid with HTS cables.

List of publications

- **Zhenyu Zhang**, Min Zhang, Jiahui Zhu, Zanxiang Nie, GuoMin Zhang, Timing Qu, Weijia Yuan, "An Experimental Investigation of Critical Current and Current Distribution Behaviour of Parallel Placed HTS Tapes," June 2015, IEEE Transactions on Applied Superconductivity, Vol. 25, No 3.

- **Zhenyu Zhang**, Jin-Geun Kim, Chul Han Kim, Sastry Pamidi, Senior Member IEEE, Jianwei Li, Min Zhang, Weijia Yuan, "Current Distribution Investigation of a Laboratory Scale Coaxial Two HTS Layers DC Prototype Cable," June 2016, IEEE Transactions on Applied Superconductivity, Vol. 25, No 3.

- **Zhenyu Zhang**, Chul Han Kim, Jin Geun Kim, Jozef Kvitkovic, Sastry Pamidi, Min Zhang, Jianwei Li, Huiming Zhang, Weijia Yuan, "An Experimental Investigation of the Electrical Dynamic Response of HTS Non-insulation Coil," Journal of novel superconductivity and magnetism. (Under review)

- Jiahui Zhu, **Zhenyu Zhang**, Huiming Zhang, Min Zhang, Ming Qiu, Weijia Yuan, "Electric Measurement of the Critical Current, AC Loss, and Current Distribution of a Prototype HTS Cable," June 2014, IEEE Transactions on Applied Superconductivity, Vol. 24, No 3.

- Jiahui Zhu, **Zhenyu Zhang**, Huiming Zhang, Min Zhang, Ming Qiu, Weijia Yuan, "Inductance and Current Distribution Analysis of a Prototype HTS Cable," May 2014, · Journal of Physics Conference Series.

- Huiming Zhang, Jiahui Zhu, **Zhenyu Zhang**, Min Zhang, Weijia Yuan, "Study of 2G HTS Superconducting Coils Using Line Front Track Approximation," April 2016, IEEE Transactions on Applied Superconductivity, Vol. 26, No. 3.

- Jianwei Li, Min Zhang, Qingqing Yang, **Zhenyu Zhang** and Weijia Yuan, "SMES/battery Hybrid Energy Storage System for Electric Buses," June 2016, IEEE Transactions on Applied Superconductivity, Vol. 26, No. 4.

- Jianwei Li, Min Zhang, Jiahui Zhu, Qingqing Yang, **Zhenyu Zhang**, Weijia Yuan, "Analysis of Superconducting Magnetic Energy Storage Used in a Submarine HVAC Cable Based Offshore Wind System," Energy Procedia 75:691-696, August 2015.

- Jianwei Li, M.S. Qingqing Yang, M.S.; Robinson Francis, PhD; **Zhenyu Zhang**, B.S.; Min Zhang, PhD; "Novel Use of Droop Control Algorithm for Off-grid Direct Drive Linear Wave Energy Converter System with SMES/battery Hybrid Energy Storage," Energy. (Under review)

Table of contents

List of Figures

List of Tables

Chapter 1

Introduction

1.1 Thesis background

Nowadays conventional power grids are under the pressure of distributing relentlessly growing electricity demand while keeping the infrastructure efficient, reliable and low cost for end users. Utility firms around the world are facing a number of challenges resulting from rapidly increasing electrical power loads. In the 21st century, the global energy demand is predicted to be doubled by 2050 and more than tripled by 2100. In 2012, 42% of primary energy was consumed in the form of electricity and is likely to rise to more than 67% by the end of 2035. Such a huge power transmission burden currently relies on aging and inadequate conventional power grids which are extremely expensive to invest in for power capacity expansion, especially in some densely populated cities where adding new power cables is practically impossible due to the limited underground space.

Along the transmission and distribution lines, 6% to 8% of the electricity produced by the power plants is lost due to the resistance of the copper or aluminium-based cables and is dissipated in the form of heat. Inefficient transmission grids also lead to environmental pollution as the majority of electricity is generated by coal-burning in some developing countries. However, the nature of conventional conductors makes it difficult to improve the efficiency without seeking innovative technologies.

The order of modern society highly relies on the safe and reliable electricity supply. A digitalized market and social service would lie in ruins with the inability to provide basic services without electricity: cash machines would stop working immediately;

petrol pumps and refineries would shut-down within a couple of hours. Back-up generators powering hospitals and stock exchanges would run out of fuel within days. Hence, the reliability is the key issue for power transmission system reconstruction.

Frequent blackouts due to conventional power grid failures encourage utilities to seek for alternative power transmission solutions. For over hundreds of years in response to rapidly increasing economic growth, modern power transmission network are becoming more and more complex with widely distributed networks spanning nationwide. However, the robustness of the power grid has been compromised, especially during the period of peak electricity demand. Every 13 days, at least one blackout has crippled parts of the United States' normal social order and this outage frequency has been kept for 30 years. In the year of 2003, a series of large electricity blackouts occurred in both North America and Europe, mainly due to an unscheduled, sudden rise in demand for electricity consumed for air-conditioning in the summer and conversely heating in the winter. Two massive blackouts which hit India on the 31st of July, 2012 resulted in catastrophic effects and left half of the national population without power, the blackout originated from disturbances on the power transmission line since power flow was beyond its rated operating limit.

Nowadays the issues of global warming and rising fossil fuel prices have boosted the development of renewable energy integration into the power grids. For instance, in eastern Germany, wind turbines during strong wind seasons can produce more than the sum of all German coal and gas plants. However, the intermittent renewable energy sources often result in the risk of regional electricity blackouts, more seriously, aging infrastructure and increasing interconnection of electricity networks may even trigger cascade blackouts.

The real reasons behind these events are the continuously rapid growth of overall electricity consumption, aging and inadequate infrastructure coupled with the integration of intermittent renewable energy sources which introduce uncertainties into the power grids. Hence, significant pressures that reconstruct a robust and efficient electrical transmission grid encourage engineers around the world to seek

alternative technology for power grid upgrading in order to prevent large power system blackouts occurring in the future.

1.2 Research motivation

The feasible and promising solutions to address the complex challenges on the power grids upgrading have been the most popular topics around the world. One of the technologies with the greatest promise future to address the challenge is the high temperature superconductor (HTS) cable. With the discovery of ceramic superconductor material, such as yttrium, barium and copper (YBCO) compound, the critical temperature of superconductor has been raised up to above the liquid nitrogen temperature (77 K), which makes the cooling cost of superconductor economic acceptable and engineering feasible. A number of types of superconducting materials are now commercially available with an affordable price for HTS applications research and industry manufacture. Hence, HTS cables are becoming a feasible application to the power grids.

Compared with conventional copper power cables, superconducting cables can offer a number of unique benefits:

- Under the same power transmission voltage level, the current carrying capability of HTS cable is three to five times than that of a conventional copper cable.
- HTS cables can carry equivalent power capacity at a much lower voltage level.
- The capital investment can be largely reduced by taking advantage of HTS cable's ability of high power transmission capacity at a much lower voltage transmission level, which enables the elimination of urban substations and associated auxiliary equipment.
- Due to the compact structure, it is possible to install HTS cables in existing underground conduits and break the urban electricity transmission bottlenecks due to the limited underground space left for new power generation and load growths.

Although the transmission losses are largely reduced by applying HTS cables into the power grids, additional power must be required to cool the superconductor down to the operating temperature. From the infrastructure investment point of view, the figure of saved losses is counteracted by the cooling power system. However, the most advantage of HTS cable that aroused the interest of engineers is the cable size reduction with the ability to carry the same power by conventional copper cable. In urban city areas, where the underground space is limited and digging additional space for new copper cable for the sake of power capacity expansion is extremely expensive. Since the power capacity of one HTS cable is equivalent to that of about five conventional copper cables and HTS cables are thermally independent of the surrounding areas, it is more suitable to be installed in the existing underground pipelines to expand the power transmission capacity than conventional cables. Hence, an inexpensive solution to ease the urban area power congestion issues is provided.

Since the copper or aluminium-based transmission cables are mainly serving in the power grid, thermal overheat due to overloading ages the cable insulation and degrades the cable transmission capacity, which eventually results to cable transmission efficiency decreasing or even electrical outage. HTS cable provides a new solution to avoid overheat by pulling power flow away from overloaded transmission lines to HTS cable itself due to the very low impedance. Reducing the overloaded power burden on existing power transmission pathways will extend the life cycle of transmission lines and enhance the power grid reliability. By partial installation of HTS cable instead of the replacement of the whole power grids has avoided the large-scale capitalized infrastructure investment. Hence, a cost-effective way for robust grid upgrading by introducing HTS cable into power grids is feasible.

1.3 The challenges and contributions of the thesis

The HTS power cable has to be outperformed to the conventional power cable in order to widespread in power grids. However, before the real application of HTS cable, there are several challenges to be addressed.

Firstly, the critical current of HTS cable is studied considering the anisotropic characteristics of 2G HTS tape. Since the critical current density of 2G HTS tape is influenced by the anisotropic characteristics, the critical current of HTS tape depends on the magnitude and orientation of the external magnetic field. In the other words, the HTS tape anisotropy is an important factor in determining the critical current of HTS cable. However, the lack of information on the anisotropic properties of 2G HTS tape poses obstacles to accurately predict the critical current of HTS cable. Hence, a reliable method is required to determine the anisotropy of 2G HTS tape. An experimental work was carried out: 2G HTS tapes were placed in the magnetic field with high uniformity and the in-field critical currents were measured varying the magnitude and orientation of magnetic field. The anisotropic characteristics of 2G HTS tapes were characterized by non-linear curve fitting using measured in-field critical currents. Additionally, due to the requirements of the cable mechanical structure, the gaps between the adjacent tapes inevitably exist, which can influence the distribution of the magnetic field in the cable and therefore, affect the critical current of the cable due to anisotropic properties of 2H HTS tape. Hence, the investigation of the gap distances on the critical current of the HTS cable was performed. However, it is difficult to adjust the gap distance freely on a completed HTS cable since all the HTS tapes are mechanically bonded on the cable copper termination. An HTS cable circuit model with parallel placed HTS tapes was designed. The gap distances among the parallel HTS tape can be adjusted freely in order to measure the critical current of the HTS tapes with various gap distances. The results indicate that if the gap distance is less than 1 mm, the critical current of HTS cable can be improved considerably.

Secondly, for multi-HTS-layer cable, imbalanced current distribution among the HTS layers reduces the power transmission efficiency significantly. Hence, an optimal strategy is developed to homogenize the current distribution. For DC HTS cable, contact resistances as the largest contribution to the cable impedance pose a considerable influence on current distribution. In order to understand the impact of contact resistances, a prototype HTS cable consisted of two HTS layers was designed and fabricated. The current distribution is quantified between the two layers. It is found out that subtle contact resistance differences will cause severely inhomogeneous current distribution among the HTS layers wound in the cable. An

FEM model considering the contact resistances has been developed to simulate the current distribution of this cable and the modelling results show that the homogenized current distribution can only be achieved by equalizing the contact resistances. On the other hand, the HTS layer inductances also largely affect the current distribution if HTS cable carrying AC transporting current. Hence, an optimal algorithm is developed by adjusting the pitch angle, radius and winding direction of each HTS layer wound on the cable in order to homogenize the AC current distribution among the HTS layers. The optimal algorithm is verified with an experimental test performed on another prototype HTS cable. The cable is designed based on the optimal algorithm and the measurement results prove the effectiveness of the algorithm.

Thirdly, a reliable AC loss measurement technique of HTS cable is studied in order to accurately quantify the HTS cable AC loss for cooling system design. However, the HTS cable with long geometry is easily affected by the surrounding electromagnetic field resulting from the copper cable connected with HTS cable in room temperature. In order to improve the measurement accuracy, the measurement method is implemented based on the electrical four probe method adopting a compensation coil to cancel the large inductive component of measured AC loss voltage from the HTS cable. The location of the copper cables is arranged to form a symmetrical current return path from the HTS cable back to the AC power source in order to eliminate the electromagnetic field surrounding the HTS cable. Additionally, the voltage potential probe should be placed at a position that the measurement device can derive the true AC loss of HTS cable. For single HTS layer cable, the probe can be placed directly on all HTS tape using ring contacts. For multi-layered HTS cable, the AC current distribution should be considered. Since it is not accessible for current measurement at each HTS layer, the probe can be placed at the cable terminals so that the total resistive losses of HTS cable are measured. The AC loss of HTS cable can be deduced based on the resistive losses contributed from the cable terminal joints. Considering the skin effect, joint resistances are modified for each applied AC current frequency so that the measured AC loss is correct.

Finally, before the real application of 2G superconducting cable installed in the power grid, the impact of the superconducting cable implemented in the power grid should be analysed and predicted in order to prevent undesirable instability. However, there

is no existing superconducting model in the power system simulation software, such as PSCAD/EMTDC. Hence, a novel superconducting component in the PSCAD/EMTDC is developed considering the detailed configuration of coated YBCO conductors. Since the resistivity of 2G HTS tape is dependent on both current density and temperature, the superconducting component is developed based on superconducting *E-J* power law coupled with heat transfer from the superconducting layer to the cryogenic envelope in PSCAD/EMTDC in order to represent real superconducting cable operating in the power system. The model can simulate the transient response of thermal and electrical behaviours among the cable former, superconducting conducting layer, shielding layer and cable cryostat when a fault current occurs to the superconducting cable. The simulation results of HTS cable turn out to be very effective to understand the maximum allowed fault current duration, so as to prevent the HTS cable from permanent damage. Further utilizing the model, the power flow, and grid losses are analysed compared with the HTS cable and conventional cable.

This thesis will investigate all the aforementioned challenges in HTS cable in order to discover an HTS power cables as a competitive application for electrical power engineering. The outline of the thesis is as follows:

- Chapter 2 presents a brief theory of the superconductivity with particularly focusing on the YBCO HTS tape. The recent development of HTS power cable is outlined and the impact of the HTS cable on power grids are discussed.
- Chapter 3 investigates the experimental determination of anisotropic characteristics of 2G HTS tape and the critical current of HTS cable is investigated by a novel HTS cable circuit model, which presents the design that can give the maximum critical current of the HTS cable.
- Chapter 4 is dedicated to homogenize the critical distribution among the HTS layers in the cable considering the influences of contact resistances and the layer inductance, in order to improve the HTS cable power transmission efficiency.
- Chapter 5 contains the measurement of the HTS cable AC loss. The AC loss of HTS cable is measured based on electrical four probe method with additional modification for eliminating the background electromagnetic influence.

- Chapter 6 presents the work that simulates HTS cable in the power grid using PSCAD/EMTDC. A novel superconducting component is developed in PSCAD/EMTDC based on the dependence of resistivity on the temperature and current density of the HTS tape, coupled with the heat transfer with the cryogenic path.
- Chapter 7 summarizes the research works in the thesis and possible improvements. The possible future solutions for long-distance superconducting cable transmission are also discussed.

Chapter 2

Overview of superconductivity and superconducting cable

2.1 Theory of type I and type II superconductors

2.1.1 Critical boundaries

Superconductor must operate in the region defined by three inter-related critical boundaries: critical current (I_c), critical temperature (T_c) and critical magnetic field (H_c), as shown in Figure 2.1. Superconductors will transit from superconductivity state to norm state if beyond any of these critical boundaries. According to the boundary condition of critical magnetic field H_c, the superconductors can divide into two types: type I and type II superconductors.

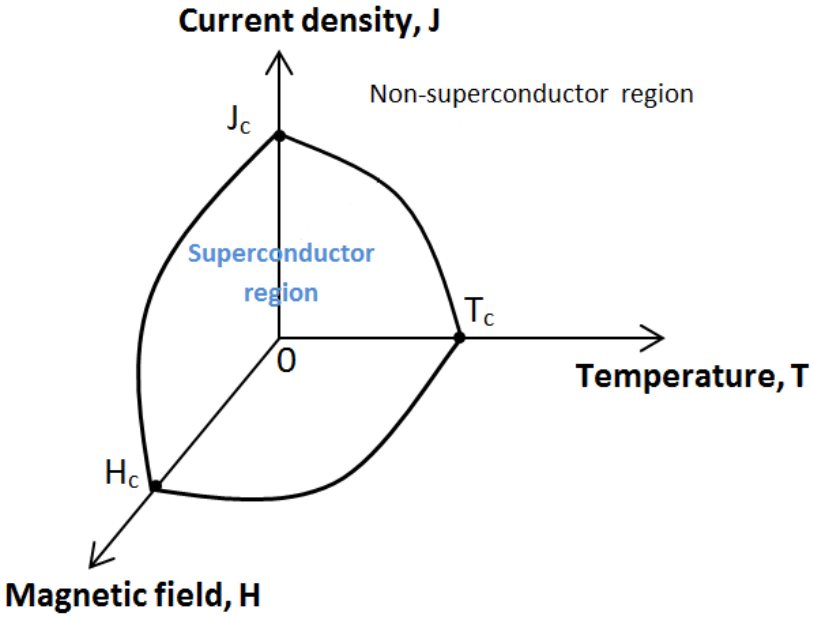

Figure 2.1: The superconductivity critical boundary.

The relationship between the external magnetic field H, the magnetisation of the superconductor material M and total flux density inside the volume of superconductor B is given in Eq. 2.1. The Meissner effect is a typical characteristic of type I superconductor, which occurs when the applied field is below the critical field H_c. Screening current is induced inside superconductor which could expel the magnetic field from the inside of superconductor, in this case, M is equal to $-H$. This effect results in the zero field inside the volume of superconductor, i.e., B is equal to 0. When H is bigger than H_c, M drops to 0 and the magnetic field fully penetrates into the superconductor, i.e., $B = \mu_0 H$. The Figure 2.2 (a) shows the type I superconductor transition phase diagram.

$$B = \mu_0(H + M) \qquad \text{Eq. 2.1}$$

The value of critical field H_c is a function of temperature T, as shown in Eq. 2.2 [1]. However, the value of the magnetic field H_c of type I superconductor is very small. For instance, the mercury would immediately revert to normal conductor if exposed in a magnetic field of 41 mT. If the type I superconductor exposes in the field above the value of H_c, it will transit to the normal state immediately. Majoirty of the metal superconducting materials are type I superconductors and their critical temperature and critical field are summarized in Table 2.1 [2].

$$H_c = H_0\left(1 - \left(\frac{T}{T_c}\right)^2\right) \qquad \text{Eq. 2.2}$$

Unlike the type I superconductors, there are two critical magnetic field boundaries for type II superconductors, a lower critical field H_{c1} and an upper critical field H_{c2}. If the magnetic field is below the lower critical field H_{c1}, the type II superconductor is in the superconducting state. If the magnetic field is over the upper critical field H_{c2}, the type II superconductor loses superconductivity completely and transits to a normal state. Between the two critical field boundaries, the magnetic field partially penetrates into the volume of superconductor in the form of vortices. This middle region is known as mix-state where the resistivity of the superconductor is zero as long as the vertices are pinned inside the superconductor. Figure 2.2 (b) shows the type I superconductor transition phase diagram. Although the lower critical field $\mu_0 H_{c1}$ of

type II superconductor is very small to roughly 0.01 T, the upper critical field $\mu_0 H_{c2}$ can reach as high as 30 T, such as Nb_3Sn, which makes the type II superconductor capable of sustaining superconductivity in the presence of a higher magnetic field. This is huge advantages to allowing the type II superconductor to be developed in the large scale power applications which always experience in a high magnetic field environment. Type II superconductors are usually made of metal alloys or complex oxide ceramics. All high temperature superconductors are type II superconductors, including BSCCO (Bismuth strontium calcium copper oxide) and YBCO (Yttrium-Barium-Copper-Oxide), which are the most achievable commercial applications since they can become superconductivity at boiling point of liquid nitrogen at 77 K, and the upper critical field limit is very high, at about 140 T [3]. Table 2.2 gives some typical type II superconductor critical field values [4].

Table 2.1: The critical temperatures T_c and critical magnetic field strengths H_c of Type I superconducting materials.

Materials	T_c/K	H_c/mT
aluminium	1.2	10
cadmium	0.52	2.8
indium	3.4	28
lead	7.2	80
mercury	4.2	41
tantalum	4.5	83
thallium	2.4	18
tin	3.7	31
titanium	0.40	5.6
zinc	0.85	5.4

Table 2.2: The critical temperatures *Tc* and upper critical magnetic field strengths Hc_2 of Type II superconducting materials.

Compounds	T_c/K	H_{c2}/T
NbZr	11	8.3
NbGe	23.6	37
NbAl	19.1	29.5
YBaCuO	93	140
BiSrCaCuO	92	107

2.1.2 Vortices and pinning flux

Unlike the type I superconductors, which either completely expel the applied magnetic field or are fully penetrated by the magnetic field, the type II superconductors manage to find a compromise situation. When a type II superconductor experiences in a weak magnetic field, $H_{c1}<H<H_{c2}$, it is in the so-called mix-state, where some of the magnetic fluxes are able to penetrate into superconductor along vortices. The term 'Vortices' was proposed by Abrikosov in 1952 [5], and later on with the developed microscope techniques, researchers are able to observe them, which prove the existence of vortices in the type II superconductors.

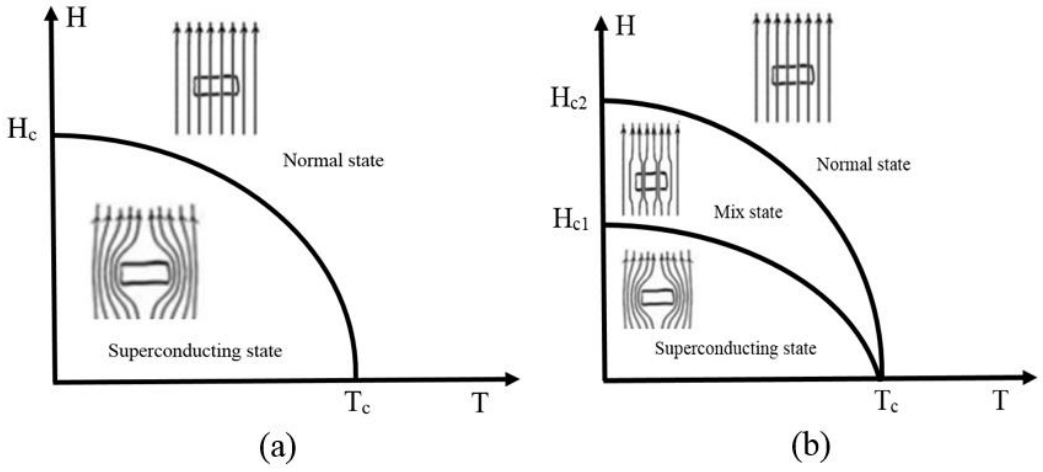

Figure 2.2: The phase diagram of type I (a) and type II (b) superconductors [6].

Figure 2.3 represents the mixed state of a type II superconductor. An external magnetic field is applied (in black) on the superconductor. Screen current (in red) is induced on the surface in order to make a screen repel the external field. The screen current is the superconducting current which is responsible for the Meissner effect. The rest of superconducting currents (in green) are induced to create vortices. These vortices allow some of the magnetic flux to go through them and thus enable part of the applied magnetic field to penetrate the superconductor without losing superconducting completely. The flux through the superconductor is called pinning flux, which cannot move freely due to the pinning force. The density of vortices is determined by the strength of applied magnetic field H. If H increases from H_{c1} to H_{c2}, the vortices become closer and their cores start to overlap. At $H_{c2,}$ the vortex and the pairing of the electrons disappear and applied magnetic field fully penetrates into superconductor resulting in reverting superconductors from superconductivity state to normal conductor state.

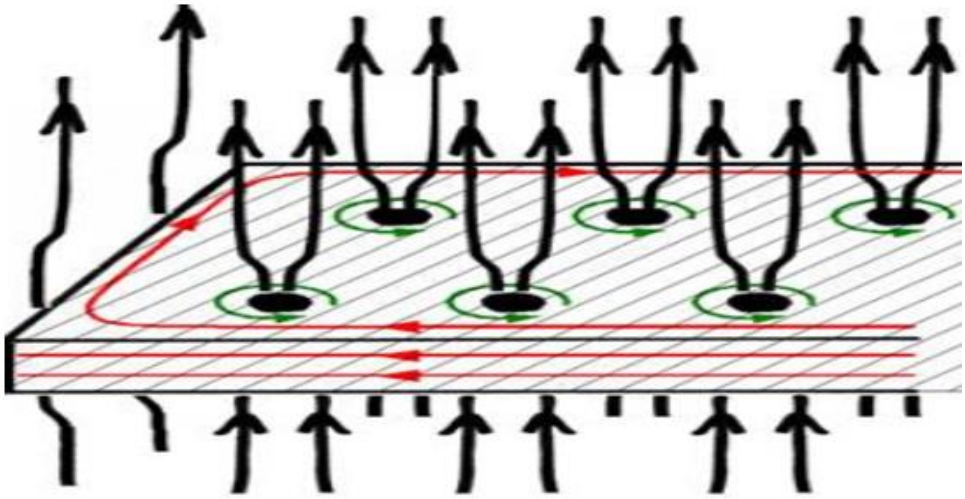

Figure 2.3: The mixed state of type II superconductor (magnetic field in black, screen current in red, superconducting current in green).

The magnetic flux in the vortices is trapped by the pinning force, which requires additional power to alter. When the type II superconductors carry DC current, no additional power is required since the induced DC magnetic field is constant in magnitude and direction. However, when type II superconductors carry AC current, the induced AC magnetic field changes in magnitude and direction at all times.

Additional power is required to overcome the pinning force in order to alter the trapped magnetic field, which results in the heat dissipation. This part of energy losses is also known as AC loss.

2.2 High temperature superconductors

2.2.1 The development and properties of the second generation high temperature superconductors

The high temperature superconductors, or HTS, were firstly discovered in 1986 by Bednorz and Muller. They found the superconductivity of compound LaSrCuO at the temperature of 30 K [7]. Later in 1986 and 1987, Paul C. W. Chu and M-K Wu discovered the superconductivity compound $YBa_2Cu_3O_7$ at the temperature of 93 K, which is known as the second generation (2G) HTS. This was a major breakthrough since the superconductivity of YBCO can be achieved by cheap liquid nitrogen at its boiling point of 77 K. All the early found superconductors can only become superconductivity cooled down by liquid helium (4.2 K) and liquid hydrogen (20 K). The cheap and achievable cooling method of liquid nitrogen makes YBCO become the most famous superconducting material for large scale power applications, such as superconducting magnetic energy storage (SMES), superconducting cable and superconducting fault current limiter (SFCL).

The dimensions of a single unit $YBa_2Cu_3O_7$ crystalline structure are shown in Figure 2.4. The dimensions of a single unit cell of YBCO are a = 3.82 Å, b = 3.89 Å, and c= 11.68 Å [8]. The Yttrium atoms are located inside the CuO_2 planes while the Barium atoms are located between the CuO_4 planes and CuO_2 planes. The crystal structure of YBCO shows highly anisotropic. The coherence length of ab plane is $\varepsilon_{ab} = 2\text{nm}$, and the coherence length of c plane is $\varepsilon_c = 0.4\text{nm}$ [6], which means along c plane, the conductivity is 10 times smaller than the ab plane. Hence, the supercurrents flow mainly along the ab plane, while the trapped magnetic field is along the c plane [9].

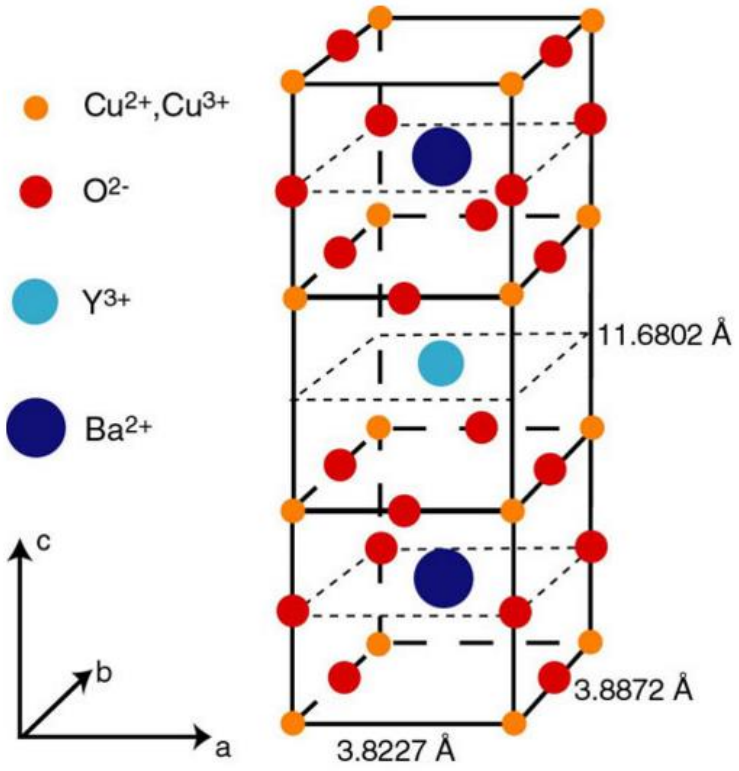

Figure 2.4: Single crystalline structure of YBCO.

The single crystalline structure of YBCO has a very high critical current density, however, the polycrystalline have a much lower critical current density due to the crystal grain boundaries between the interfaces. In fact, the presence of the grain boundaries largely limits the maximum achievable critical current in HTS wires. The critical current is suppressed exponentially by the misorientation α of the grain boundary. Figure 2.5 shows the schematic of the YBCO polycrystalline grain boundary, where only the CuO_2 layer is shown [10]. When the grain boundary angle is over a certain value, which depends on the material, the supercurrent cannot flow across the boundary. The improvement of this defect of the HTS relies on the complicated fabrication method and the improvement of the critical current of HTS wire depends on minimizing the grain boundary misorientation angle α.

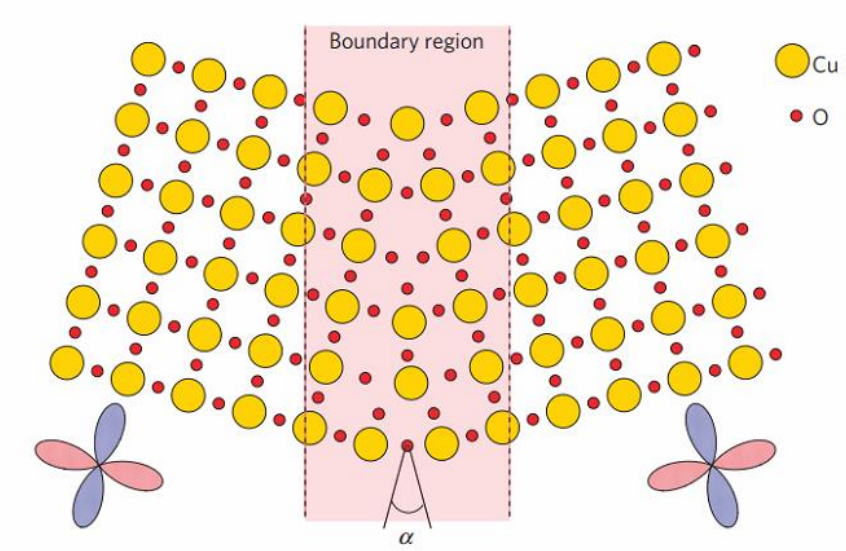

Figure 2.5: Schematic diagram of YBCO symmetric grain boundary [10].

2.2.2 Properties of 2G HTS commercial wires

High temperature superconductors are classified into two categories: first generation and second generation. Most of the commercially available HTS materials which are made of BSCCO (Bi-Sr-Ca-Cu-O) are referred as the first generation high temperature superconductor since 1990. The superconducting material powder is filled into silver matrix forming BSCCO multi-filaments as shown in Figure 2.6. However, the heavy reliance on the silver makes the BSCCO wire too expensive for commercial development.

The majority of high temperature superconductor manufacturers are migrating to new second generation high temperature superconductor development with the rear earth (Re)-based Barium-Copper-Oxide compound, including Y (Yttrium), Sm (Samarium), Nd (Neodymium) and Gd (Gadolinium). In this thesis, all the works are using Yttrium based barium-Copper-Oxide second generation (2G) superconducting tape. The terms of tape are interchangeable with HTS tape, YBCO tape and coated conductor, which are referred to the same superconducting material as shown in Figure 2.7. This is because apart from the considerable reduction in production cost, the ReBCO HTS tapes offer the following advantages:

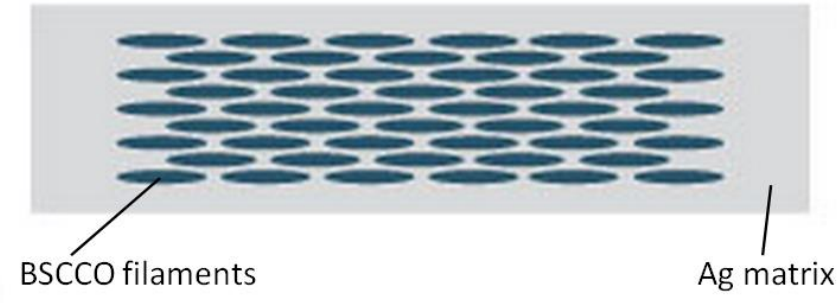

Figure 2.6: The structure of the BSCCO HTS cross-section.

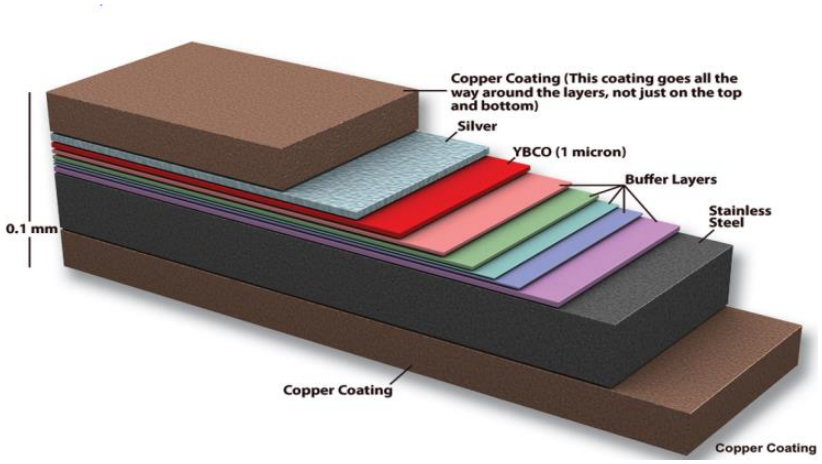

Figure 2.7: The structure of YBCO superconducting tape.

1) The compact dimensions: the total thickness of the YBCO HTS tape is around 0.1 mm depending on the different manufacturers while the overall thickness of BSCCO HTS tape is typically around 0.4 mm, which makes the engineering current density of YBCO tape improved considerably. As shown in Figure 2.7, the typical structure of the YBCO tape consists of about 1 μm YBCO superconducting layer deposited on a stack buffered substrate, which is about 50–100 μm in thickness. The materials of the substrate vary with the manufacturers. Non-magnetic nickel alloy, typically Hastelloy^{R} C276, is used as a substrate by SuperPower^{R} [11] while the magnetic textured Ni-W is used by American Superconductor Corporation (AMSC) [12]. The YBCO layer is covered with a 2 μm thickness silver layer and laminated by surrounding copper stabilizer.

2) Higher *n* values: the *n* values of YBCO tapes are typical between 20 – 30 while the *n* values of BSCCO tape is generally lower than 18 [13], hence, the resistance of YBCO tape is capable of rising abruptly within a few milliseconds. The sharply increased resistance of YBCO tape from superconductivity state to normal state makes it very suitable for superconducting fault current limiters.

3) Available for the long length: all the superconductor manufacturers are endeavoring to achieve the target of producing long length YBCO HTS wire. In 2006, SuperPower^{R} successfully scaled up the YBCO HTS wire manufacturing facilities, which makes the single piece of over 400 m YBCO HTS tape deliverable. After 2008, SuperPower further increased the longest length of single HTS piece to 1000 m, which improved the performance of large scale high field superconducting magnet [11] [14].

4) Improved in-field performance: due to the high aspect ratio and anisotropic of YBCO HTS tape, the critical current of the wire is heavily affected by the magnitude and angle of the magnetic field. Especially in the coil application, the overall critical current is determined by the innermost turn with the field angle from 15 to 30 degrees [15]. Recently developed advanced pinning YBCO HTS tapes have greatly enhanced the in-field performance by SuperPower. As the field angle dependence of critical current shown in Figure 2.8, the performance of ReBCO HTS tape is improved by replacing Gd with Sm and further improved by doping Zr in the GdBCO [11].

5) Enhanced mechanical properties: the YBCO HTS tape fabricated by SuperPower is capable of withstanding stress level up to 700 Mpa without any degradation [11]. This feature enables HTS wire experiencing high stress in the high field magnet coils or high-speed superconducting machines.

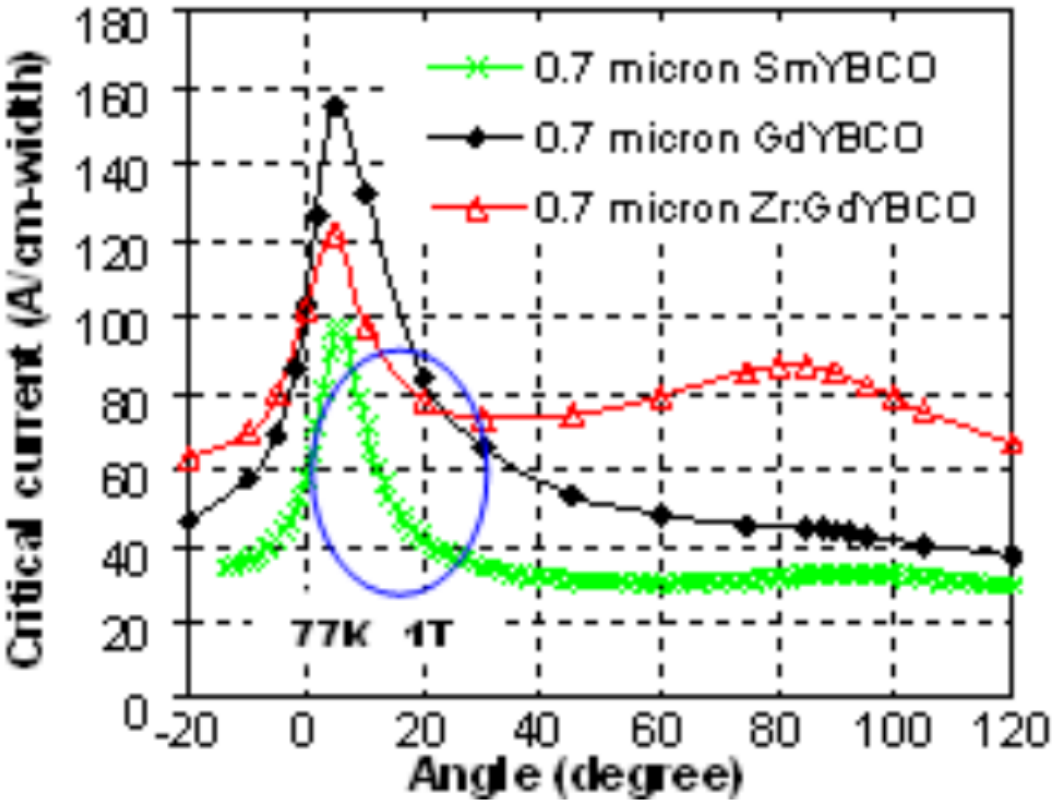

Figure 2.8: The field angle dependence of ReBCO critical current tape [16].

2.2.3 The fabrication process of YBCO HTS wire

There are several YBCO HTS tape manufacturers: SuperPower, American Superconductor (AMSC), SuporOx and SuNam. Their manufacturing techniques differ from each other and hence result in the different performance of YBCO HTS tapes. The manufacturing technique of SuperPower is based on the IBAD/MOCVD (Iron Beam Assisted Deposition/Metal Organic Chemical Vapour Deposition). A stack of buffer layers is sputtered on the Hastelloy substrate to form a biaxial texture. The YBCO layer is deposited on the buffer layer using MOCVD. A thin silver layer is sputtered on the YBCO layer in order to improve the electrical conductivity. A surrounding copper stabilizer layer covers the tape for enhancing the mechanical strength [17].

The manufacturing approach of AMSC YBCO HTS tape (Amperium tape) is based on the RABiTS/MOD (Rolling Assisted Biaxially Textured Substrate/Metal Organic Deposition). The buffer layers are sputtered onto a metal alloy Ni-W substrate and the

YBCO layer are deposited on the buffer layer by MOD. A silver layer covers the YBCO layer to improve the electrical conductivity. All the layers are laminated between two metal stabilizer layers, which are brass, copper or stainless steel [18].

The production approach developed by SuperOX in 2006 is based on a combination of long length electropolished non-magnetic NiCrW rolled-annealed biaxially textured substrate (RABiTS) substrates with reel-to-reel MOCVD [19]. In 2014, the production is based on electropolishing of Hastelloy tapes, IBAD-MgO texturing, magnetron sputtering of the buffer layers and PLD of the HTS layer [20].

SuNam has developed a batch-type reactive co-evaporation system with a drum in a dual chamber, denoted as Evaporation using Drum in Dual Chamber (EDDC) to deposit YBCO layer on long-length metallic templates. The deposition parameters can be uniformly controlled by a large chamber so that kilometre-long HTS tape can be fabricated by only increasing the drum size without significant modification of the system's basic structure [21].

2.2.4 State-of-the-art YBCO HTS tapes

Due to the high aspect ratio of the cross-section of YBCO HTS wire, the AC loss will cause refrigerating issues for power applications. In recently years, several research groups are endeavouring to reduce the AC loss by implementing striation to superconducting tape [22]. The aspect ratio is largely reduced by dividing the single HTS superconducting layer into several filaments, as shown in Figure 2.9, where the YBCO layer, silver layer, buffer layers and substrate layer are cut by a laser ablation [23]. The reduction of the AC loss directly determined by the number of the filaments of striated YBCO tape. However, the degradation of critical current significantly depends on the number of the filaments due to the removal of superconducting material. Therefore, a compromise between the critical current degradation and the AC loss reduction should be optimized by carefully selecting the number of the filaments.

Figure 2.9: The multi-filamentary YBCO HTS tape cross-section [24].

For example, the AC loss reduction of 4 YBCO tapes with 12 mm in width and same length were studied by the number of the striated filaments. One tape was not striated and used as the reference. The other 3 tapes were striated into 12, 24 and 48 filaments and labelled as L2, L3 and L4, respectively. The AC loss measurement was performed with applied external magnetic field and the results are shown in the Figure 2.10 [25]. It can be seen that the magnetization AC loss is reduced with the number of the filaments striated.

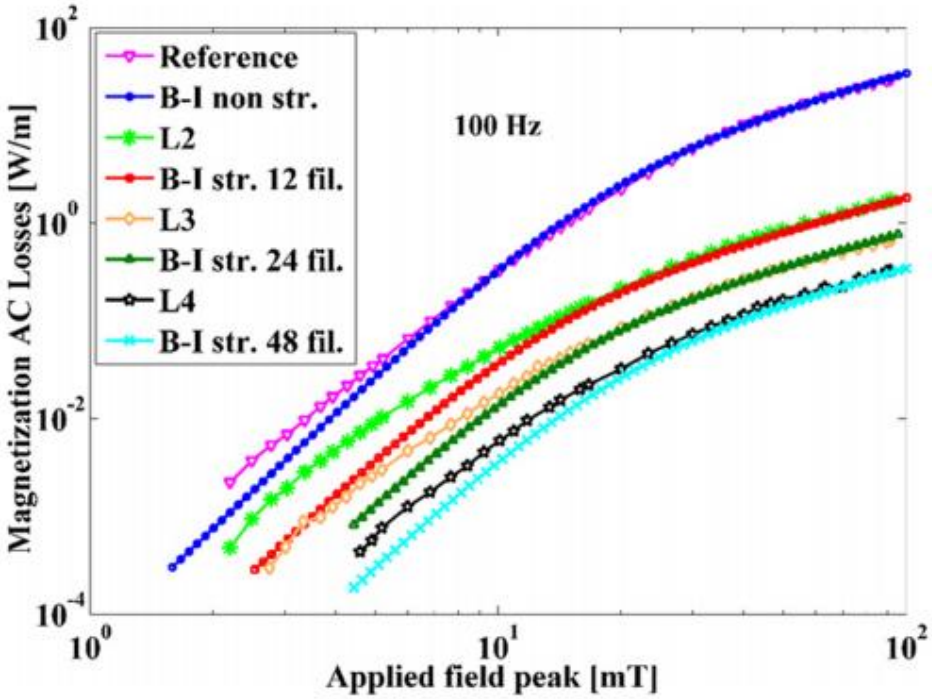

Figure 2.10: Magnetization AC loss of striated YBCO tape at 100 Hz for reference (L1), 12-filament (L2), 24-filament (L3), and 48-filament (L4) tapes [25].

2.3 Critical state of high temperature superconductor

Since the defects are deliberately introduced into the crystalline of YBCO superconductor to improve the in-field performance, the applied magnet flux can penetrate into the superconductor through the defected crystal lattice in the form of vortices when it exceeds the lower critical magnetic field boundary H_{c1}. A pinning force exerted on the pinning centre of vortices will balance the Lorentz force which pushes the vortices to move. The distribution of the vortices penetrated into the superconductor is determined by the balanced applied field or transporting current and the pinning force. The penetration depth of the vortices depends on the magnitude of the applied magnetic field or transporting current. The surface layer of the superconductor with low applied field or current is in the so-called critical state while the interior of the superconductor is shielded by screening current without current or applied field.

2.3.1 Bean model

For normal metal conductors, the relationship between the current and the electric field is described by Ohm's law. However, for a superconductor, a different critical state expression is needed. Bean model is one of the simplest and widely used critical state models. The Bean model focuses on the macroscopic behaviour of the superconductor properties, obtained from the experimental results of the relationship between the critical current and the electric field, which is particularly useful for engineering application since the microscope is not in interest. Bean model states that the current density in the superconductor has only three values, either 0 where no magnetic field is induced in the superconductor or equal to the critical current density where the magnetic field is induced. Eq. 2.3 describes the Bean model [26].

$$J = \begin{cases} 0, & \text{if } |B| = 0 \\ \pm J_c, & \text{if } |B| \neq 0 \end{cases} \qquad \text{Eq. 2.3}$$

Bean considered superconducting tape as only an infinitely long slab with a thickness of 2a as shown in Figure 2.11. Since the thickness of the slab is very thin, with only about 1 μm, only the applied field that is the parallel to the wide face (z-axis) are needed to consider. Ampere's law in Eq. 2.4 can be simplified into Eq. 2.5 since only the field along the z-axis is considered.

$$\nabla \times \mathrm{H} = \mathrm{J} = J_c \qquad \text{Eq. 2.4}$$

$$^{\mathrm{dB}}/_{\mathrm{dx}} = \mu_0 \mathrm{J}_c(\mathrm{x}) \qquad \text{Eq. 2.5}$$

From Eq. 2.5, it can be seen that the distribution of magnetic field flux within the superconductor will linearly decrease to zero where the critical current disappears along the slab. As shown in Figure 2.11 (a), where only the external magnetic field *B* is applied along the z-direction without transport current *I*, the magnetic field inside the superconductor slab induced by screening circulating superconducting current is also along the z-axis but with opposite direction to the applied external magnetic field due to the shielding effect of type II superconductor. The solid line occurs when the applied external magnetic field increases so that the magnet field inside the superconductor is fully penetrated in the slab, from Eq. 2.5, the fully penetrated field is expressed as $B_p = \mu_0 J_c a$, while the corresponding circulating superconducting current density is distributed in the whole slab with opposition direction. The Figure 2.11 (b) shows the magnetic field distribution with only applied transporting current without external magnetic field. Since the transport current is along the y-axis, the magnetic field inside the superconductor slab due to the shielding effect is along the z-axis with opposite direction. As shown in the solid line, when the applied transport current *I* is equal to the critical current I_c, the magnetic field in the superconductor slab reaches the maximum value and can be obtained from Eq. 2.5 as $B_{max} = {}^{\mu_0 I_c}/_{2}$.

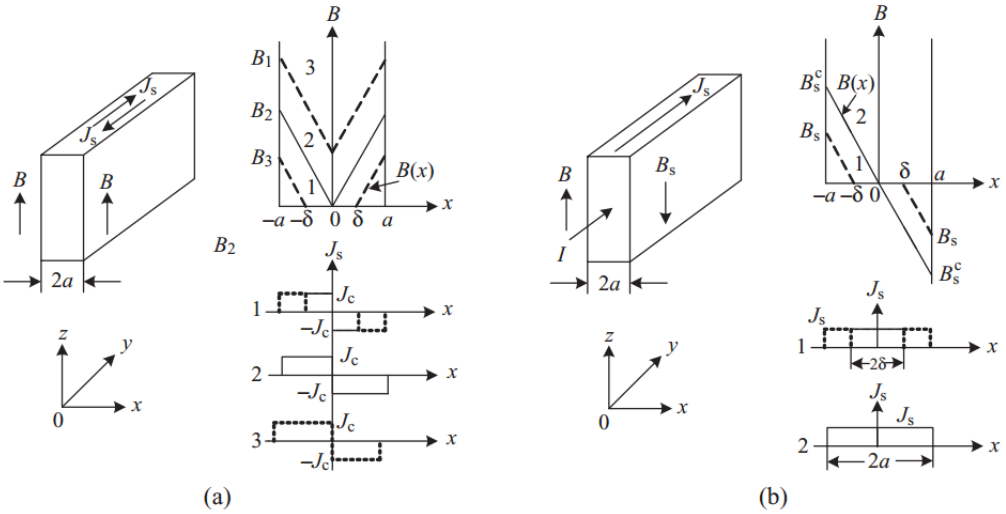

Figure 2.11: The distribution of the magnetic field and current density based on the Bean model under (a) applied external magnetic field *B* without transport *I* and (b) applied transport current *I* without external magnetic field *B* [27].

2.3.2 *E-J* power law

The Bean model is suitable well for most of the low-temperature superconductors (LTS), but not applicable for most of the HTS. Other than theoretical superconductor where only superconducting or non-superconducting mode exists with infinitely sharp transition, the transition is gradual for practical HTS tape according to the flux creep theory proposed by Anderson. It stated that the transition is not discontinuous [28]. Rhyner proposed the *E-J* power law as expressed in Eq. 2.6 to describe the non-linear relationship between the current density and electric field for an HTS tape, which fits well with DC experimental testing for many HTS tapes [29].

$$E(J) = E_c \left(\frac{J}{J_c}\right)^n \qquad \text{Eq. 2.6}$$

where *E(J)* is the voltage drop across the superconductor, E_c is the critical electrical field of 1 μV/cm, *J* is the transporting current density of HTS tape, J_c is the critical current density at 1μV/cm criterion. According to the international standard criterion (IEC), J_c takes the value when the voltage drop across the superconductor is 1 μV/cm in self-field at 77 K (liquid nitrogen temperature). n is the exponent. A

superconducting tape can be hence characterized by an $E-J$ curve, as shown in Figure 2.12. For the transition from superconducting state (zero resistance) to non-superconducting state (resistive state), the higher n value leads to a sharper transition in the $E-J$ curve and Bean model for superconducting wire comes from infinite n values. For 20 < n < 30, it is a good approximation for YBCO HTS tapes.

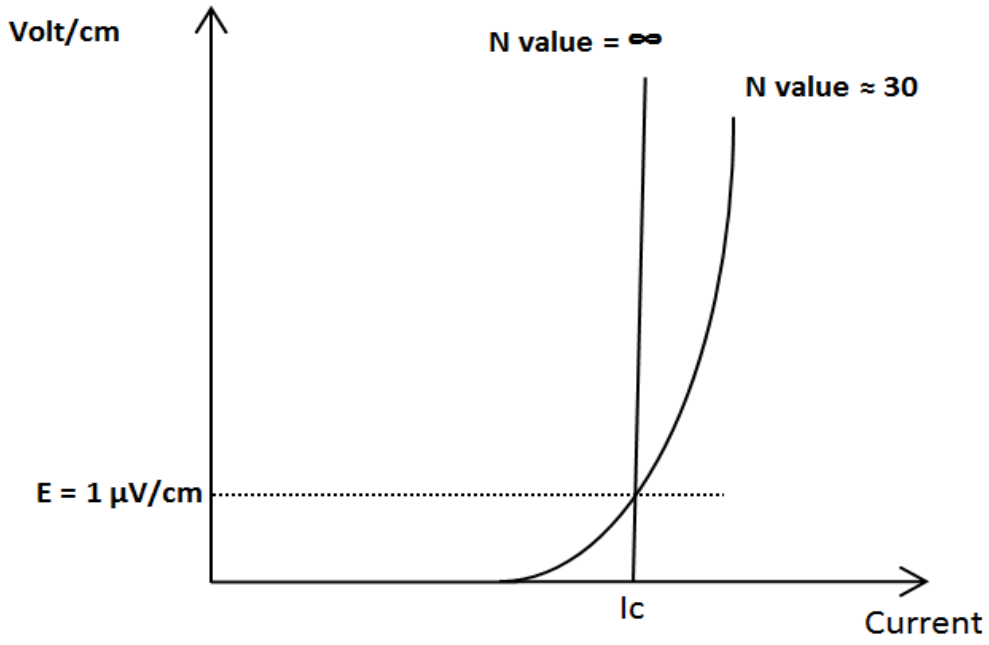

Figure 2.12: The sketch of *E-J* curves when N = ∞ for Bean Model and N = 30 for practical HTS tape.

2.4 Review of HTS power cables

2.4.1 The HTS cable system

2.4.1.1 The configuration of the HTS power cable

The HTS cables can be classified into two categories based on the cooling type for insulation: warm dielectric (WD) HTS cable, where the insulation of the cable is at the room temperature; cold dielectric (CD) HTS cable, where the insulation of the cable is at the cryogenic temperature. The major differences are the conventional cross-linkable polyethylene compounds (XPLE) insulation material used in the copper underground cable can be still used in the warm dielectric HTS cable. However, in the cryogenic environment, a material known as Polypropylene laminated paper (PPLP) can be used as the insulation for CD HTS cable due to the properties that PPLP can keep flexible for bending the cable and withstanding a high breakdown voltage in the liquid nitrogen environment. There are some WD HTS cable projects around the world, such as the 33.5 m/35 kV/2 KA WD HTS cable project in Yunnan, China in 2004. This technology is replaced by the CD HTS cable in the superconducting cable R&D projects afterwards. Figure 2.13 shows the typical structure of the single phase CD HTS cable.

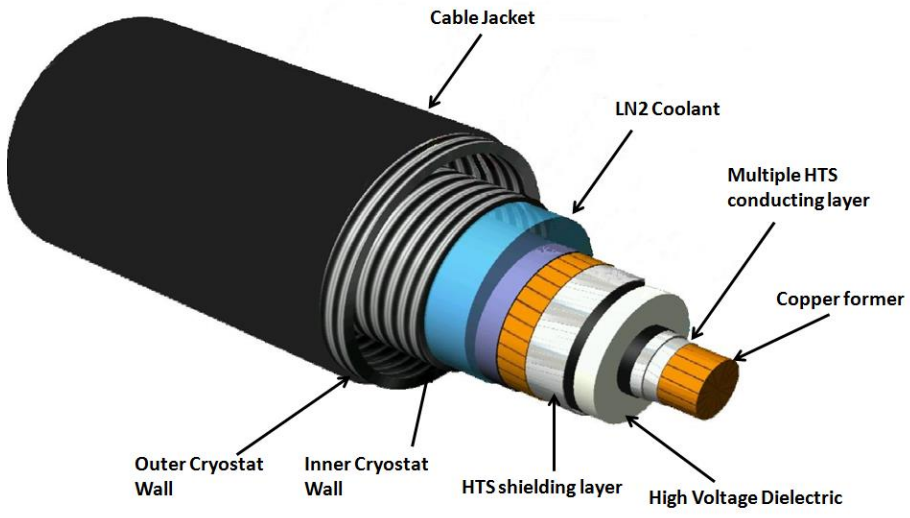

Figure 2.13: The configuration of single core DC HTS cable.

The functions of each layer in CD HTS cable are discussed as below:

- Copper former: the frame of the cable and conducting a certain amount of overload current when the HTS cable is in faulty condition to prevent HTS tapes from permanent damage.
- HTS conducting layers: the main current conducting layer, multiple conducting layers can increase the current carrying capacity.
- PPLP cold dielectric layer: the insulation layer that can withstand high transmission voltage in the cryogenic environment.
- HTS shielding layer: the shielding layer that prevents the leakage of the electromagnetic field.
- Cryogenic coolant: Constantly provides liquid nitrogen coolant to refrigerate the superconducting cable in order to operate below the critical temperature.
- Inner and outer cryostat walls: The vacuum room between the inner and outer cryostat can provide thermal insulation to prevent thermal leakage.

Another more compact configuration is three electrical phases of HTS conductors are concentrically wound on a single cable core, known as triaxial cable [30]. Figure 2.14 shows the configuration of the triaxial HTS cable. Each phase is separated by PPLP insulation layers which are immersed in the circulating LN_2 cooling path as well. This compact size is not achievable by using conventional cable. Since the difference of phase angle of each electrical phase is 120^0, the combination of the three phase current is zero, it significantly reduces the stray field outside the cable. Unlike the superconducting shielding layer required for the single core HTS cable, only copper is needed for shielding the stray field. Hence, the usage of superconducting material is reduced to one-half for triaxial HTS cable.

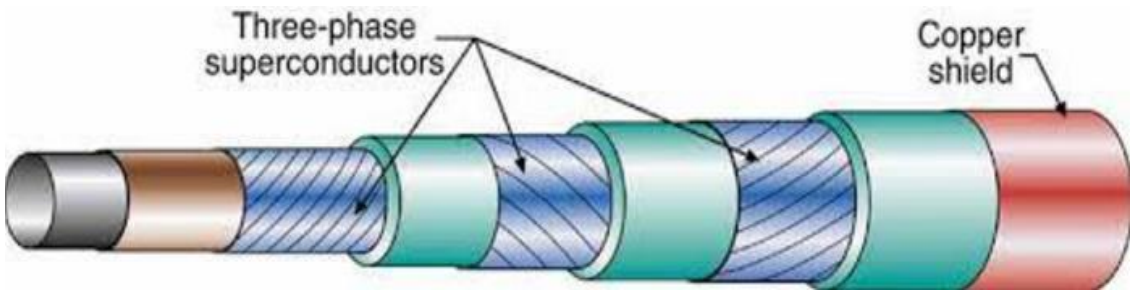

Figure 2.14: Configuration of the triaxial CD HTS cable [31].

2.4.1.2 Insulation layer of superconducting cable

The design of the PPLP insulation for CD HTS cable has not been standardized so far. The different material properties of the PPLP compared with the XLPE make the conventional cable insulation design experience not applicable for the CD HTS cable. Generally, this research subject focuses on the electrical breakdown voltage of laminated PPLP paper when immersed in the liquid nitrogen. Even tiny bubbles in the insulation layers will affect the electric stress distribution and the nitrogen gas may become conductivity under occasionally extreme high voltage. Due to this reason, the practical superconducting cable projects always operate at sub-cooled liquid nitrogen temperature at 70 K and high pressure of liquid nitrogen flow to ensure no bubbles in the dielectric insulation, especially during a fault. Until now, the PPLP insulation design is based on the empirical formula from the experimental measurement results [30]. Figure 2.15 shows the sketch of the insulation layer of the HTS cable.

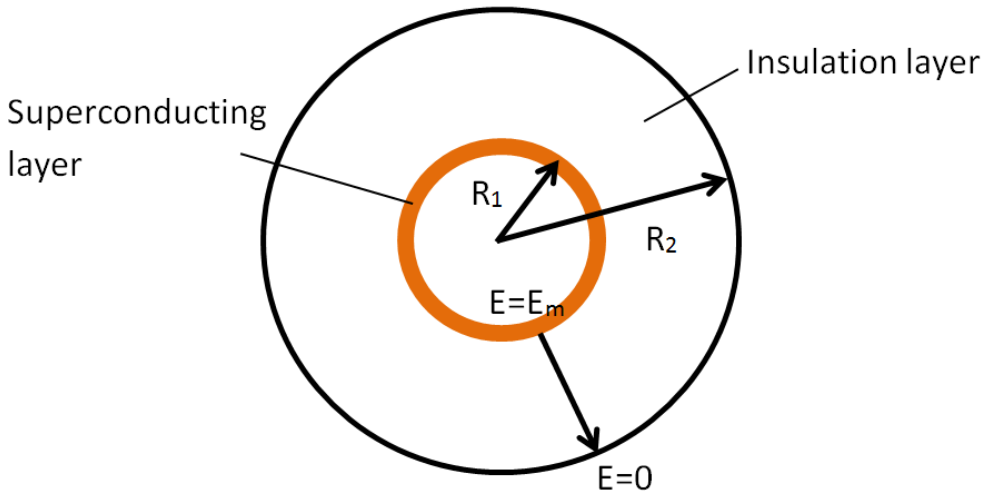

Figure 2.15: the schematic of the insulation for the CD HTS cable.

The maximum electrical stresses E_m takes place at the surface of the superconducting conducting layer and assuming the zero electrical potential is at the outer side of the insulation layer. If the thickness of the insulation layer is less than 50 mm, i.e., the voltage level of the HTS cable is less than 200 kV, the electrical stress E_m can be expressed as Eq. 2.7:

$$E_m = At^{-B} \quad \text{Eq. 2.7}$$

where the constant A is equal to 47.8 kV/mm and B is equal to 0.1. t is the thickness of the PPLP insulation layer. According to Gauss's law applied to cylinder geometry, the electrical stress can be calculated by Eq. 2.8[30]:

$$E_m = \frac{V}{R_1 ln(R_2/R_1)} \quad \text{Eq. 2.8}$$

where V is the applied voltage of the HTS cable, the thickness of the insulation can be expressed as Eq. 2.9:

$$t = R_1(e^{V/(E_m \cdot R_1)} - 1) \quad \text{Eq. 2.9}$$

Taking 20% of the extra safety margin into consideration, the actual thickness of PPLP insulation of CD HTS cable is set to be 1.2t [32]. This equation is applicable to the cable of voltage rating below 200 kV.

2.4.1.3 The cooling system for superconducting cable

A superconducting cable cooling system contains a cooling station, cable terminations and cryostat with LN_2 feeding lines. The outline of the system is shown in Figure 2.16. The LN_2 circulates in the cable loop to provide cooling source. A circulation pump is installed in the LN_2 circulating loop to ensure a certain amount of LN_2 flow rate and pressure. Heat is dissipated in the LN_2 circulating loop resulting in the inlet and outlet temperature difference, which is usually controlled within 5 K [33] by the additional heat exchange device. There are two techniques to remove the heat by primary heat

exchange: one is using a bulk LN_2 container as the primary cooling source, which is the so-called open loop cooling system; and another one uses cryocoolers, which is the so-called closed loop cooling system. Regularly refilling the LN_2 container is required for the open loop cooling system while only electrical power is required after initial cooling by LN_2 for the closed loop cooling system. However, for long distance HTS cable with closed loop system, a considerable amount of investment is required for cryocoolers, which compromises the economical operation for HTS cable [34]. Hence, the majority of the long distance HTS power cable projects are implemented with an open loop cooling system, while the closed loop system is more applicable to short distance HTS cable in the submarines, ships or aircraft.

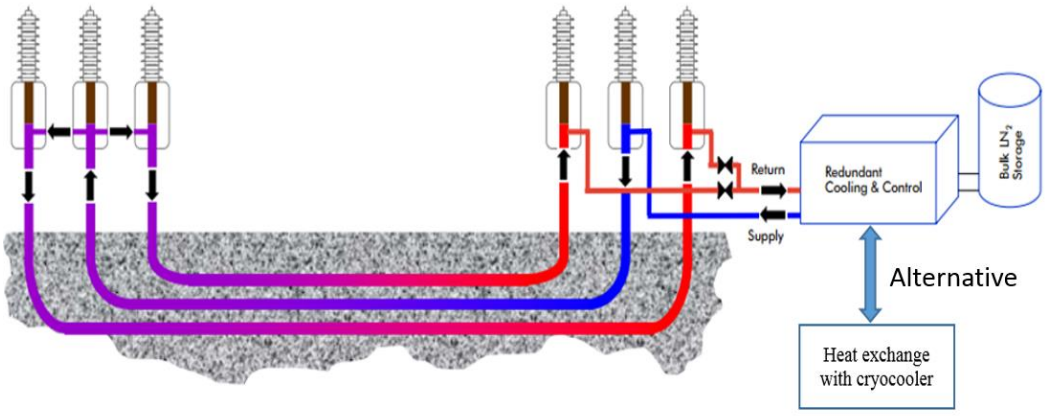

Figure 2.16: The self-circulating cooling system for superconducting cable.

2.4.2 The history of superconducting cable development

Although the superconductivity phenomenon was discovered since 1911, it was not used in large-scale power applications since the low-temperature superconductors require extremely high capital investment, especially for power transmission cables. Only after 1987, the discovery of high temperature superconductor ($Bi_2Sr_2Ca_2Cu_3O_{10}$ silver-sheathed) triggered the development of superconducting electrical power cable since the significantly simplified cooling method can be achieved by LN_2.

Prototype superconducting power cable projects were initially carried out in Japan since 1993, by Sumitomo Electric Industries, Ltd. The Ag-sheathed Bi-2223 tapes were used for the cable construction since they were the first commercially available.

The cable length is 7 m with a critical current of 1000 A [35]. From 1997 to 1999, Sumitomo Electric demonstrated a 30 m long 66kV/1kA superconducting power cable, which made considerable progress on the issues of long superconducting cable manufacturing process, large current capacity, and reliable dielectric in LN_2 environment [36].

Following the Southwire in the US and the NKT in Denmark, the world's third superconducting cable operating in the power grid was developed in China by Innopower Superconductor Cable Co., Ltd in 2004. The 3-phase 35kV electric system contains three single-phase HTS cable with six HTS layers, total 112 Bi-2223 tapes were used for each cable. The total cable length is 33 m flange to flange with rated operating current of 2 kA_{rms}. This project utilized warm dielectric, hence, XLPE is used as the cable insulation material. Until 2012, it has been the superconducting cable in the world with the longest operational time and transmitting the most electrical power in the real grid [37].

The 34.5 kV HTS power cable project in Albany, NY was the first superconducting cable fabricated by YBCO tapes supplied by SuperPower. Compared with 1G tapes, the YBCO tapes are superior in higher critical current density, mechanical properties and the thermal stability. The major accomplishments of this project are fewer conductors been used thanks to the compact size of YBCO HTS, and the high current density results in a considerable reduction in cable capital investment [38].

In 2014, the longest high temperature superconducting cable in the world was successfully installed into the electrical power grid in Germany. The total length of the HTS cable is about 1 km connecting two substations in the city of Essen, which is the pilot project supported by REW, Nexans and KIT, referred as 'AmpaCity'. The design of the AmpaCity superconducting cable is based on the three-phase concentric structure. The cable former is a hollow former made of the corrugated tube, which is used as the cooling channel of the LN_2. All the three phases are concentrically wound around the cable core and separated by PPLP insulation layers. The cable core is placed in the cryostat with a thermally insulated vacuum space. As a result of installing AmpaCity superconducting cable, 4 out of 10 110/10 kV transformer substations were demolished in the downtown area of Essen by using 10 kV HTS

cable system. In comparison with the conventional 110 kV cable system, 10 kV HTS cable has much simpler structure and requires mush less room for cable underground conduit and equipment installation. The overall investment of 10 kV HTS cable system is much lower than the conventional 110 kV power cable in the grid [39]. Table 2.3 summarizes the superconducting cable projects carried out around the world.

Table 2.3: Summaries some of the HTS cable projects carried out around the world.

Company	Rating	Length	Material	Location	Year
Sumitomo	22.9 kV/1.25 kA	100 m	Bi2223	Gochang	2006
Innopower	35 kV/2 kA	33 m	Bi2223	Yunnan	2004
VNIIKP	20 kV/1.4 kA	200 m	Bi2223	Moscow	2010
Sumitomo	34.5 kV/800 A	350 m	Bi2223	Albany	2006
Nexans	10 kV/400 MVA	1000 m	Bi2223	Essen	2013
Nexans	10 kV/1 kA	30 m	YBCO	Madrid	2008
LS cable	22.9 kV/ 50 MVA	400 m	YBCO	Seoul	2011
Sumitomo	66 kV/ 5kA	15 m	YBCO	TECOP	2012
Nexans	138 kV/ 1.8 kA	30 m	YBCO	Hannover	2007

2.4.3 Integration of HTS cable in the electrical power network

Compared with conventional underground power cables, the properties of HTS cable have profound benefits on upgrading the existing power grid. Firstly, the advantages of the low impedance of the HTS cable is able to transmit the same power capacity at much lower voltage or deliver high power at the same voltage level. The efficiency of the power grid can be improved significantly. Secondly, the investment of the HTS cable construction work is much lower than the conventional underground power cable in the high-density urban cities, which could be an alternative solution for the distribution power network upgrading projects. Thirdly, the mix of the conventional underground power cables and HTS cables in the grid is inevitable in the near future based on the current development of the HTS cables projects, hence, there is considerable impact on the power flow of the grid due to the very low impedance characteristics of the HTS cable installing into power grids [40].

2.4.3.1 Reconfiguration of the conventional power grid by integrating HTS power cable

Due to the very low impedance of HTS cable, very little resistive losses dissipated along the transmission line compared with the conventional copper cable. Hence, it no longer requires high voltage level to transmit the power to reduce the energy losses. Alternatively, a much lower voltage can fulfil the energy transmission efficiency requirements. Figure 2.17 gives the comparison between conventional XLPE cable and HTS cable with power transmission capacity with rated voltage level [41]. It can be seen that if the 230 kV voltage level is required for XLPE cable to transmit 500 MVA power, equivalently, only 69 kV voltage level is required for HTS cable to transmit the same amount of power. Based on this principle, fewer substations and switchgear are required, as shown in the Figure 2.18. The electrical power can be even ideally transmitted from power plants directly to the distribution networks without any substations. Hence, huge investment saving is possible for the HTS cable grid construction [42].

2.4.3.2 The cost-effective of the HTS installation

Although the cost of superconducting materials is much more expensive than the metal conductors, currently, the cost of copper is 6-22 $/kA·m while the YBCO is typically around 200-500 $/kA·m, the overall construction cost and the maintenance of the HTS cable are cheaper than the copper cable in the high popularity area. Considering the land cost of cable construction project, the HTS cable can be a cheap solution for solving the power congestion in the inner city by replacing the conventional power cable in the same underground electrical cable conduits since the investment of the underground cable largely comes from the extremely limited and valuable underground space. More than five times power transmission capacity upgrading can be achieved by HTS cable through the existing underground cable conduits space with barely any losses. Figure 2.19 shows the estimation of cable construction cost comparison between the XLPE cable and HTS cable. It can be seen that the overall cost of HTS cable is much lower due to the advantage of cost reduction in the cable conduits and switchgear.

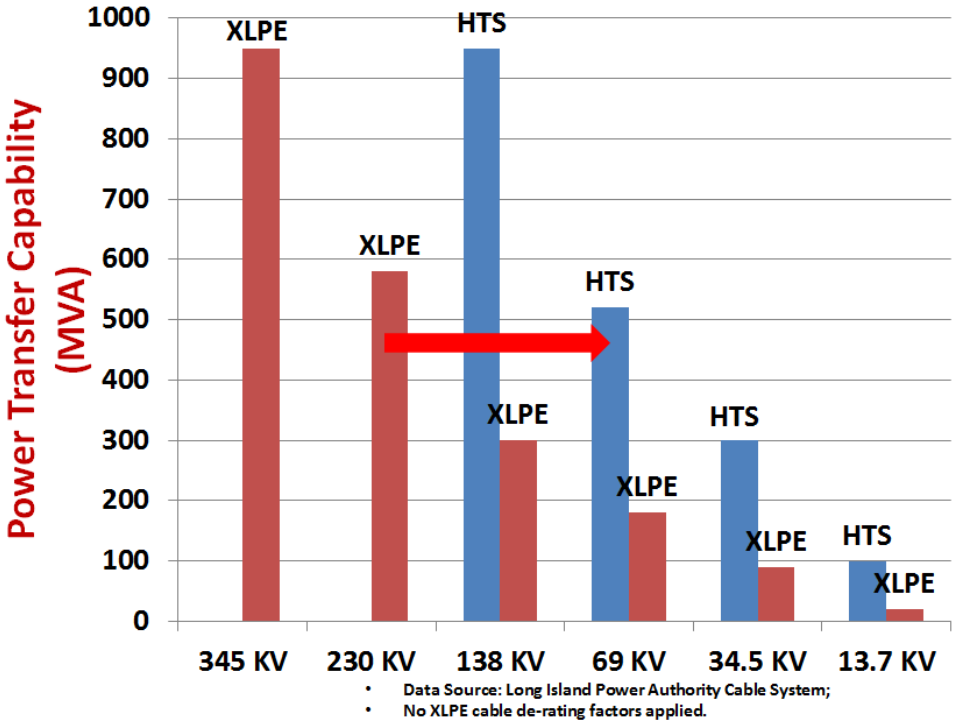

Figure 2.17: The power transmission capacity and voltage level of XLPE cable and HTS cable.

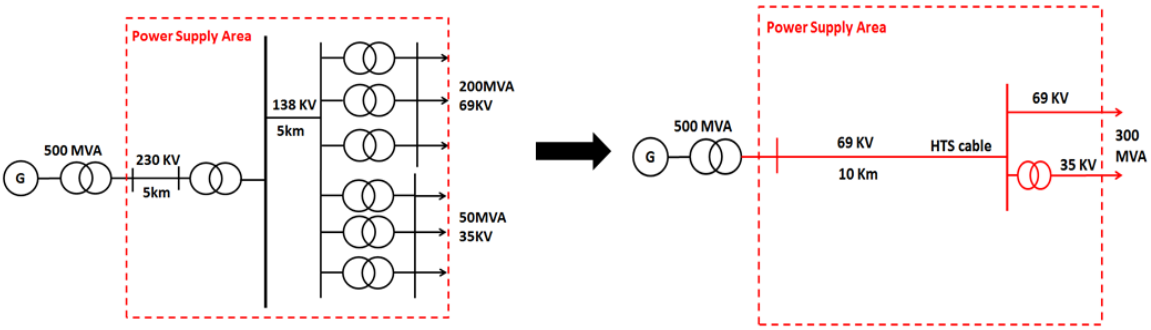

Figure 2.18: The simplified power network replaced by HTS cable.

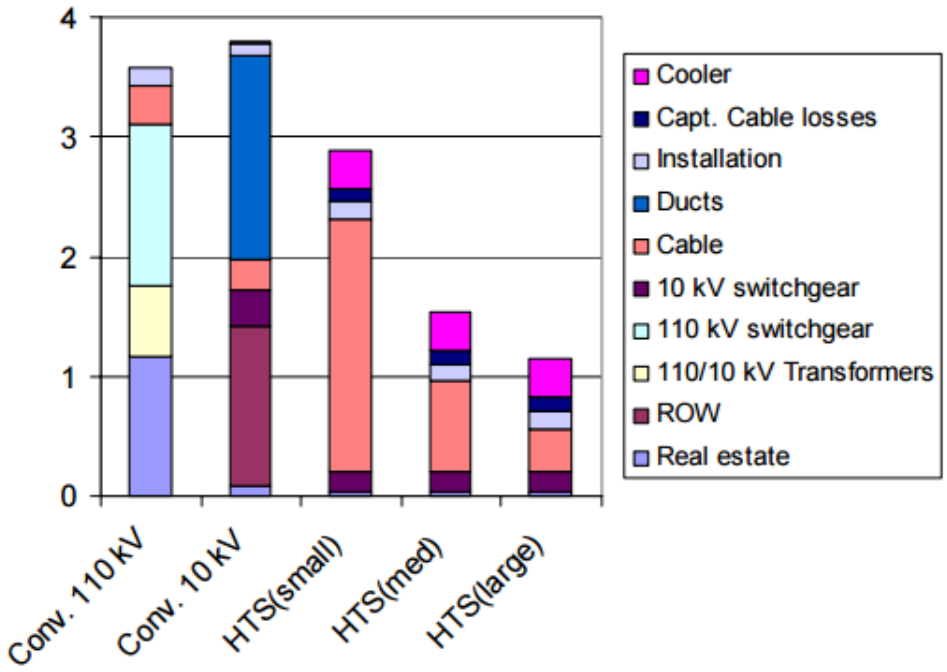

Figure 2.19: The construction cost comparison between the XLPE cable and HTS cable [31].

2.4.3.3 Impact of power flow by installing HTS cable into conventional power grid

Although the properties of HTS cable can largely improve the transmission efficiency of power grids, the expensive initial investment and cost of the maintenance will make the utilities very cautious to completely replace all conventional cables with HTS cables. In the near future, the combination of conventional cables parallel with HTS cables will exist in grids as shown in Figure 2.20 [43]. The HTS cable can be treated as very low impedance cable. Since the HTS cables are capable of carrying bulk power and the impedance is very small, the issue of large power immediately diverted into the path with low impedance may cause grid instability without proper control of power flow. However, a simple device, such as phase angle regulator module, can be placed in series with the HTS cable can be used to control the power flow so that the power can be 'pulled' into the HTS cable or 'push' back to the conventional power grid when necessary. This is an advantage of enhancing the controllability of power flow in a simple way [44].

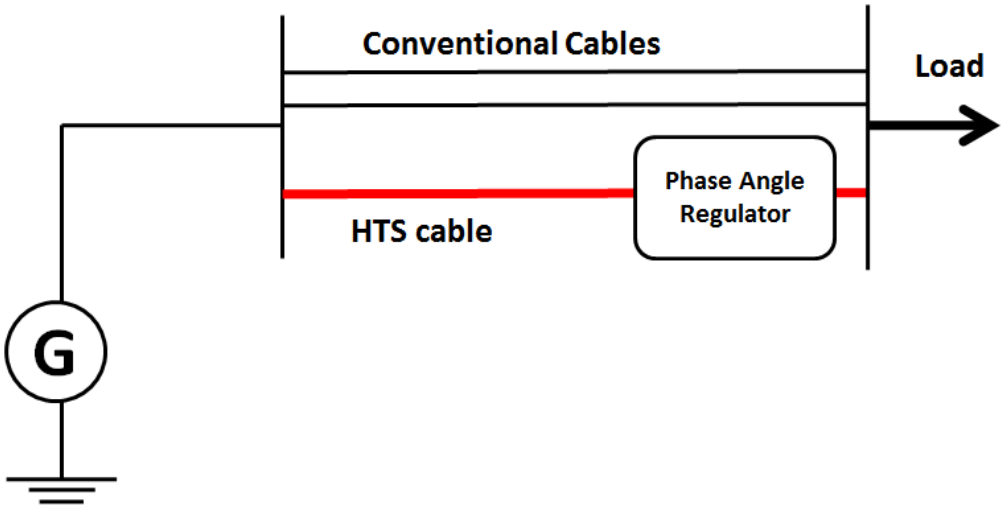

Figure 2.20: The structure of the conventional cables and HTS cables.

2.5 Current challenges with HTS cable

Currently, the long single-piece length of YBCO HTS wire is available for massive commercial production up to 1000 m and the longer length is also available with splices. The YBCO HTS tape has compact overall size and higher engineering critical current and the cost-performance of 2G HTS wires have been significantly improved in recently R&Ds. Due to these, the project in the dissertation is mainly focusing on the 2G HTS wire to fabricate and test the superconducting power cable. However, there are several challenges to investigate before applied the YBCO HTS power cable into the real power grid.

- The design of the HTS cable should focus on the maximization of critical current because of relatively expensive of YBCO HTS tape. The YBCO HTS tape has a flat and thin cross-section and its critical current is sensitive to the magnitude and orientation of the external magnetic field and the tapes wound in the cable experience magnetic field in the cable. Hence, it is necessary to understand the factors that influence the critical current of HTS cable. This will be investigated in Chapter 3.

- The design of the HTS cable should also focus on the maximization of transmission efficiency. Unlike the convention power cable, each individual HTS tape in the cable takes a crucial part of transporting current. Hence, all HTS tapes

are expected to carry the same amount of current in order to achieve maximum current capacity. But once the current is distributed from cable termination to each HTS tape, it is difficult to control and monitor the distributed current among the tapes. On the other hand, the negligible resistance of HTS tape makes the inductance dominating the cable impedance, which can also affect the current distribution. Hence, the investigation of the homogeneous current distribution of HTS cable is the key to improving the transmission efficiency. This will be investigated in Chapter 4.

- The cooling system is an essential part of HTS power project. The heat that is dissipated due to AC loss of HTS cable needs to be constantly removed by a cooling system. However, the lack of reliable model makes it difficult to predict the AC loss of HTS cable. The experimental measurement method provides an alternative solution but it is still difficult to directly measure due to the AC loss is extremely small. Detailed measurement method and several improvements of HTS cable AC loss measurement will be discussed in Chapter 5.

- The behaviour of HTS cable in the meshed power grid is still unknown due to the current superconducting cable R&D projects are in small scale. Since the stability of power grids is crucial, it is necessary to anticipate the influences of the HTS cable integrated into power grids using power system analysis tool before applying superconducting cable into power grids. Detailed superconducting component developed in PSCAD/EMTDC and impact of HTS cable integrated into the power grids will be presented in Chapter 6.

Chapter 3

The investigation of critical current for YBCO HTS cable

The critical current is an important parameter in the description of the performance of YBCO HTS cable. The effect of the anisotropic characteristics of the HTS tape on the cable critical current is considered in this chapter. The HTS cable wound with YBCO tapes is subjected to magnetic cable field. Due to the anisotropic characteristics of YBCO HTS tapes, it is necessary to know the field dependent critical current density of YBCO HTS tapes in the cable geometry. An FEM method implemented with modified Kim model demonstrates that the anisotropy changes the current density distribution inside the HTS tapes wound in the cable and the gap distance between the adjacent tapes changes the cable magnetic field distribution. Therefore, the gap distances determine the cable critical current due to the anisotropic characteristics. An equivalent HTS cable circuit model was designed in order to investigate the behaviour of critical current affected by various gap distances between the parallel placed HTS tapes. The results show that the critical current of the HTS tape in the cable field can be significantly increased if the gap distance is less than 1mm. The results are also modelled using FEM numerical methods to calculate the magnetic field distribution to verify the experimental results. The presence of contact resistances between the HTS tapes and cable joints are inevitable during HTS cable fabrication process. A short prototype HTS cable has been constructed to investigate the influence of contact resistances on cable critical current compared with anisotropic influences. The results show that the contact resistance has dominated the current sharing of each HTS tape in the cable so that the influence of anisotropy becomes less important.

3.1 Critical current of HTS cable influenced by anisotropic characteristics

YBCO HTS tapes have offered significant advantages for power cables since the manufacture of long length YBCO HTS tape has become available, and high critical current density has been achieved in high irreversibility fields, hence, YBCO HTS tapes have become a promising solution for power cable development. As defined in the sketch of Figure 3.1, due to the anisotropic characteristics of the YBCO HTS tapes, critical current density $J_c(B,\theta)$ depends on both the magnitude B and the direction θ of the local magnetic field [15]. Although scientists are looking for solutions in order to enhance the pinning force of vortices in all directions for improving the field dependency of $J_c(B,\theta)$, due to the high aspect ratio of YBCO HTS tape, the pinning force of vortices parallel to the *c* axis is much weaker than that parallel to the *ab* axis. As a result, the magnetic field *B* that is parallel to the *c* plane has a larger influence on critical current density than that parallel to the *ab* plane [45]. YBCO HTS tapes no longer experience self-field once assembled as cable structure, instead, they experience low magnetic cable field, usually less than 0.1 T or 0.2 T [46]. Hence, the critical current density of HTS tapes in the cable is affected by both the magnitude and orientation of the cable magnetic field due to the anisotropy. In other words, the cable magnetic field distribution influences the critical current of YBCO tapes in the cable. Constant current density as critical state model is inadequate to determine the critical current of HTS cable. In order to accurately analyse the critical current of HTS cable, quantitively determining the anisotropic field dependence $J_c(B,\theta)$ of YBCO HTS cable is required. Once the $J_c(B,\theta)$ of the specific tape is determined, the critical current density of HTS cable can be accurately predicted by FEM numeric modelling.

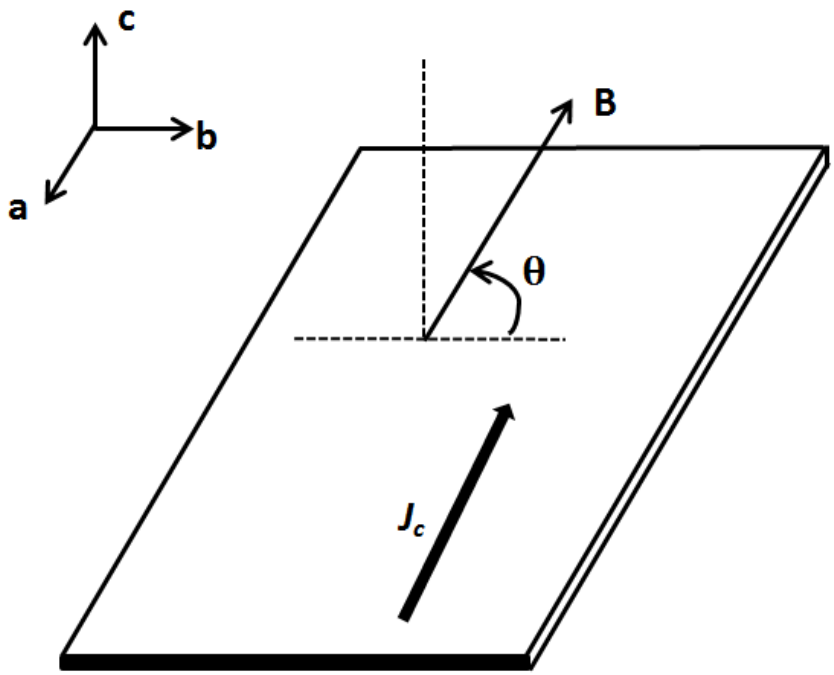

Figure 3.1: The sketch of the YBCO HTS tape under external magnetic field B with an orientation angle of θ, J_c is the critical current density.

3.1.1 Experimental characterization of anisotropy of YBCO HTS tape

The Kim model provides a useful engineering solution to describe how the critical current density varies with local magnetic field due to YBCO HTS tape anisotropy [47, 48], but there is a lack of accuracy due to the properties of the YBCO tapes varying with suppliers. The direct interpolation of experimental data gives a fine description of tape anisotropy [49], but it requires measurement points to be taken at every orientation with respect to the magnetic field, and the accuracy is compromised at low magnetic field due to tape self-field influence. Alternatively, the $J_c(B,\theta)$ field dependency of critical current density can be described by the modified Kim model, which only takes into account the YBCO tape anisotropy for two magnetic field components, $B_{\parallel}$ and $B_{\perp}$. $B_{\parallel}$ is the magnetic field parallel to the tape ab axis and $B_{\perp}$ is the magnetic field that is parallel to the tape c axis [50]. Hence, the $J_c(B,\theta)$ field dependence of critical current density can be simplified to the $J_c(B_{\parallel},B_{\perp})$ field dependency, which can be determined from the in-field critical current measurement with external magnetic field. In this way, the characterization of YBCO tape anisotropy becomes simple but accurate to be used in Cartesian coordinate related

models. This can be achieved using conventional electromagnet with some modifications. However, the problem still exists since the $J_c(B_{\parallel}, B_{\perp})$ field dependent critical current density is difficult to measure accurately in low magnetic field due to the influence of the tape self-field. Hence, in this section, the in-field critical current of YBCO HTS tape was measured up to 700 mT with respect to the $B_{\parallel}$ and $B_{\perp}$magnetic field directions, so that the problem can be solved by performing a regression on the high-field critical current measurement data to find out the constants in modified Kim model and extrapolating $J_c(B_{\parallel}, B_{\perp})$ to obtain the low-field values [51].

3.1.1.1 The setup of in-field critical current of YBCO HTS tape measurement system

The macroscopic anisotropic property of YBCO HTS tape yields the critical current of the tape varying with the magnitude and orientation of magnetic field [52]. Therefore, the in-field critical current degradation measurements can be performed when YBCO HTS tape is placed in the external magnetic field. Firstly, a critical current measurement system was set up. Figure 3.2 is the overall schematic of the critical current measurement system. The superconducting tape is connected to a DC power supply and a shunt resistance in series. The liquid nitrogen bath is provided to cool the superconducting sample down to 77 K. The measurement system is fully programmable depending on the purpose of the experiment using LabVIEW. For the critical current of superconductor measurement, the LabVIEW program consists of three sections: data acquisition (DAQ), output current control and quench protection. Figure 3.3 shows the flowchart of the measurement program configuration [53]. The initial parameters are firstly input into the program, including the current ramping rate, sample length and limit of protection voltage. The data acquisition card stores the data, while the superconducting sample voltage and current values are continuously monitored by quench protection section. If the sample is not quenched, i.e., the limit of protection voltage is not reached, the current will continuously increase. Otherwise, the current stops increasing. In this way, a closed loop control is implemented in the program to protect the superconductor from permanent damage. The temperature is monitored throughout the whole measurement process by PT 100 thermal couples.

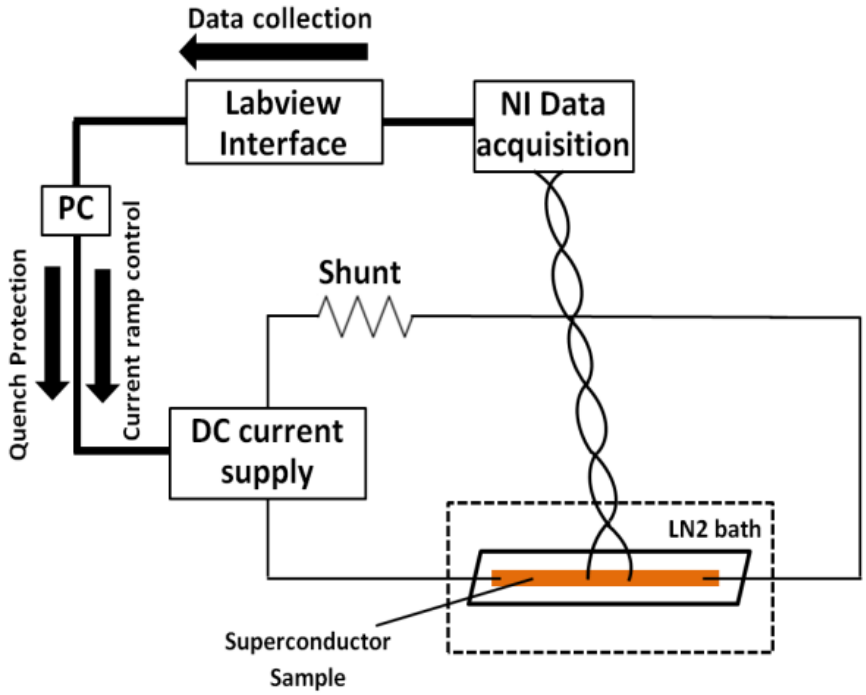

Figure 3.2: The schematic of the critical current measurement system.

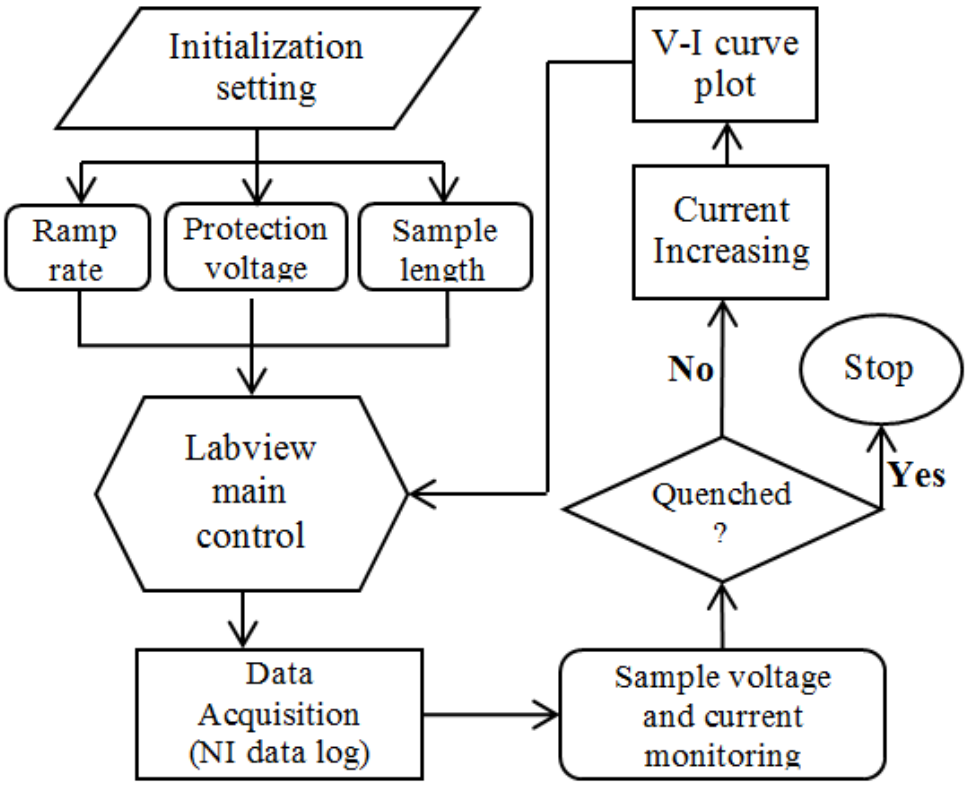

Figure 3.3: The flowchart of critical current measurement system configuration.

The DC current from the power supply is set with variable ramp rates. Figure 3.4 gives an example of charging and discharging ramping rates. The charging ramp rate becomes slower when approaching the critical current I_c to prevent damaging the superconductor, which is also the reason that the fast discharging ramp rate is usually set. The ramping current can be stopped at any point in order to investigate the properties of the superconducting applications with a steady DC current. In the case of any unexpected incidents occurring during the measurement, one can abort the ramping current at once. In order to allow users to interact with the power supply and data acquisition card through graphic icons and visual indicators, a graphic user interface (GUI) is developed using LabVIEW, as shown in Figure 3.5. The functions of the interface include V-I curve plotting, ramping current control and protection.

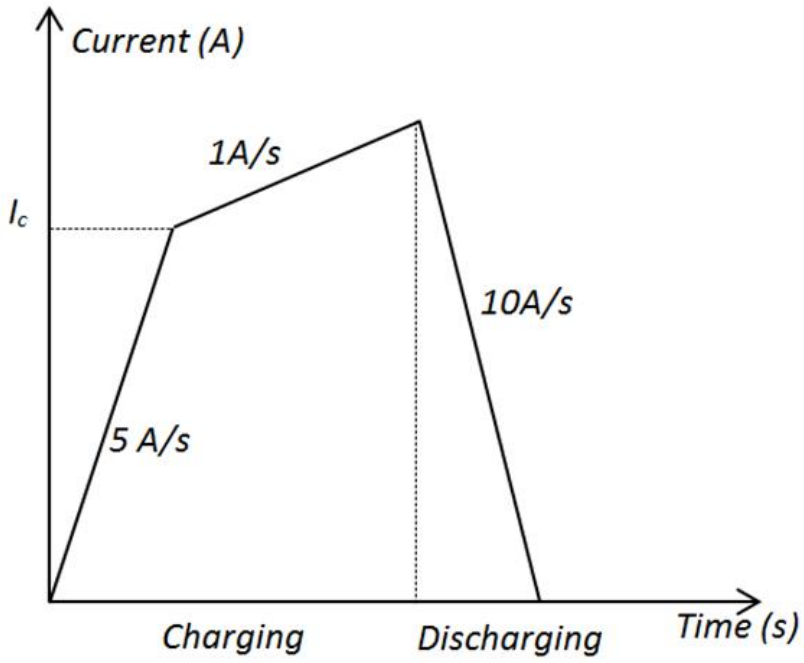

Figure 3.4: The DC current ramping rates example.

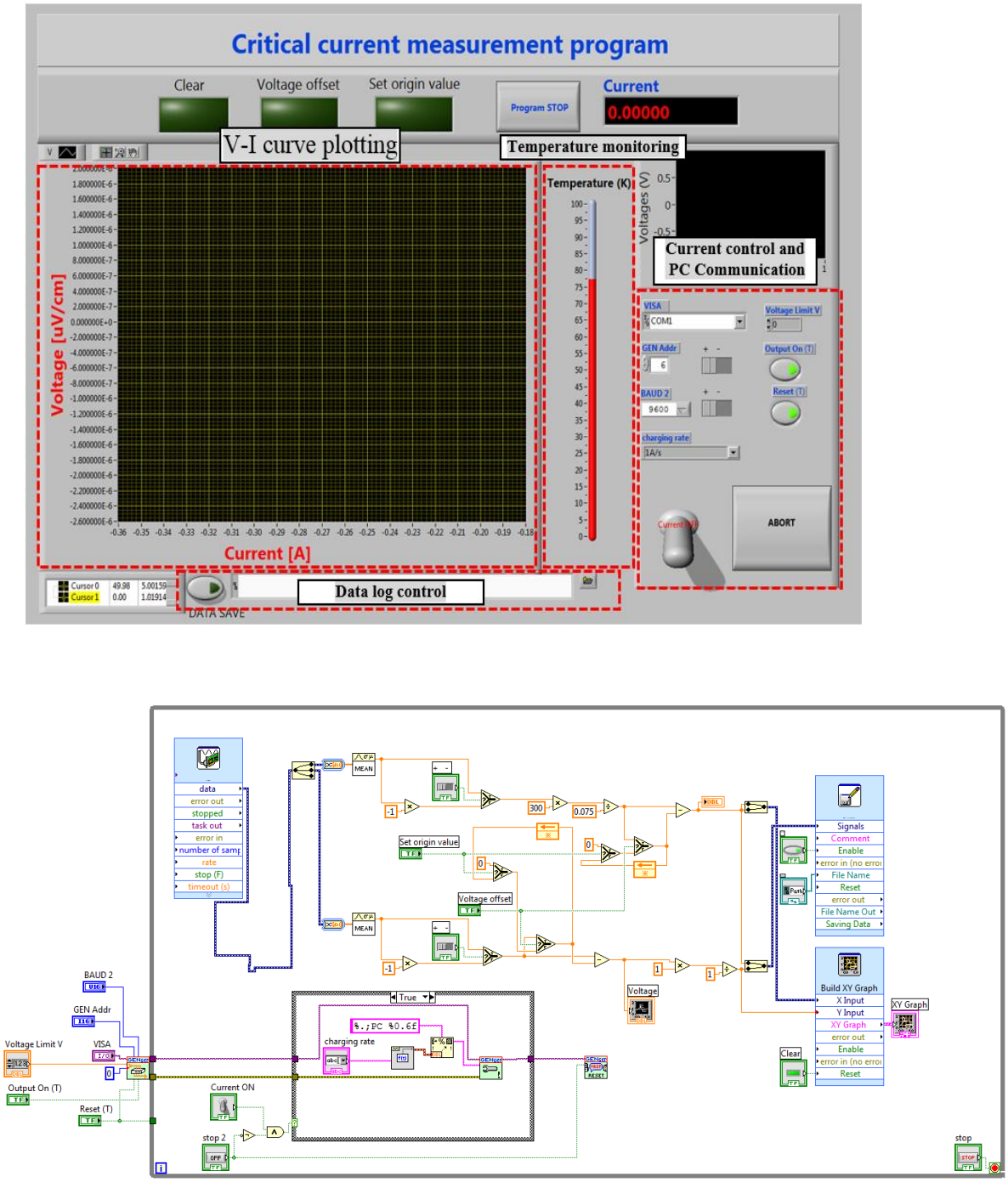

Figure 3.5: The GUI of measurement program developed using LabVIEW.

The critical current of YBCO HTS tape from SuperPower is measured at its own self-field using the critical current measurement system. The tape specifications are given

in Table 3.1. The tape was immersed in the LN_2 bath and a pair of voltage taps was soldered on the tape with an interval of 7 cm. The voltage signal was recorded by DAQ and displayed in LabVIEW GUI interface. Figure 3.6 shows the critical current measurement results of the tape. Under the 1μV/cm criterion, the critical current was measured at 130 A in the self-field, which is consistent with the minimum critical current as shown in Table 3.1 provided by the supplier.

Table 3.1: The HTS tape specification.

Items	Parameters
Supplier	SuperPower
Tape ID	2G YBCO SCS 4050
Laminate	Surrounding copper
Min I_c (77 K, self- field)	124 A
Average width	4 mm
Average tape thickness	0.1 mm
Average YBCO layer thickness	1 μm

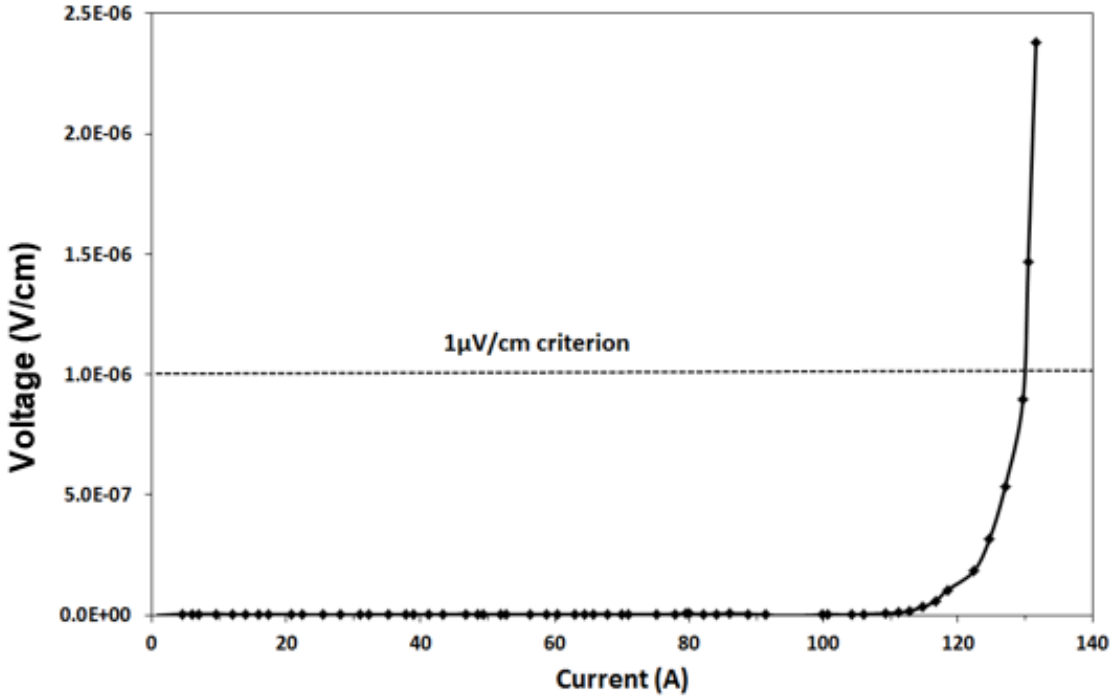

Figure 3.6: Critical current measurement result of YBCO HTS tape.

In order to measure the in-field critical current degradation of HTS tape, a completed electromagnetic field generator system was set up. Figure 3.7 shows the overall measurement setup. An electromagnet generator with two pole heads can generate a uniform magnetic field between the pole heads. A gauss meter is used to measure the average magnetic flux density in the centre of the pole heads. The electromagnetic field generator is powered by a voltage DC power source (225 V/28 A). Since the magnetic strength is linearly proportional to the current, the magnetic field can be controlled by varying the output current of the DC source. In high field measurements of 1 T to 3 T, the electromagnet generator is charged with current up to 28 A, which requires a cooling source to remove the dissipated heat. A self-circulating water chiller is used to cool the electromagnet generator down to the permissible operating temperature. The gap distance between the pole heads is adjustable for different sizes of the testing sample. However, the uniformity of the magnetic field is very sensitive to the gap distance. According to the supplier, the average central magnetic field uniformity $\Delta H/_H$ can reach as high as 1 % if the pole heads gap distance is less than 1 cm. Hence, the measurement that requires high uniformity of magnetic field should ensure that the pole head distance is sufficiently small.

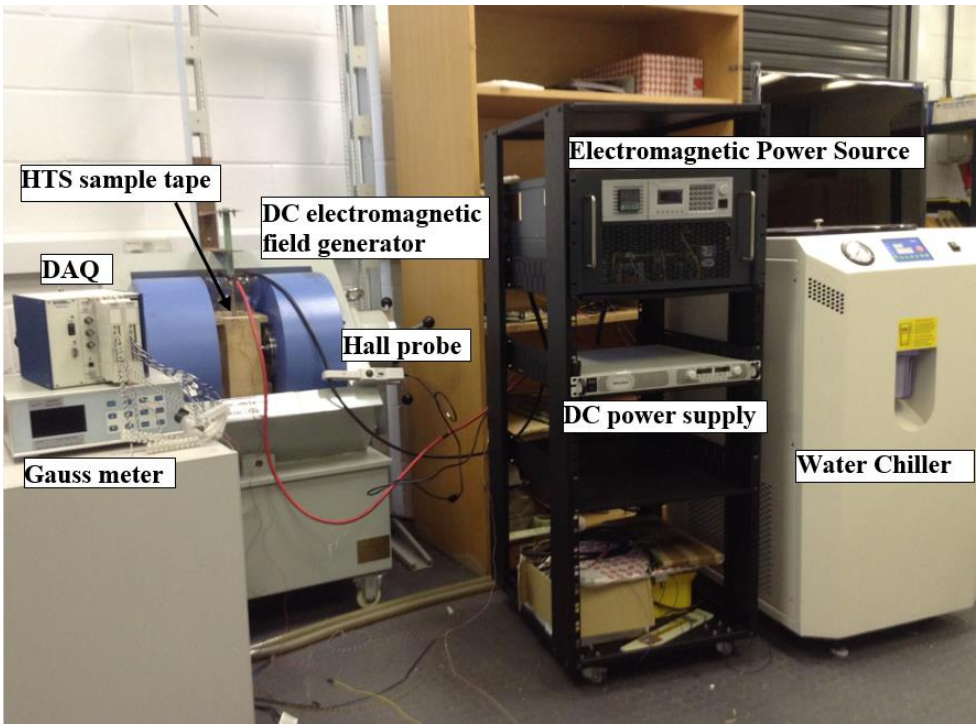

Figure 3.7: The setup of HTS tape field dependence measurement system

The YBCO HTS tape was placed in the centre of the pole heads to ensure the uniformity of the magnetic field is acceptable for in-field critical current measurement. An HTS tape sample holder is designed so that the HTS tape can be set at various angles with respect to the magnetic field. For this measurement, high uniformity of magnetic field is required because the properties of HTS tape are very sensitive to the magnetic field orientation due to anisotropy. In order to keep the pole heads gap distance sufficiently small and ensure enough liquid nitrogen for HTS tape cooling, a volumetric flask is used with sealed bottleneck downwards and cut bottom upwards is used as a LN_2 container. Figure 3.8 shows the sample holder in the electromagnetic field generator. The 4 mm wide SuperPower YBCO HTS tape was measured in a 500 mT magnetic field with varying orientation from 0^o to 180^o and the measured angular dependence of critical current is shown in Figure 3.9. The specifications of the tape can be found in Table 3.1. It can be seen that the tape has a maximum critical current with the field parallel to the tape and a minimum value with the field close to the perpendicular orientation, which is consistent with results reported in [54].

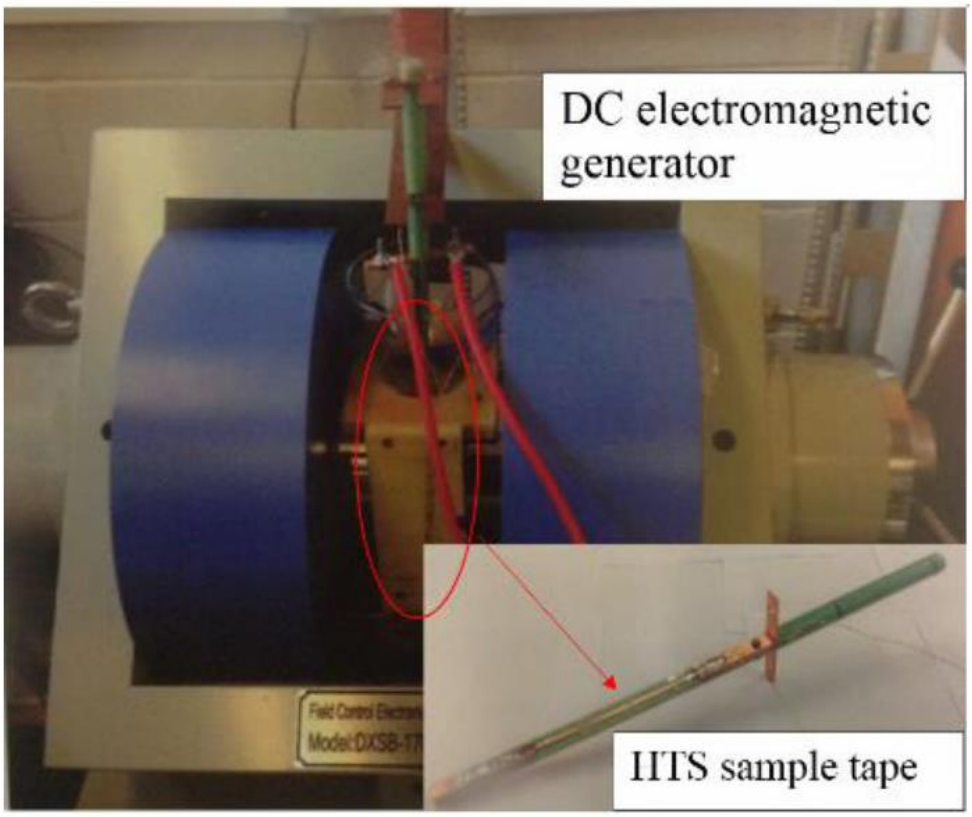

Figure 3.8: The HTS sample holder placed in the applied magnetic field.

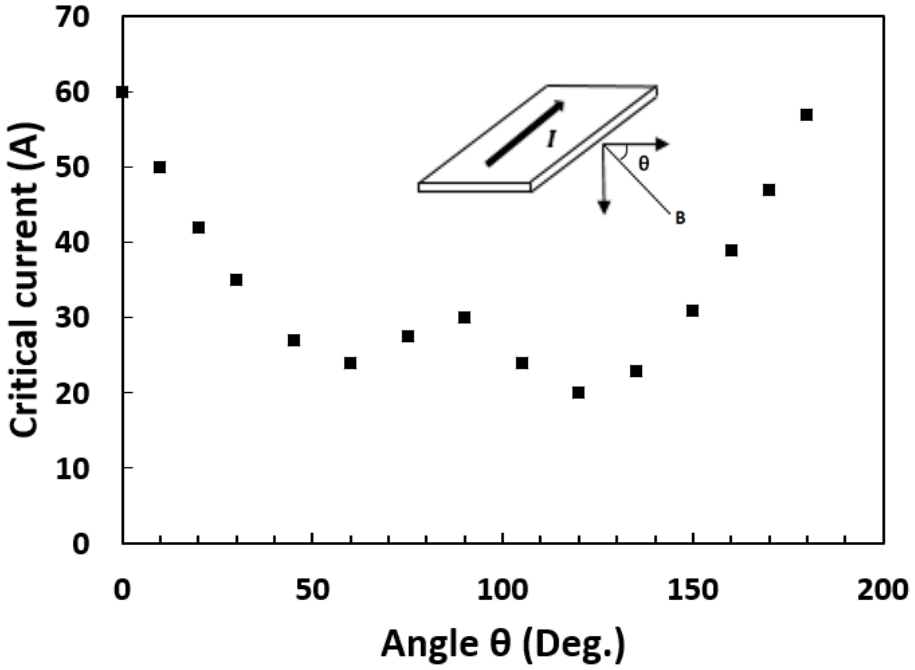

Figure 3.9: Measured angular dependence of critical current of YBCO HTS tape in 500 mT external magnetic field.

3.1.1.2 Determination of anisotropic characteristics of HTS tape by non-linear curve fitting

The $J_c(\mathrm{B}_{\parallel}, \mathrm{B}_{\perp})$ field dependence of YBCO tape is expressed by the modified Kim model as shown in Eq. 3.1 [50]. Considering the tape anisotropy, there are four parameters to be determined: critical current density of YBCO tape in the self-field J_{c0}, anisotropic scaling factor k, reference field B_0, and Kim model exponent α, which varies from the in-field properties of YBCO tapes from different manufacturers [55, 56]. These parameters can be extracted from experimental measurement of in-field critical current $I_c\,(B_{\parallel}, B_{\perp})$. In this case, an assumption has been made that the field dependence of the critical current density is considered to be the average value in the YBCO tape transversal area.

$$J_c(B_{\parallel}, B_{\perp}) = \frac{J_{c0}}{\left(1 + \frac{\sqrt{k^2 |B_{\parallel}|^2 + |B_{\perp}|^2}}{B_0}\right)^{\alpha}} \qquad \text{Eq. 3.1}$$

The SuperPower YBCO tape with 4 mm width has been measured in a 77 K LN_2 bath. As shown in Figure 3.6, the critical current is 130 A in the self-field. Since the modified Kim model only contains two variables: $B_{\parallel}$ and $B_{\perp}$, the tape was characterized in an external magnetic field of varying magnetic field strength with respect to the parallel and perpendicular field orientation, respectively. The measured field dependence of I_c ($B_{\parallel}, B_{\perp}$) is shown in Figure 3.10. The measurement results show that the critical current of the tape is less sensitive to the parallel field compared with the perpendicular field. In other words, the reduction of the critical current in the perpendicular field is more than that in the parallel field.

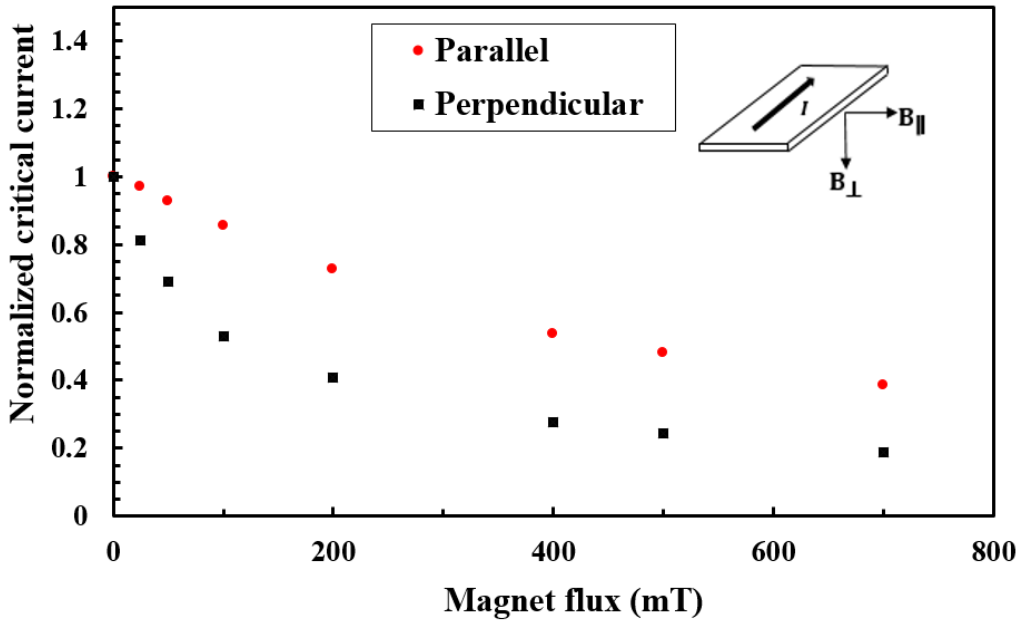

Figure 3.10: The measurement results of the in-field critical current of YBCO HTS tape.

Based on the assumption of average field dependence of critical current density, when the measured field dependence of I_{cm} ($B_{\parallel}, B_{\perp}$) of YBCO HTS tape is used to fit the modified Kim model, the integration of calculated in-field critical current density J_{cf} ($B_{\parallel}, B_{\perp}$) over the tape transversal area S should be consistent with the measured critical current, I_{cm} ($B_{\parallel}, B_{\perp}$). Hence, determination of J_{c0}, k, α and B_0 in the J_{cf} ($B_{\parallel}, B_{\perp}$) equation can be achieved through minimizing the difference between the measured I_c ($B_{\parallel}, B_{\perp}$) values. The tape's self-field critical current density J_{c0} can be calculated by dividing the measured self-field critical current by the tape transversal

area *S*. By observing Eq. 3.1, when only $B_\perp$ is applied, the parameter k is not applicable and then the parameters α and B_0 can be found using Eq. 3.2. When only $B_\parallel$ is applied, with the known α and B_0 values, the parameters k can be found using Eq. 3.3. There are many minimization algorithms that can be used in order to find these parameters, such as the Nelder-Med simplex algorithm [57]. However, the "Solver" function in Excel for non-linear curve fitting is implemented in this case [58]. Once the minimal values of Eq. 3.2 and Eq. 3.3 are known, the relevant parameters B_0, k and α in Eq. 3.1 are determined, which are summarised in Table 3.2.

$$minf(B_0, \alpha) = min \sum_i (I_{cm}(\mathrm{B}_\perp) - \int_S J_{cf}(\mathrm{B}_\perp, B_0, \alpha) \cdot dS)^2 \quad \text{Eq. 3.2}$$

$$minf(k) = min \sum_i (I_{cm}(\mathrm{B}_\parallel) - \int_S J_{cf}(\mathrm{B}_\parallel, k) \cdot dS)^2 \quad \text{Eq. 3.3}$$

where *i* is the number of in-field critical current measurement points.

Table 3.2: The fitting parameters of modified Kim model.

Parameters	values
Reference field B_0 (T)	0.0607
Kim model exponent k	0.2376
Anisotropy scaling factor α	0.6482
Self-field critical current density J_{c0} (A/m^2)	3.125×10^8

In order to validate the parameters in J_{cf} $(B_\parallel, B_\perp)$, the tape critical currents with respect to the parallel and perpendicular field are calculated and plotted in Figure 3.11. The deviation between the experimental measurement results and the curve fitting results is calculated using Eq. 3.4. The average deviation in the parallel field is 4 % while in the perpendicular field it is 1.7 %. A good consistency is obtained and the parameters are valid.

$$Dev. = \frac{1}{i}\sqrt{\sum_{i}(I_{cm} - I_{cf})^2} \times 100\% \qquad \text{Eq. 3.4}$$

It is worth mentioning that difference between the fitting curve and measurements in the parallel field is due to the fact that the YBCO HTS tape is less sensitive to the parallel field due to the anisotropy. Particularly in the low field, the external magnetic field can be distorted by the tape's self-field, which leads to the fitting curve results less than the measured values. But as far as engineering applications are concerned, this kind of accuracy can be considered as adequate. The determined parameters in $J_{cf}\,(B_{\parallel}, B_{\perp})$ can be used as inputs to calculate the field dependence of critical current density in any field magnitude and orientation. In HTS cable, if only the tape anisotropy is taken into account, the critical current is influenced by the magnetic field interaction among the HTS tapes in the cable. With the information of magnetic field dependence on critical current density, the performance of the HTS cable can be predicted by numerical modelling for cable design.

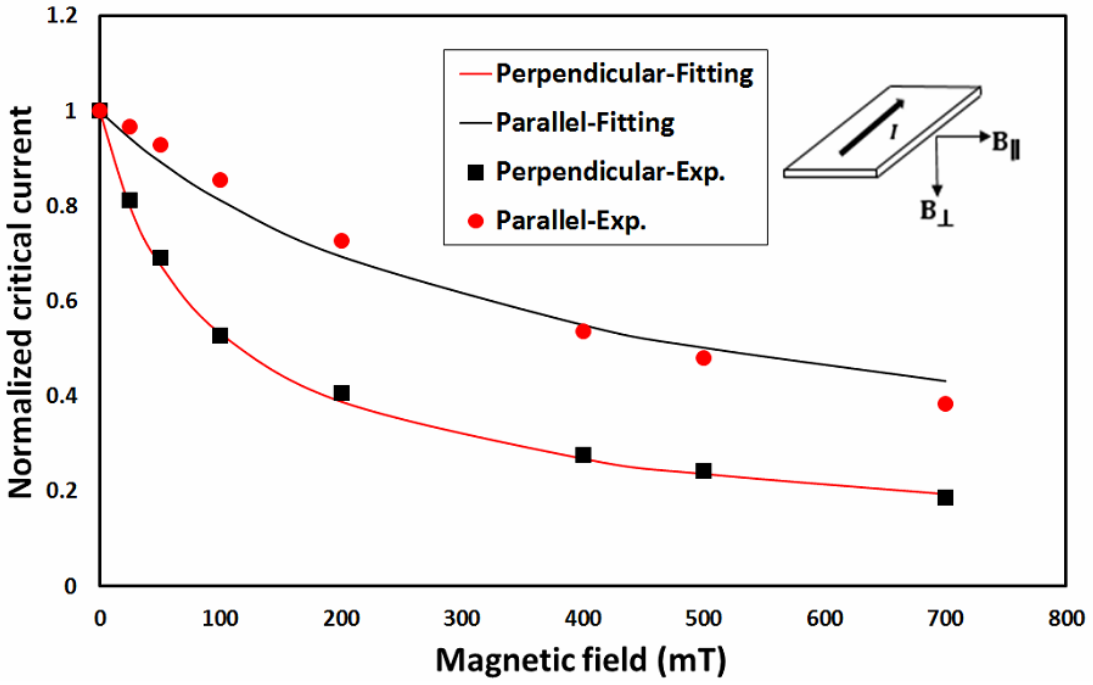

Figure 3.11: The fitted curves compared with the measured critical current in external perpendicular and parallel magnetic field, respectively.

3.1.2 The modelling of HTS cable critical current density influenced by anisotropic characteristics

3.1.2.1 The theory of FEM modelling

The magnetic field distribution of HTS cable can be conveniently solved by numerical method. Finite Element Method (FEM) is one of the numerical methods. There are three main methods of FEM for superconducting numerical modelling.

(1) The $\boldsymbol{A} - V$ formulation. Dependent variable is magnetic vector potential $\boldsymbol{A}$ [59].
(2) The $\boldsymbol{T} - \Omega$ formulation. Dependent variable is current vector potential $\boldsymbol{T}$ [60].
(3) The $\boldsymbol{H}$ formulation. Dependent variables are magnetic field components: H_x, H_y and H_z [61].

Maxwell's equations can be solved by the methods (1) to (3), which is essentially the same in principle to solve the partial differential equations (PDEs). Many commercial FEM modelling packages are available for the PDEs. But only recently the commercial software, such as Comsol, has the ability to solve the highly nonlinear relationship between the electric field and the current density in the YBCO HTS tape [61]. In this section, the FEM is implemented based on the H formulations by solving a set of Maxwell equations in 2D space with three dependent variables H_x, H_y and H_z using Cartesian coordinate system. In the 2D model, the Cartesian coordinates are assumed to have an infinite length in the z direction. Hence, Ampere's law in Eq. 3.5 can be substituted into Eq. 3.6, considering the magnetic field to be distributed in the x-y plane only.

$$\nabla \times \boldsymbol{H} = \boldsymbol{J} \qquad \text{Eq. 3.5}$$

$$J_z = \frac{\partial H_y}{\partial x} - \frac{\partial H_x}{\partial y} \qquad \text{Eq. 3.6}$$

and the Faraday's law can be derived from Eq. 3.7 to Eq. 3.8:

$$\nabla \times \boldsymbol{E} = -\mu_0 \frac{d\boldsymbol{H}}{dt} \quad \text{Eq. 3.7}$$

$$\begin{bmatrix} \frac{\partial E_z}{\partial y} \\ -\frac{\partial E_z}{\partial x} \end{bmatrix} = -\mu_0 \mu_r \begin{bmatrix} \frac{\partial H_x}{\partial t} \\ \frac{\partial H_y}{\partial t} \end{bmatrix} \quad \text{Eq. 3.8}$$

The property of superconductor is characterized by an *E-J* power law, which is expressed in the Eq. 3.9. It describes the superconductor's highly non-linear relationship between the electric field and current density during the transition when the current is approaching the critical current.

$$\boldsymbol{E_z} = E_c(\frac{\boldsymbol{J}}{J_c(\mathrm{B}_\parallel, \mathrm{B}_\perp)})^n. \quad \text{Eq. 3.9}$$

where $E_c = 1\ \mu V/cm$ is the voltage criterion of superconductor critical current. J is the current density with respect to the tape transversal area. Critical current density $J_c(B_\parallel, B_\perp)$ is varied with the magnetic flux distribution around the superconductor tape. The modified Kim model can be used to describe the field dependent critical current density $J_c(\mathrm{B}_\parallel, \mathrm{B}_\perp)$ variation due to the anisotropy [50]. The $J_c(\mathrm{B}_\parallel, \mathrm{B}_\perp)$ is expressed in Eq. 3.1. The parameters k, α, B_0 can be obtained as described in the section 3.1.1.2. A governing equation in 2D can be then obtained from Eq. 3.5 to Eq. 3.9, which can be fitted in the general form PDE in COMSOL, as expressed in Eq. 3.10.

$$\begin{bmatrix} \frac{\partial(E_c(\frac{\frac{\partial H_y}{\partial x} - \frac{\partial H_x}{\partial y}}{J_c(\mathrm{B}_\parallel, \mathrm{B}_\perp)})^n)}{\partial y} \\ \frac{\partial(E_c(\frac{\frac{\partial H_y}{\partial x} - \frac{\partial H_x}{\partial y}}{J_c(\mathrm{B}_\parallel, \mathrm{B}_\perp)})^n)}{\partial x} \end{bmatrix} = -\mu_0 \mu_r \begin{bmatrix} \frac{\partial H_x}{\partial t} \\ \frac{\partial H_y}{\partial t} \end{bmatrix} \quad \text{Eq. 3.10}$$

The PDE equations can be solved by Comsol combining the relevant boundary conditions. Dirichlet and Neumann boundary conditions are used to describe most of the electromagnetic situations, and can be configured by Comsol. Without external applied magnetic field, the boundary condition can be set as $H_x = H_y = 0$. Then, the current density and magnetic flux distribution of HTS cable can be modeled. The performance of the cable with complicated magnetic flux interaction among the tapes can be predicted.

3.1.2.2 The modelling of current distribution of HTS cable considering the gap distance

The polygonal arrangement of the HTS tapes wound around a cylinder copper former is known as a common structure of HTS cable. Since it is not possible to fabricate the HTS cable without gap among the tapes due to the mechanical fragility and manufacturing process, the size of the gap affects the magnetic flux distribution in the cable and the HTS tape is very sensitive to the magnitude and orientation of magnetic field due to the anisotropy, all these combined makes the estimation of critical current of HTS cable complicated. In the HTS cable design, the number of the YBCO tapes wound in the cable is usually designed based on the current rating while the initial radius of the cable is determined by a cylinder copper former, which is designed to withstand the fault current. If the number of HTS tape is fixed, the gap distance is determined by the cable radius and tape width. In order to accurately estimate the performance of HTS cable, it is essential to know how the gap distance affects the cable critical current due to the anisotropy. With the FEM modelling presented in section 3.1.2.1, the critical current density of HTS cable influenced by the anisotropic characteristics can be modelled considering the magnetic interaction among the HTS tapes. Table 3.3 gives three cables with various gap distances. The width and number of the tape are fixed, hence, the gap distance can be changed by the cable diameter.

Table 3.3: The parameters of the modelled HTS cable geometry

No.	Cable radius/r (m)	Tape width/w (m)	No. of tapes/*N*
(1)	0.008	0.004	10
(2)	0.01	0.004	10
(3)	0.02	0.004	10

Based on the parameters in Table 3.3, a filling factor is defined in order to describe the gap distance between the neighboring tapes with respect to the cable radius, as shown in Eq. 3.11 [62]. The high filling factor describes small gap distance. The filling factors with respect to the cable radii (1)-(3) in Table 3.3 are 0.79, 0.64 and 0.31, respectively.

$$\mathrm{ff} = \frac{N \cdot w}{2\pi r} \qquad \text{Eq. 3.11}$$

The HTS cable based on the parameters in Table 3.3 can be modeled using the FEM numerical method presented in section 3.1.2.1 and the anisotropic characteristics of YBCO tape are considered. The modeling results are plotted in Figure 3.12. It can be seen that the YBCO tapes in the cable with filling factor of 0.79 no longer experience self-field. The magnetic flux at the edges of the tapes is compensated by the adjacent tapes, which results in the magnetic field perpendicular to the wide face of the tape partially reduced. It can be predicted that magnetic flux will be distributed along the cable circumference only if the filling factor is equal to 1. When the filling factor reduces to 0.31, few magnetic flux can be compensated between the adjacent tapes, and the YBCO tapes experience a magnetic field similar to the self-field. It can also be predicted that the tapes will experience the self-field when the filling factor is equal to 0. The calculation results of current density of YBCO tapes in the cable at 0.7 I_c are plotted in Figure 3.13, it can be seen that the $J_c(B)$ depedence decreases the tape current carrying ability, as the reduced critical current density due to the magnetic field results in further penetrated into the tape. From the modeling results, it can be concluded that the gap distance can affect the magnetic flux distribution of the HTS cable and hence affect the current distribution due to the anisotropic characteristics of

YBCO tape. From the measurement results of Figure 3.10, it can be deduced that the magnetic field perpendicular to the tape wide face has more impact on degrading the critical current than that parallel to the wide face. Therefore, the assumption can be made that a small gap distance can increase the critical current of the YBCO HTS cable, considering the anisotropic characteristics. This will be further investigated in section 3.2.

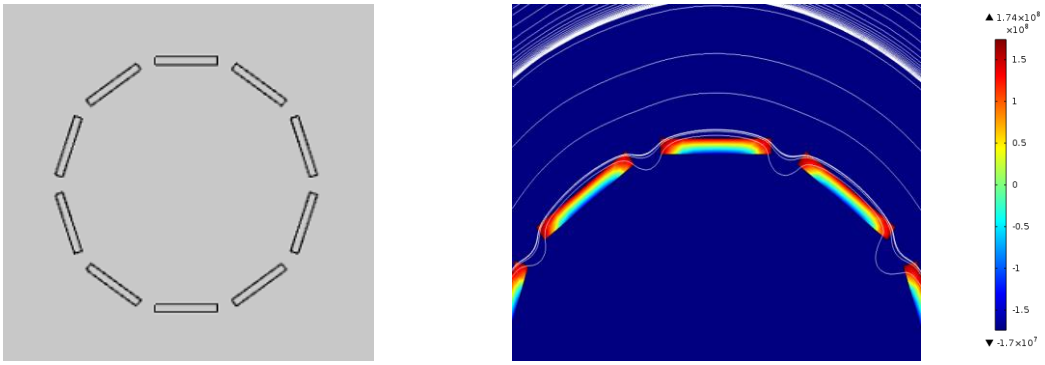

(1) $ff = 0.79$

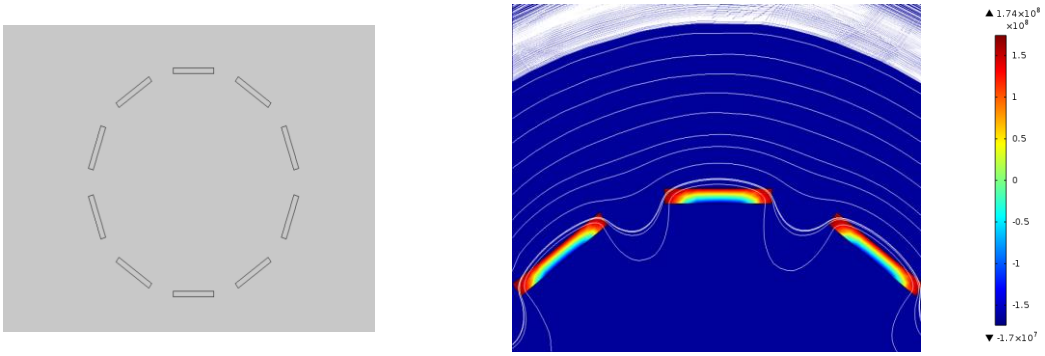

(2)$ff = 0.64$

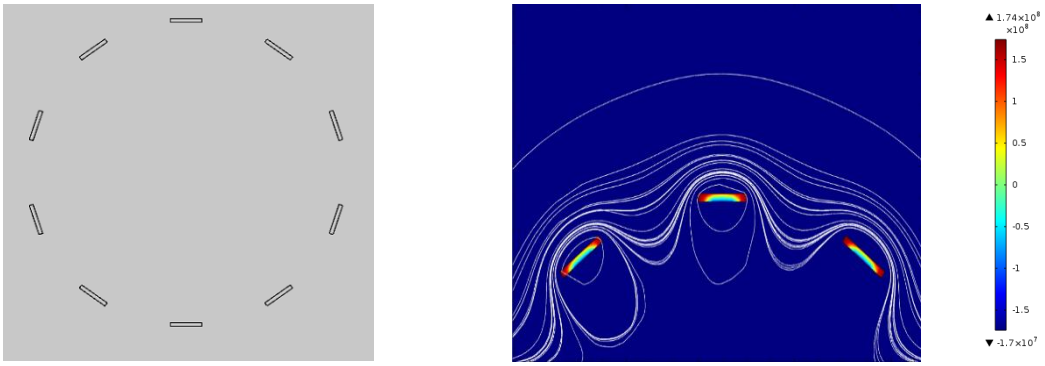

(3)$ff = 0.31$

Figure 3.12: The white line represents the magnetic flux distribution and the surface colour represents the critical current density.

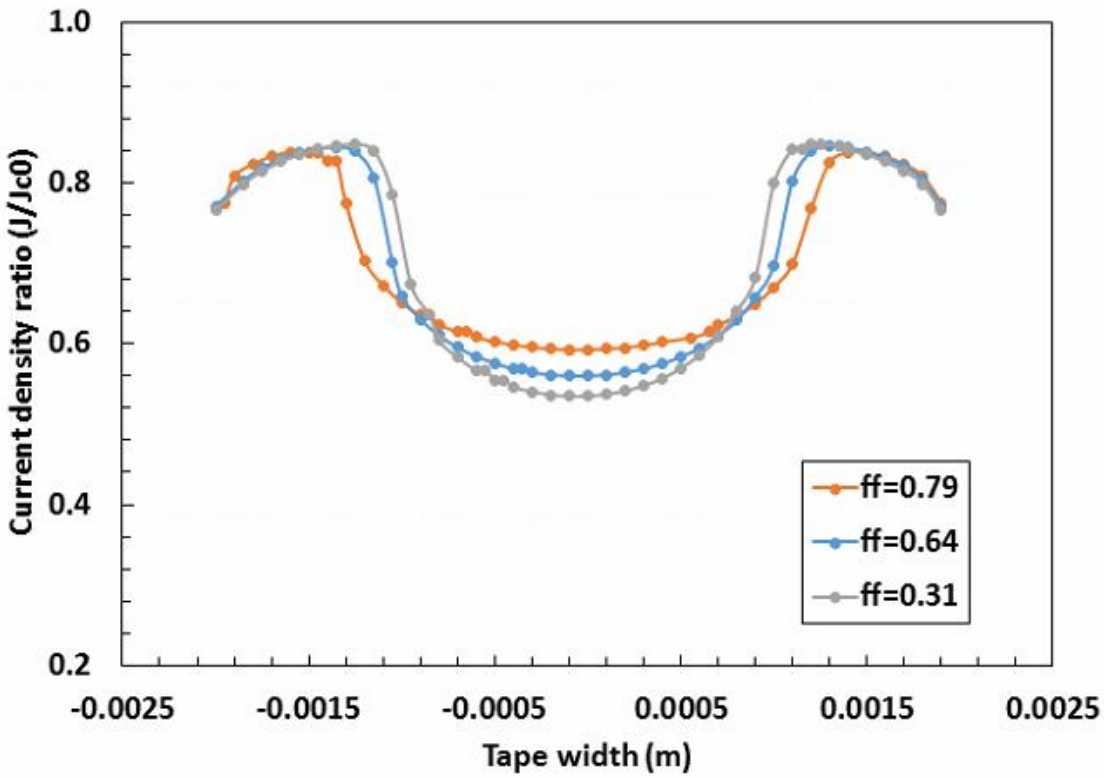

Figure 3.13: The current density distribution of YBCO tape wound in the cable at $0.7I_c$ with various filling factors.

3.2 Experimental study of HTS cable critical current affected by gap distances

For HTS cable construction, it is not possible to adjust the gap distance freely once the HTS tapes are soldered on the cable terminations. In order to experimentally investigate the extent to which the critical current of the HTS cable is affected by various gap distances, an HTS cable circuit model with adjustable gap distance is designed. However, for short cables, the current distribution is usually unbalanced due to the influence of the contact resistances [54]. The designed HTS cable circuit model should be able to eliminate the influence of contact resistance so that the gap distance is the only factor that influences the cable critical current. In this section, detailed cable circuit model design and measurement results are presented.

3.2.1 The HTS cable circuit experiment

To make the gap distances adjustable, an HTS cable circuit model has been designed based on the HTS cable configuration, as shown in Figure 3.14. Three HTS tapes are used to represent the conducting layer of the cable. Each tape is series connected with a shunt resistor and soldered (soldering points A-F) on the copper plates separately. The gap among the tapes can be adjusted continuously. Another copper rod is soldered on the copper thin sheets (soldering points G and H) to act as the copper former in the HTS cable for the purpose of bypass the exceeding current. A shunt resistance is also series connected with the copper rod. G10 fibreglass is used as the whole model former.

The model can have two electrical topologies with some simple modifications: (a) series topology and (b) parallel topology, as shown in Figure 3.15. As the contact resistances of soldering points A to H are practically hard to keep at exactly the same value, the current repartition among the tapes should be taken into account. For the topology (a), all the branches containing HTS tapes are in series connection for the purpose of eliminating the contact resistance influence. The direction and the magnitude of the current through each HTS tape are therefore controlled to be the same and the ideal HTS cable with various gap distances is simulated [63-65]. For topology (b), all the branches are in parallel connection such that the effect of the contact resistance on cable critical current can be investigated by measuring the current through each branch.

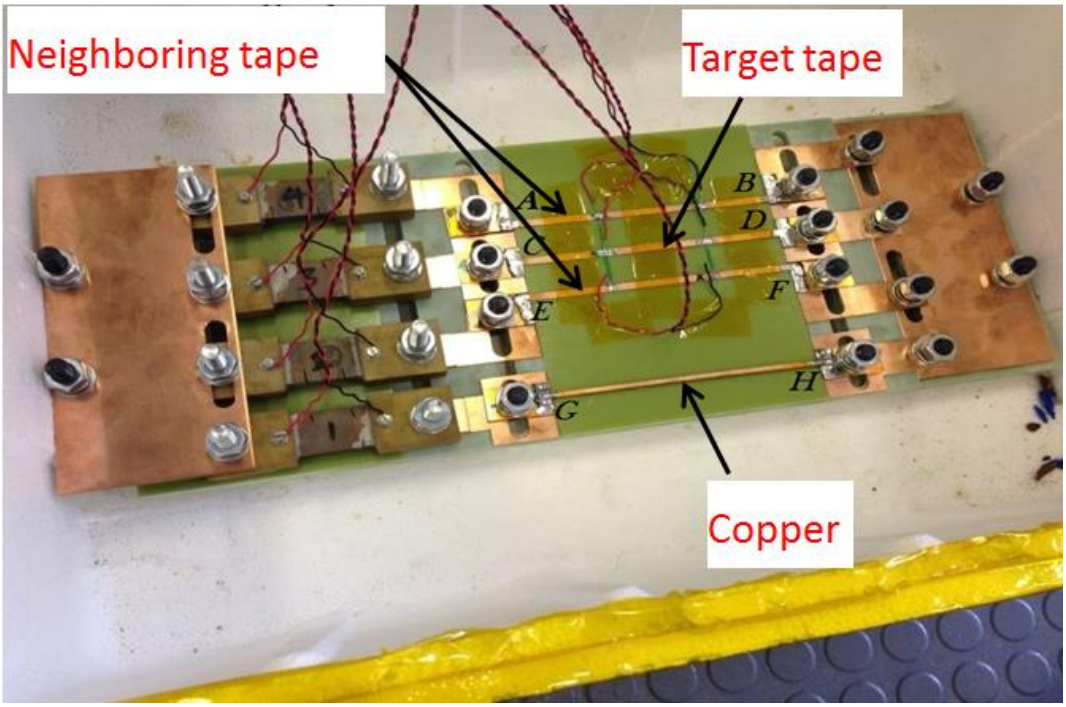

Figure 3.14: The HTS cable circuit model.

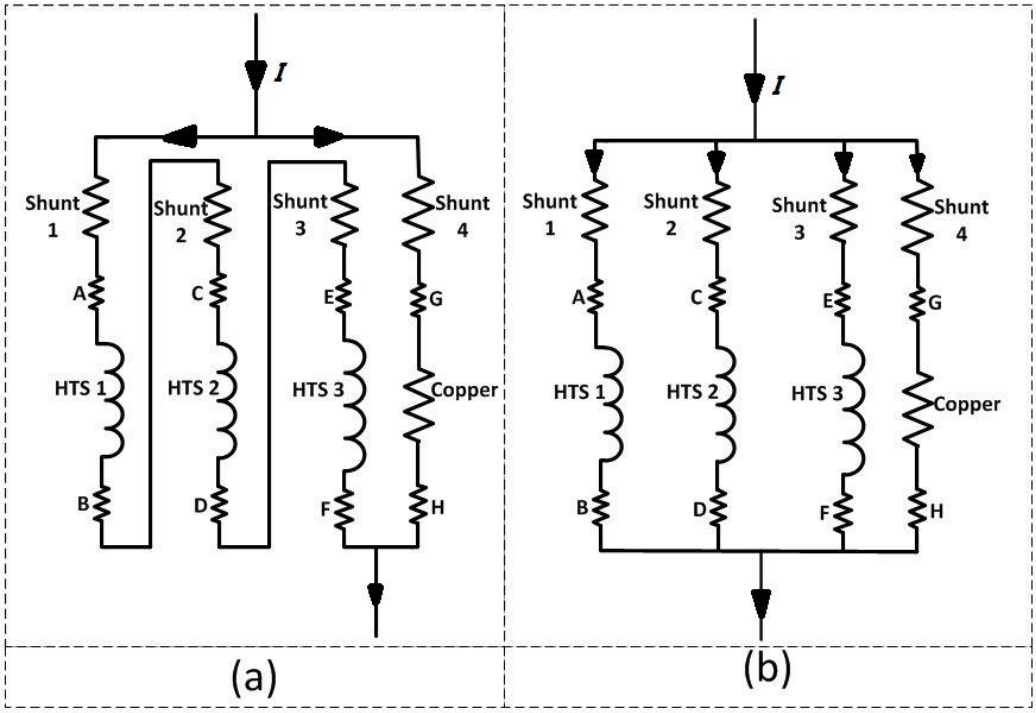

Figure 3.15: Topologies of HTS cable circuit model: (a) Series connection and (b) Parallel connection.

3.2.2 The influence of gap distance on critical current of HTS cable circuit model

The neighboring tapes (tape AB and tape EF) symmetrically affect the magnetic flux distribution of the middle HTS tape in the HTS cable circuit model (tape CD). The middle HTS tape is the target tape, therefore, represents the real situation of all HTS tapes in the HTS cable if the winding pitch is neglected. To investigate the extent to which the critical current of the target tape is affected by the gap distance and tape width, 4 mm and 12 mm wide HTS tapes are measured at different gap distances through topology (a) circuit configuration, respectively.

The whole HTS cable circuit model was immersed into a LN_2 bath; four shunt resistors with 400 A /60 mV rating were used to monitor the current flowing through each branch. However, the resistivity of shunt is a function of temperature, which drops with a decrease in temperature. In the 77 K cryogenic temperature region, the reduction of the resistance of the copper is significant. About 8 % resistance drop of the shunt resistor was observed when cooled down to 77 K. Therefore, the original current-voltage ratio from the manufacturer should be replaced with the calibrated one for better measurement accuracy. This is achieved by calibrating the shunt resistor in the 77 K LN_2 with a standard shunt in the room temperature.

The HTS tape with the lowest critical current value in the series connection determines the measurable critical current values. As the critical current of the SuperPower HTS tape used in the test is not evenly distributed (0.33% standard deviation of I_c). The HTS tape with the lowest critical current among the three tapes is deliberately placed in the middle position (soldering points C and D) as the target tape. The critical current is measured by DAQ which is monitored and controlled by LabVIEW in PC [53].

The critical current of the 4 mm in width target HTS tape is chosen at the experimental value of 69.7 A, and the 12 mm target HTS tape is 429 A in self-field.
Table 3.4 summarizes the specifications of the target tapes used in the test. Figure 3.16 shows the measurement results. Group 1 is the critical current test of 4 mm width HTS tapes separated with the gap distances of 0.4 mm, 4 mm and 10 mm. The critical

current of the target HTS tape is recorded successively. Group 2 is the critical current test of 12 mm width HTS tapes separated with the same gap distances of Group 1. The critical current of target HTS tape in the middle position was also recorded and compared with a single tape in the self-field.

Table 3.4: Specifications of the target HTS tape.

	Critical current in self-field (A) @ 77K	Stabilizer	structure	Dimension (width ×thickness)
Tape 1	69.7	Surrounding copper	Non-ferromagnetic Hastelloy (IBAD)	$4.2\ mm \times 0.1\ mm$
Tape 2	429			$12\ mm \times 0.1\ mm$

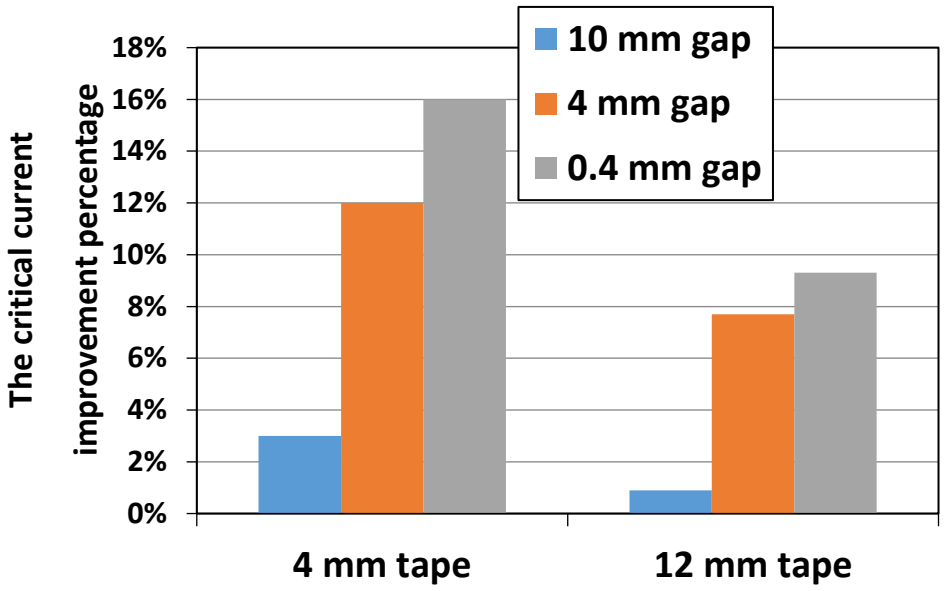

Figure 3.16: The critical current of target HTS tapes at difference gap distances from experimental results.

From the Figure 3.16, it can be seen that the critical current will be significantly increased when the gap distance is sufficiently small for both HTS tapes of 4 mm and 12 mm in width. However, the amount of critical current improvement of 12 mm

width HTS tape is less than that of 4 mm width HTS tape at the same gap distance. Therefore, from the evidence of experimental results, the influence of gap distance is weak for wider HTS tapes. One should consider that narrow HTS tape is an advantage to construct HTS cable.

3.2.3 FEM Modelling of magnetic field distribution for parallel placed HTS tapes

The magnetic field distributions and critical currents of the HTS cable circuit model for both 4 mm and 12 mm wide tapes have been calculated in 2D FEM by COMSOL, in order to analyze and verify the experimental results. The detailed modeling is presented in the section 3.1.2.1. Three 4 mm and 12 mm in width SuperPower HTS tapes were modeled, respectively, these have the same geometry with the experimental tapes. The parameters in Eq. 3.1 are: $k = 0.2952$, $B_0 = 0.04265\ T$, and $\alpha = 0.7$, which are obtained as described in section 3.1.1.2. $n = 21$ for *E-J* power law. J_{c0} is the average critical current density in the self-field. Assuming that the thickness of the tape is 100 μm, $J_{c0} = 1.7 \times 10^8 A/m$ for 4 mm tape and $J_{c0} = 10.7 \times 10^8 A/m$ for 12 mm tape. The $B_{\parallel}$ and $B_{\perp}$are the magnetic flux components that are parallel and normal to the wide face of the HTS tape, respectively. Due to the anisotropic property and high aspect ratio of YBCO HTS tape, the $B_{\parallel}$ can be ignored as $B_{\perp}$ has larger effect on the field dependence of critical current density [15]. The total current of each HTS tape can be calculated by integrating the current density J_z with the cross area *S* of the superconductor as in Eq. 3.12.

$$I = \int_S J_z \, dS, \qquad \text{Eq. 3.12}$$

and the average electrical field E_z can be calculated by integrating the electrical field over the superconductor cross section area and divided by the cross section area. Figure 3.17 shows the critical current simulation results of 4 mm and 12 mm wide tapes in self-field, respectively. A good agreement with the experimental test results as shown in Table 3.4 is obtained.

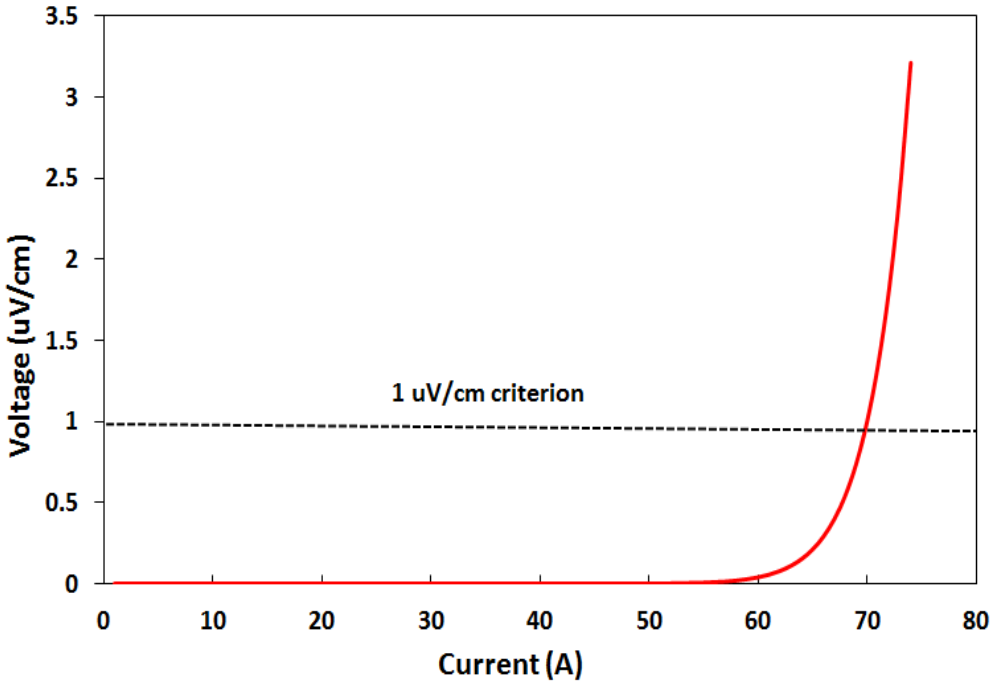

(a)

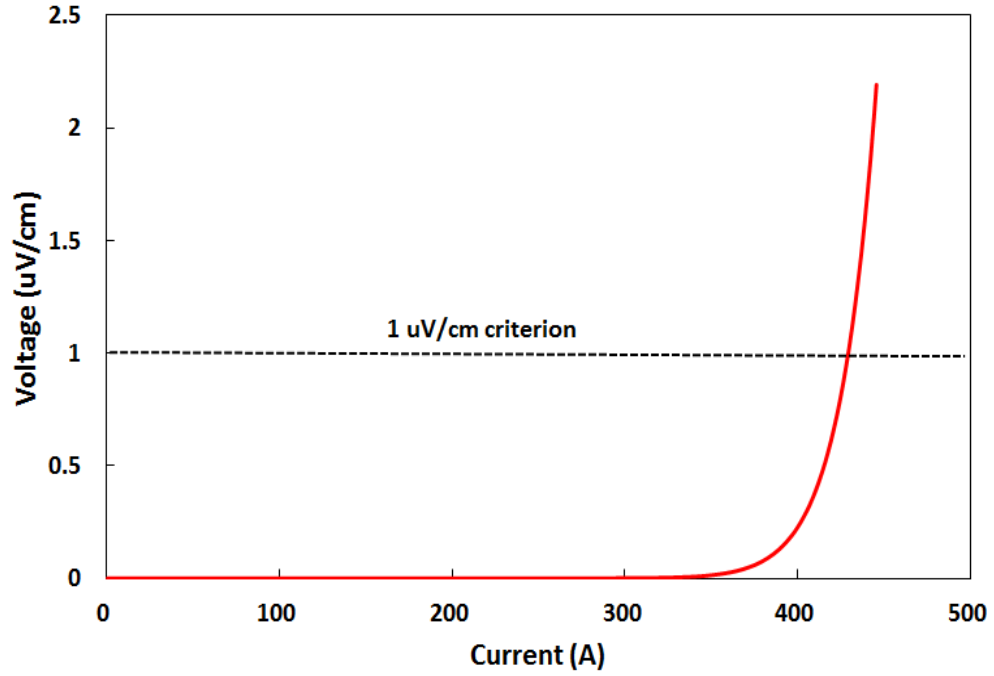

(b)

Figure 3.17: The critical current simulation results of (a) 4 mm width (b) 12 mm width HTS tapes.

The same geometry of HTS cable circuit model has been modeled in 2D FEM using Comsol. Each of the three HTS tapes is constrained with the same current. Figure 3.18 shows the magnetic flux distribution lines of 4 mm wide HTS tape. It is shown that the magnetic flux around the edge of the middle tape are significantly compensated when the gap distance reduces to less than 1 mm. Figure 3.19 shows that the critical current of the middle tape improves significantly once the gap distance is less than 1 mm. However, the simulated critical current improvement at 0.4 mm is less than the measurement values. The possible reasons for the discrepancy in the amount of the increased critical current between the experimental and FEM results are i) the critical current density of the tape used in the HTS tape modeling is only the average value, which ignores the nonhomogeneous superconducting material. ii) The parameters of field dependence of the current density formula of HTS tape in the modeling are less accurate in low field application. iii) The influence of the external magnetic field generated by the copper cable between HTS tapes interconnection in the practical experimental is not taken into account in the FEM simulation. However, in general, the FEM calculation results verify the experimental results of critical current improvement with decreased gap distance for both 4 mm and 12 mm width HTS tapes. The magnetic flux components normal to the middle HTS tape are partially compensated by surrounding tapes, which will ease the effect of the magnetic flux on the critical current compared with a single tape in the self-field.

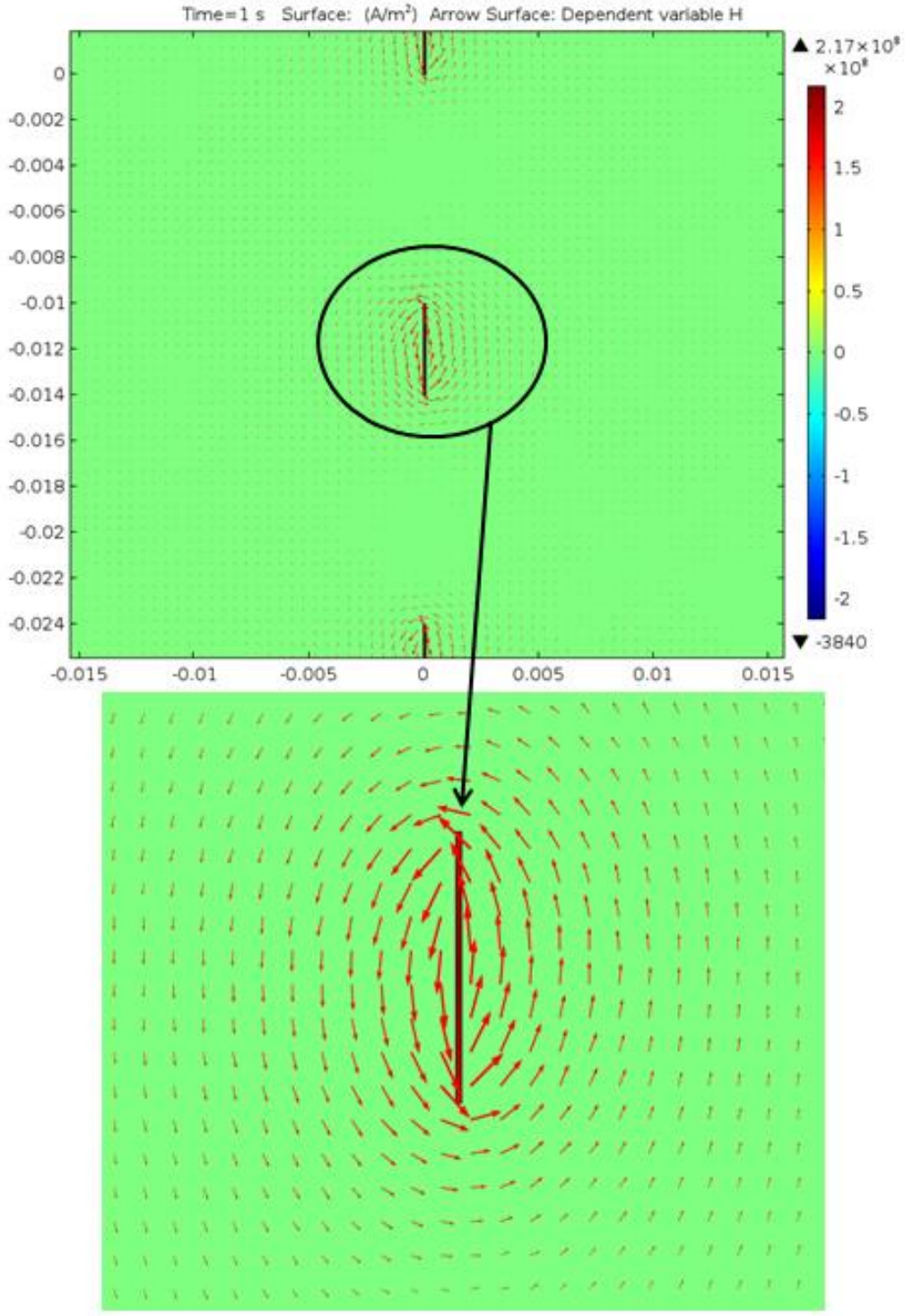
Time=1 s Surface: (A/m²) Arrow Surface: Dependent variable H
▲ 2.17×10⁸
×10⁸
2
1.5
1
0.5
0
-0.5
-1
-1.5
-2
▼ -3840
0
-0.002
-0.004
-0.006
-0.008
-0.01
-0.012
-0.014
-0.016
-0.018
-0.02
-0.022
-0.024
-0.015
-0.01
-0.005
0
0.005
0.01
0.015

(a) 10 mm

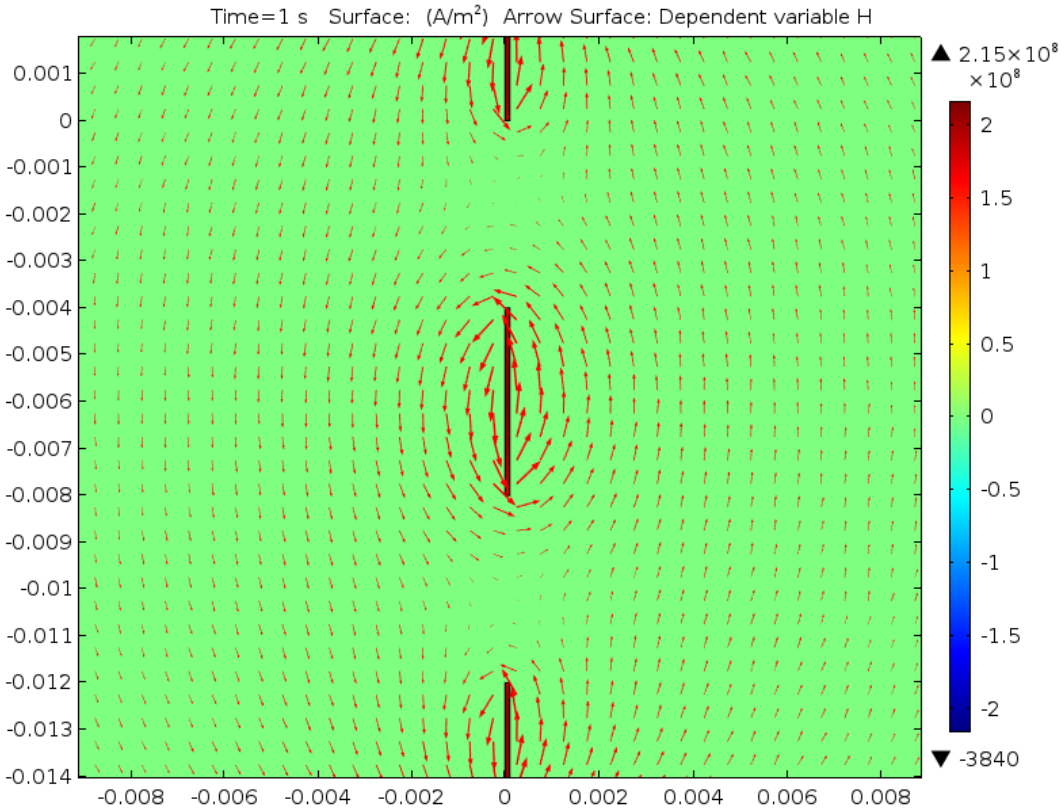
Time=1 s Surface: (A/m²) Arrow Surface: Dependent variable H
0.001
0
-0.001
-0.002
-0.003
-0.004
-0.005
-0.006
-0.007
-0.008
-0.009
-0.01
-0.011
-0.012
-0.013
-0.014
-0.008 -0.006 -0.004 -0.002 0 0.002 0.004 0.006 0.008
▲ 2.15×10⁸
×10⁸
2
1.5
1
0.5
0
-0.5
-1
-1.5
-2
▼ -3840

(b) 4 mm

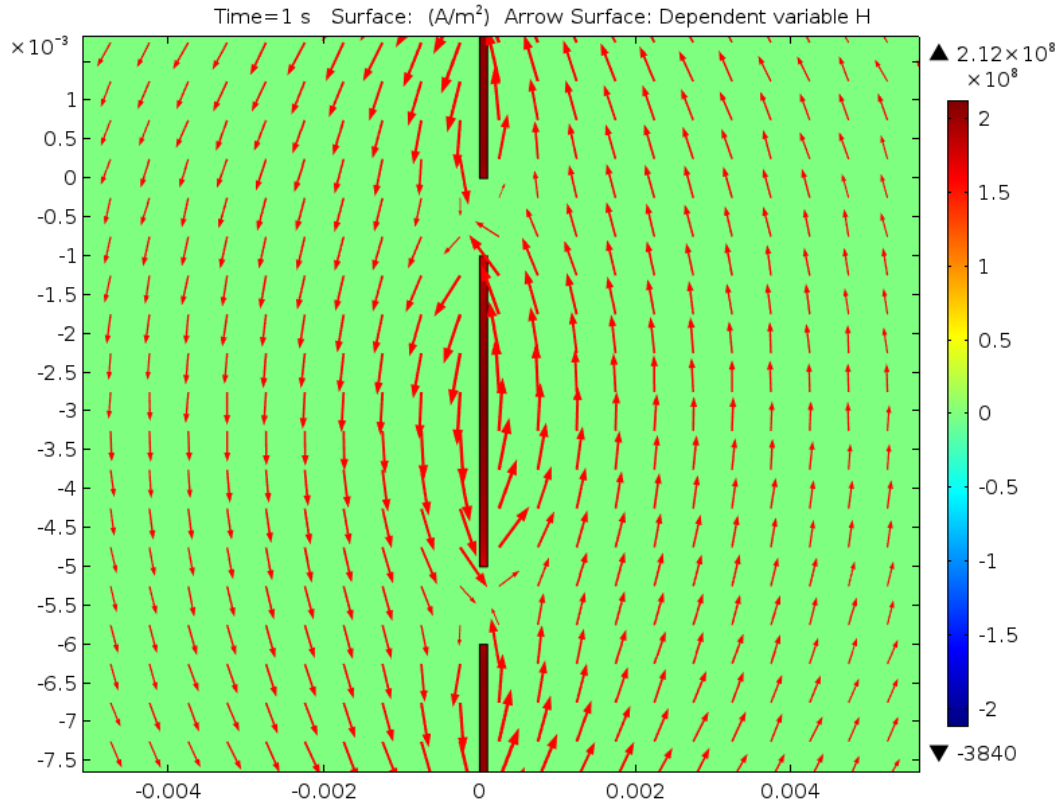
Time=1 s Surface: (A/m²) Arrow Surface: Dependent variable H
×10⁻³
1
0.5
0
-0.5
-1
-1.5
-2
-2.5
-3
-3.5
-4
-4.5
-5
-5.5
-6
-6.5
-7
-7.5
-0.004 -0.002 0 0.002 0.004
▲ 2.12×10⁸
×10⁸
2
1.5
1
0.5
0
-0.5
-1
-1.5
-2
▼ -3840

(c) 1 mm

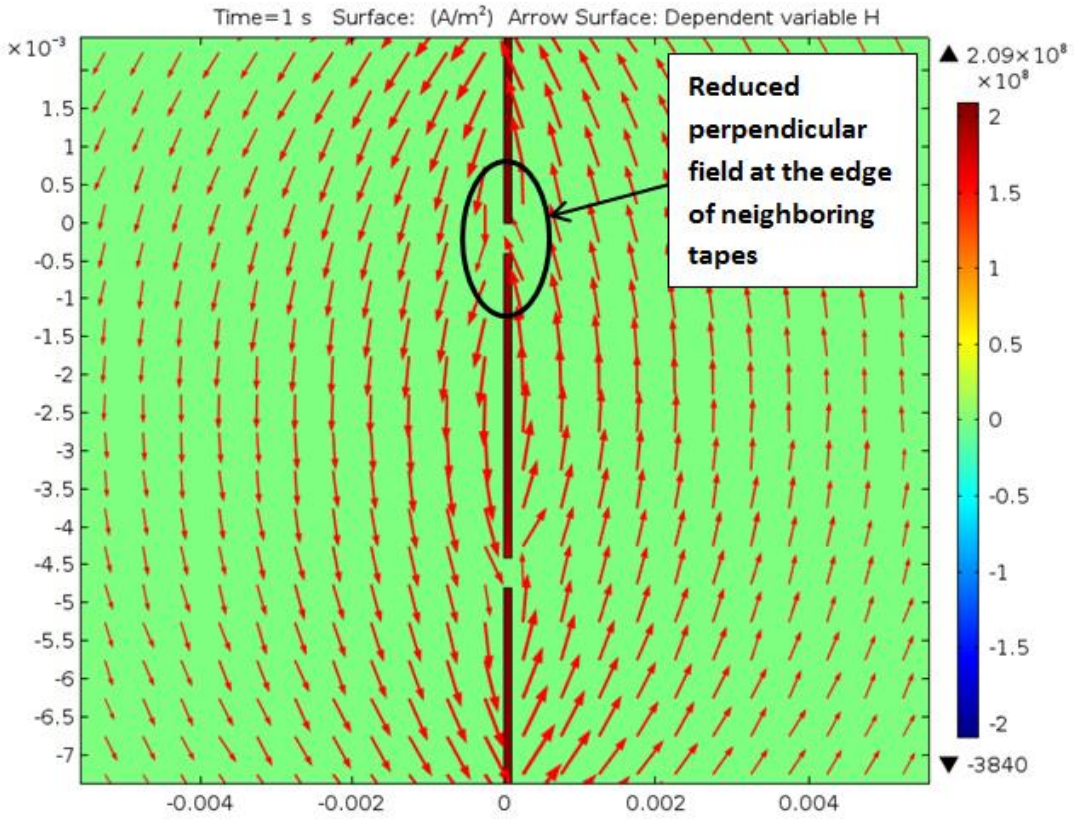

(d) 0.4 mm

Figure 3.18: The magnetic flux distribution arrows of three 4 mm width HTS tapes at gap distances of (a) 10 mm, (b) 4 mm, (c) 1 mm and (d) 0.4 mm.

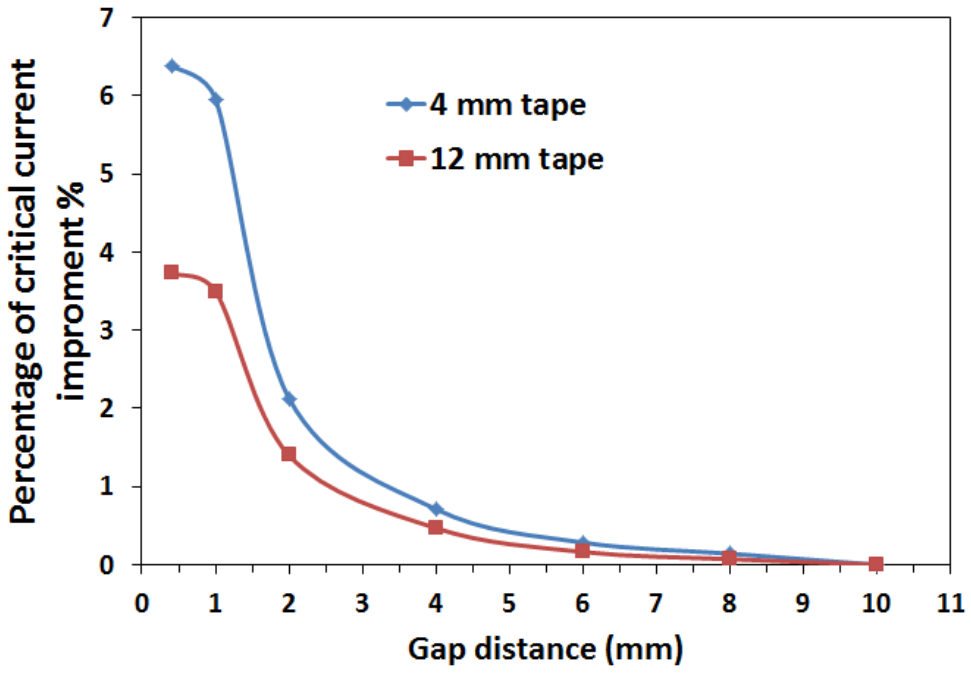

Figure 3.19: The critical current improvement at difference gap distances based on 2D FEM calculation results.

The width of HTS tape wound in the cable is an interesting question to consider. From the experimental results, the improvement of narrow HTS tapes is better than wide HTS tape at small gap distance. But the total superconducting material of narrow tape is less than the wide tape, which results in the overall critical current of cable made of narrow tapes being less than the one made of wide tape. The flexibility of the HTS cable is also affected by the width of the tape to be chosen. If the cable requires a small bending diameter, then a large pitch angle of tape is necessary, which results in less space in the layer to fit HTS tapes. The chose of the width of HTS tape to wind the cable depends on the cable application. The HTS tapes with widths of 2 mm, 4 mm, 6 mm and 12 mm are commercially available. The small bending diameter for the power cable is not necessary, hence, 4 mm width tapes are usually used in HTS power cable projects. Some conductor on round core (CORC) cables are wound with 12 mm width tapes for small cable bending diameter [66].

3.2.4 Current distribution of HTS cable considering the contact resistances

The cable circuit model in the section 3.2.1 is electrically connected in series in order to eliminate the contact resistance. But contact resistance from the cable terminal cannot be avoided since the HTS tapes are only connected in parallel in the cable for achieving high current carrying capacity. Hence, it is necessary to examine the influence of the contact resistance from the cable terminal on the critical current distribution and compare it with the influence of tape anisotropy.

The real HTS cable has at least two cable terminals, which consist of the joints between the copper conductor from room temperature to the HTS tapes in 77 K. For long cables, the cable splices introduce additional contact resistance. The HTS tapes can be either soldered or compressed firmly on the copper terminals to form a rigid connection. The connection should be mechanically and electrically reliable. The presence of contact resistance between the copper part and the HTS tapes part cannot be ignored in practice, and due to the resistance of HTS tape is nearly zero, while the order of magnitude of resistance from the copper terminals is in milliohm [67], the influence of the contact resistance on the current distribution of HTS cable is therefore

extremely significant. The inhomogeneously distributed current in the HTS cable will result in the degradation of power transmission efficiency.

The topology (b) of the HTS cable circuit model was used to investigate the influence of the contact resistances on the current distribution, as the soldering points A–F will introduce contact resistances in each current branch. Three 4 mm wide SuperPower IBAD YBCO HTS tapes (I_c = 70 A) were separated in gap distances of 0.4 mm, 4 mm and 10 mm, respectively. Total current I_{total} = 200 A was fed into the copper bus bar and distributed into the three HTS tape branches and one copper bar branch. The results show that, in all gap distances, the HTS tape between the soldering points C and D has the 35% I_{total} current while the HTS tapes between A, B and E, F have 17.5% I_{total} current, respectively. The rest of the 30% I_{total} current flows through the copper rod. Therefore, from the evidence of the measured current distribution, the contact resistances of soldering points A, B and E, F cause the current to be severely unevenly distributed and the contact resistances dominate the current distribution. The anisotropic characteristics of the YBCO tape have nearly no influence.

The further investigation involves a short prototype HTS cable consisted of 4 Superpower HTS tapes in 4 mm width, which was constructed to verify the observed results from topology (b), as shown in Figure 3.20. The HTS tapes 1 - 4 are firmly compressed on the copper former, which results in the presence of contact resistances (a) to (d). The measured critical currents of the tapes are about 70 A. Critical currents of each HTS tape in the cable were measured, shown in Figure 3.21. From tape 1 to tape 4, the measured critical currents are 81.2 A, 84.7 A, 70.2 A, and 97.9 A, respectively. The measured critical currents in the cable have been shifted due to the different contact resistances (a)–(d). The tape with the lowest contact resistance (c) quenches first, and likewise the tape with highest contact resistance (b) quenches last. The total current flowing through the four HTS tapes is about 334 A. However, the total cable transport current is 520 A, about 24% of the total cable current flows through the copper former. Hence, the copper conducts a considerable amount of current in the cable due to the contact resistances.

The reason for this phenomenon is that the dramatically increased quenching resistance of HTS tape is still less than the contact resistance, which will result in the

domination of the contact resistance on the current distribution for parallel placed HTS tapes. Therefore, the contact resistance should be minimized and the value should be quantified. Further work will be continued with the investigation of the contact resistance influence, this will be discussed in Chapter 4.

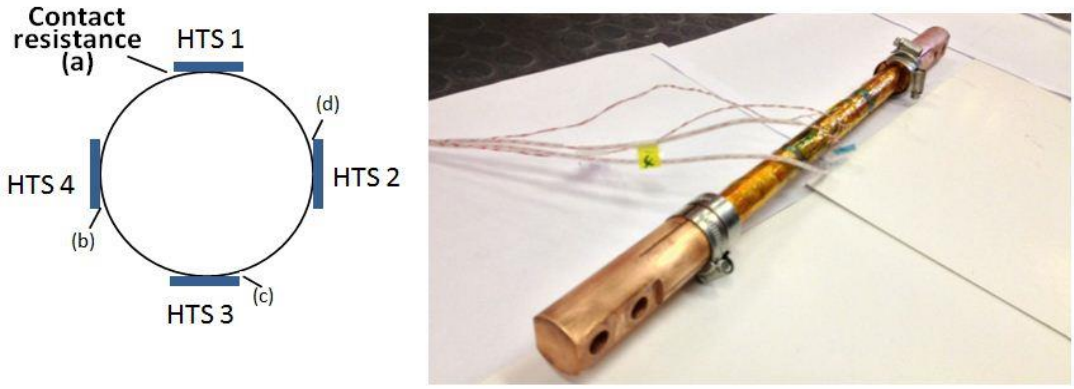

Figure 3.20: The prototype short HTS cable composed of 4 HTS tapes.

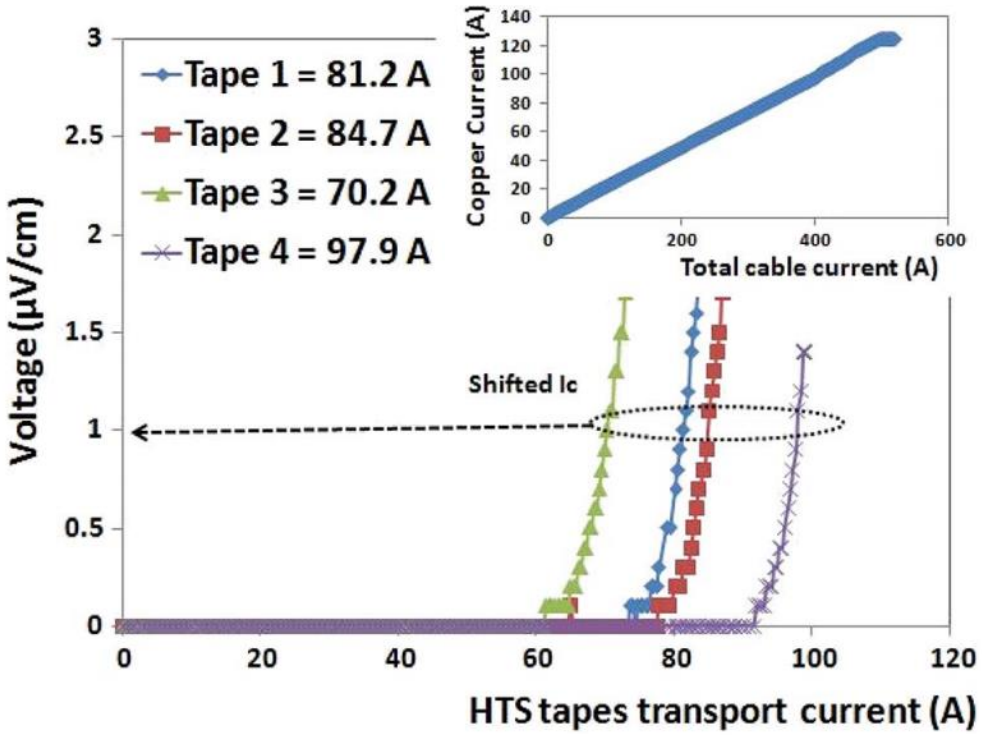

Figure 3.21: Shifted critical current measurement results of each HTS tape in the cable.

3.3 Summary of the investigation

The anisotropy of HTS tape is characterized based on the modified Kim model, the important parameters α, k and B_o are determined using in-field critical current measurement values. Once the anisotropic dependence of critical current density is characterized, it can accurately predict the critical current of HTS cable with multi-tape structure. The effect of the gap distances on the critical current of the HTS cable circuit model is investigated. The results from the experimental measurements and FEM calculations show that the total critical current will improve significantly if the gap distance is less than 1 mm. Therefore, if the influence of anisotropy is the only factor to be considered, the HTS cable should be designed with minimum gap distance among the tapes. However, the contact resistances have a significant impact on the cable critical model current distribution. Uneven distribution of the current of each HTS tape will result in the reduction of overall cable critical current. Nevertheless, since the HTS cables are only subjected to their own low cable magnetic field, if the contact resistances are taken into the consideration, the influence of the HTS tape anisotropy is negligible while the contact resistances dominate HTS cable critical current. This will be further discussed in Chapter 4.

Chapter 4

Homogenization of current distribution of multi-layer HTS cable

In this Chapter, a prototype HTS cable consisted of two HTS layers was constructed. In order to quantify the contact resistances of the cable, the DC measurement was firstly performed on the cable wound with only the inner HTS layer in advance of the measurement of completed cable with both HTS layers. It turns out that the non-uniform current distribution among each layer mainly results from the contact resistance with operating current less than the cable critical current and tends to become uniform when the operating current increases towards the cable critical current. A modified 2D H formulation which takes account of the voltage drop due to the contact resistances of the cable termination has been applied to simulate the current distribution of the cable and it predicts that the homogenized current distribution of multi-layer HTS cable can be achieved if the contact resistances are the same for each HTS layer, even considering the influence of anisotropy. In AC condition, due to the influence of HTS layer inductance, the current distribution among the multilayer structure could be non-uniform, which leads to an increase in the AC loss. Therefore, an optimal algorithm based on the impedance matching has been developed to achieve evenly distributed current among HTS layers in the cable. Since the resistances of the HTS conductors are nearly negligible compared with inductive impedance, the current distribution is dominated by the inductance of each HTS layer. For this reason, the self and mutual inductance of HTS cable are investigated in terms of the cable structural parameters: radius, pitch angle and winding direction. And the current distribution can be optimized by adjusting the inductance of each HTS conducting layer. An optimal algorithm is developed to theoretically optimize the current distribution for HTS cable. A short prototype HTS cable based on the optimal algorithm has been constructed and current distribution has been experimentally measured to validate the optimal algorithm.

4.1 Homogenization of current distribution of multi-layer HTS cable considering the contact resistances

Coaxial multi-layer HTS cable has large current transmission capacity, but may cause the current distribution to be non-uniform among each layer due to the contact resistances, which will, in turn, affect the power transmission efficiency, especially for the laboratory scale HTS cable, where the length of the cable is limited within several meters. Although the contact resistances from the cable terminations can be carefully controlled and minimized, if cable carries DC transporting current, the subtle difference in contact resistance among HTS tapes still has an influence on the current distributions among layers in the cable resulting in a significant impact on cable performance. Therefore, it is crucial to understand the current distribution among each HTS layer before applying to the power grid. In [68] and [69], the current distribution among each HTS tape was measured with separated cable terminals. In [70], the current distribution of a single HTS layer cable was measured indirectly through a group of hall sensors. In [71], the current distribution of HTS twisted stacked transmission cable (TSTC) cable is also obtained by hall sensors. In [72], the critical current of CORC cable is determined from the voltage across the cable terminals due to the non-uniform current distribution of each tape. However, to the authors' best knowledge, the current distribution for multi-layer HTS power cable is rarely reported. Hence, in this section, a prototype HTS cable has been constructed to investigate the current distribution among each HTS layer considering the cable terminal contact resistance effect.

Simulation of the cable current distribution is carried out in order to find out the solution of homogenizing the current distribution. Based on the work in [73], modified 2D H formulation is implemented, which takes into account the electrical field drop due to terminal contact resistances. As known from Chapter 3, due to anisotropy, the current distribution of the cable is also affected by the configuration of cable composing YBCO HTS tapes experiencing in the cable magnetic field. Anisotropic characteristics due to the magnetic field of the cable are also implemented into the modelling.

4.1.1 HTS cable design and current distribution measurement

4.1.1.1 The HTS cable fabrication

The prototype HTS cable was hand-made using 4-mm wide SuperPower 2G HTS. Due to the results of the previous work in Chapter 3 [74], minimum gap distance can maximize the cable total critical current. The cable consists of two HTS layers with minimum gap distance between the adjacent tapes. Instead of copper former, a G10 tube is used as the cable former for the purpose of mechanical support, and elimination of current bypassed by the cable former. The winding direction of each HTS layer is opposite to minimize the axial flux in the cable [75]. Table 4.1 gives the summary of the cable specification.

The termination contains two steps of joints with inner and outer HTS layers, respectively. Each HTS layer was helically wrapped around the former and soldered on the pre-tinned cable terminal steps with Indium [76], as shown in Figure 4.1 (a) and (b). Figure 4.1 (c) shows the schematic of the cable configuration. To minimize the contact resistance, the length of each step is 7 cm and the corresponding contact resistance is expressed as R_1 and R_2 as combined resistances from both ends of inner and outer layers, respectively. The winding tension is carefully controlled in order to minimize the differences between the magnitudes of R_1 and R_2. There is a PPLP insulation layer between the inner and outer HTS layer for the purpose of preventing the inter-layer current flowing.

Table 4.1: The specifications of the HTS cable.

Tape parameters	Values	Cable parameters	values
Manufacturer	SuperPower	No. of layers	2
Fabrication process	IBAD	No. of tapes in the inner layer	10
Thickness of HTS layer, μm	1	No. of tapes in the outer layer	10
YBCO tape width, mm	4	Average gap *d*, mm	0.1
Overall tape thickness, mm	0.1	G 10 former O.D., mm	14.3
Stabilizer	Copper	Diameter of the inner layer, mm	14.3
Substrate	Hastelloy	Pitch angle of inner layer	20^0
Sample critical current I_c	130 A	average gap of the inner layer HTS tapes, mm	0.49
Batch minimal critical current	127 A	Diameter of the outer layer, mm	16
Minimal bending diameter, mm	11	Pitch angle of outer layer	30.6^0
n value	29.8	average gap of the outer layer HTS tapes, mm	1.02
Total length of tape required, m	23	total cable length, m	1.46

(a)

(b)

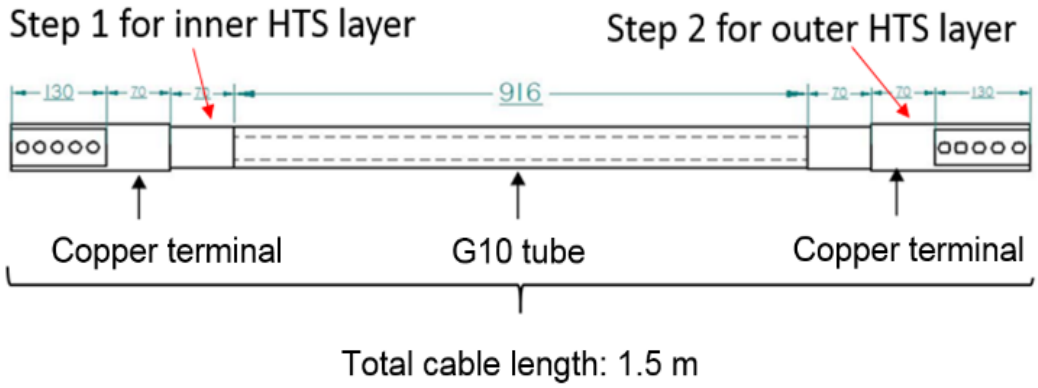

(c)

Figure 4.1: The HTS cable construction: (a) The fabrication of 1 m HTS prototype cable, (b) The cable termination, (c) The schematic of the cable configuration.

4.1.1.2 The experimental measurement of current distribution

The critical current of the HTS tape used to wind the cable was firstly tested based on the critical current measurement setup as presented in section 3.1.1.1 [53], the measured sample tape critical current is I_c = 130 A and the n value is 29.8. The entire HTS cable was tested in a similar way after the cable was completely immersed in the LN_2 bath, as shown in Figure 4.2. The current distribution among the two HTS layers is difficult to directly measure, because the current will automatically inject into each layer through cable termination, and the shunt resistance can only measure the total current of the cable. In [77], Kim et al, proposed to use two different Rogowski coils wrapped around each layer to measure the current. This is effective to measure the AC but less sensitive to DC. In the case of DC transporting current, a novel way has proposed to indirectly measure the current of each layer taking advantage of the relevant contact resistances.

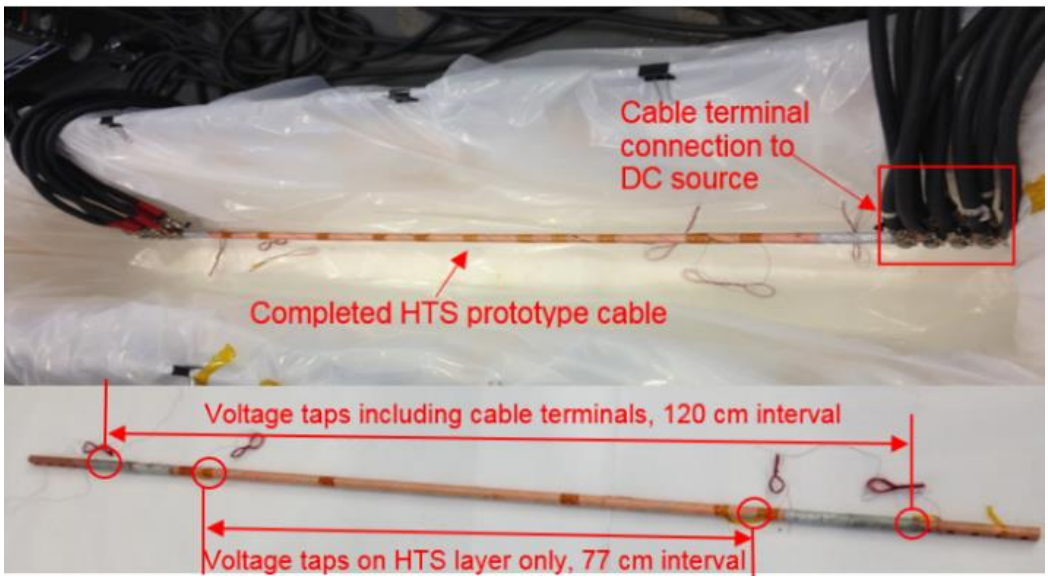

Figure 4.2: The entire HTS cable immersed in the LN2 bath for testing

In the DC measurement, there are two pairs of voltage taps for each HTS layer: Pair I with 77 cm interval includes only the HTS conducting layer; Pair II with 120 cm interval includes the copper terminals and HTS conducting layer. Pair I is used to measure the critical current based on the $1\mu V/cm$ criterion, hence, the total quench

voltage of each HTS conducting layer detected by the voltage tap is 77μV. Pair II is used to obtain the contact resistance. The magnitude of contact resistances R_1 and R_2 are mainly determined by the soldering area, and can be assumed to be constant once the fabrication of the cable is finished. When the inner HTS layer is wound on the cable, the cable with single HTS layer was charged with DC ramping current to measure the contact resistance R_1. Due to the zero resistance of the HTS under DC transporting current, the voltage taps pair II can only pick up the voltage drop across the contact area V_s. The contact resistance can be calculated from the current I_s of the cable with single HTS by a shunt resistor, as shown in Eq. 4.1. The measured critical current of the inner HTS layer is shown in Figure 4.3 . The measured curve contains an inductive voltage. The inductive voltage is detected due to the helical configuration of the HTS layer. The I-V curve of the inner HTS layer can be retrieved by removing the inductive component manually.

$$R_1 = {}^{V_s}/_{I_s} \qquad \text{Eq. 4.1}$$

After the second HTS layer was wound on the cable, the current of the inner layer can be obtained by contact resistance R_1 as expressed in Eq. 4.2.

$$I_1 = {}^{V_1}/_{R_1} \qquad \text{Eq. 4.2}$$

where V_1 is the voltage drop of inner layer contact area. The contact resistance of the outer layer R_2 can be calculated as shown in Eq. 4.3.

$$R_2 = {}^{V_2}/_{(I_t - I_1)} \qquad \text{Eq. 4.3}$$

where I_t is the total current of the cable with two HTS layers, and V_2 is the voltage drop across the contact area of the outer layer. The contact resistances of R_1 and R_2 can act as shunt resistors connected solely to the relevant HTS conducting layer, so the current distribution among inner HTS layer I_1 and outer HTS layer I_2 can be

worked out based on contact resistances as shown in Eq. 4.1 and Eq. 4.3, as expressed in Eq. 4.4.

$$I_2 = {}^{V_2}/_{R_2} \quad \text{Eq. 4.4}$$

Although the magnitude of the contact resistances may vary with temperature, due to the heat dissipated in the joint parts when current is injected into the HTS layers from the copper termination, this can be largely avoided by fast current ramp rate (> 200 A/s) to prevent heat accumulation. The DC ramping test results of the completed cable are shown in Figure 4.4. The inductive voltages of both inner and outer HTS layers are developed after 1 s when the DC current starts to ramp up. The cable axial magnetic flux contributed by the inner and outer layer is opposite due to opposite winding directions. Hence, the inductive voltage of the outer HTS layer decreases with gradual increase in inner HTS layer current. At a time of about 3.5 s, the outer HTS layer is converted to a flux-flow resistive region [78] with a resistive voltage appearing, and the majority of the current injects into the inner layer resulting in a slightly increased inductive voltage. The sharp transit in voltage of both layers appears at total cable current of 2400 A, where both layers are completely quenched. Measured I-V curves of inner and outer layers are shown in Figure 4.5 as a function of current at each layer obtained by Eq. 4.1 to Eq. 4.4. Table 4.2 summarizes the results.

Table 4.2: The critical currents measurement results of HTS cable with two layers.

	Inner layer	Outer layer	Whole Cable
Ic (A)	1260	1190	2450
R_c (μΩ)	3.01	1.02	-

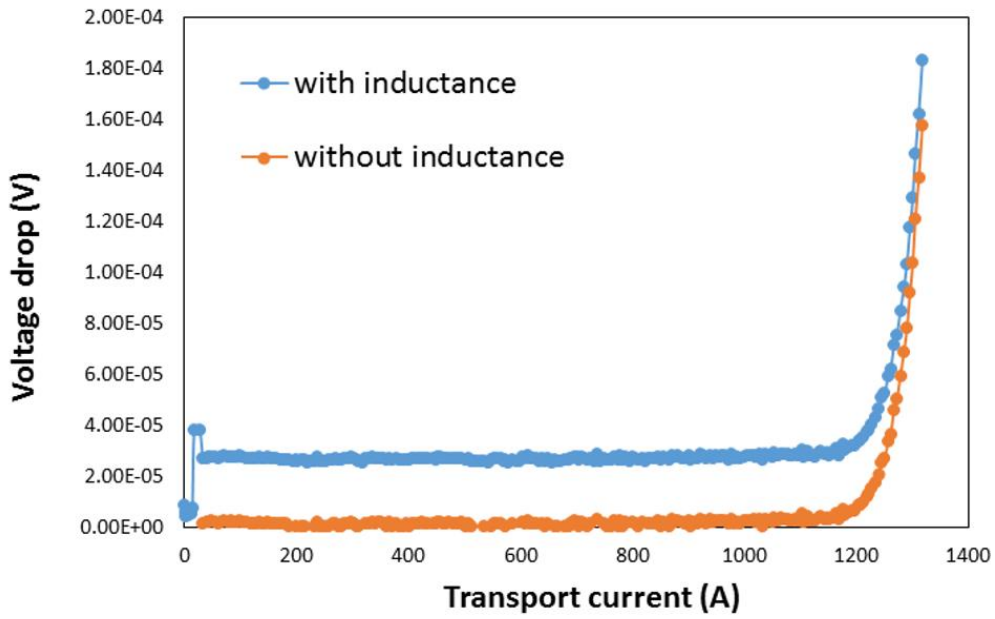

Figure 4.3: The critical current measurement result of HTS cable inner layer.

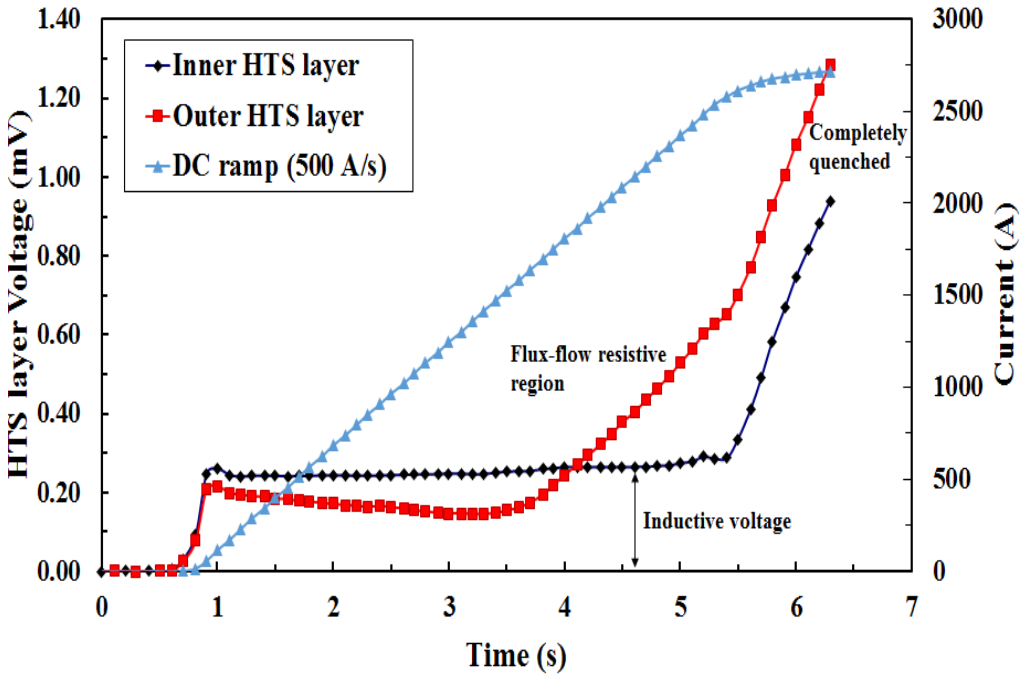

Figure 4.4: The DC ramp current testing results.

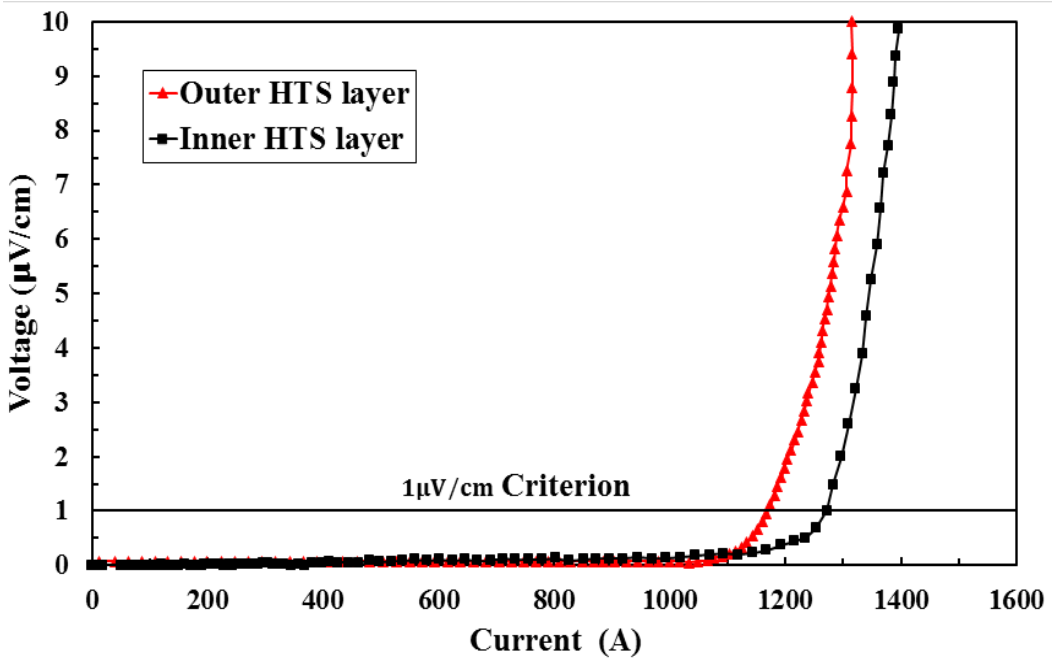

Figure 4.5: I-V curves of inner and outer HTS layers.

4.1.2 2D FEM model of HTS cable current distribution

4.1.2.1 Modelling parameters for anisotropy of YBCO HTS tape wound in the cable

In order to investigate the current distribution density among each layer, the modified H formulation is implemented into the 2D FEM modelling using COMSOL, which considers the contributions of the voltage drop over the terminal contact areas. The twisted pitch angle of HTS tapes is assumed to be ignored in 2D modelling, and all tapes in the cable experience the cable magnetic field. Hence, if the properties of the tape do not change along the cable length, 2D modelling is sufficient to describe the full profile of the cable magnetic flux and the HTS cable critical current affected by the cable magnetic field. In this case, the field dependence of the critical current density of HTS tape wound in the cable should be known. The experimental

characterization was performed to obtain the data for the dependence of the critical current with respect to the applied external magnetic field. The determination for $J_c(B)$, as exprssed in Eq. 4.5, of the tapes in the HTS cable can be refered to the section 3.1.1.

$$J_c(B_\parallel, B_\perp) = \frac{J_{c0}}{(1 + \frac{\sqrt{k^2|B_\parallel|^2 + |B_\perp|^2}}{B_0})^{\alpha}} \quad \text{Eq. 4.5}$$

4.1.2.2 Modelling of HTS cable current distribution with contact resistances [73]

In the 2D modelling of the HTS cable, the cross-section of the cable is assumed to be along the z direction with infinite length, hence, all the parameters are considered to be per unit length. The HTS cable is modelled without considering the cable ends effect and each HTS tape is modelled as a rectangle with high aspect ratio, typically more than 100. A set of Maxwell's Eq. 4.6 to Eq. 4.9 are used in order to obtain the general form PDEs in Comsol.

$$\nabla \times \boldsymbol{E} = -\frac{\partial \boldsymbol{B}}{\partial t} \quad \text{Eq. 4.6}$$

$$\nabla \times \boldsymbol{H} = \boldsymbol{J} \quad \text{Eq. 4.7}$$

$$\boldsymbol{B} = \mu \boldsymbol{H} \quad \text{Eq. 4.8}$$

$$\boldsymbol{E} = \rho \boldsymbol{J} \quad \text{Eq. 4.9}$$

Combining Eq. 4.6 to Eq. 4.9 with some substitutions, the governing PDE becomes Eq. 4.10.

$$\nabla \times (\rho \nabla \times \boldsymbol{H}) = -\mu \frac{\partial \boldsymbol{H}}{\partial t} \quad \text{Eq. 4.10}$$

In Eq. 4.10, the *E-J* power law is used to describe the sharp transit of the superconductor property, *n* is chosen to be 30 and E_c = 1 $\mu V/cm$.

$$\boldsymbol{E_{sc}} = \rho \boldsymbol{J} \qquad \text{Eq. 4.11}$$

where $\rho = \frac{E_c}{J_c(B_\parallel, B_\perp)} \cdot \left|\frac{J}{J_c(B_\parallel, B_\perp)}\right|^{n-1}$. The influence of anisotropic characteristics of YBCO tape is taken into account. The field-dependence of critical current density $J_c(B_\parallel, B_\perp)$ of the YBCO tape wound in the cable is determined through experimemal characterization. Since the 2D model neglects all the cable terminal ends effects, the governing PDE form expressed in the Eq. 4.10 must be modified in order to consider the effect of the terminal resistances on the current distributions among the HTS layers. The voltage drop that purely contributed by the contact resistance E_R can be expressed as Eq. 4.12.

$$\boldsymbol{E}_R = R_i I_i, i = 1{,}2 \qquad \text{Eq. 4.12}$$

where *i* is the number of HTS layer in the cable. A modified electrical field can be the summation of the purely contributed field from the superconductivity part $\boldsymbol{E_{sc}}$ and the purely contributed field from the contact areas part $\boldsymbol{E_R}$, as expressed in Eq. 4.13.

$$\boldsymbol{E} = \boldsymbol{E}_{sc} + \boldsymbol{E}_R \qquad \text{Eq. 4.13}$$

A modified governing equation Eq. 4.14 is obtained. The values of contact resistances used in the modelling are obtained from the experimental test results from Table 4.2. The current distribution density can be solved using COMSOL and the results are shown in Figure 4.6.

$$\nabla \times (\rho \nabla \times \boldsymbol{H} + \boldsymbol{E_R}) = -\mu \frac{\partial \boldsymbol{H}}{\partial t} \qquad \text{Eq. 4.14}$$

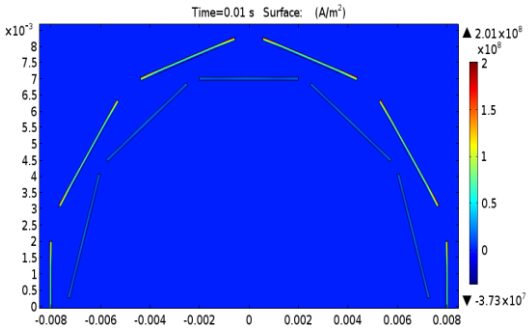

(a) I = 0.11 Ic

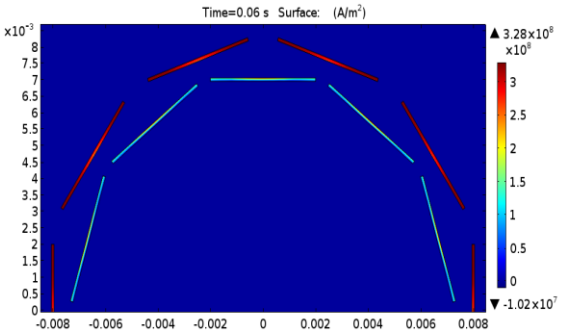

(c) I = 0.68 Ic

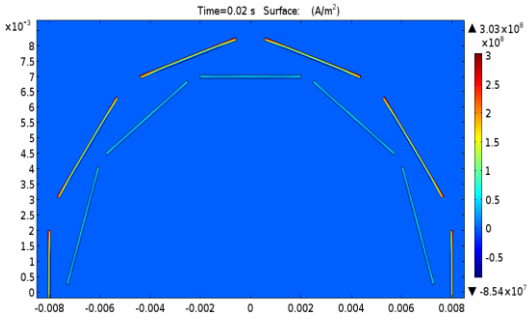

(b) I = 0.23 Ic

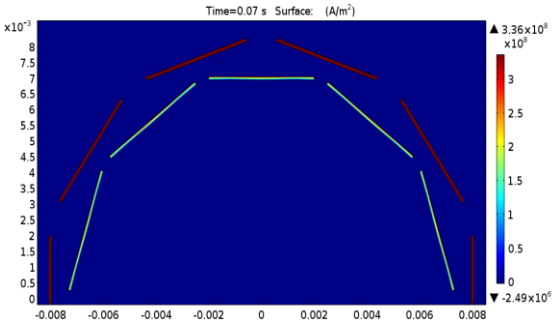

(e) I = 0.8 Ic

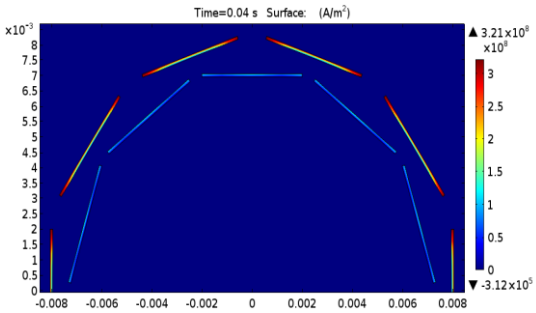

(c) I = 0.46 Ic

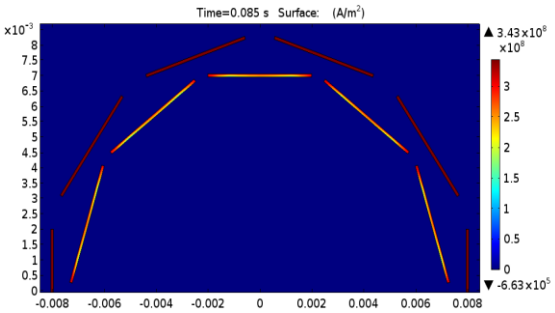

(f) I= 0.97 Ic

Figure 4.6: The modelling results of current density distribution among two HTS layers with respect to the total cable critical current.

The average current value of each HTS layer is determined by applying DC ramping current using pointwise constraint from Comsol. Based on Eq. 4.11 to Eq. 4.14, the current will distribute into each HTS layer considering the effect of terminal contact resistance $\boldsymbol{E_R}$. The distributed current of each layer can be obtained by integrating the current density across the area $\boldsymbol{S_i}$ of each HTS layer as in Eq. 4.15:

$$\boldsymbol{I_i} = \int_{S_i} \boldsymbol{J}\, ds_i, \qquad i = 1,2 \qquad \text{Eq. 4.15}$$

The current distributions at each layer obtained from experimental and simulation works are with good consistency, shown in Figure 4.7. It can be seen that the outer HTS layer conducts current dominantly and increases to critical current value at total cable current of about 1500 A due to less contact resistance on the outer layer. The majority of the current starts to inject into the inner HTS layer after the outer HTS quenching. Both layers start to quench with approaching uniform current distribution.

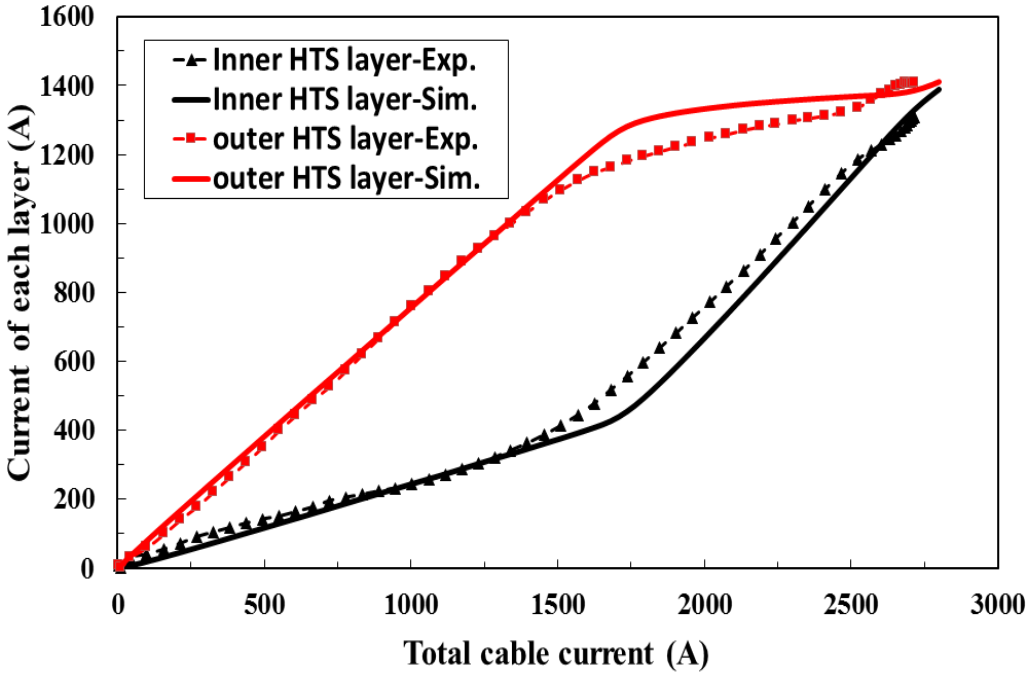

Figure 4.7: The experimental and the simulation results of the current distribution.

In order to have an even distribution of the current among the HTS layers, the influence of contact resistances should be minimized. This can be obtained by changing the contact resistance values in the FEM HTS cable model. Table 4.3 gives three groups of contact resistance combinations, and the current distribution simulating results are shown in Figure 4.8 by implementing with these three groups of contact resistances. It can be seen that the current distribution of inner and outer layers tend to be equalized as the difference of contact resistances become small. But till now, it is still not practical to completely eliminate the difference of the contact resistances affecting individual HTS layer.

Table 4.3: Three groups of contact resistances.

Group no.	Inner HTS layer contact resistance ($\mu\Omega$)	Outer HTS layer contact resistance ($\mu\Omega$)
(1)	3	1
(2)	1.5	1
(3)	1	1

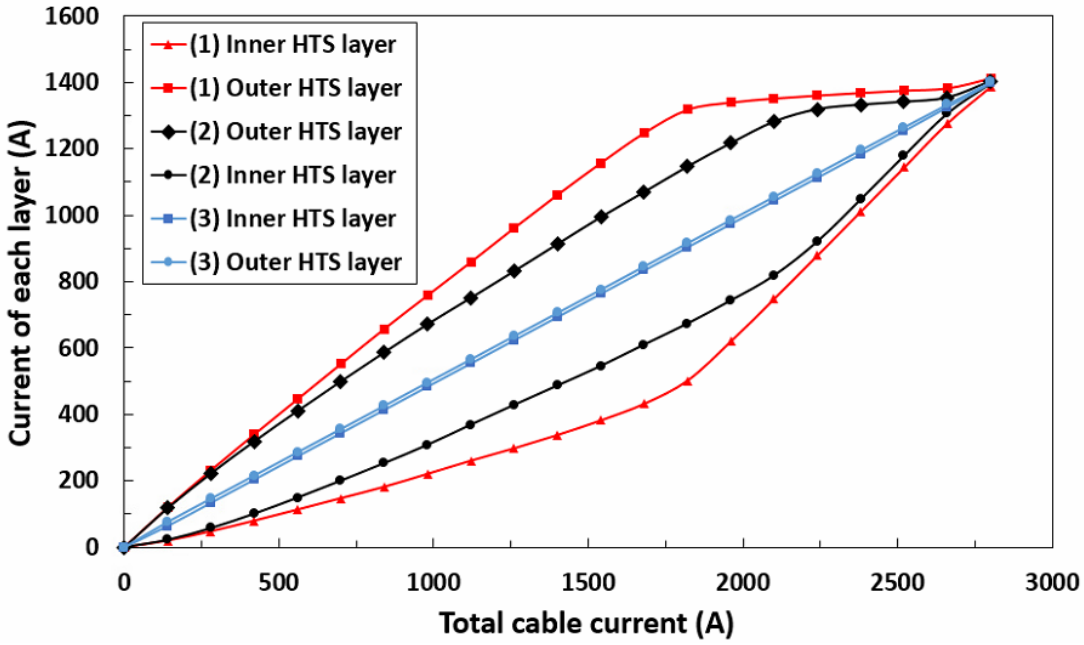

Figure 4.8: The simulation results of homogenized current distribution.

4.2 Homogenization of current distribution of multi-layer HTS cable considering the inductances

If the HTS cable carries AC transporting current, the inductance of HTS layer in the cable is not negligible. On the contrary, the influence of the HTS cable inductance is more significant than the contact resistance, especially for the long transmission cable. Hence, the current repartition is not possible to be balanced among the HTS layers unless the inductance of each HTS layer is equal. In this section, the homogenization of current distribution of multi-layer HTS cable is investigated considering the inductance for each HTS layer.

4.2.1 The analytical formulas of the inductance

The structure of the typical CD HTS triaxial cable with multiple conducting layers is sketched in Figure 4.9. It consists of former, multiple HTS conducting layers, PPLP insulation layer and copper shielding layers. Figure 4.10 gives a schematic diagram of one HTS conducting layer in where r is the radius of conducting layer, P is the winding pitch for a single HTS tape, β is the pitch angle of HTS tapes wound in the cable, and w is the width of the HTS tape. From the schematic, it can be seen that the relationship of the winding angle and winding pitch is shown in Eq. 4.16.

$$P = \frac{2\pi r}{\tan\beta} \qquad \text{Eq. 4.16}$$

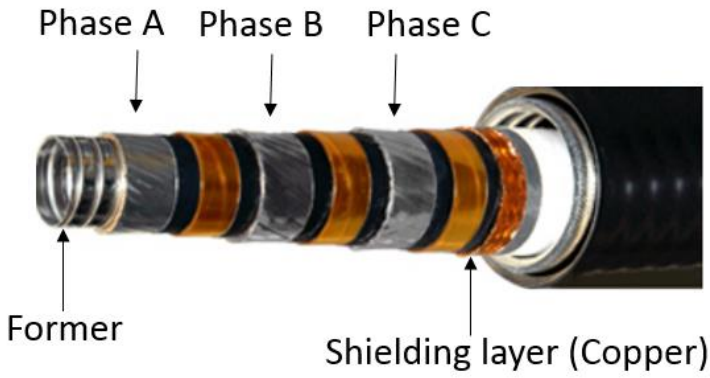

Figure 4.9: The configuration of CD HTS cable with multiple conducting layers.

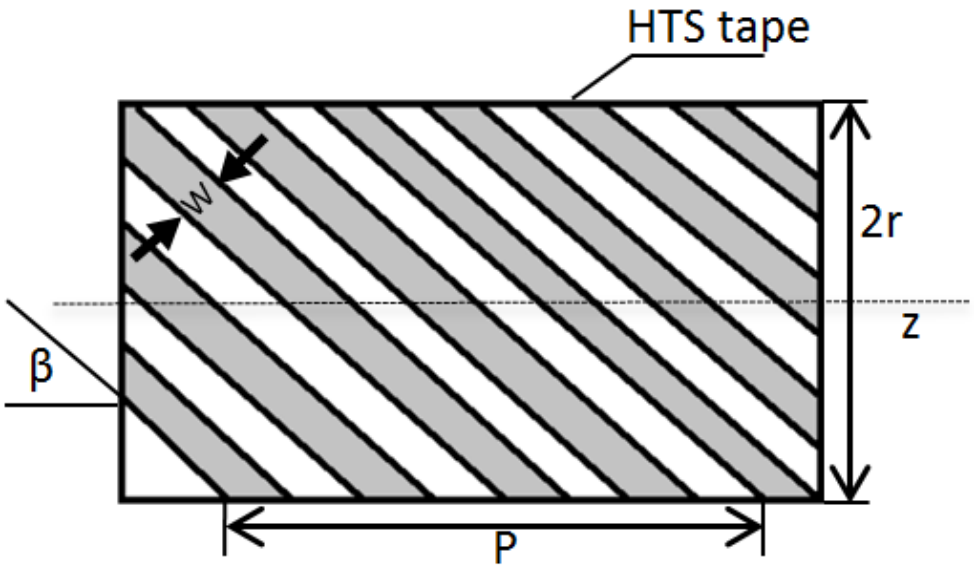

Figure 4.10: 2D schematic diagram of HTS cable conducting layer.

The helically wounding structure of HTS layer in the cable results in complicated magnetic field distribution, hence, the analytical solution of HTS layer inductance is not straightforward. As shown in Figure 4.11, the magnetic field of each HTS tape is affected by not only AC transporting current, but also cable radius, pitch and winding direction. Each HTS tape in i^{th} layer experiences axial (B_{iz}) and tangential ($B_{i\theta}$) components of magnetic field with respect to the cable axial. The analytical solution is not possible to obtain without necessary assumptions as follows:

- In HTS cable, the resistance is assumed to be negligible compared with the inductance, hence only the inductance is taken into account.
- Although the contact resistances will also affect the current distribution of HTS cable carrying AC transporting current, they are ignored in this analysis in order to focus on the influence of the inductance.
- Based on the discussion in Chapter 3, the gap between the adjacent HTS tapes should be minimized for maximized cable critical current density. It is also known that the influence of the gap distance due to the anisotropy of YBCO HTS tape is negligible compared with contact resistance. Similar reason with the last assumption, the gap distance is assumed to be zero so that all the HTS tapes within one pitch are considered as one conductor.

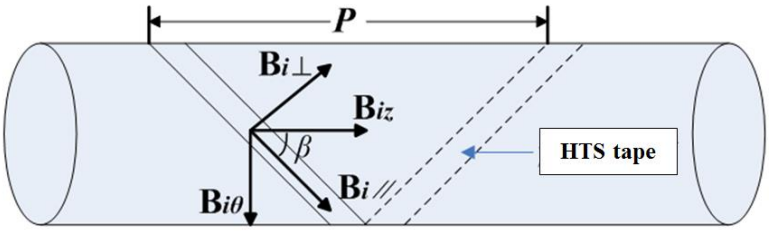

Figure 4.11: The magnetic field of tapes in HTS cable.

Based on the assumptions, the HTS layer in the cable can be simplified to an ideal solenoid coil without resistance. The analytical solution of the inductance of solenoid can be used to solve the inductance of HTS cable. As shown in Figure 4.12, consider a solenoid coil of length *l* and *N* turns, when a current *I* flows in the solenoid, a uniform axial field can be calculated as Eq. 4.17.

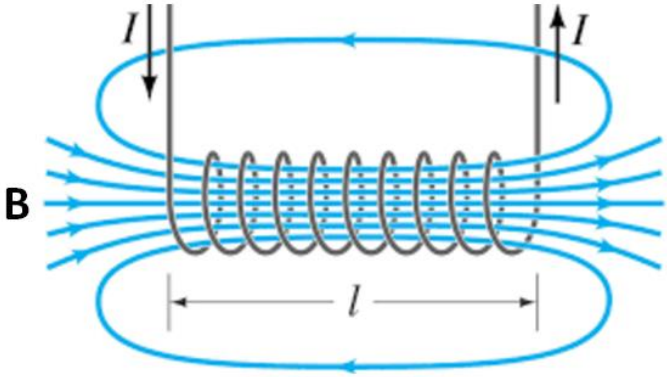

Figure 4.12: The sketch of a solenoid coil.

$$\mathrm{B} = \frac{\mu_0 NI}{l} \qquad \text{Eq. 4.17}$$

where μ_0 is the permeability of free space: $4 \times 10^7 \mathrm{H} \cdot m^{-1}$. Assuming no gap among the tapes in HTS cable, one pitch length of HTS cable can be calculated as Eq. 4.18 and total enclosed magnetic field of i^{th} HTS layer in the cable can be calculated as Eq. 4.19.

$$P = \frac{l}{N} \quad \text{Eq. 4.18}$$

$$B_{iz} = \frac{\mu_0 I_i}{P_i} \quad \text{Eq. 4.19}$$

where I_i is the current of the i^{th} layer and P_i is the pitch length of the i^{th} layer. Additionally, the HTS power cable usually has larger pitch length compared with an ideal solenoid coil. The magnetic field outside the layer cannot be ignored. From Ampere's law, the i^{th} HTS layer also experiences a considerable large tangential field as expressed in Eq. 4.20.

$$B_{i\theta} = \frac{\mu_0 I_i}{2\pi r_i} \quad \text{Eq. 4.20}$$

where r_i is the radius of the i^{th} layer. In solenoid coil, the total axial flux φ is linearly proportional to the current I, which gives the inductance as $L = {}^{\varphi}/_{I}$. The total axial flux in the solenoid coil can be calculated as $\varphi = NBA$, where A is the cross-section area of the solenoid coil. Considering Eq. 4.17, the inductance of the solenoid coil can be expressed as $L = {}^{\mu_0 N^2 AI}/_{l}$. The energy stored in the coil can be calculated as $W = \frac{1}{2}LI^2$, with some substitutions, the magnetic energy density φ inside the solenoid is shown in Eq. 4.21.

$$\varphi = \frac{B^2}{2\mu_0} \quad \text{Eq. 4.21}$$

Since HTS cable is similar to the solenoid coil, the energy stored inside the HTS layer can be calculated using Eq. 4.21. Additionally, the energy stored outside the HTS layer is not negligible. Assuming that there is no magnetic field leakage outside the HTS cable, therefore, the maximum space of energy stored outside the HTS layer is restricted by the shielding layer. Then the total energy stored in the i^{th} HTS layer can

be calculated by Eq. 4.22, and then the self-inductance of the i^{th} HTS layer can be found as Eq. 4.23.

$$P_{total} = \frac{1}{2\mu_0}\int_0^{r_i} {B_{iz}}^2 \cdot 2 \cdot \pi \cdot r dr + \frac{1}{2\mu_0}\int_{r_i}^{D} {B_{i\theta}}^2 \cdot 2 \cdot \pi \cdot r dr \qquad \text{Eq. 4.22}$$

$$L_i = \mu_0 \frac{\pi r_i^2}{P_i^2} + \mu_0 \frac{ln\left(\frac{D}{r_i}\right)}{2\pi} = \frac{\mu_0}{4\pi}(tan\ ^2 \beta_i + 2ln(\frac{D}{r_i})) \qquad \text{Eq. 4.23}$$

where L_i is the self-inductance of the i^{th}HTS layer (H/m), β_i is the pitch angle of i^{th} HTS conductor layer and *D* is the radius of the shielding layer of HTS cable. For multi-HTS-conducting layers, the magnetic energy also stores between the HTS layers. Applying the similar analysis of HTS layer self-inductance, the mutual inductance between the i^{th} and j^{th} layers can be found as Eq. 4.24 [79].

$$M_{ij} = M_{ji} = \frac{\mu_0}{2\pi}(\frac{\alpha_i \alpha_j}{2}\frac{r_i}{r_j} tan(\beta_i)\, tan\left(\beta_j\right) + ln(\frac{D}{r_j})) \qquad \text{Eq. 4.24}$$

where α_i is the winding direction of the i^{th} layer and *i, j* is layer number, *i, j* = 1, 2, 3, 4, ···. It can be concluded from Eq. 4.23 and Eq. 4.24 that both the self and mutual inductance of each HTS layer in the cable only vary with radius *r*, pitch angle β and winding direction α. Hence, the current distribution among the HTS conducting layers can be varied by adjusting these three parameters of cable geometry.

4.2.2 The inductance analysis of the multi-layer HTS cable varying with HTS cable geometry

A 22.9 kV/1.5 kA cold dielectric (CD) triaxial HTS cable has been proposed in the theoretical analysis. The cable has 4 HTS conducting layers and 2 HTS shielding layer. The radius of the HTS conducting layer starts from the former. The purpose of the former is to provide a mechanical support for HTS tapes and to temporarily carry

fault current when a fault occurs. For safety reason, the radius of the former can be extended from R_f to 1.2 R_f, where R_f depends on the HTS cable fault current level. The minimum radius of the copper former is initially set to be 12.24 mm. The thickness of each layer is 0.25 mm including the insulation between the layers. Then the radii of the other HTS layers are adjusted accordingly. Lay 4 and lay 5 is separated by a PPLP cable insulation layer with a thickness of 13.95 mm. The structure parameters of the cable are described in Table 4.4.

Table 4.4: The structure parameters of CD triaxial HTS cable.

Layer no.	Radius r (mm)	Pitch angle (β)	Winding direction
1	12.24	27°	+1
2	12.49	27°	+1
3	12.47	27°	-1
4	12.99	27°	-1
5	26.94	27°	+1
6	27.19	27°	-1

4.2.2.1 Radius (*r*)

To investigate the effect of the radius on the HTS layer inductance, an increment step of 0.2 mm is used and the maximum radius of the former is set at 14.05 mm. The radius of each HTS layer varies with the same increment step. The pitch angles and winding directions of all layers are fixed in this case. The inductance variation of each HTS layer and total inductance of the HTS cable in terms of the radius is shown in Figure 4.13 and Figure 4.14, respectively. The calculation is based on the Eq. 4.23 and Eq. 4.24 using MATLAB code. The calculation results show that the self and mutual inductance of each HTS layer decrease with increased cable radius. The total inductance of the whole HTS cable linearly decreases with the increased cable radius.

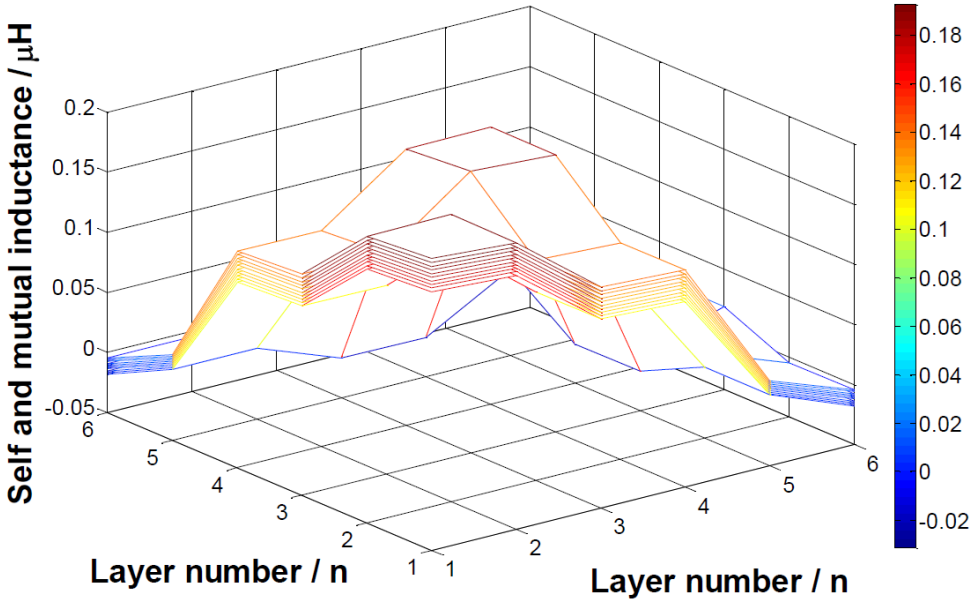

Figure 4.13: Self and mutual inductance varying with HTS layer radius.

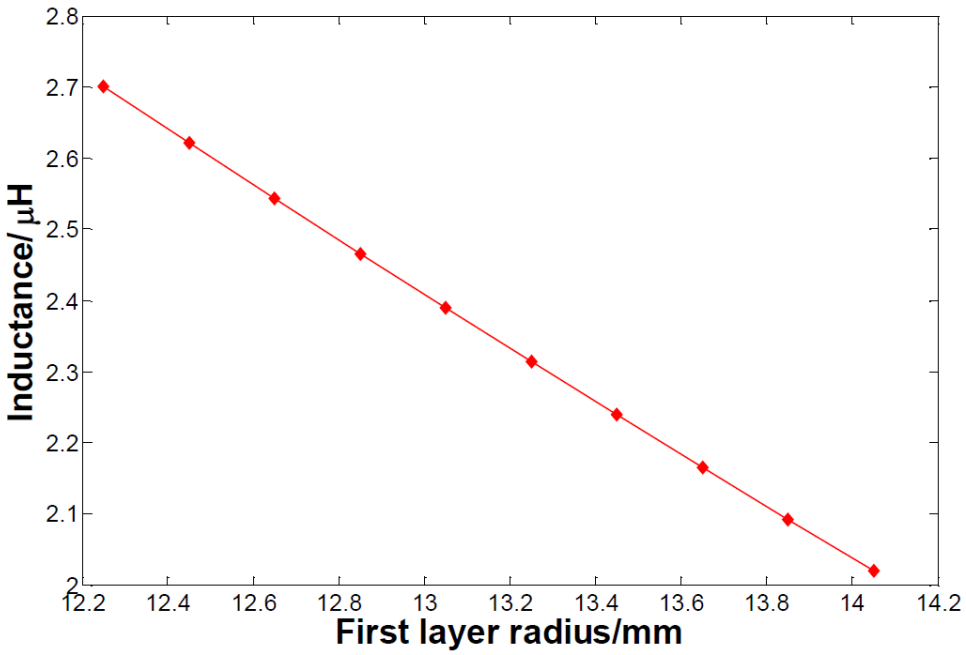

Figure 4.14: Total inductance of HTS cable varying with first layer radius.

4.2.2.2 Pitch angle (β)

The pitch angle of each HTS layer is initially set to be $27^0$and the maximum pitch angle is 81^0 with an increment step of 6^0, which is applied to each layer for every calculation, in order to investigate the inductance variation in terms of pitch angle at fixed radius and winding directions. Figure 4.15 gives the result of the inductance of the first HTS layer varying with pitch angle. It can be seen that the self and mutual inductances of each HTS layer are increasing with increased pitch angle. The negative mutual inductances are due to the opposite winding direction between the two relevant layers, which results in a negative current component induced in the first layer. The remaining HTS conducting layers have similar results. Figure 4.16 shows that the total inductances of all the HTS conducting layers in the cable increase as an approximately quadratic function varying with pitch angle.

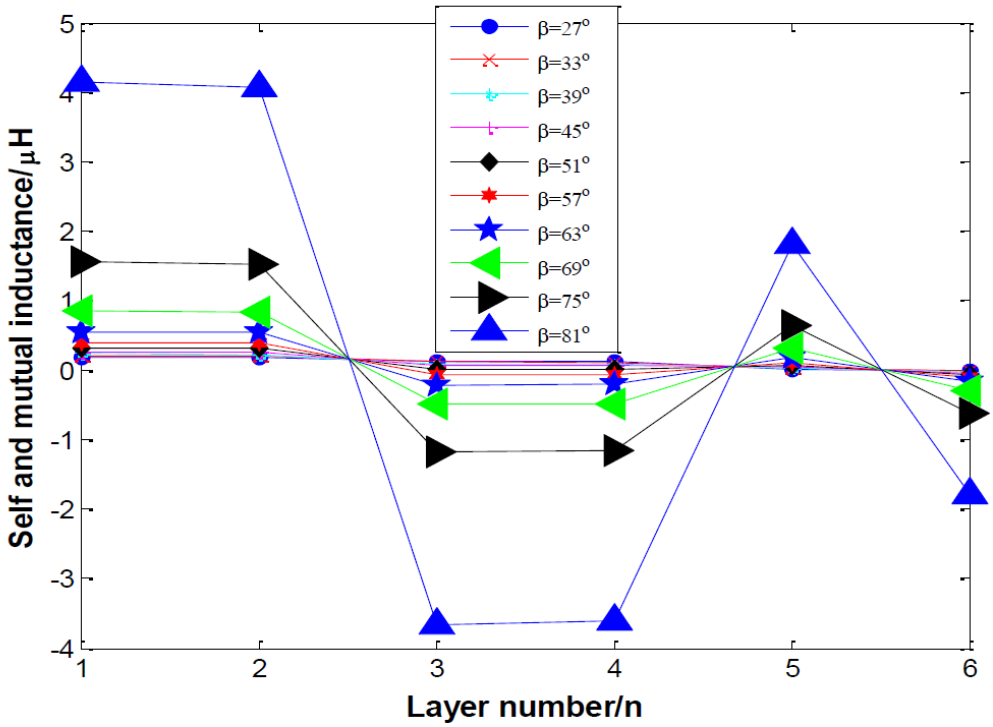

Figure 4.15: Self and mutual inductance varying the pitch angle of first HTS layer.

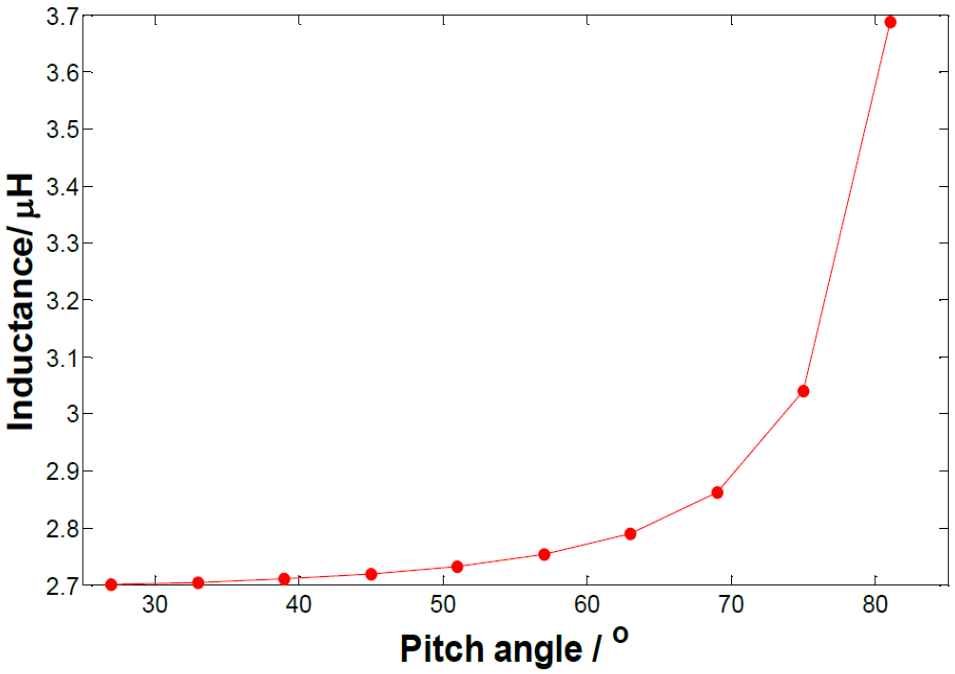

Figure 4.16: Total inductance of HTS cable varying the pitch angle of the first layer.

4.2.2.3 Winding direction (α)

Table 4.5 shows the 12 groups of winding direction combination for each HTS layer of the cable ('+1' means clock-wise direction and '-1' means anticlockwise direction). The Eq. 4.24 shows that only the mutual inductance varies with different winding directions. Therefore, the self-inductance is not included in this part of analysis. To minimize the cable axial and tangential flux, the total HTS layer number should be even, such that the sum of the winding direction coefficients $\sum_i^n \alpha_i$ can be equal to zero. However, as shown in Figure 4.17, the mutual inductances of the groups 1 to 4 are similar as well as the group 5 to 12. There is no obvious effect of winding direction on the total cable mutual inductance.

Table 4.5: Winding directions combination of CD HTS cable.

Group no. \ Layer no.	1	2	3	4	5	6
1	1	1	-1	-1	1	-1
2	1	1	-1	-1	-1	1
3	-1	-1	1	1	1	-1
4	-1	-1	1	1	-1	1
5	1	-1	1	-1	1	-1
6	1	-1	1	-1	-1	1
7	-1	1	-1	1	1	-1
8	-1	1	-1	1	-1	1
9	1	-1	-1	1	1	-1
10	1	-1	-1	1	-1	1
11	-1	1	1	-1	1	-1
12	-1	1	1	-1	-1	1

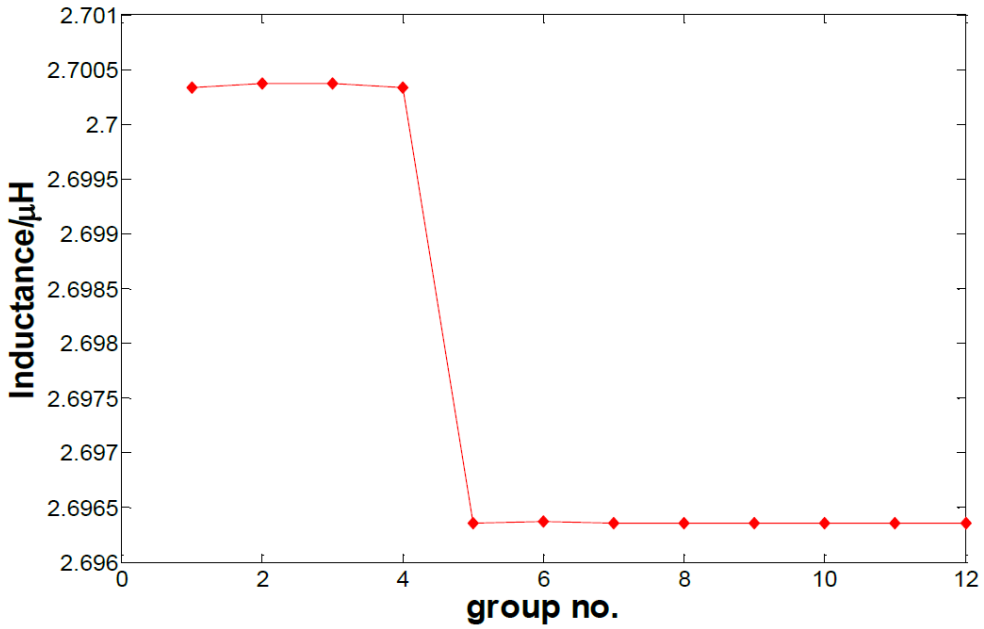

Figure 4.17: Total inductance of HTS cable varying with all combination of winding directions.

4.2.3 The current distribution optimization for triaxial HTS cable

4.2.3.1 The equivalent electrical circuit of triaxial HTS cable

The mathematical equivalent electrical circuit is implemented based on the cross-section configuration of HTS triaxial cable as shown in Figure 4.18. The equivalent electrical circuit is shown in Figure 4.19. The radii of each electrical phase and copper shielding layer are R_a, R_b, R_c and R_s, respectively. Each HTS phase is represented as an inductance L with a series connected resistor R, where $R \ll L$. The inductance of each layer contains self-inductance and mutual inductance. It should be noted that in this particular triaxial HTS cable, there is no copper former as cable core. Instead, a hollow corrugated tube is used as cable former, which benefits from the reduction of weight and high efficiency for cooling channel. Hence, in the electrical equivalent circuit, there is no component representing the cable former. The self-inductance and mutual inductance of each HTS layer, or each electrical phase in this case, can be calculated from Eq. 4.23 and Eq. 4.24, respectively. The equivalent electrical circuit also contains the shunt capacitance of the triaxial HTS cable and its magnitude is comparable to the conventional cable. The shunt capacitance cannot be ignored when considering the dielectric losses, which is determined by the PPLP insulation thickness. Eq. 4.25 gives the expression of the capacitance per unit length [80].

$$C_{ij} = \frac{2\pi\varepsilon_r\varepsilon_0}{\ln(\frac{r_j}{r_i})} \qquad \text{Eq. 4.25}$$

where, $i, j = 1,2,3$, and $r_j > r_i$. $\varepsilon_r\varepsilon_0$ is the dielectric constant of PPLP materials. From the configuration of the HTS triaxial cable electrical equivalent circuit shown in Figure 4.19, the current of each phase can be calculated from Eq. 4.26 in terms of the matrixes of resistance, inductance and capacitance.

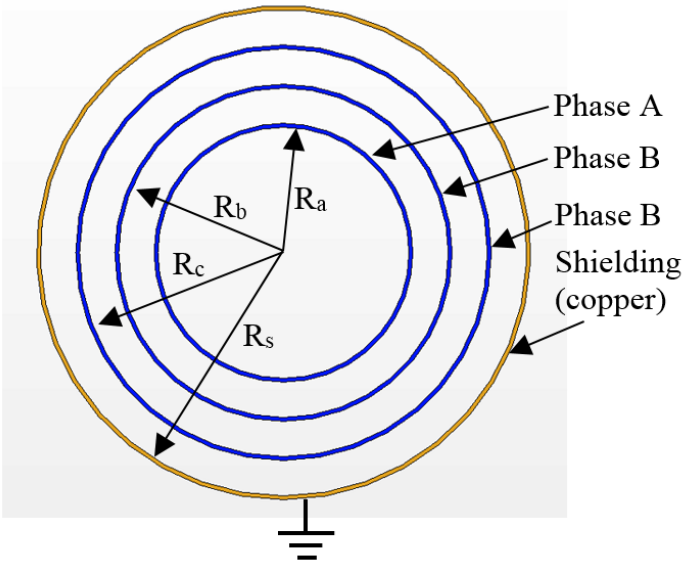

Figure 4.18: Cross section of triaxial cable.

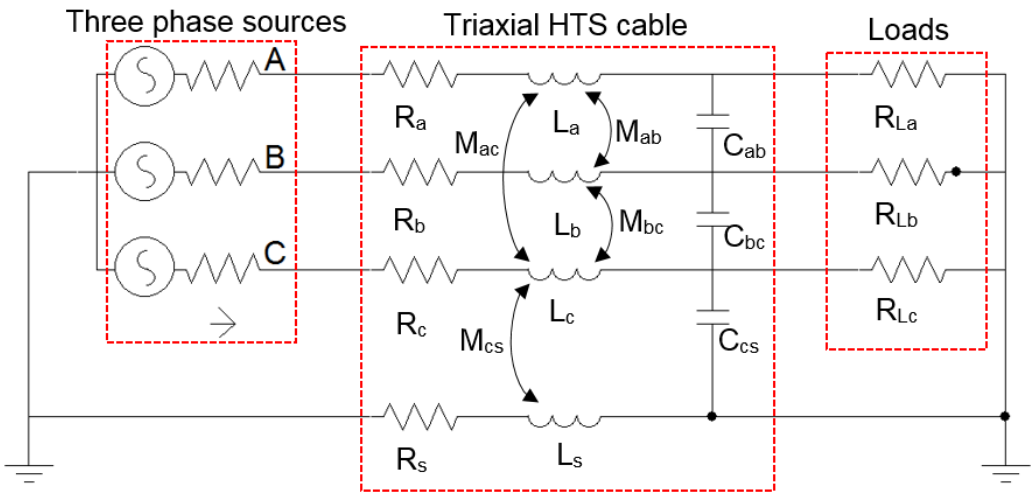

Figure 4.19: Equivalent electric circuit of triaxial HTS cable system.

$$\begin{pmatrix} I_a \\ I_b \\ I_c \\ I_s \end{pmatrix} = \left(\frac{1}{j\omega} \begin{pmatrix} L_a & M_{ab} & M_{ac} & M_{as} \\ M_{ba} & L_b & M_{bc} & M_{bs} \\ M_{ca} & M_{cb} & L_c & M_{cs} \\ M_{sa} & M_{sb} & M_{sc} & L_s \end{pmatrix}^{-1} \right.$$

$$+ j\omega \begin{pmatrix} C_{ab} & -C_{ab} & 0 & 0 \\ -C_{ba} & C_{ba} + C_{bc} & -C_{bc} & 0 \\ 0 & -C_{bc} & C_{cb} + C_{cs} & -C_{cs} \\ 0 & 0 & -C_{cs} & C_{cs} \end{pmatrix} \qquad \text{Eq. 4.26}$$

$$\left. + \begin{pmatrix} R_a & 0 & 0 & 0 \\ 0 & R_b & 0 & 0 \\ 0 & 0 & R_c & 0 \\ 0 & 0 & 0 & R_s \end{pmatrix}^{-1} \right) \begin{pmatrix} V_a \\ V_b \\ V_c \\ V_s \end{pmatrix}$$

4.2.3.2 The algorithm development for optimizing current distribution

Assuming that only the inductive impedance dominates the impedance of each electrical phase in the HTS triaxial cable, the current distributed into each HTS layer is determined by the inductance, which can be adjusted in terms of radii, pitch angles and winding directions of HTS layer. The current distribution of a 22.9 kV/1.5 kA triaxial HTS is calculated based on Eq. 4.26. The specifications of the cable are described in Table 4.6. Before optimization, the pitch angles and winding directions are chosen randomly. The thickness of the PPLP insulation layer is calculated based on the cable voltage level and the number of tapes in the layer is based on the current rating. The length of the cable is considered to be in unit length. The inductance of each phase which is used in the calculation can be obtained based on Eq. 4.23 and Eq. 4.24. The calculation result is shown in Figure 4.20. It can be seen that the current distribution is inhomogeneous. Hence, the inductances of the each HTS phases need to be matched in order to achieve homogeneous current distribution. Although the inductance of each HTS phase can be adjusted in terms of the radii, pitch angle and winding direction. The radius of each phase may be predetermined due to: the diameter of the cable former is determined by the requirement of the fault current toleration; the thickness of the insulation is calculated from the voltage level of the

cable; the number of HTS tapes are designed according to the cable current rating, which also

affects the radius of each HTS layer. Hence, the most realistic parameters that can be adjusted are pitch angle and winding direction. An algorithm is developed based on the pitch angle and winding direction of each phase as dependent variables. The flowchart in Figure 4.22 shows the procedures of the optimization algorithm.

The current and voltage specifications in Table 4.6 are used as the initial parameters in the algorithm to calculate the radii of the electrical phases, insulation thickness and the number of the tapes for each phase. If the copper is used as the cable former, the requirement of the cable fault current toleration determines the radius of the former. On the other hand, if the hollow tube is used as a cable former, the number of the innermost HTS layer decides the initial radii of the cable. The initial parameters, including the radii, pitch angle and winding direction, are used to solve the matrix equation Eq. 4.26 to obtain the current of Phase A ($I_a(X_a)$), Phase B ($I_b(X_b)$) and Phase C ($I_c(X_c)$). The maximum and minimum currents of the three phases can be obtained as Eq. 4.27.

$$\begin{aligned} \boldsymbol{X} = [\boldsymbol{X_a}; \boldsymbol{X_b}; \boldsymbol{X_c}] &= \left[r_a, \alpha_a, \beta_a; r_b, \alpha_{b,} \beta_{b;} r_c, \alpha_c, \beta_c\right]; \\ \boldsymbol{I_{max}} &= Max[I_a(X_a), I_b(X_b), I_c(X_c)]; \\ \boldsymbol{I_{min}} &= Min[I_a(X_a), I_b(X_b), I_c(X_c)] \end{aligned} \qquad \text{Eq. 4.27}$$

Then the program will decide whether the difference of the phase currents is acceptable based on the judgement condition. If it fails to accept, the pitch angle and winding direction as dependent variables will be updated to recalculate the current of each electrical phase. When the difference of each phase current is satisfied by the judgement condition, it means the current difference of each phase is minimal and optimization process ends. The pitch angles and winding direction from the optimized results are shown in Table 4.6 after optimization. In this program, the judgement condition *F(X)* is expressed as Eq. 4.28. With the optimized pitch angle and winding direction of each layer of the triaxial HTS cable, the current distribution is calculated and the result is shown in Figure 4.21.

$$F(X) = minf(X) = I_{max} - I_{min} \quad \text{Eq. 4.28}$$

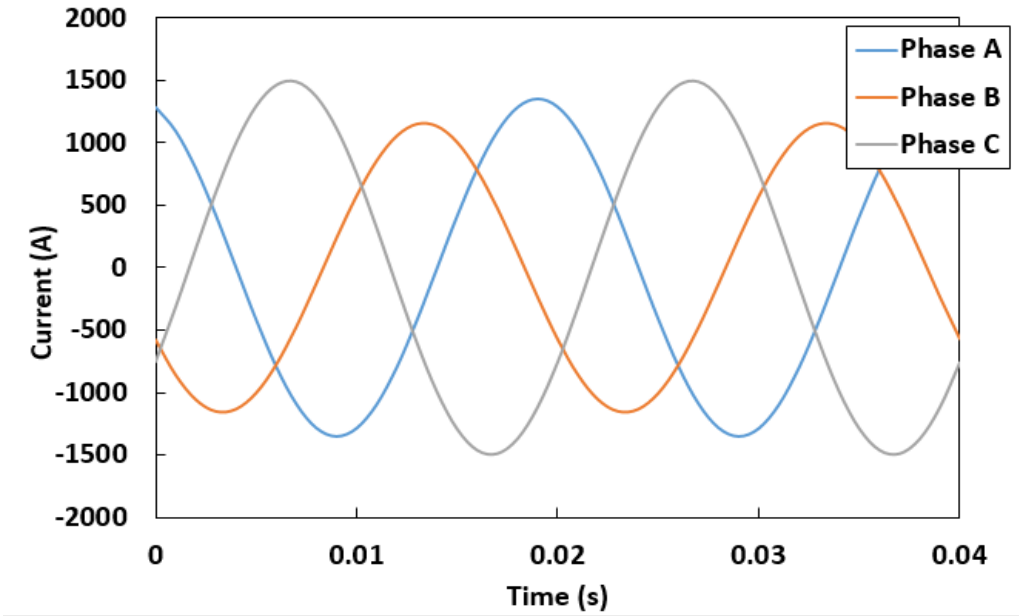

Figure 4.20: The current distribution of HTS triaxial cable before optimization.

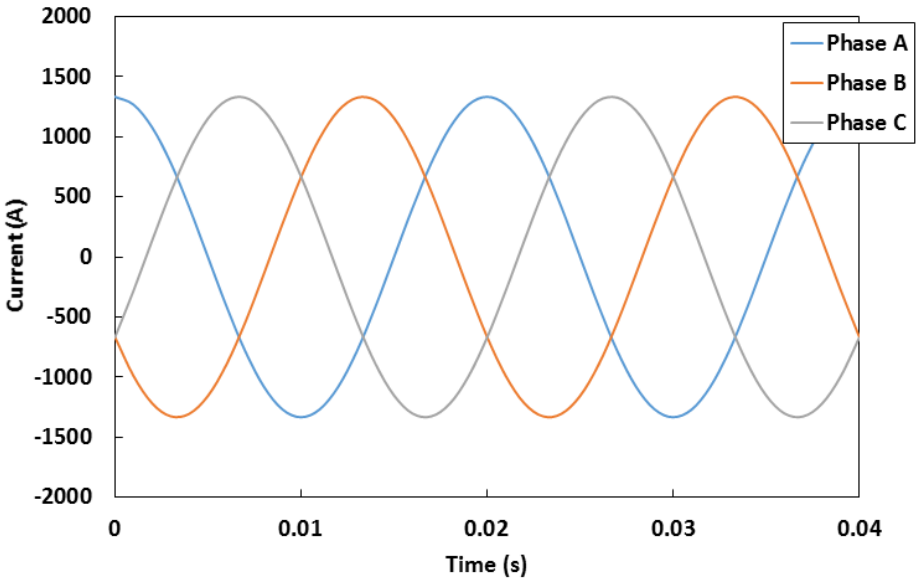

Figure 4.21: The current distribution of HTS triaxial cable after optimization.

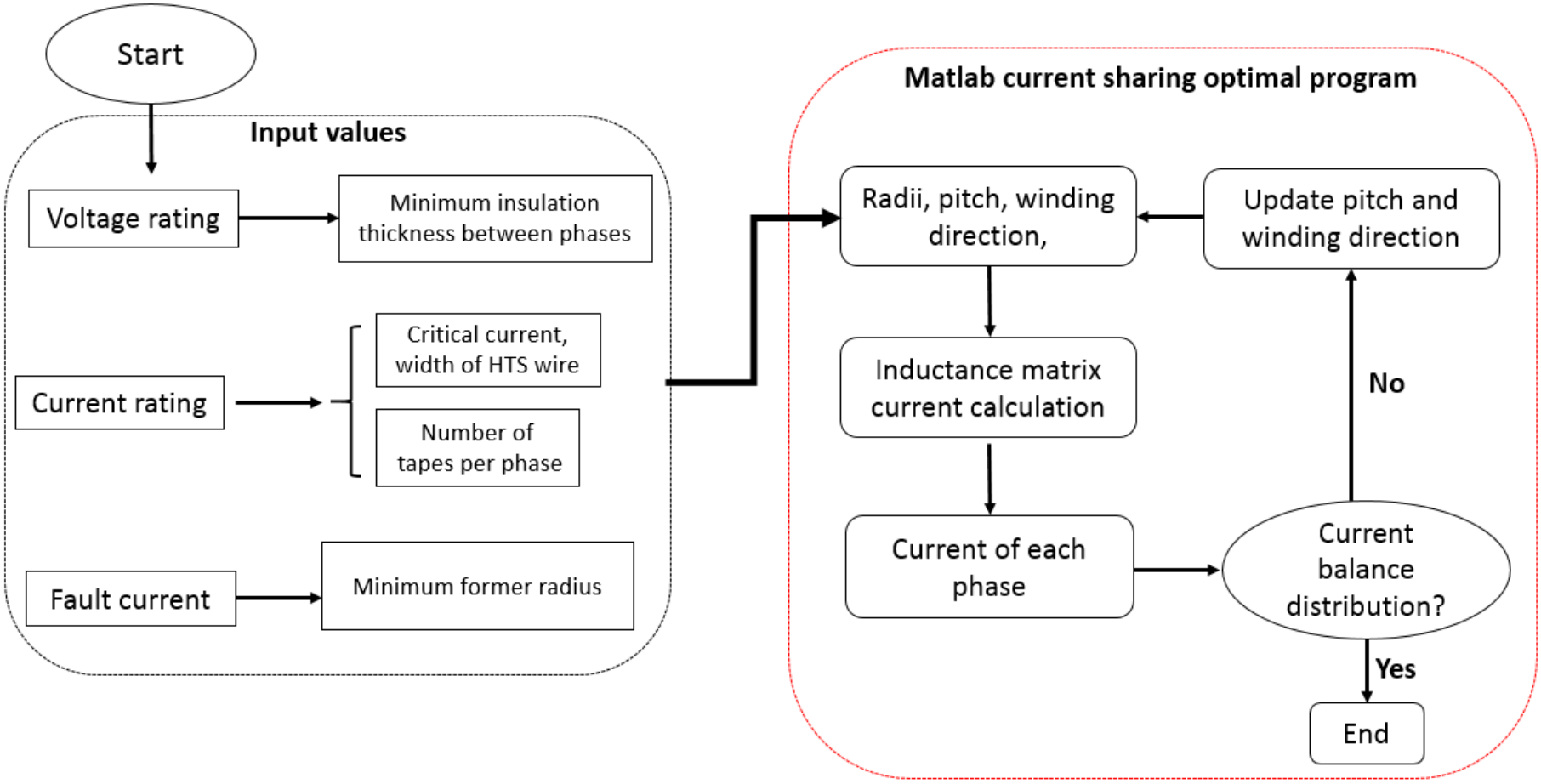

Figure 4.22: The flowchart for the optimization of triaxial HTS cable current distribution.

Table 4.6: Specifications of 22.9 kV/1.5 kA triaxial HTS cable before and after optimization.

Before optimization		After optimization
Parameters	Values	Values
Voltage rating (kV)	22.9	22.9
Current Capacity (kA)	1500/phase	1500/phase
HTS wire	YBCO, 4 mm wide	YBCO, 4 mm wide
Radius of each phase (mm)	16/21/26	16/21/26
Insulation thickness (mm)	5, PPLP	5, PPLP
Number of tape per phase	18,24,27,27	18,24,27,27
Withstand fault current (kA)	25	25
Pitch angle (deg.)	30/20/45/20	16/19/45/40
Winding direction	+1/+1/+1/-1	+1/-1/-1/+1

The deviation of operating current of each electrical phase *Dev*., which indicates the current of each electrical phase I_{phase} deviates from the average operating current $I_{avg.}$, can be defined by Eq. 4.29. The average operating current of the triaxial HTS cable is 1.3 kA and Table 4.7 shows the current deviation of each electrical phase with respect to average operating current, before and after optimization. It shows that the most unbalanced phase deviates 14 % with respect to the average operating current without optimization while negligible current of each phase deviates with respect to the average operating current after optimization. It proves that the currents of three electrical phases become homogenized after implementing the optimal algorithm.

$$\boldsymbol{Dev.}(\boldsymbol{X}) = \frac{\left|I_{phase} - I_{avg.}\right|}{I_{avg.}} \times 100\% \qquad \text{Eq. 4.29}$$

Table 4.7: Current deviation of each electrical phase comparison before and after optimization.

Electrical phase	Before optimization	After optimization
Phase A	1.5 %	0.07 %
Phase B	13.4 %	0.07 %
Phase C	11.9 %	0.06 %

4.2.3.3 Experimental measurement of current distribution of a prototype HTS cable

In order to validate the optimal algorithm, a 0.2 m, 132 kV/1.5 kA prototype cable consisted of two HTS layers has been designed and built, as shown in Figure 4.23. The cable is composed of two Bi-2223 HTS conducting layers wound on a copper former of 9 mm in radius. The pitch angle is optimized based on the optimal algorithm. The optimized pitch angles for each HTS conducting layer are 20^0 and 11^0, respectively. The PPLP insulation is placed between the HTS conducting layer and HTS shielding layer. Table 4.8 summarizes the specifications of the cable design. The current of each HTS layer was measured by Rogowski coils wrapped around the

copper current leads connected with each HTS layer, shown in Figure 4.24. AC current was conducted to HTS cable though the copper current leads. The lengths of the current leads are the same in order to minimize the effect of the resistances of copper leads. The data are recorded by the DAQ and LabVIEW interface. The measurement results are shown in Figure 4.25, where 600 A and 800 A current were charged into the cable, respectively. However, the measured current of each layer is not exactly evenly distributed partly due to the inaccurately controlled pitch angle during the cable constructing process, and the optimized algorithm is based on the self and mutual inductance formulas which ignore the gaps among tapes of each layer in the inductance calculation. Additionally, the contact resistances between the copper current leads and HTS layers are comparable to the inductance of HTS layers in the short HTS cable. Hence, the contact resistances from the copper current leads also cause the unequal distribution of current. But in general, it is expected to have a homogeneous current distribution among the HTS layers when the cable length increases to more than hundreds of meters.

Table 4.8: Parameters of the Prototype HTS cable.

Characteristics	Items	Values
Copper former	Radius	9 mm
1st conducting layer (BSCCO)	Radius	10.4 mm
	Pitch angle	20°
	Tape number	8
2nd conducting layer (BSCCO)	Radius	10.8 mm
	Pitch angle	11°
	Tape number	9
PPLP insulation layer	Thickness	13.7 mm
Shielding layer (BSCCO)	Radius	24.9 mm
	Pitch angle	25°

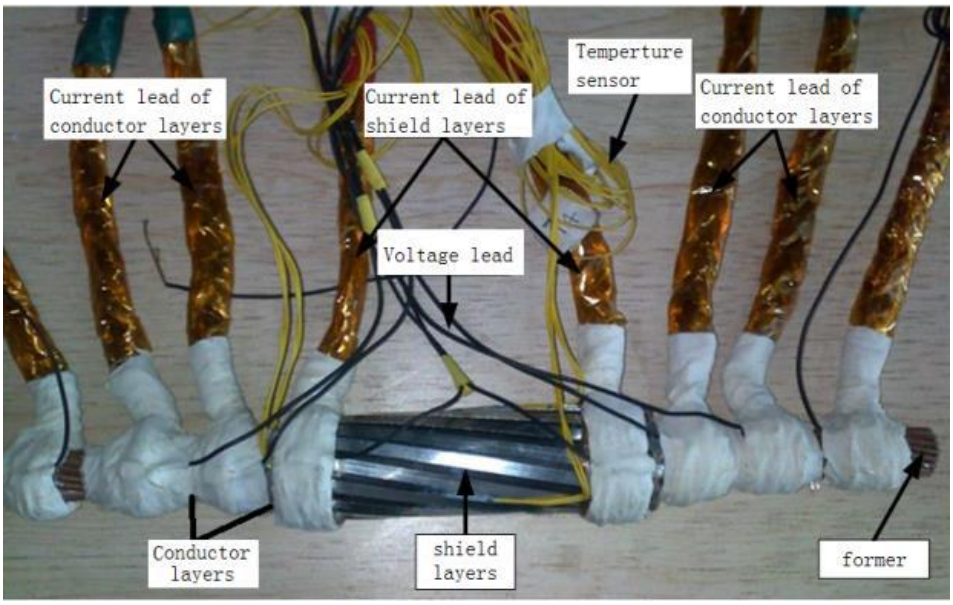

Figure 4.23: 0.2 m, 132 kV/1.2 kA prototype HTS cable.

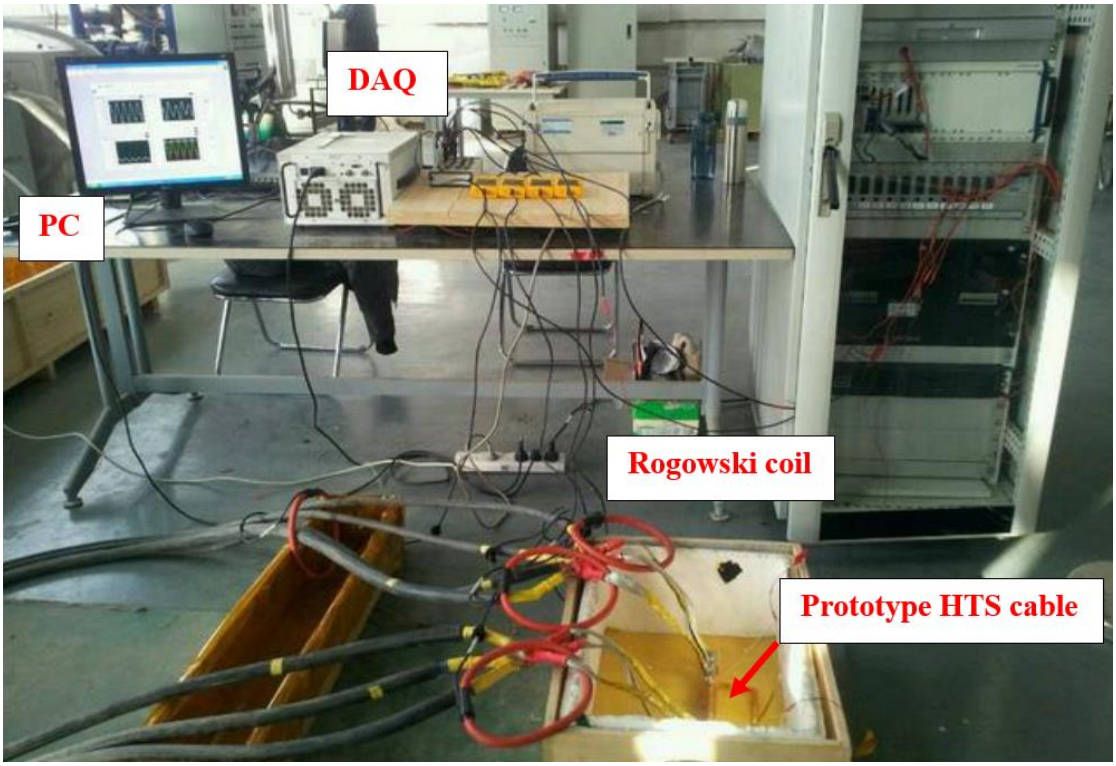

Figure 4.24: Current distribution measured by Rogowski coils.

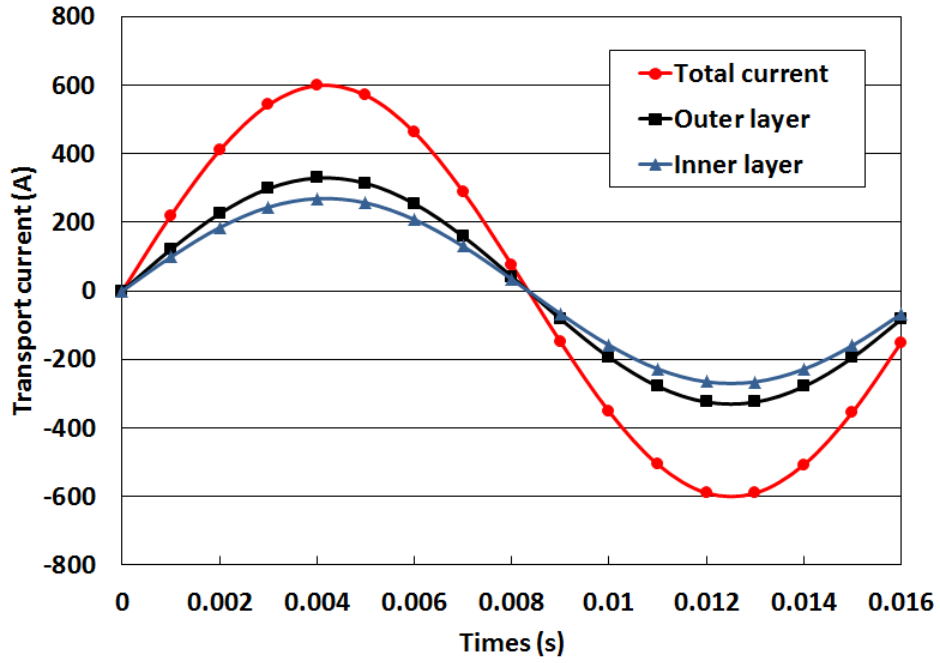

(a)

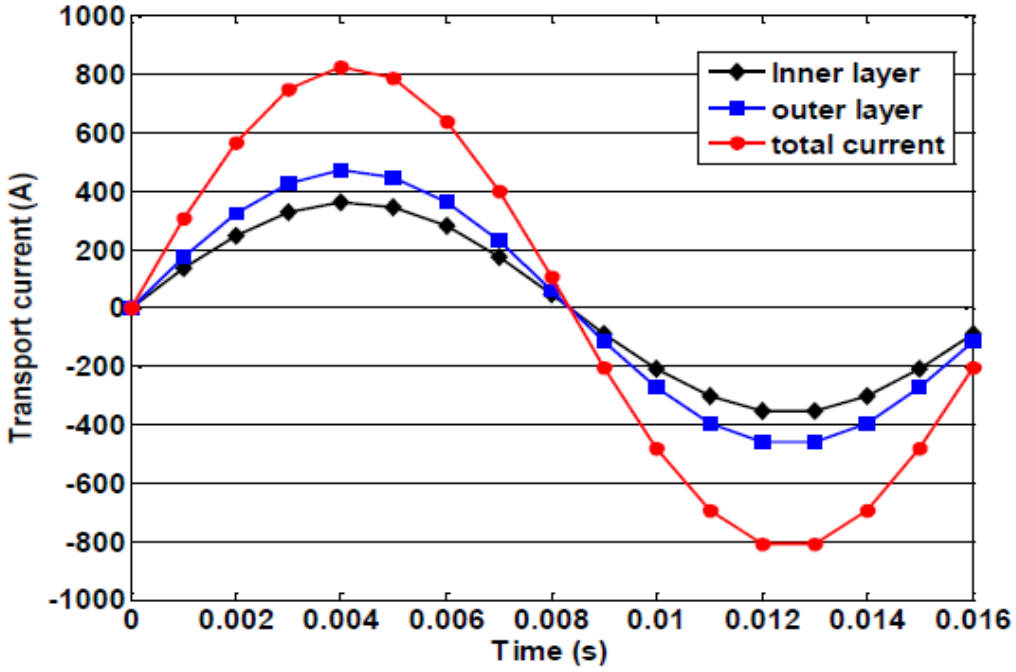

(b)

Figure 4.25: Current distribution testing results of HTS cable at 60 Hz with total transport current of (a) 600 A and (b) 800 A.

4.3 Summary of the investigation

The homogenization of current distribution has firstly discussed the influence of the contact resistances. A prototype cable consisted of two YBCO HTS layers was built and tested for the current distribution among each layer. Taking advantage of the termination contact resistances, no extra devices are needed for the current distribution measurement. The accuracy of the method has been verified by 2D modelling based on the H formulation. It is found out that the cable current injected into each HTS layer will inevitably be affected by different terminal contact resistances and hence result in non-uniform current distribution. For engineering applications, if the operating current is lower than the cable critical current, the HTS cable will always operate under the situation of uneven current distribution among HTS layers, which will affect the transmission efficiency and may damage the HTS tapes. Therefore, further work should optimize the design of the cable terminals that will make the current distribution become homogeneous.

The homogenization of current distribution has then discussed the influence of the HTS layer inductance in the cable. The self and mutual inductances of HTS cables have been investigated in terms of the radii r, pitch angles β and winding directions α. The inductance varying with cable geometry is discussed. The current distribution of an HTS triaxial cable has been homogenized by an optimal algorithm, and the result shows homogeneous current distributed among the HTS conducting layers. Another 0.2 m long, 132 kV/1.2 kA prototype two-layer HTS cable has designed based on the optimal algorithm. The current distribution of the two-layer HTS BSCCO prototype cable was measured to validate the optimal design method. A long, but equal in length, copper current leads are connected with each HTS layer in order to minimize the influence of resistance of the copper current leads on the current distribution. The measurement results show that the current is almost evenly distributed into two HTS layers. However, the contact resistances from the cable terminal still pose a significant influence on the current distribution of a short cable.

Chapter 5

AC loss investigation of HTS cable

In this chapter, a reliable experimental measurement of HTS cable AC loss is presented. The various mechanisms of HTS cable AC loss are discussed, including hysteresis losses, eddy current losses, coupling losses and ferromagnetic losses. To quantify the AC loss is essential for HTS cable design, but the lack of reliable models hinder the accurate calculation of cable AC loss. The experimental measurement based on electrical four probes method provides a reliable way to quantify the cable AC loss. However, the large inductive voltage of the HTS cable will significantly influence the true AC loss signal so that it is difficult to directly measure the AC loss; the sensitive measurement devices are easily affected by the background AC magnetic fields surrounding the HTS cable; and for multi-layer HTS cable, slight differences in contact resistances to different HTS layer can cause non-uniform current distribution, which aggravates measurement difficulty. In order to address the challenges. An inductive compensation coil is adopted to compensate the inductive component of measured voltage to the similar level of the resistive part of the measured voltage so that the resulting voltage of compensation coil and measured signal can represent the true AC loss signal; a symmetrical current return path was implemented to minimize the influence of background AC magnetic fields; and for multi-layer HTS cable, the total losses of entire cable were measured, including the terminal ohmic losses. Taking into account the skin effect, the AC loss of HTS layers was obtained by subtracting the losses contributed from the cable terminals. The experimental measurement results are compared with the calculation results based on 2D FEM modelling and the discrepancies are described in terms of the assumptions made in the coil. It suggests that 2D FEM model is not adequate to calculate the cable AC loss in terms of the helical wounding geometry.

5.1 The mechanism of HTS cable AC loss

Superconductors can carry DC transporting current with zero resistance and hence no losses occur, but a certain amount of power is dissipated for superconductors to transport DC under the external magnetic field or AC current due to AC loss. The required power will cause energy dissipation (AC losses) in the form of heat. The dissipated heat has to be removed from the cryogenic environment by a cooling source. About 15 W power is required to remove 1 W heat dissipation from the superconductor according to [81], which means a cooling penalty of 15 should be considered. The utilities will accept HTS cable as an alternative solution only if the total power consumed by the superconductor device is less than that of existing equivalent power devices. Therefore, it is important to quantify the AC loss in order to pave the way for designing high-efficiency cooling systems to enhance the competitiveness of superconducting cable.

Technical HTS tapes consist of different material apart from superconducting materials. For YBCO coated conductors from SuperPower, due to the vulnerability of the superconducting layer, a surrounding copper stabilizer (SCS) layers are used to coat the superconducting tape to make it mechanically robust. Since the links between YBCO grains are weak, the YBCO film should be deposited on a biaxially textured substrate based on the Ion Beam Assisted Deposition (IBAD) fabrication method in order to achieve high current density [82]. The main layers of the YBCO HTS tape are sketched in Figure 5.1. Depending on the applications and operating condition, all the materials can give a significant contribution to the total AC loss. The AC loss contributions are summarized into four categories as depicted in Figure 5.1 [83]:

(1) the hysteresis losses of the superconducting material caused by the pinning force preventing the magnetic flux from freely leaving or entering the superconducting material in the AC magnetic field, and hence the heat dissipation is accompanied for a completed AC cycle.

(2) Eddy current losses of the metal (typically copper, brass or stainless steel) stabilizer layer caused by the circulating current in the metal body induced by the AC magnetic field.

(3) Ferromagnetic losses caused by hysteresis cycles of the substrate layer if its material is magnetic.

(4) Coupling losses caused by the current circulating through multiple superconducting layers via a metal matrix.

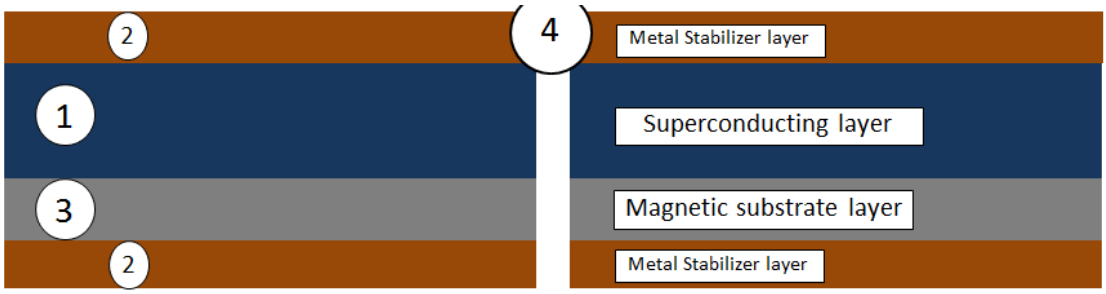

Figure 5.1: The YBCO HTS tape with several layers and the AC loss contributions.

5.1.1 The eddy current losses

The eddy current is closely related to the AC field frequency and the resistance of the metal layer [84-86]. Under a very high-frequency AC field, very little eddy current penetrates into the metal layer due to the skin effect δ, as in Eq. 5.1. Which means, although the low resistivity of the metal layer results in less eddy current joule heating, the small penetration depth will increase the effective resistance of the penetrated region. The eddy current losses in the thin-film superconductor can be estimated by Eq. 5.2 in [27, 87].

$$\delta = \sqrt{\frac{\rho}{\mu_0 \pi f}} \qquad \text{Eq. 5.1}$$

$$P_{eddy} = \frac{4\mu_0}{\pi} \frac{twf^2}{\rho} I_c^2 h(i) \qquad \text{Eq. 5.2}$$

where ρ is the resistivity of the metal layer, f is the frequency of the AC field, and t and w are the metal layer thickness and width, respectively. I_c is the critical current of the superconducting tape. $h(i)$ is the modified index of the eddy current in the superconductor tape [83]. From Eq. 5.2, it can be seen that high frequency of the AC field and low resistivity of the metal will result in big eddy current losses. Therefore, at low frequency, the resistivity of the metal layer should be increased accordingly in order to reduce the eddy current losses. In addition, it largely depends on the frequency of magnetic field. The property of eddy current losses is a square dependence of frequency ($P \propto f^2$). At a sinusoidal current wave of 60 Hz and a temperature of 77 K, even the thickness of the metal stabilizer layer is 50 times thicker than that of superconducting layer, the eddy current losses of the metal layer are only 1/70 of the hysteresis losses of the superconducting layer [88]. Hence, operating at low frequency field, the eddy current loss is not the main source contributed to the AC loss of HTS cable.

5.1.2 Ferromagnetic losses

In order to improve the weak-link inter-grain of the YBCO superconducting thin-film tape during the fabrication process, the YBCO superconducting layer can be deposited on a biaxial texture magnetic substrate layer based RABiTS fabrication method [86]. The characteristic of the irreversible magnetic cycle of the magnetic substrate will result in the ferromagnetic loss, which contributes an important part to the total AC loss in high AC field [89]. Nickel was initially used as the substrate in the RABiTS method for producing YBCO coated conductors. However, the high ferromagnetic loss of Nickel makes it unacceptable for superconducting applications in AC field. With the implementation of a nickel alloy such as Ni-W as the substrate, not only can the substrate be made mechanically robust, but the ferromagnetic loss reduction can also be improved [90]. The most commercially available nickel alloy is Ni_5W. The ferromagnetic losses can be calculated more precisely by numerical methods. But the empirical expression of the ferromagnetic losses given by Eq. 5.3 is used.

$$P_{FM} = Cf(coth(kB)^m - \frac{1}{(KB)^m}) \quad \text{Eq. 5.3}$$

If the schematic dimensions of the Ni_5W substrate are as shown in Figure 5.2, where *a* = 0.2 cm and *d* = 75 μm, then the constants in Eq. 5.3 are *m* = 1.2, *C* = 2 and *k* = 0.28 [27]. However, if the ferromagnetic materials are not used, the ferromagnetic losses can be eliminated. The YBCO tape from the SuperPower is manufactured by IBAD method, which uses a non-ferromagnetic material Hastelloy as substrate. Hence, The HTS cable can avoid the ferromagnetic losses using this kind of tape.

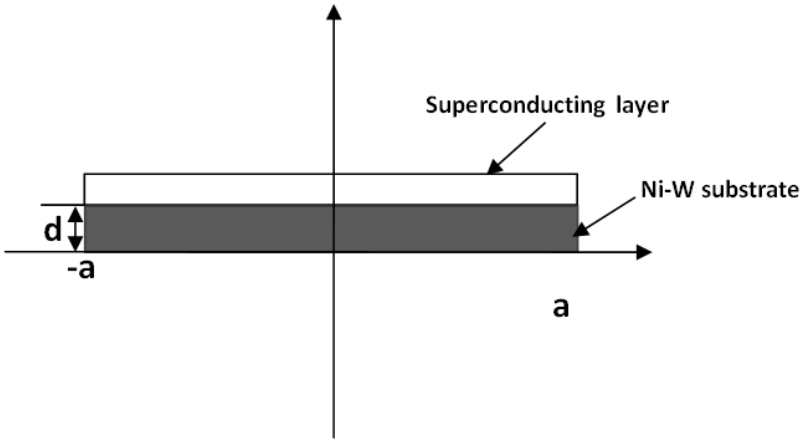

Figure 5.2: The YBCO coated conductor with Ni-W alloy substrate.

5.1.3 Coupling losses

In AC magnetic field, coupling currents are induced in a superconductor consisted of separated filaments embedded in a normal metal matrix, as shown in Figure 5.3. The coupling losses in the HTS cable has similar nature with the eddy current losses: the losses occur in a normal metal conductor when a current loop induced by AC magnetic field goes from one superconducting filament to another via the metal matrix. The induced magnetic energy is stored in the loop, which will cause joule dissipation as the coupling current loop contains a resistive path of a normal conductor. The calculation of the coupling loss in multifilament superconductor tapes is analytically complex. But the general rule of reducing coupling current losses is by either increasing the resistivity of the metal matrix or twisting the superconducting

filaments so that deposition of the filaments is transposed with a smaller coupling current loop in which less magnetic energy is stored [91]. For YBCO coated conductor based cable exposed in high magnetic field, the coupling current loop mainly induced among the HTS tape and cable copper ends, which will be largely reduced because of the high resistance of the copper ends. Hence, in the low magnetic field, coupling losses can be ignored in YBCO HTS cable.

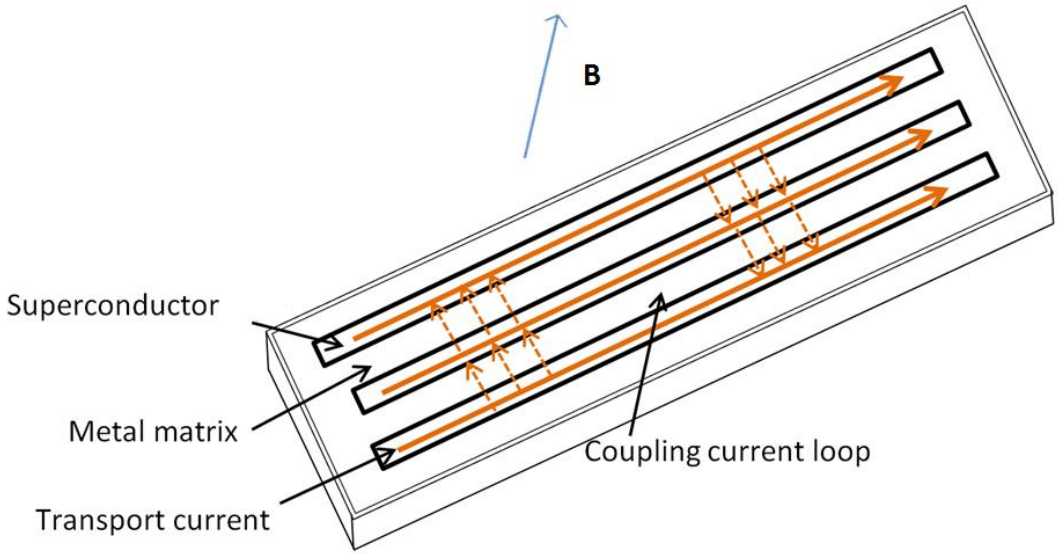

Figure 5.3: Schematic of the multi-filament superconducting tapes with coupling current loops.

5.1.4 Hysteresis losses

Unlike type I superconductor, in which the applied external magnetic flux cannot penetrate, partial flux can penetrate into YBCO superconductor in the form of vortex pinning due to the flaws in the YBCO crystal structure. The magnetic flux pinned in the volume of the superconductor cannot move freely without additional power. In this way, the flux is said to be pinned into the vortices and once the distribution of the vortices is established, additional power is required for any rearrangement due to the reaction of the pinning force [92, 93]. Additionally, the flux enters into the superconductor does not leave in the same way as it enters, hence, the heat dissipated is known as magnetisation hysteresis losses.

When a superconductor carries DC transport current, the flux distributions in both magnitude and direction are fixed and therefore the distribution of the vortices is constant. DC current can flow through the superconductor permanently without any resistance. However, when there is an AC transporting current flowing through the superconductor, the self-field plays the role of applied external magnetic field. As both the magnitude and direction of magnetic flux will vary periodically under the AC field, it is inevitable that the redistribution of vortices in the volume of the superconductor is required at all times. Similar to the magnetisation hysteresis losses, additional power is required to overcome the pinning force exerted on the vortices [94]. The HTS tapes wound in the cable are exposed in the cable field with relative low magnitude, typically 0.1 T. Hence, AC transporting current hysteresis losses are the main source contributed to HTS cable AC loss.

If only AC transporting current hysteresis losses are considered, there are analytical solutions of AC loss available for three types of simplified cable geometry in 2D. As shown in Figure 5.4, (a) is the mono-block model, of which the superconducting layer is assumed to be a hollow cylinder. There is no gap between each individual superconducting tape; a current sheet is therefore assumed for the mono-block model. Eq. 5.4 gives the formula of a mono-block prediction of AC loss [97, 98]. (b) is the Norris model, of which the cable is assumed to be composed of a number of single tapes wound straight onto the cable former. The magnetic flux redistribution due to the influence of the neighbouring tapes is completely ignored. Hence, the AC loss of the cable for the Norris model is the sum of the AC loss of each tape based on the Norris equation [99], given by Eq. 5.5. (c) is the Majoros model, of which the gaps are taken into consideration as compared to the Norris model. Eq. 5.6 gives the formula of AC loss for the Majoros model [100].

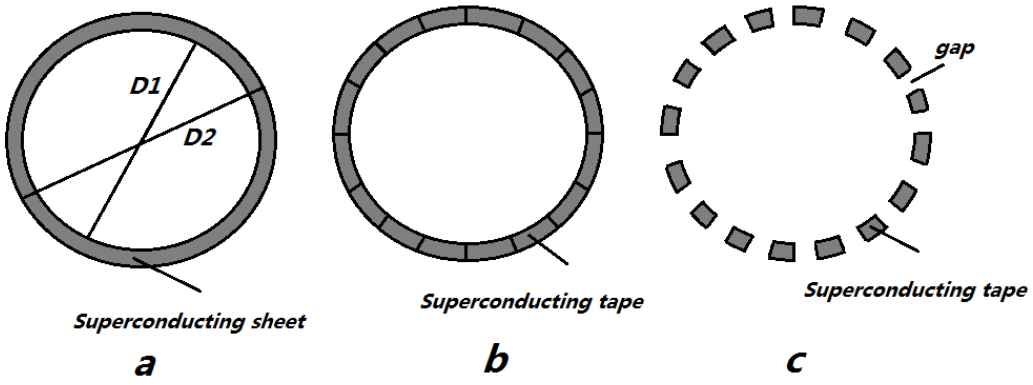

Figure 5.4: The simplified cable models: (a) the mono-block model; (b) the Norris model; (c) the Majoros model.

$$Q_m = f\frac{\mu_0 I_c^2}{2\pi h^2}((1-i_{ac}h)i_{ac}h + 2(1-i_{ac}h)ln(1-i_{ac}h)) \quad \text{Eq. 5.4}$$

$$Q_N = fN\frac{\mu_0 I_{cc}^2}{\pi}((1-i_{ac})\,ln(1-i_{ac}) + (1+i_{ac})\,ln(1+i_{ac}) - i_{ac}^2) \quad \text{Eq. 5.5}$$

$$Q_m = fN\frac{\mu_0 I_{cc}^2 g^2}{\pi w^2}(2\,ln\left|cos\left(\frac{1}{2}\pi i_{ac}\right)\right| + \frac{1}{2}\pi i_{ac}\,tan(\frac{1}{2}\pi i_{ac})) \quad \text{Eq. 5.6}$$

where the parameters are: $h = \frac{D_2^2 - D_1^2}{D_2^2}$; D_1 and D_2 are the inner and outer radii of the cable conducting layers, respectively; $i_{ac} = {}^{I_m}/_{I_c}$; I_m is the amplitude of the AC transport current; and I_c is the critical current of the whole HTS cable. $I_{cc} = {}^{I_c}/_{N}$; N is the number of superconducting tapes in all layers and hence I_{cc} refers to the average critical current of the single tape in the cable. w is the width of the single superconducting tape, g is the gap between the individual tape in the cable and f is the frequency of the transport current. Based on the analytical solution, the characteristic feature of HTS cable AC loss per cycle is independent of frequency.

5.2 AC loss measurement of HTS cable

The helical geometry of HTS cable makes computing the AC losses complicated. The HTS cable AC loss can be approximately obtained by the analytical solutions, ignoring the effect of the twisted pitch in the cable. The assumption that all the tapes in the cable carry the same current differs from the real cable situation since the twisted pitch, wind direction and contact resistance affect the current distribution of the tapes. Therefore, an analytical solution can only be used as an approximate prediction of HTS cable AC loss. In order to obtain accurate values for the HTS cable AC loss, an experimental measurement method can be implemented on prototype HTS cable.

5.2.1 Challenges of the AC loss measurement

There are many challenges involved in measuring the AC loss of HTS cable accurately. The AC loss is quite small in magnitude compared with the electronic test circuit, which can easily be affected by noise pollution from the electromagnetic background field. The AC loss voltage co-exists with more than one source of inductive voltage and the inductive voltage of the superconductor is 100–1000 times higher than the AC loss voltage, which makes it impossible to measure AC loss without removal of the inductive voltage since only the resistive voltage represents the true AC loss. The inductive voltage of the superconductor should be properly compensated, as over-compensating or under-compensating the inductive voltage will result in significantly increased measurement error, which raises a challenge for the inductive compensation technique.

The AC loss measurement of HTS cable is different from other applications, such as HTS coils. Most HTS power cable is constructed with a multi-layer structure and each layer contains a number of HTS tapes; the imbalanced current distribution issues will cause errors in AC loss measurement. However, in [101], an HTS cable has been designed in such a way that all the HTS tapes wound in the cable are connected in series so as to eliminate the imbalanced current distribution issues. But the cable configuration of the HTS cable differs significantly from the practical HTS power

cable, and the magnitude of the cable transportation current is limited by the HTS tape, which makes it impossible to measure AC losses at high current levels. In addition, the length of the HTS cable is long enough to be significantly affected by the electromagnetic background field, which will introduce considerable error into the AC loss measurement.

5.2.2 Measurement methodology

Three methods are typically used to measure the AC loss of superconducting materials: the electrical method, the magnetic method and the calorimetric method. The electrical method is used to measure the transport current and in-phase voltage of the superconducting cable to obtain the AC loss. The magnetic method is used to calculate the AC loss by obtaining the hysteresis loop of the superconducting sample by a pick-up coil. The calorimetric method is used to measure the temperature variation in the cryogen or the boil-off gas due to heat dissipation caused by AC loss. Table 5.1 gives a comparison between the electrical method, the magnetic method and the calorimetric method [102-104].

Table 5.1: The measurement technologies of AC losses.

Measurement technologies	Suitable superconducting applications	Advantages	Disadvantages
Electrical method	Short samples or cable	High accuracy and fast speed	Easily affected by background noise
Magnetic method	Small samples such as SQUID	Very high accuracy	Slow measurement speed
Calorimetric method	Large-scale coil samples or samples with complicated electromagnetic field background	Simple and low cost of measurement implementation	Low accuracy and low speed. High thermal insulation required

5.3 The AC loss based on the electrical four probe method

The magnetic method is not suitable for measuring the cable AC loss since it is difficult to fabricate a pick-up coil for complex geometry application, such as for cable. Both the calorimetric method and the electrical method can be utilized for measuring the AC loss of superconducting cable with transportation current. The advantage of the calorimetric method is the elimination of the background electromagnetic influence. But since the cable has large current carrying capacity, the high current in the cable copper terminals will cause a significant amount of liquid nitrogen to be evaporated in the boil-off chamber, several orders of magnitude more than the amount of boiled liquid nitrogen solely due to cable AC loss. An intensive calibration is required in this case. Hence, the electrical method is more suitable for measuring the AC loss of superconducting cable. In the following sections, the electrical method is used to measure the AC loss of the HTS cable based on DAQ and lock-in amplifier techniques, and the measurement between these two techniques are compared.

5.3.1 Measurement based on DAQ

The schematic of the measurement circuit diagram is shown in Figure 5.5. It consists of three sections: the power section, the measurement section and the cable section. As the high amplitude AC transporting current at various frequency ranges is required in the power section, a power amplifier provides power to the step-down transformer which can provide up to 3000 A_{rms} current within the frequency range of 30–300 Hz. The cable section contains the superconducting cable and cryostat. As the impedance of the measurement section is very low, it must be isolated from the power amplifier by the transformer to prevent damage to the HTS cable. In the measurement section, National Instruments' data acquisition (DAQ) card is used to record the current and voltage signal of the cable. The four probe method is used to pick up the voltage drop of the cable and current transducer, respectively.

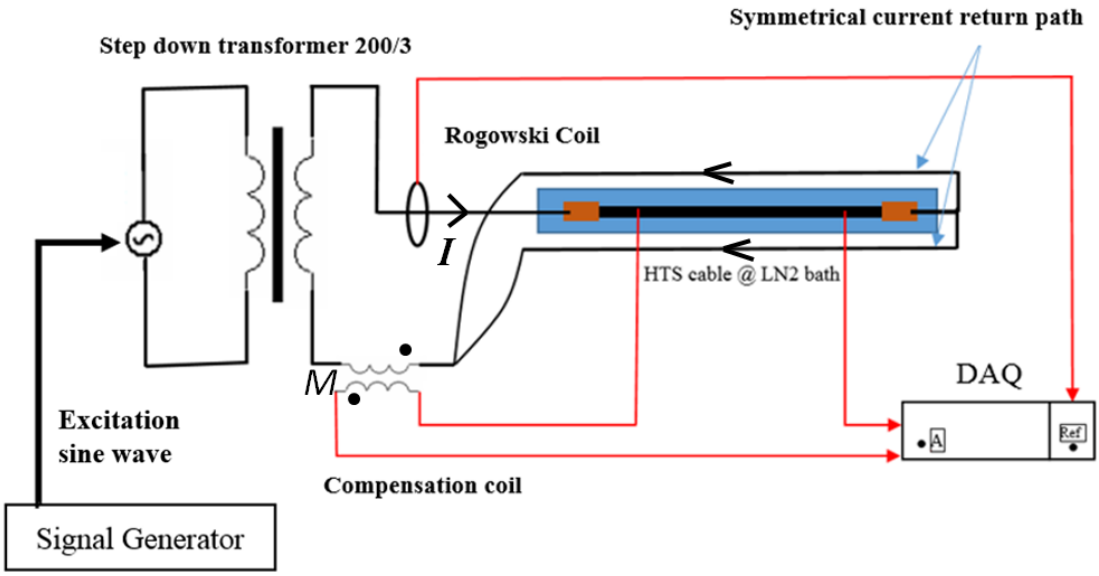

Figure 5.5: The AC losses measurement setup based on National Instruments' DAQ.

The principle of the electrical method is to measure the transport current and in-phase voltage across the superconducting cable. The term 'in-phase' refers to the purely resistive component of the HTS cable voltage. When the AC current is flowing through the HTS cable,the magnitude of induced voltage component that is phase shifted 90º to the current is 100–1000 times larger than the resistive voltage [105]. Hence, the in-phase resistive voltage signal will be buried by the inductive voltage if the inductive voltage is not removed.

For the HTS cable structure, the induced inductive voltage is considerably higher than the single tape due to the HTS tapes helically wound on the former, making it similar to the solenoid coil. Hence, a cancellation coil has been utilized to compensate the inductive voltage so that only resistive voltage is left. The measured voltage V_s of the HTS cable includes two components: a resistive voltage RI due to heat dissipation and an inductive voltage due to the large self-inductance and mutual inductance between the cable HTS conducting layers. Eq. 5.7 expresses the measured voltage of the superconducting cable:

$$V_s = RI + j\omega LI \qquad \text{Eq. 5.7}$$

Only the resistive component in Eq. 5.7 represents the AC loss voltage. The mutual inductance M between the primary coil and the secondary compensation coil can be adjusted by shifting the secondary coil. The purely inductive voltage detected from the compensation coil is expressed by Eq. 5.8:

$$V_c = j\omega MI \qquad \text{Eq. 5.8}$$

As demonstrated in Figure 5.6, the inductive component in V_s is adjusted by subtracting the voltage of the secondary coil voltage V_c from V_s. When M is equal to L, the resulting voltage V_r is purely resistive, as shown in Eq. 5.9:

$$V_r = V_s - V_c = RI + j\omega(L - M)I = RI \qquad \text{Eq. 5.9}$$

The resulting voltage is in phase with the current I flowing through the HTS cable, and the multiplication of the resulting in-phase voltage and transport current gives the AC loss, as shown in Eq. 5.10:

$$Q = \frac{V_r \cdot I}{l \cdot f}\ (J/m/cycle) \qquad \text{Eq. 5.10}$$

where l is the length of the HTS conducting layer of the cable and f is the frequency of the transport current.

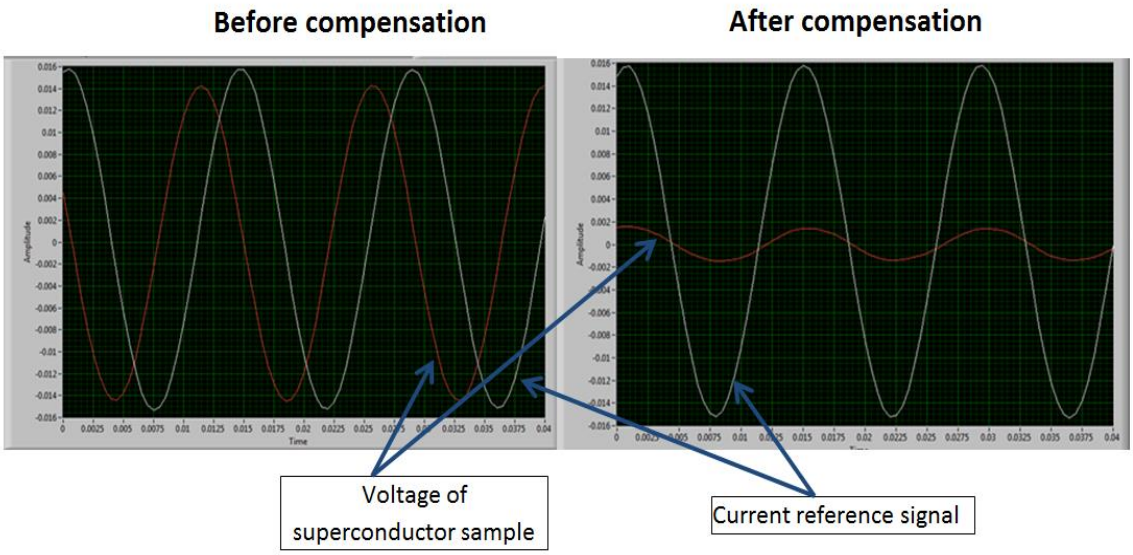

Figure 5.6: The detected voltage signal from the HTS cable with the current reference signal before and after compensation.

5.3.2 Measurement based on lock-in amplifier

The schematic of the measurement circuit diagram is shown in Figure 5.7 [106]. Apart from the measurement section, the power section and the cable section are the same as above. The NI DAQ is replaced with a lock-in amplifier. Since the lock-in amplifier has sensitivity as low as nanovolt, it is expected to be able to improve the measurement accuracy of the HTS cable AC loss signal. There are many sources of background noises, such as the thermal noise in the wire, magnetic field interface, in the experimental measurement circuit. The NI DAQ measurement device is capable of filtering out the noise with a frequency several times larger than the frequency of the AC loss signal through the internal bandpass filter. But noises with frequencies close to the frequency of the AC loss signal cannot be filtered, as they are detected together with the AC loss. However, a lock-in amplifier is implemented because it uses a technique known as phase-sensitive detection in order to single out the component of the signal at a desired reference frequency and phase. Noises at any other frequencies are rejected and do not affect the measurement. In this way, the signal-to-noise can be largely improved [107].

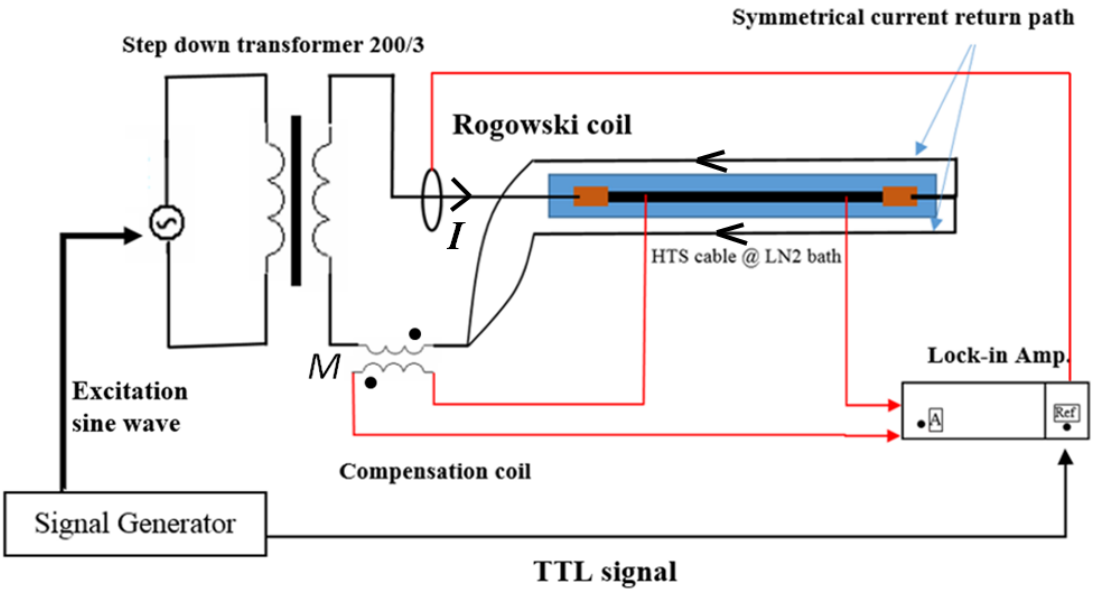

Figure 5.7: The AC loss measurement setup based on the lock-in amplifier.

A reference signal of the lock-in amplifier which is used to lock the HTS cable voltage signal is provided by the TTL signal from the excitation source, i.e., the signal generator. The clean 5 V reference square-wave TTL signal has a frequency that is exactly the same as the current in the HTS cable. The TTL square wave has a higher signal-to-noise ratio than the sine wave with the same frequency and phase, which makes it an ideal reference signal. In order to extract the HTS cable AC loss voltage which is in phase with the current, it is crucial to synchronize the phase of the reference signal with the phase of the HTS cable current signal. A Rogowski coil is used to detect the phase and magnitude of the HTS cable current signal. Compared with the shunt resistor, the Rogowski coil has several unique benefits: the shunt resistor has some inductance which shifts the current phase while the phase of the output signal from the Rogowski coil is the same as the current signal. A commercial Rogowski coil, such as the Fluke current clamp meter used in this measurement, has a small phase-sensitive error. For AC frequencies below 100 Hz, the phase error is $\pm 1^0$ [108]. The commercial Rogowski coil can also shield the background electromagnetic noise. Once the phase of the reference signal from the lock-in amplifier is synchronized with the phase of the cable current, the resistive voltage and inductive voltage of the HTS cable voltage can be extracted separately and shown in the lock-in amplifier ‘X’ and ‘Y’ displays, respectively. The value shown in the ‘X’ display is the AC loss voltage.

Although the lock-in amplifier can separate the resistive part and the inductive part of the HTS cable voltage signal, the voltage of the inductive part is nearly 1000 times that of the resistive part due to the helical configuration of HTS tapes wound in the cable. Non-ignorable errors exist unless the inductive part of the signal can be compensated to the same order of magnitude as the resistive part. Therefore, a compensation coil which is connected inversely polarized to the inductance of the superconductor is used for the measurement similar to the DAQ method. The compensation should be adjustable in order to find the best position in which to cancel or minimize the inductive part of the HTS cable voltage, and the compensation coil should ideally be placed in the same cryogen as the superconductor sample to reduce the unwanted resistance of the coil. Because of the significant improvement of the measurement accuracy by using the lock-in amplifier, there is no need to continuously adjust the compensation coil to obtain the exact AC loss signal that is in phase with the current, since the measurement errors often occur when the compensated voltage signal is slightly shifted from the current signal but it is hard to observe this subtle phase difference in Figure 5.6. It is only needed to minimize the inductive voltage to the same order of magnitude as the AC loss voltage signal, and then the lock-in amplifier is able to distinguish the AC loss voltage from the measured HTS cable voltage. The following steps summarize the AC loss measurement procedures using the lock-in amplifier. The measurement component setups for DAQ and the lock-in amplifier are shown in Figure 5.8.

1) Connect the signal generator to the power amplifier to provide an excitation sine wave source. The TTL signal from the signal generator is connected to the external reference source of the lock-in amplifier.

2) Synchronize the phase of the lock-in amplifier reference signal with the phase of the HTS cable current signal using the Rogowski coil.

3) Use the lock-in amplifier to extract the AC loss voltage signal while adjusting the compensation coil to minimize the inductance to the same level of the extracted AC loss signal to obtain a more accurate AC loss voltage.

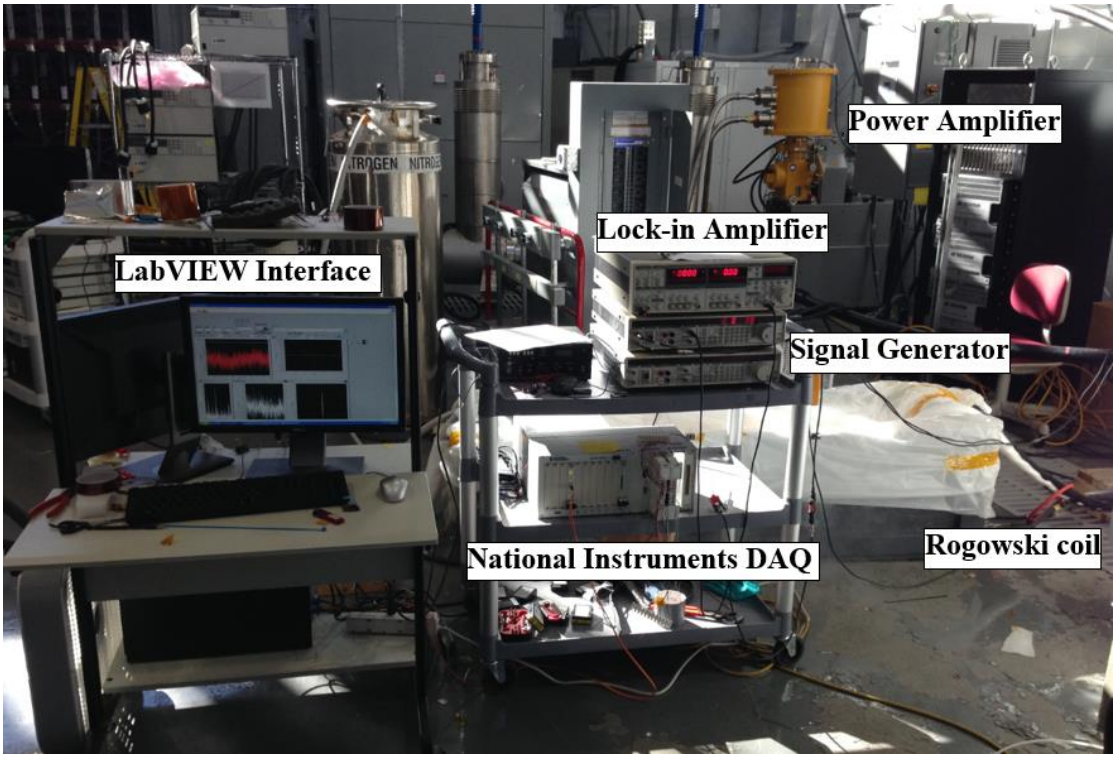

Figure 5.8: The AC loss experimental measurement setup.

5.3.3 Symmetrical current return path

The AC loss measurement of the HTS cable is easily affected by the electromagnetic background field. Unlike other HTS applications, HTS cable has very long length and high AC current. The high AC current in the copper cable can induce a considerable electromagnetic field around the HTS cable, which significantly impacts on the AC loss measurement. The impact of the electromagnetic field generated from the step-down transfer is also considerable due to the high winding inductance. One should endeavour to minimize these surrounding electromagnetic field influences. Two copper cables placed on each side of the HTS cable carry the current returning to the AC power source. The two current return cables are separated by a distance of 40 cm and located with the same distance to the HTS cable so that a symmetrical current return path is utilized in the measurement, as shown in the circuit diagrams in Figure 5.5 and Figure 5.7. The distribution of electromagnetic field from the copper cables is

plotted in Figure 5.9. The copper cable I and copper II carry the same amount of current and the direction of the current is the same, hence, the electromagnetic field is almost zero in the middle region. The relevant experimental setup is shown in Figure 5.10. At the end of the HTS cable, two separated copper cables are symmetrically placed on each side of the HTS cable in order to eliminate the electromagnetic field inside the loop, where the HTS cable is placed in the loop. As seen from Figure 5.9, ideally, if the HTS cable is located in the centre between the two copper cables, then the HTS cable is not affected by the magnetic field from the copper cables. But this causes some difficulties during the practical setup. Nevertheless, in the experiment, much effort has been made to reduce the vertical distance between the HTS cable and copper cables as small as possible so that the influence of the surrounding electromagnetic interface is minimized. Additionally, in order to minimise the influence of the electromagnetic field from the transformer on the compensation coil, as shown in Figure 5.10, the compensation coil is placed in a maximum distance to the transformer (not shown).

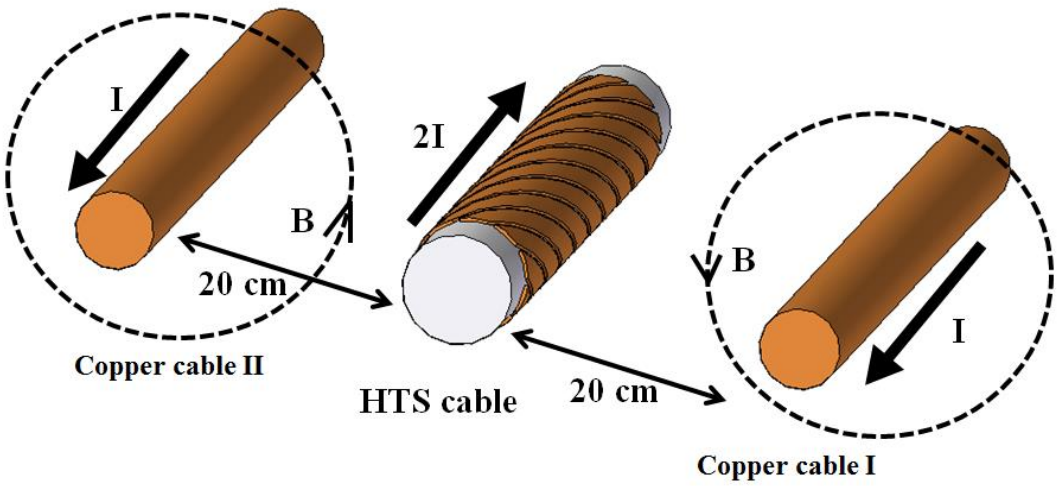

Figure 5.9: The position of the two current return cables with respect to the HTS cable.

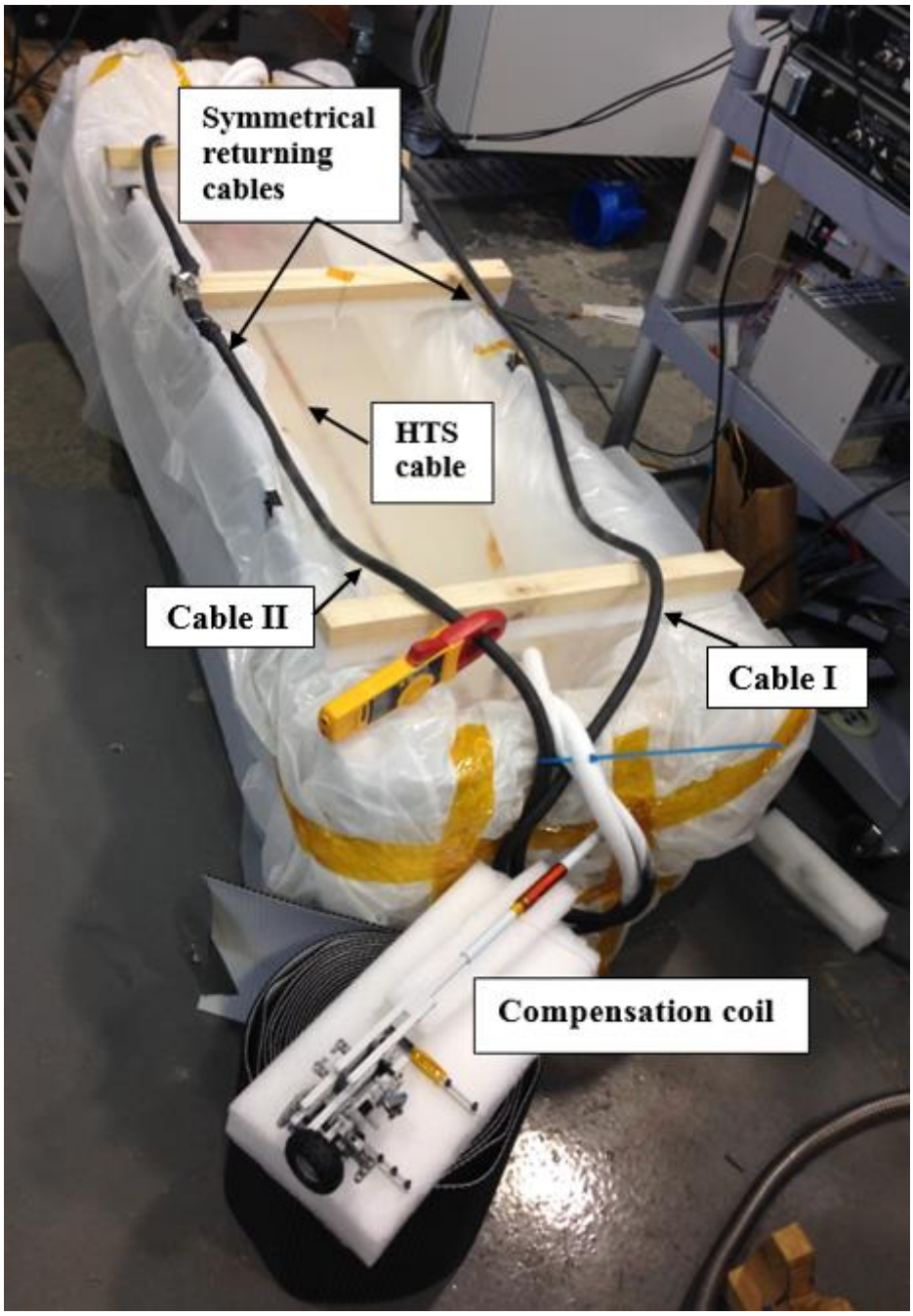

Figure 5.10: The AC loss experimental measurement setup with symmetrical current return path.

5.4 AC loss measurement results

5.4.1 Superconducting cable consisted of single HTS layer

Utilizing the measurement techniques described above, AC loss measurement is implemented on the prototype HTS cable presented in Chapter 4. The specifications of the HTS cable can be found in Table 4.1. The AC loss measurement was first carried out with only an inner HTS layer wound on the cable. The measurement results are shown in Figure 5.11. Two measurement methods are implemented and compared. Based on the lock-in amplifier technique, as shown in Figure 5.11 (lines with markers), the AC loss of the HTS cable was measured with three frequencies of AC transport current: 50 Hz, 100 Hz and 150 Hz. The reason to choose these frequencies is because the test was performed in the USA, where the power frequency is 60 Hz. None of the test frequencies are the power frequency and its harmonic frequencies, since all the measurement devices are charged with 60 Hz current from the mains, the induced electromagnetic field will pollute the AC loss voltage with the same frequency, which is not possible to be filtered out. In order to verify that only the AC loss was measured, the measurement was performed at various frequencies so that it can be checked that the losses per cycle are independent of the measuring frequency. Based on the DAQ technique, as shown in Figure 5.11 (plain lines), the AC loss of the HTS cable was measured with the same frequencies as the lock-in amplifier technique, but the compensated AC loss voltage signal at 50 Hz low currents (50–100 A) was unstable and it was not possible to obtain a reliable AC loss. Hence, the AC loss at 50 Hz is discarded. From the results at current less than 200 A, the AC loss is twice as high as the results of the lock-in amplifier technique. Once the AC transport current is larger than 200 A, the DAQ measurement results are consistent with the lock-in amplifier measurement results. This is because the AC loss is approximately the cubic of transport current. At low currents (about $0.1I_c$), AC loss is very small compared with AC loss at high currents. This results in inaccurate measurements due to the inadequate sensitivity of DAQ for small signals. Compared with both measurement techniques, it can be concluded that they are both suitable for HTS cable AC loss measurement at high currents. But it would be an advantage to using a lock-in amplifier to measure AC loss at low currents.

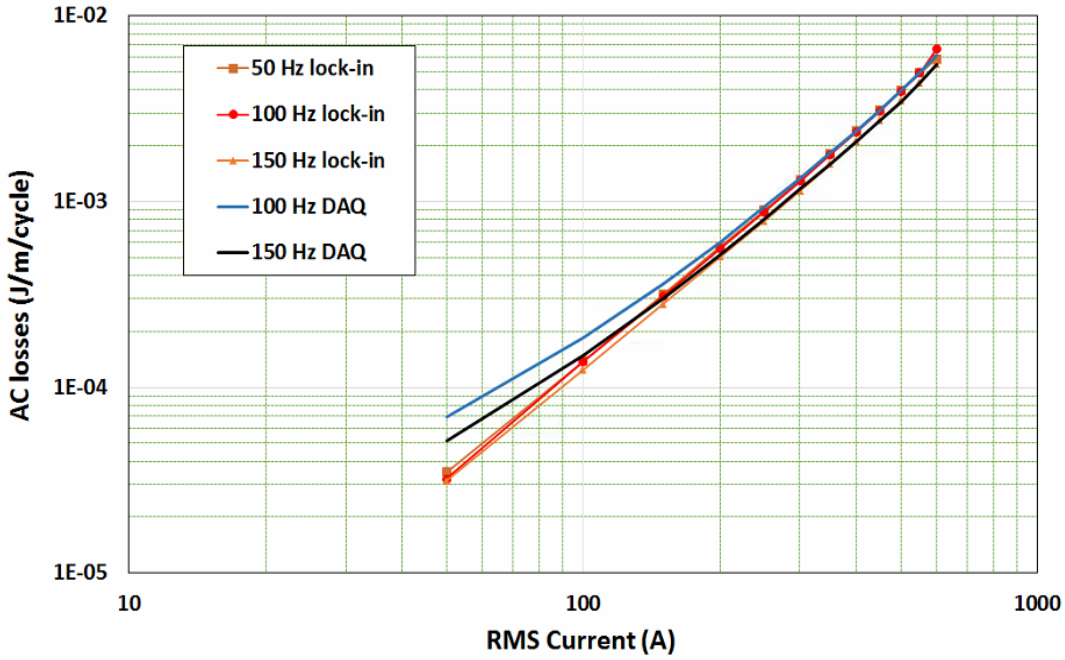

Figure 5.11 Comparison of measurement results between the DAQ and the lock-in amplifier methods.

The AC loss of the HTS cable was calculated based on the analytical method and FEM numerical method, respectively. The mono-block can give an estimation of the HTS cable AC loss calculation results, the mono-block equation can be found in Eq. 5.4. As shown in Figure 5.14 (dotted line), it can be seen that the measurement results are about an order of magnitude higher than the calculated results. The reason for the discrepancy is that the mono-block assumes a hollow cylinder as the geometry of the HTS cable, completely ignoring the gaps among the HTS tapes, and resulting in an ideal circular magnetic field along the cable circumference. Without the perpendicular field, the AC loss of the HTS tapes in the cable is reduced due to the anisotropic influence of the tape. Additionally, during the fabrication of the HTS cable, HTS tapes are helically wound with tension applied. This possibly results in critical current degradation and an increase in AC loss. Therefore, the measurement results are expected to be generally higher than the mono-block calculation results.

Then, the HTS cable was modelled based on a numerical method to estimate the AC loss using Comsol. The FEM model is based on the H formulation, as discussed in section 3.1.2, the current density distribution inside the HTS tape and the magnetic

field distribution in the HTS cable are calculated using the governing equation, as expressed in Eq. 5.11. The resistivity of the superconductor can be expressed by Eq. 5.12, and then the AC loss per cycle can be calculated as in Eq. 5.13.

$$\nabla \times (\rho(J) \cdot \nabla \times H) = -\mu_0 \frac{\partial H}{\partial t} \quad \text{Eq. 5.11}$$

$$\rho(J) = \frac{E_c}{J_{cx}} (\frac{J_z}{J_{cx}})^{n-1} \quad \text{Eq. 5.12}$$

$$Q_{loss} = \int_0^{1/f} \int_S E_z \cdot J_z dS dt \quad \text{Eq. 5.13}$$

where $E_c = 1\mu V/cm$ and $n = 30$. Since all YBCO tapes have a non-superconducting zone at the edges, considering the critical current reduction close to the edge of superconductor, the inhomogeneous critical current density distribution along the width of a superconductor is taken into account [109]. The illustration figure is shown Figure 5.12.

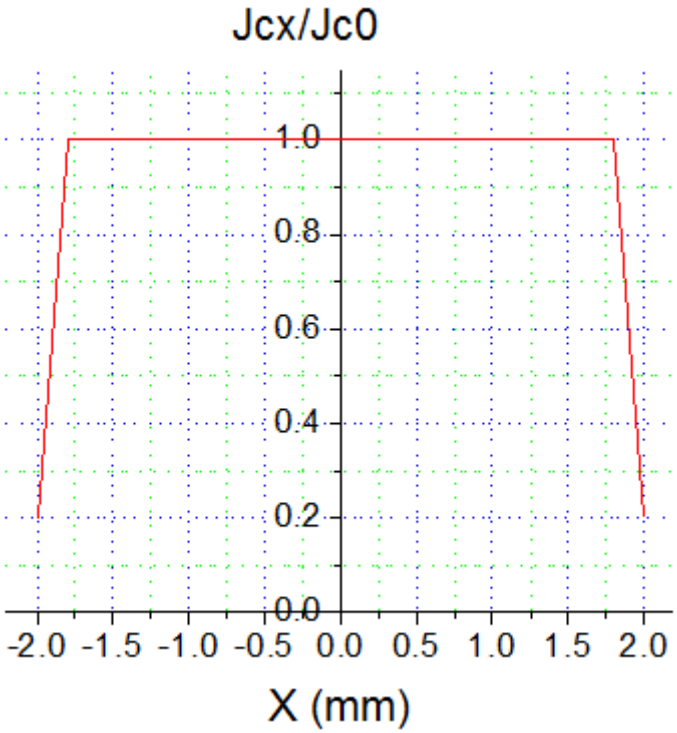

Figure 5.12: Critical current density distribution along the width of HTS tape.

$J_{c0} = 3.125 \times 10^{10}\ A/m^2$ is the average critical current of HTS tape wound in the cable, which is obtained based on a thickness for the HTS tape of 1 μm and a critical current of 125 A. The integration of the critical current density across the area of HTS tape equals to the critical current of HTS tape, as expressed in Eq. 5.14.

$$\int_{T_{sc}} \int_{W_{sc}} J_{cx} dxdy = I_c \qquad \text{Eq. 5.14}$$

where J_{cx} is the critical current density and W_{sc} means the width of superconductor, T_{sc} is the thickness of superconductor and $I_c = 125\ A$ is the critical current of HTS tape wound in the cable. The HTS cable consisted of single layer is modelled in 2D FEM model using Comsol. In the modelling, the number of mesh elements inside the HTS tape is inversely proportional to the thickness of the tape and the square mesh is used in order to maintain the similar aspect ratio for each mesh element [96]. The square mesh implemented in the HTS subdomain is shown in Figure 5.13.

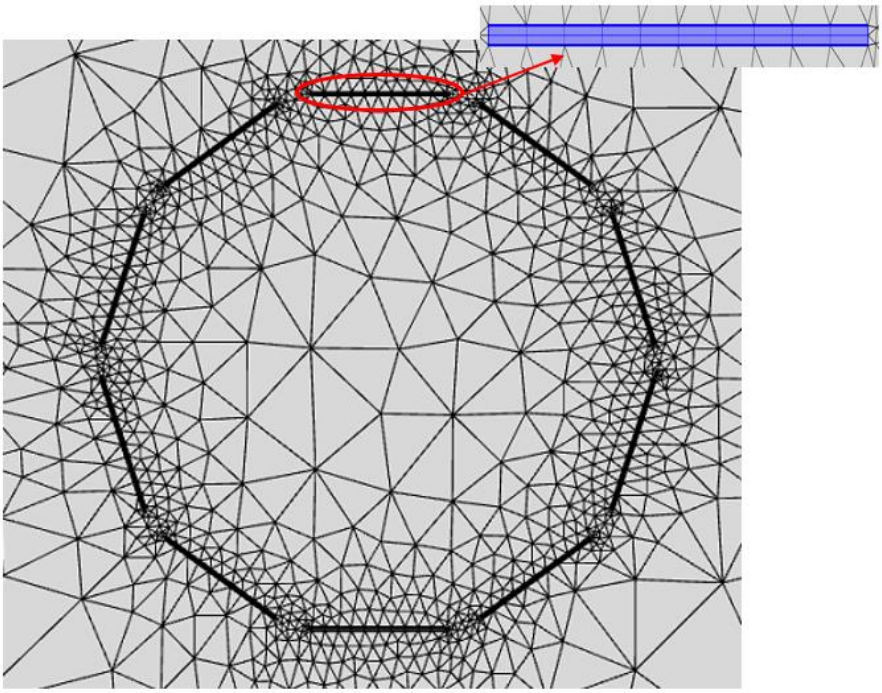

Figure 5.13: The square mesh elements in the HTS tape subdomains.

The 2D FEM AC loss calculation results are shown in Figure 5.14 (black line with square markers), in comparison with the AC loss measurement based on the lock-in amplifier. It can be seen that the FEM measurement results generally agree with the measurement results at high currents. However, the discrepancy exists at low currents ($0.1I_c$ to $0.2I_c$) and the reasons are outlined: there are some difficulties in directly implementing the FEM approach to model the real HTS cable geometry. For mechanical reasons, the HTS tapes in each layer are helically wound around the cable former with a pitch length of every regular interval. Hence, the modelling of HTS cable involves 3D geometry, so the necessary computing memory and time increase enormously compared with 2D geometry. Additionally, the contact resistances from two cable terminals will cause uneven current distribution among the HTS tapes. The inhomogeneous properties along the length of HTS tape are also not possible to be taken into account in the model. Hence, the model represents the simplest scenario, which is quite different from the HTS cable in practice.

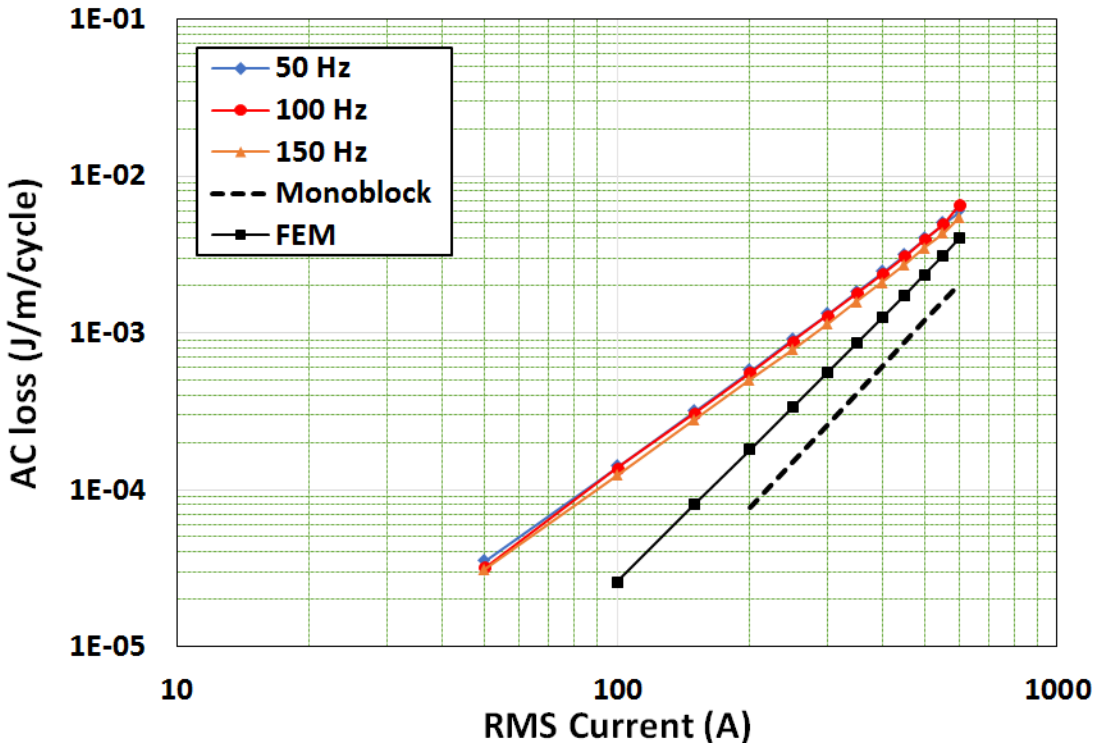

Figure 5.14: Lock-in AC loss experimental measurement results at 50 Hz, 100 Hz and 150 Hz, compared with the FEM and mono-block model calculation results.

5.4.2 Superconducting cable consisted of two HTS layers

The AC loss was measured with the cable consisted of two HTS layers based on lock-in amplifier technique. The specifications of the double HTS layer cable can be found in Table 4.2. The measurement of AC loss for the double HTS layers cable is non-trivial work since the AC current distribution is not easy to obtain accurately, which makes it invalid to use voltage taps attached to each HTS layer in order to obtain the AC loss voltages. The uniform distribution of current in each HTS layer is yet to be confirmed since the cable layer inductances combined with the terminal contact resistances affect the current distribution. In order to rule out the issue of the current distribution during the measurement, the voltage taps are placed at the cable terminals. In this case, only the total cable current is considered so that the current redistribution effects as a function of terminal resistance and layer inductance is eliminated. The product of in-phase voltage and current $IV_{in-phase}$ gives the total ohmic losses, which contains the resistive losses from the cable terminals $I^2 r_{copper}$. This part of the losses must be removed in order to obtain the actual AC loss Q_{hyts}, as shown in Eq. 5.15.

$$Q_{hyts} = Q_{tot} - Q_{copper} = IV_{in-phase} - I^2 r_{copper} \quad \text{Eq. 5.15}$$

If the value of r_{copper} is directly taken from the DC contact resistances listed in Table 4.2, then the measurement results are shown in Figure 5.15 (a). The measured AC loss slightly depends on the AC frequency and the higher frequency gives the lower AC loss results. This result is against the properties of eddy current losses and the hysteresis losses, hence it is not the true AC loss. However, considering the skin effect, the value of r_{copper} is actually frequency dependent. The DC contact resistance cannot be used for correction of the AC loss measurement in Eq. 5.15. The value of r_{copper} has to be modified based on the AC current penetration depth in Eq. 5.1. Figure 5.15 (b) shows the AC loss measurement results with corrected r^*_{copper} values due to skin effect. Then the AC loss is frequency independent, which shows the true AC loss, i.e., hysteresis losses, was actually measured.

In order to draw comparisons with the AC loss of one layer, the current is normalized to the relevant cable critical currents, which can be found in Table 4.2. The current of

the HTS cable with one layer is normalized to the critical current of 1260 A and the current of the HTS cable with double layers is normalized to the critical current of 2450 A. At the same percentage of HTS cable critical current, the AC loss of the double HTS layer is 10 times higher than the single HTS layer. For the HTS cable with one single layer, the magnetic field that is perpendicular to the tape wide face can be partially compensated with a sufficiently narrow gap. However, the outer HTS layer will produce a perpendicular magnetic field which can be superimposed into the gaps of the inner HTS layer. Therefore, the AC loss was increased in the inner HTS layer. On the other hand, the HTS tapes in the second layer experienced an additionally magnetic field generated by the current flowing through the inner HTS layer, which increases the AC loss of the outer layer. The average gaps in the outer HTS layer are inevitably larger than the inner layer due to the increased diameter when it is not possible to add one more tape to reduce the gap. In this case, even with the same number of tapes as the inner HTS layer, the AC loss of the outer HTS layer could be higher than the inner layer. Overall, it is expected that the AC loss of the double HTS layer cable will be higher than for the cable with one single layer [110].

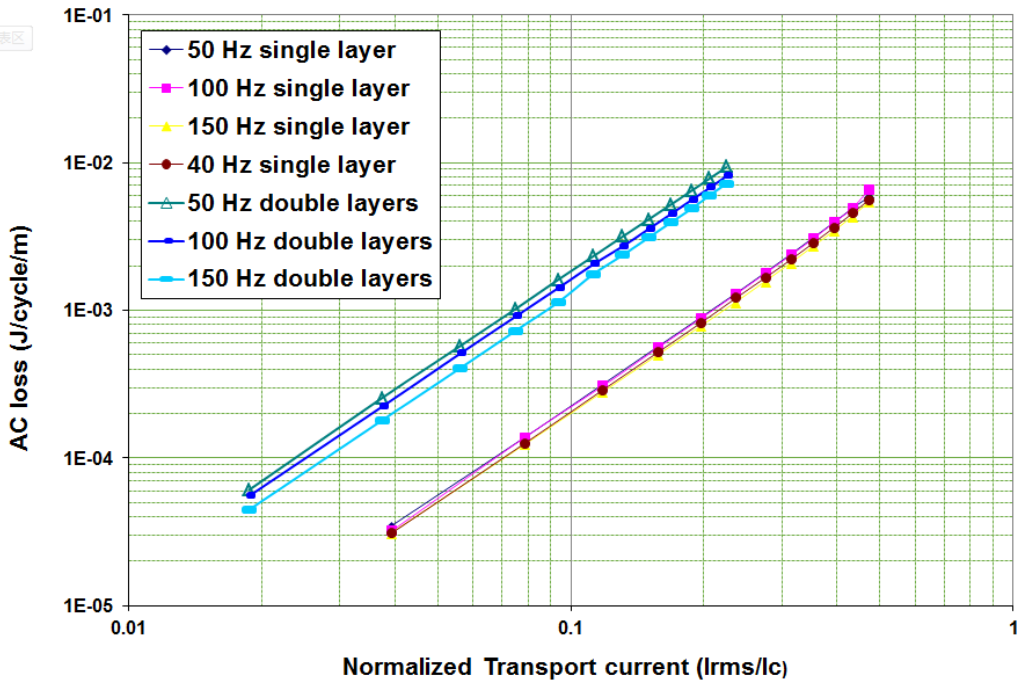

(a)

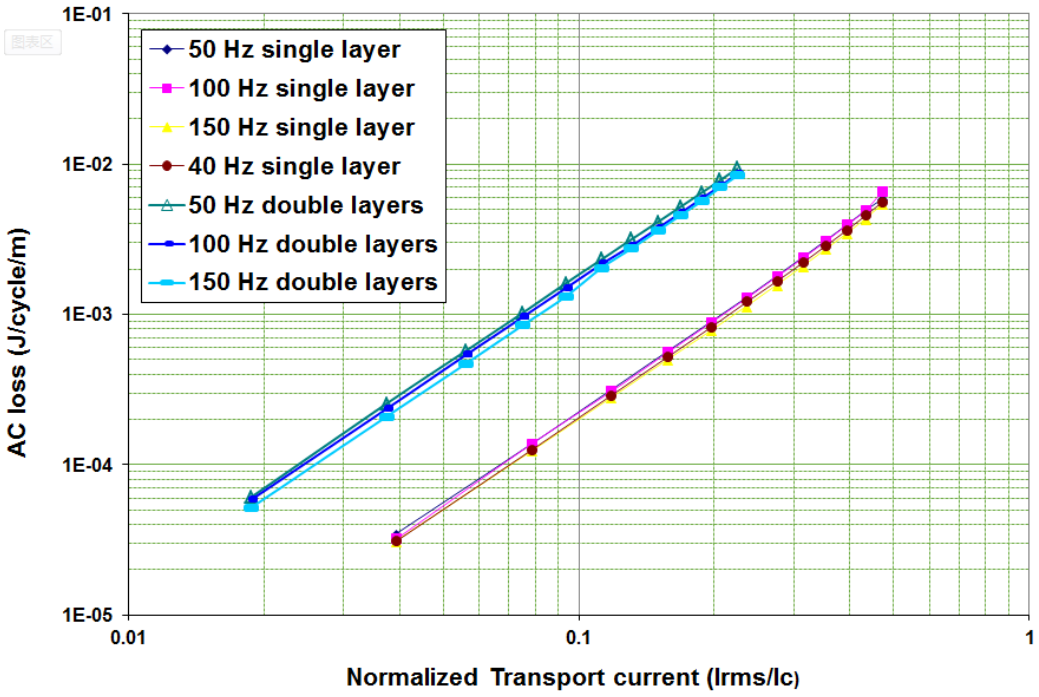

(b)

Figure 5.15: The AC loss measurement of cable with double HTS layers: (a) removed DC joint resistive losses, (b) removed AC joint resistive losses.

5.4.3 Possible sources for measurement errors

Great care has been taken in order to eliminate the AC loss measurement errors; for example, the step-down power transformer and the power amplifier are located at a considerable distance from the HTS cable due to the inside winding inductance producing a large electromagnetic field. The compensation coil was placed at opposite sides of the location of the power amplifier and the transformer, as shown in Figure 5.10. However, there are small sources that contribute to the measured AC losses, such as eddy current losses, which are proportional to the squared frequency. It is difficult to distinguish the eddy current loss voltage from the AC loss voltage since they are at the same frequency. The symmetrical current return path containing two copper cables is another source of measurement error. Ideally, the magnetic field enclosed in the loop can be compensated by the symmetrical current return cables, which requires the same current flowing through each cable. During the AC loss measurement, the current of each return cable was measured and the measurement results are shown in Figure 5.16. It can be seen that Cable I (the cable on the right side

in Figure 5.10) has more current than Cable II (the cable on the left side in Figure 5.10). The current ratio of Cable I/Cable II is 0.55, which results in a small electromagnetic field in the enclosed loop that could increase the AC loss of the HTS cable. Slightly different copper cable diameters and joint resistance can lead to this problem. Hence, one should consider placing copper cables that are as similar as possible in the LN_2 in order to reduce the copper resistance effect.

The AC loss measurement results of the cable with double HTS layers vary slightly with frequency; however, it is expected that the AC loss is independent of the frequency. The measurement error may be due to the cable terminal resistive losses included in the AC loss measurement of the cable with double HTS layers, and losses from the cable terminals are much higher than the AC losses. Since the current distribution among the two HTS layers is not uniform and it is difficult to know the exact AC current of each layer, the AC loss measurement accuracy could be improved by artificially forcing the current evenly distributed into each HTS layer. One way that this can be done is to deliberately connect each HTS layer with two large resistors, respectively. The resistance of the two resistors should be large enough that the difference of contact resistance can be ignored; the current distribution will then be dominated by the newly added big resistors, which can be controlled.

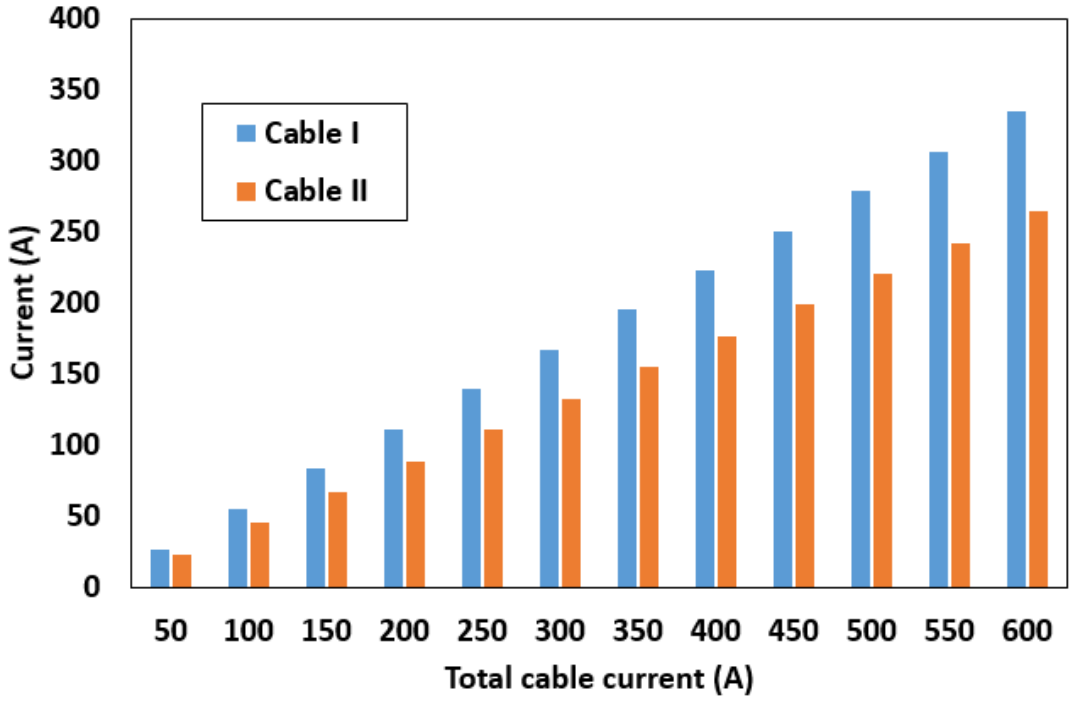

Figure 5.16: The current sharing of the two symmetrical return cables.

5.5 Further measurement improvements

There is always a small amount of current flowing through the compensation coil, no matter how big the input resistance of the voltage meter. It is inevitable to include losses caused by the current in the compensation coil together with the AC loss voltage signal. Therefore, the entire compensation coils may need to be placed in LN_2 to reduce the resistivity of the coil. Additionally, a thin (typically 34 AWG) and flexible cryogenic wire should be used to reduce the magnitude of the current in the compensation coil. In this way, difficulties may occur when adjusting the compensation coil in the LN_2 environment. Hence, the number of turns of the compensation coil should be carefully designed such that the induced inductive voltage from the compensation coil is in the same order of magnitude as the inductive voltage of the HTS cable.

It is widely accepted that the AC loss of HTS cable should be less than $0.33\ W/kA \cdot m$ in order to be competitive with conventional copper transmission cable [111]. The measurement results for the AC loss of the cable with the single HTS layer from Figure 5.11 give $Q = 0.005\ J/m/cycle$ at 600 A, which gives $P = 0.42\ W/kA \cdot m$, and the measurement results for the AC loss of the cable with two HTS layers from Figure 5.15 give $Q = 0.009\ J/m/cycle$ at 600 A, which gives $P = 0.75\ W/kA \cdot m$. Hence, the target of $0.33\ W/kA \cdot m$ could not be attained. This may be caused by the imbalanced current distribution among individual HTS tapes, or some of the HTS tapes may be saturated even if the transport current is well below the critical current of the cable. Since, in general, the AC transporting current losses of the HTS superconducting tapes are strongly dependent on the current, i.e., $P \sim I^3$, the AC loss increases exponentially when the current is close to the critical current [112]. Inhomogeneous current distribution between the HTS layers of the cable causes part of the HTS tapes to carry current close to the critical current, while the rest of the HTS tapes carry little current, which results not only in increased AC losses, but also in poor power transmission efficiency. Ideally, each individual tape should carry the same amount of transport current, which can be achieved by increasing the contact resistance. But this is not practical since it will cause large additional ohmic dissipation in the resistances themselves. However, assuming that all the individual

tapes carry the same amount of current in each layer, respectively, then the imbalanced current distribution can be assumed to occur only among the HTS layers. It is practical to achieve balanced current distribution among the HTS layers, since the impedances of the HTS layers can be adjusted by layer radius, pitch angle and winding direction. But the length of the cable should be long enough so that the inductive impedance can well exceed the contact resistance to balance the current flow among the HTS layers. This has been discussed in section 4.2 with a detailed solution.

Chapter 6

Development of a YBCO HTS power cable model in PSCAD/EMTDC for power system analysis

In this chapter, the impact of integrating HTS cable into the power grids is analysed in detail. A novel superconducting component is developed in PSCAD/EMTDC (Power System Computer Aided Design/ Electromagnetic Transients including DC) to consider the detailed configuration of coated YBCO conductors. The resistivity of YBCO HTS tape is dependent on both the current density and the temperature. Hence, the YBCO HTS cable is developed in PSCAD/EMTDC based on the superconducting E-J power law coupled with the heat transfer from the superconducting layer to a cryogenic envelope, in order to represent the real HTS cable operating in the power system. The model can simulate the transient response of thermal and electrical behaviours among the cable former, the superconducting conducting layer, the shielding layer and the cable cryostat when a fault current occurs in the HTS cable. The simulation results of the HTS cable turn out to be very effective for understanding the maximum allowed fault current duration, so as to prevent the HTS cable from permanent damage. The impact of the superconducting cable on the meshed power grid is analysed considering its characteristics of very low impedance using PSCAD/EMTDC. The analysis compares the power flow, grid losses and voltage profile of the power grid between the HTS cable and conventional XLPE cable. It is found that although the performance of the superconducting cable is superior to the XLPE cable in terms of easing the power transmission congestion, reducing the total grid losses and improving voltage profile, the fault current level is at least three times higher than for the conventional cable, which may require current limiting devices as a protection method.

6.1 Overview of the investigation

6.1.1 The features of a modern power grid

With the rapid growth in electricity consumption over the last decade worldwide, the complexity of modern power grids has been unprecedented. The interconnection between the regional grids for improving the economy and reliability of power transmission has made the synchronization among the grid very important. The penetration of intermittent renewable energy in the power grid, for the reduction of greenhouse gases, has posed significant challenges to the effective operation of grids. The co-existence of HVAC and HVDC power transmission for large capacity and long distance transmission has increased the difficulties of power flow stability.

However, the challenge of reducing transmission line losses for efficiency improvement has been a difficulty from the early stages of the grid. Thanks to progress in technology and equipment, for example, the total grid losses in China have been reduced from 9.67% in 1978 to 6.39% in 2011. Although a significant reduction in transmission line losses has been achieved, the difficulties still exist, hindering the reduction in losses much further down. Nevertheless, if the total power line losses can be reduced to less than 1%, then over 13 million tons of coal would be saved each year [113]. HTS cable, with its negligible losses compared with conventional cables, proves to be a promising solution in addressing this challenge.

6.1.2 The challenge of integrating HTS cable into the power grid

Although the capabilities of high power transmission capacity and low transmission losses of superconducting cable make it attractive for utilities to insert into the existing power grid, the effect of very low impedance of the HTS cable will need to be carefully analysed when the HTS cable is placed in parallel with conventional cables in a large-scale meshed grids. Correctly anticipating the influence of the superconducting cable on the power grid will improve the transmission capabilities in terms of efficiency and capacity.

The controllability of the power flow in the current power grids is limited and the high power is naturally distributed into the low impedance path. Therefore, considering the very low impedance of the HTS cable compared with conventional cable, the sudden integration of the HTS cable into the power grid will cause turbulence and power flow re-routing in the meshed grid. In [114], the installation of one new HTS cable is able to increase the transmission capacity of the meshed power grid, but the significant influence on the power flow not only changes the amount of power in each branch but also reverses the power flow direction in one of the transmission lines. In the case of a fault in the transmission line, the fault current capacity of the superconducting cable is always higher than the conventional cable [115], which requires a proper protection strategy, such as the deployment of superconducting protection devices, such as superconducting fault current limiter (SFCL).

Unlike conventional transmission cable, superconducting cable requires cooling power to be constantly provided at all times during operation. The total energy saving of superconducting cable should be the combination of reduction of resistive losses and consumption of cooling power required. Although the total losses including the cooling power are only one-third of the total losses of the conventional cable [116], it should be subject to the power transmission load. Electricity consumption varies from time to time and hence so does the load on the transmission line. Due to the cost of maintenance of the superconducting cable, the economy is compromised during light loading compared to the conventional cable. Therefore, the location of the HTS cable in the power grid becomes crucial.

6.1.3 The implementation of the superconductor in PSCAD/EMTDC

PSCAD/EMTDC is one of the most powerful simulation tools in the power system. PSCAD (Power System Computer Aided Design) is the graphical user interface while EMTDC (Electromagnetic Transients including DC) is a program estimating electromagnetic transients. The graphics-based models can be compiled into the Fortran language, computed in the EMTDC and the results can then be transferred back to PSCAD to display. The highly developed PSCAD/EMTDC provides a large

number of power system components which make the power system simulation very convenient. Unlike the conventional power components, whose resistivity is maintained constant during the fault condition, the characteristic of superconducting resistance is a function of current density and temperature, and a circular dependency arises because the current density calculation contains the resistivity, leading to a resistivity that is dependent on itself. Hence, it is essential to simulate the behaviour of the superconducting cable in the power system before using it in power grids. However, there is no existing superconducting component that can be directly used in PSCAD/EMTDC. Hence, the development of a superconducting component in PSCAD/EMTDC is necessary. In [117-119], a superconducting cable model is developed based on the experimental results of superconducting characteristics. In [120], a superconducting cable model is developed by modifying an existing underground cable component in PSCAD/EMTDC.

However, the detailed structure of the coated YBCO HTS tape configuration, which is composed of a thin superconducting layer deposited on a substrate layer with surrounding copper or stainless steel coating, is not taken into consideration in previous work. In the following sections, the superconducting component will be developed in such a way that the resistivity of the HTS tape is a piecewise function of the temperature for each layer of HTS tape, considering the coated structure of the YBCO tape in PSCAD/EMTDC. A three phase triad power transmission cable is constructed using the developed superconducting component in PSCAD/EMTDC. A fault current is applied to the cable in order to determine the effect of fault current duration on the thermal stability of the cable. The impact of the superconducting cable on the meshed power grid is analysed using the HTS cable developed in PSCAD/EMTDC. The analyses compare the power flow, grid losses and voltage profile of the power grid between the superconducting cable and conventional XLPE cable.

6.2 The transient characteristic simulation of superconducting power cable using PSCAD/EMTDC

6.2.1 The mathematical representation of YBCO HTS tape

The typical configuration of YBCO HTS tape, which is used to fabricate a superconducting cable, is shown in Figure 6.1. It shows that the YBCO superconducting thin film is deposited onto buffered substrates covered by silver film and protected by copper stabilizer layers on both sides. The superconducting cable is composed of a number of YBCO tapes helically wound around the cylinder copper former, which usually forms a multi-layer structure in order to achieve high current carrying capacity. The resistivity of the HTS tape ρ_{HTS} is negligible during the normal operating conditions, hence $\rho_{HTS} = 0$ is applied. However, since the resistivity of HTS is closely affected by the external applied current density and temperature, and the thermal capacity of the YBCO HTS tape is very low compared with conventional conductors, the situation becomes complicated for the transient state when a fault current occurs. Hence, the coupling of HTS resistivity with applied current and temperature becomes necessary in PSCAD/EMTDC HTS cable model development.

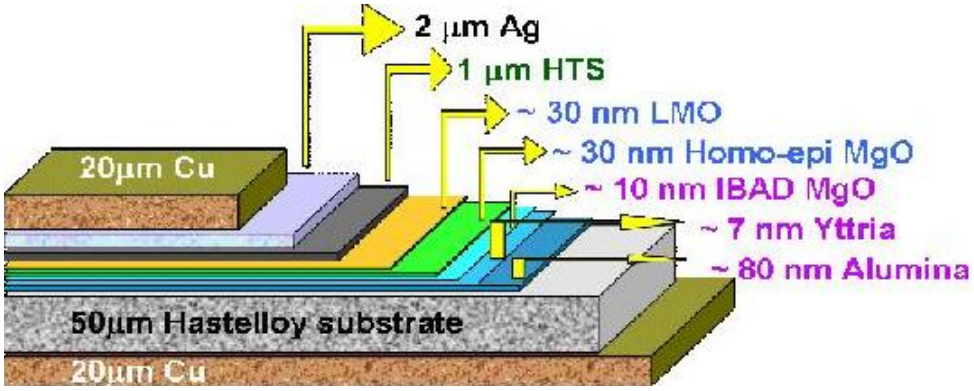

Figure 6.1: The configuration of 2G YBCO HTS tape.

The critical temperature and critical current are two important variables that directly determine the resistivity of HTS tape. Mathematically, the temperature dependence of the critical current density of YBCO tapes is proposed by [121] and described using the Eq. 6.1.

$$J_c(T) = \begin{cases} J_c(T_{ref})\left(T_{ref}\dfrac{(T_c - T)^{\alpha}}{(T_c - T_{ref})^{\alpha}}\right) & \text{when } T_{ref} < T < T_c \\ 0 & \text{when } T > T_c \end{cases} \quad \text{Eq. 6.1}$$

where α is 1.5 which is applicable to YBCO and Bi-2223 superconducting material. T_{ref} is the reference temperature, and an operating temperature of 70 K for the HTS cable is used as a reference temperature [34, 122]. $J_c(ref) = 3.5 \times 10^{10}$ A/m^2, and $T_c = 92\ K$ is the reference critical current density and critical temperature of the YBCO HTS tape, respectively.

6.2.1.1 The resistivity of 2G HTS YBCO tape

For a YBCO coated conductor, the YBCO superconducting layer is in parallel with the copper stabilizer layer. If the current is less than the critical current value, the current flows through the superconducting layer because of zero resistance. However, the resistivity of the YBCO layer will sharply increase when the current exceeds the critical current, which forces the majority of the current to be diverted into the copper stabilizer layer. Moreover, from Eq. 6.1, the current density of the YBCO layer is 0 if the temperature is above the critical temperature level. Therefore, the resistivity of the YBCO superconducting tape can be mathematically considered as a piecewise function of applied current and temperature.

(1) When the applied current I is less than the critical current I_c and the temperature of the HTS tape T is less than the critical temperature T_c, the superconductor is considered to be in the superconductive state. The resistivity $\rho_0 = 0$ describes this state.

(2) When $I > I_c$ and $T < T_c$, the YBCO layer quenches, which results in the appearance of resistance. The highly non-linear relationship of the superconductor between the current and the voltage is described using the *E-J* power law, and the resistivity of the superconductor can be calculated using Eq. 6.2:

$$\rho_{HTS} = \frac{E_c}{J_c(T)}\left(\frac{J}{J_c(T)}\right)^{N-1} \qquad \text{Eq. 6.2}$$

where $\mathrm{E_c} = 1\mu\mathrm{V/cm}$ is the critical electrical field. The N value is usually between 21 and 30 for YBCO tapes. When the applied current is greater than the critical current, a joule heating effect occurs due to the exponential rise in ρ_{HTS}, leading to the rise in temperature of the superconducting material.

(3) When $T > T_c$, the YBCO layer completely loses superconductivity and converts into a normal state. The applied current is then diverted into the copper stabilizer layer and again joule heating occurs in this copper layer, resulting in a dramatic rise in temperature. In this case, the resistivity of the superconductor is considered to be equal to the resistivity of the copper, which is a function of the temperature as expressed in Eq. 6.3 [122]:

$$\rho_{cu} = (0.0084T - 0.4603) \times 10^{-8} \qquad 77\,K < T < 250\,K \qquad \text{Eq. 6.3}$$

6.2.1.2 The heat transfer of YBCO HTS tape

The YBCO HTS tape has improved thermal conductivity thanks to the copper stabilizer layer. The heat exchange with an LN_2 cryogenic envelope is very efficient and the temperature difference of LN_2 along the axial direction of the cable depends on the almost negligible losses of the thermal leak; hence, the temperature of the LN_2 is maintained almost constant along the length of a cable less than 1 km long. An example of this is illustrated by an 80 kV 500 m HTS cable demonstration project in KEPCO. The dissipated heating will be removed by pressurized flowing LN_2, resulting in a temperature difference of less than 3 K between the superconducting

cable inlet and the outlet terminals [123]. Hence, in the following thermal transfer analysis, only the temperature gradient in the cable transversal area is considered. The temperature of the 2G YBCO superconducting tape is considered as a piecewise function of the fault current.

(1) When fault current occurs, $I > Ic$:

Based on the law of conservation of energy, and assuming that there is no thermal exchange with the external environment, the heat generated by the superconductor is absorbed by the superconductor itself and the LN_2 envelope. The amount of heat that is absorbed by the superconductor results in an increase in the superconductor temperature while assuming that there is no temperature variation in the LN_2 envelope, since the duration of the fault current is quite small. The joule heating generated from the superconductor is expressed as Eq. 6.4:

$$Q_{joule} = I^2 rt \quad \text{Eq. 6.4}$$

where t is the time and r is the resistance of the superconductor, which can be obtained from the resistivity of superconductor ρ_s based on Eq. 6.2 and Eq. 6.3, the length l of the cable and area A of the superconductor in the transverse area. The resistance superconductor is expressed in Eq. 6.5:

$$r = \rho_s \frac{l}{A} \quad \text{Eq. 6.5}$$

The amount of heat in joules absorbed by the superconductor is calculated based on the heat capacity c and the mass m of the superconductor, as shown in Eq. 6.6:

$$Q_{HTS} = cm\Delta T = cdAl(T_{n+1} - T_n) \quad \text{Eq. 6.6}$$

where d is the density of the superconductor, and ΔT is the temperature increment, expressed as $T_{n+1} - T_n$ in each iteration step. The heat exchange rate represents the cooling ability and is described by the heat transfer coefficient h.

There is currently no analytical expression for *h* to represent the efficiency of removing the dissipated heating from superconductor to cryogenic envelope. But in general, an empirical formula can be used, as in Eq. 6.7 [124]:

$$h = \alpha \Delta T^{\beta} + k \quad \text{Eq. 6.7}$$

where the parameters α, β and k are dependent on the temperature variation interval. The amount of heat in joules generated from the superconductor, which can be removed by the LN_2 cryogenic envelope, is calculated as Eq. 6.8:

$$Q_{LN2} = 2hwlt(T_{n+1} - T_{in}) \quad \text{Eq. 6.8}$$

where *w* is the width of the superconductor, *2wl* is the total area of the wide face of the HTS tape and $T_{in} = 70$ K is the temperature of LN_2. The area of the transverse face is ignored due to the high aspect ratio of the 2G YBCO HTS tape. Assuming there is no heat leakage, the thermal equilibrium equations can be obtained as expressed in Eq. 6.9:

$$Q_{HTS} = Q_{joule} + Q_{LN2} \quad \text{Eq. 6.9}$$

The temperature of superconductor T_{n+1} is updated at each calculation iteration over a time interval ΔT and can be calculated based on Eq. 6.4 to Eq. 6.9 with some substitutions, as expressed in Eq. 6.10:

$$T_{n+1} = \frac{Q_{joule} + cdAlT_n - 2T_{in}hwlt}{cdAl - 2hwlt} \quad \text{Eq. 6.10}$$

(2) When the fault current finishes, $I < I_c$:

The fault current ends and the superconductor starts to convert from the normal state to the superconductive state, only if it is not permanently damaged. The previously generated heat is continuously removed by LN_2 and the temperature of the superconductor gradually decreases back to operating temperature, as expressed in Eq. 6.11:

$$T_{n+1} = \frac{cdAlT_n - 2T_{in}hwlt}{cdAl - 2hwlt} \quad \text{Eq. 6.11}$$

The parameters used in Eq. 6.4 to Eq. 6.11 are summarized in Table 6.1. It should be noted that the density of the YBCO superconducting layer is approximately equal to the density of the copper. As the copper stabilizer is much thicker than the rest of the layers, the mass of the copper dominates.

Table 6.1: Values of parameters used in Eq. 6.4 to Eq. 6.11.

Parameters	Values
Width of the YBCO tape (w)	0.004 m
Transverse area of the YBCO tape (A)	4×10^{-9} m^2
Length of the cable (l)	1 km (unit length)
Thermal capacity of YBCO[125] (c)	200 J/kg · K
Density of the YBCO tape (d)	8.8×10^3 kg/m^3

6.2.1.3 The development of the superconductor component in PSCAD/EMTDC

The superconductor component developed in PSCAD/EMTDC needs to be able to fully characterize the non-linear transition of the resistivity of the entire tape and describe the temperature profile. New component development in PSCAD/EMTDC requires a program based on Fortran language, which is very difficult for the user to compile and modify. However, a much more convenient method can be realized thanks to the PSCAD/EMTDC interface with MATLAB through standard Fortran programming. The characteristics of a new component in PSCAD/EMTDC can be programmed in MATLAB using the C language. In each calculation iteration, MATLAB is called by PSCAD/EMTDC. The relevant parameters in the PSCAD/EMTDC circuit are used as the input values for MATLAB and the output values from MATLAB are sent back to the PSCAD/EMTDC circuit for the next calculation iteration.

In the case of the superconductor model, the temperature and resistance of the superconductor are calculated in MATLAB based on the current values from the PSCAD/EMTDC circuit. The Eq. 6.4 to Eq. 6.11 are programmed in MATLAB in order to update the new resistance and the temperature, which are used to calculate the current and voltage of the superconductor in the next iteration. The duration of iteration step is set based on the PSCAD/EMTDC circuit simulation solution time step, usually 25 μs is used. Figure 6.2 shows the flow diagram of the superconducting component calculation iteration in PSCAD/EMTDC interfaced with MATLAB.

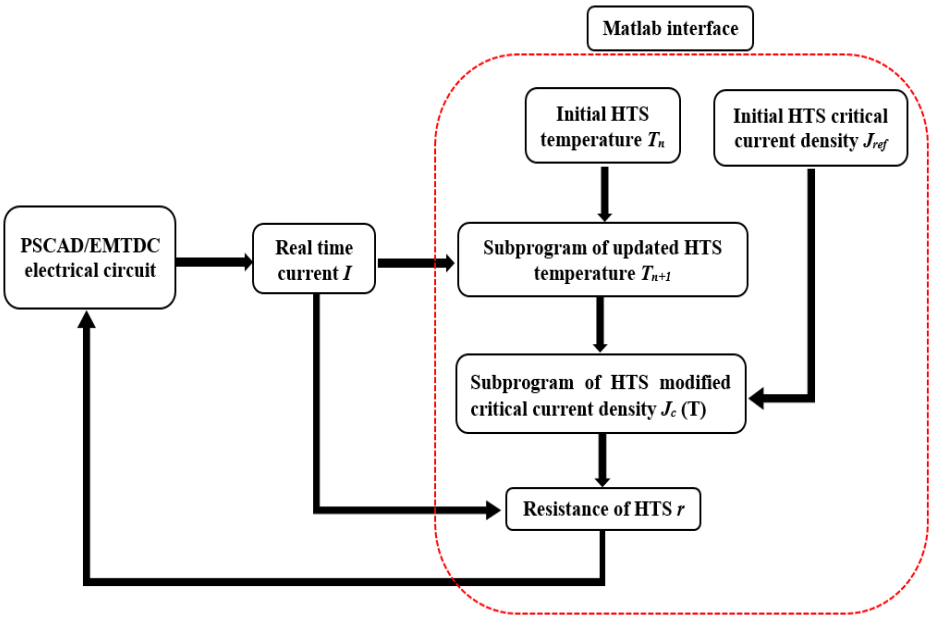

Figure 6.2: Flow diagram of the superconducting component calculation iteration in PSCAD/EMTDC interfaced with MATLAB.

The developed HTS component is simulated in a simple PSCAD/EMTDC electrical circuit, as shown in Figure 6.3. A variable resistor is used as the superconductor component since its resistance can be programmed using MATLAB to characterize the superconducting profile. The variable resistor is programmed based on the YBCO tape. An inductor is connected in series with the variable resistor considering the inductive voltage, which is dominating in low AC current values. Figure 6.4 (a) shows the simulation results of the YBCO HTS tape when the peak value of AC transport current I_{peak} has been gradually increased to the critical current I_c. It can be seen that

the voltage profile of the HTS tape is not a standard sinusoidal wave. This is because when the current is approaching the critical current value, a resistive voltage that is in phase with the current increases sharply due to the non-linear voltage-current relationship as shown in Eq. 6.2. The phase of voltage is shifted 90º to the current when $I_{peak} < I_c$ due to the tape inductance dominates in this case. Figure 6.4 (b) is the experimental measurement of the YBCO tape when $I_{peak} = 0.9I_c$. The voltage sharply increases when the current approaches the peak value. Due to the measured tape inductive voltage, the voltage is not zero when the peak current is less than I_c. It should be noted that the current shown in Figure 6.4 (b) is the voltage signal from the Rogowski coil rather than the real current value, because the current value is not concerned here. However, a similar measured voltage profile for the superconductor is obtained as the simulated result. Hence the developed superconductor component in PSCAD/EMTDC is valid, which can be further implemented in the HTS cable simulation.

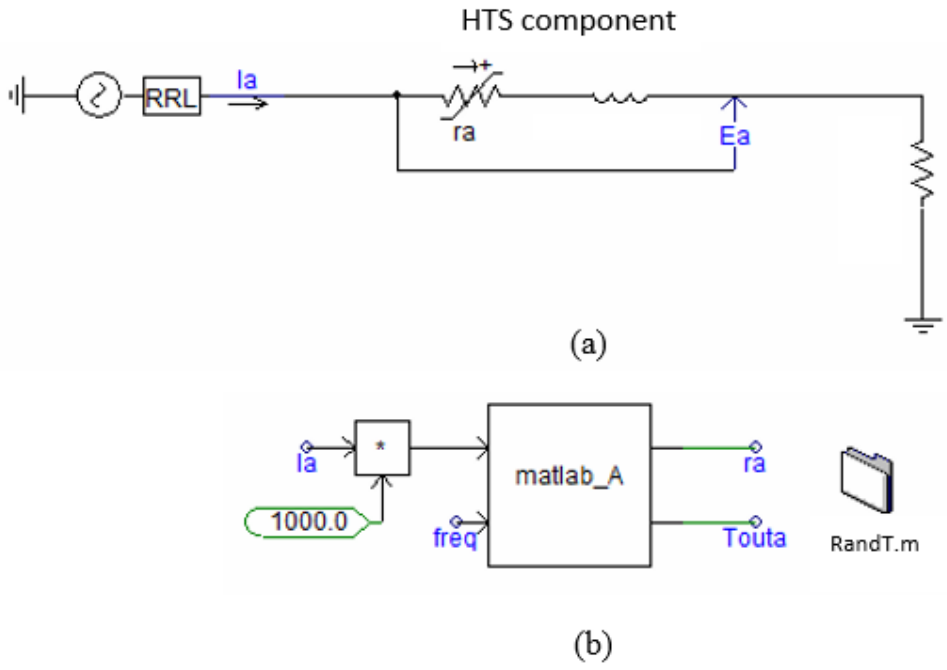

Figure 6.3: (a) Testing circuit of the HTS component developed in PSCAD/EMTDC. (b) MATLAB interface with PSCAS/EMTDC.

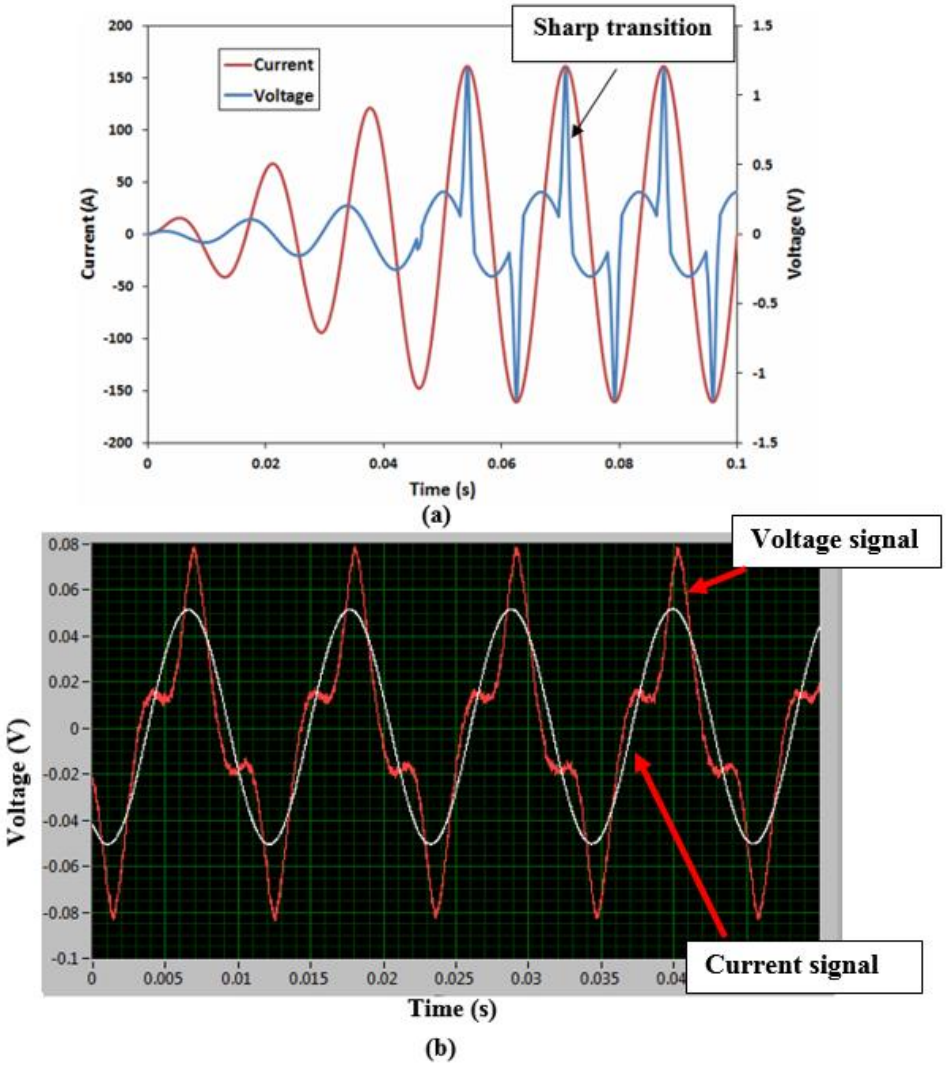

Figure 6.4: (a) The superconducting component simulation result in PSCAD/EMTDC. (b) The YBCO tape experimental measurement result.

6.2.2 Modelling of HTS cable in PSCAD/EMTDC with a fault current

The transient characteristics of the triad HTS cable are simulated in PSCAD/EMTDC when a fault current occurs. The triad HTS cable is modelled based on the specifications in Table 6.2. It consists of three HTS cables sharing one cryostat and each cable has its own cable core carrying one electrical phase. Figure 6.5 shows the configuration of the triad HTS cable in the electrical system using PSCAD/EMTDC. The conducting layer of each phase is composed of YBCO HTS tapes helically wound

on the copper former. A variable resistor is used to represent the HTS conducting layer, which is programmed as HTS conductor as presented in section 6.2.1.3. A constant resistor in parallel with the variable resistor is used to represent the copper former. The HTS shielding layer is also considered in this cable model. There are two typical configurations for the HTS shielding layers: (1) the shielding layers are grounded; (2) the shielding layer is used as the current return path, which is suitable for a DC transmission cable or a short AC power cable. For a long AC superconducting power cable, the shielding layers are grounded to prevent magnetic field leakage. The HTS tapes, which are also helically wrapped around the cable, are used as the shielding layers and are represented by variable resistors in PSCAD/EMTDC. The HTS conducting layer and the shielding layer are electrically coupled by a mutually coupled wire pre-defined in PSCAD/EMTDC. The inner and outer cryostat layers are shown as constant resistors and are grounded to the earth [118].

The transient characteristics of the superconducting cable current are simulated when the phase A to ground fault is applied to the cable at 0.1 s for a duration of 0.06 s. The simulation results are shown in Figure 6.6. It can be seen from Figure 6.6 (a) that the fault current of phase A is 20 kA for 3 full sinusoidal cycles. Due to the star connection, the currents of phase B and phase C are not affected by the fault current. The fault current that is actually conducted by the HTS layer is shown in Figure 6.6 (b), where only the first two fault current cycles strike in the superconducting layers while the third cycle is limited by the HTS tapes. As shown in Figure 6.6 (c), the copper former conducts nearly half the third cycle of the fault current and continuously conducts the operating current for 0.05 s in the duration between the fault current ends and the superconducting layer starts conducting the operating current.

The variation of the temperature and resistance of the superconducting layers causes current redistribution between the superconducting layer and the copper former. As shown in parts (d) and (e) of Figure 6.6, the first two cycles of the fault current slightly raise the temperature of the conducting superconductor layer and cause the resistance to appear. Apart from the heat that is removed by the cryogenic path, the

rest heat has been absorbed and accumulated in the superconducting layer, and the temperature gradually increases. When the temperature reaches 92 K, the superconducting layer quenches and converts to a normal state. The resistance of the superconducting layer increases sharply and half of the fault current redistributes into the copper former, which is now a path with relatively low resistance. Massive heat is generated by the superconducting layer and the copper former, resulting in a dramatic increase in temperature. After the fault current ends, the heat is continuously removed by the LN_2 cryogenic path and the temperature decreases gradually. The copper former conducts the majority of the operating current, before the temperature of the superconducting layer decreases down to 92 K. The resistance of the superconducting layer drops to zero immediately when the temperature reaches 92 K. The superconducting layer again starts conducting the operating current once it has reverted to a superconductivity state.

Table 6.2: Specifications of the superconducting cable.

Items	Values
Capacity (MW)	300
Rating voltage (kV)	22.9
Rating current (kA)/phase	1.5
Operation current (kA)/phase	1.1
Cable structure	Triaxial
Dielectric type	Cold dielectric
Cryogenic refrigeration system	Closed loop LN_2 self-circulation
Operating temperature (K)	70
YBCO HTS tape critical current	125A @ 77K from SuperPower
YBCO HTS tape thickness (mm)	0.001
YBCO HTS tape width (mm)	4
Insulation thickness (mm)	5
Length of the cable (km)	1

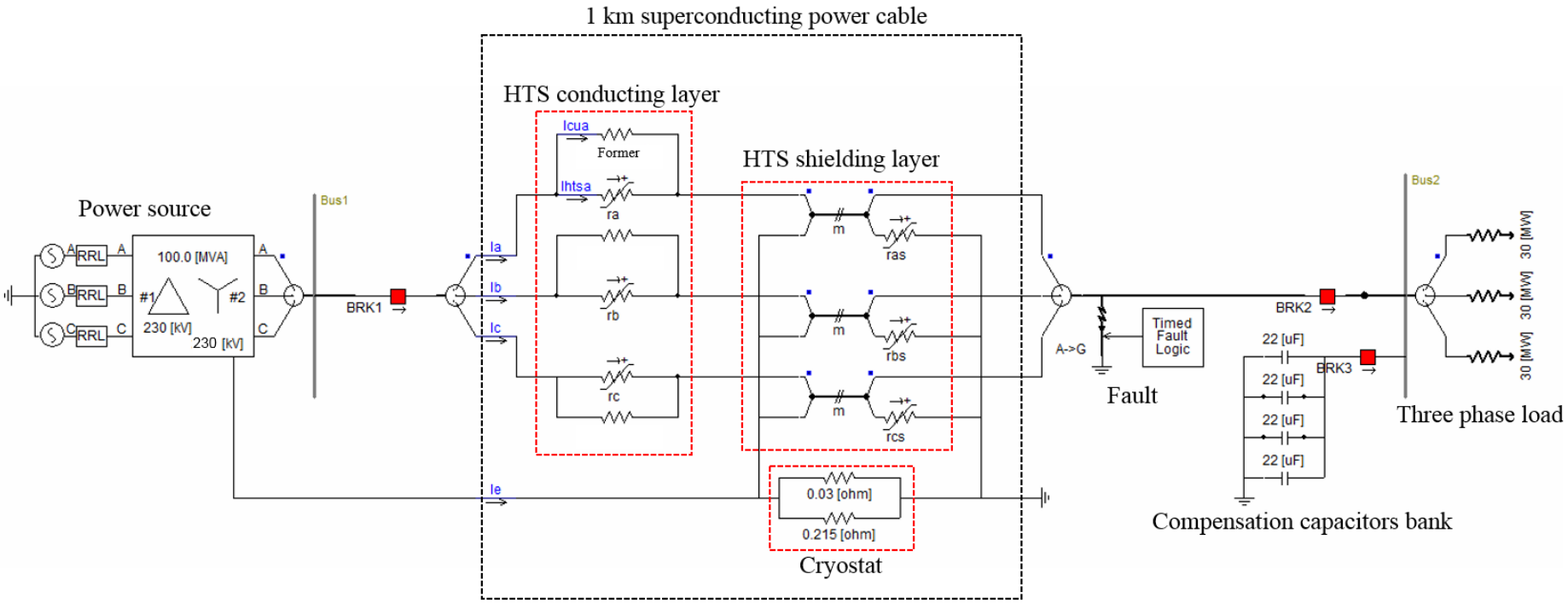

Figure 6.5: Simulation electrical circuit of 230 kV superconducting cable in PSCAD/EMTDC.

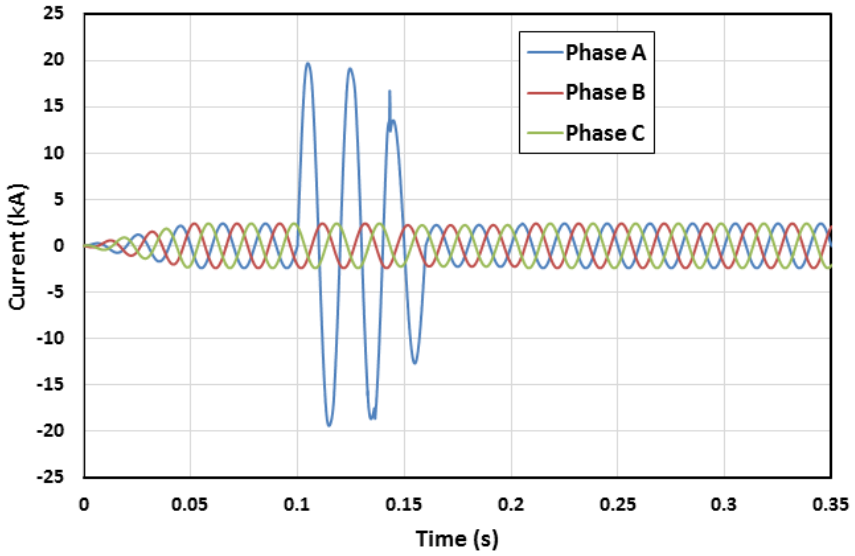
Phase A
Phase B
Phase C
Current (kA)
Time (s)
25
20
15
10
5
0
-5
-10
-15
-20
-25
0
0.05
0.1
0.15
0.2
0.25
0.3
0.35

(a)

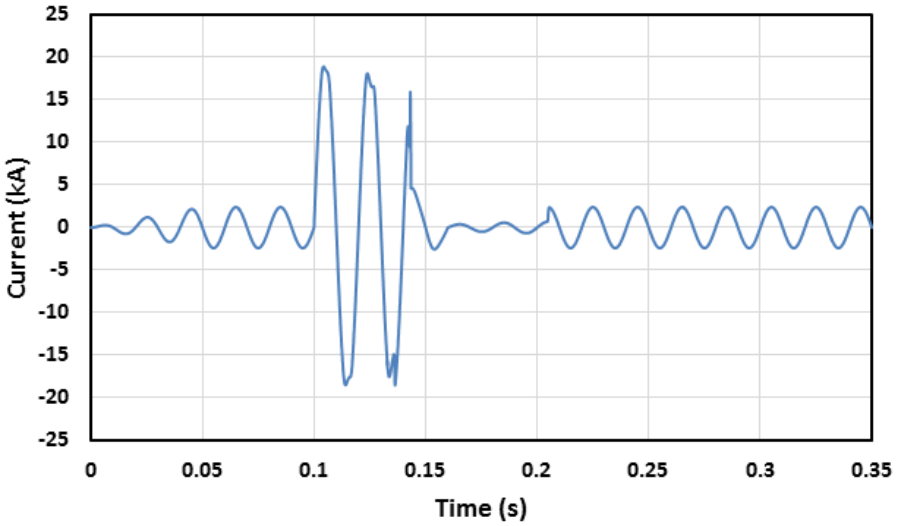
Current (kA)
Time (s)
25
20
15
10
5
0
-5
-10
-15
-20
-25
0
0.05
0.1
0.15
0.2
0.25
0.3
0.35

(b)

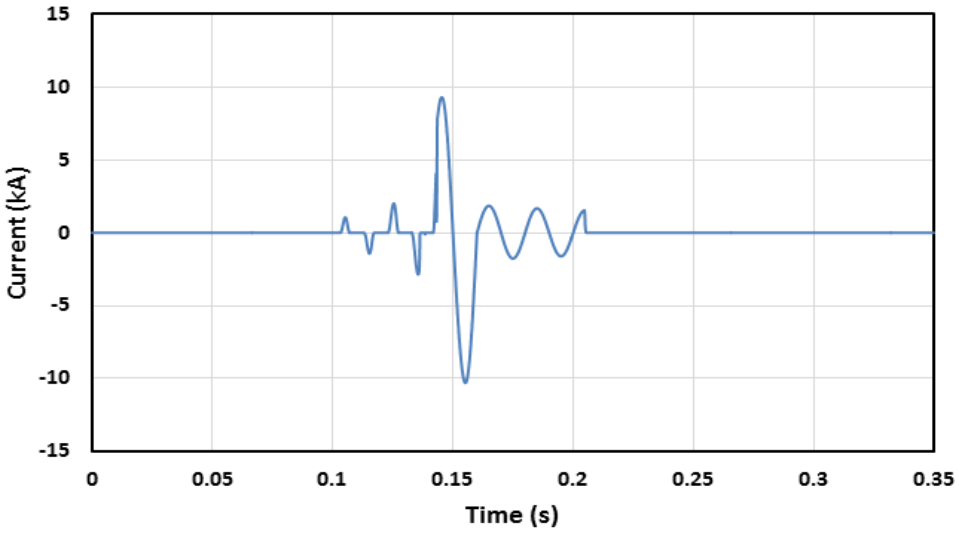
Current (kA)
Time (s)
15
10
5
0
-5
-10
-15
0
0.05
0.1
0.15
0.2
0.25
0.3
0.35

(c)

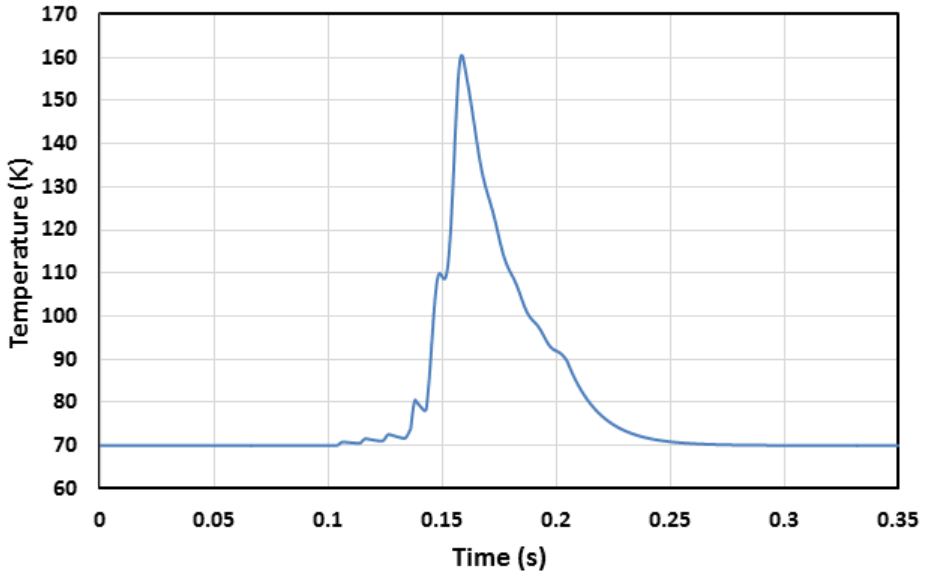

(d)

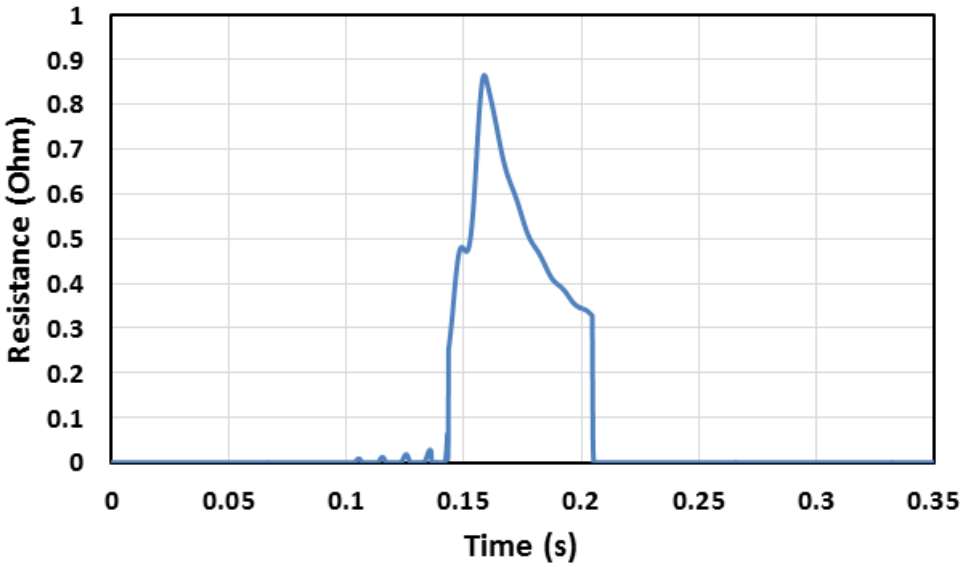

(e)

Figure 6.6: PSCAD/EMTDC simulation results of superconducting cable with A to ground fault current happening at 0.1 s for a duration of 0.06 s. (a) Three phase current. (b) Current of the superconducting layer. (c) Current of the copper former. (d) The temperature of the superconducting layer. (e) The resistance of the superconducting layer.

In some cases, fault currents in the power grid are likely to last longer than 0.06 s and can cause the temperature of the superconducting tapes in the cable to increase rapidly. If the temperature is over 500 K, the superconducting tapes will be permanently damaged and they will not revert back to the superconducting state. In this case, the circuit breaker must be tripped before the HTS tapes reach the maximum permissible temperature. Figure 6.7 shows the temperature of the HTS tapes wound on the cable increased with a 20 kA fault current applied. The temperature increase rate depends on the heat transfer coefficient, which can be improved by increasing the LN_2 flow rate in the cable cryogenic envelope. If the maximum permissible operating temperature is 110 K and the temperature that can damage the HTS tapes is 573 K, then the circuit breaker must trip the HTS cable off the grid within this temperature margin.

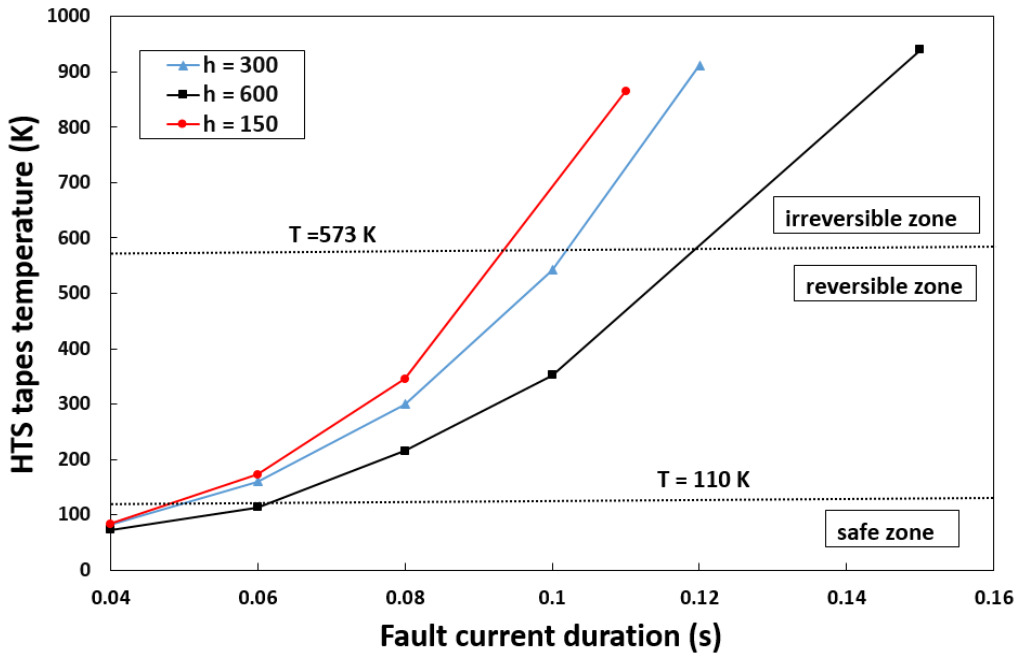

Figure 6.7: Temperature increase of the HTS tapes with various heat transfer coefficients under a 20 kA HTS cable fault current.

6.3 The impact of the superconducting cable in a meshed power grid

6.3.1 The impedance of the superconducting cable

For long distance power transmission, the resistance of the superconducting power cable is not zero because of the AC losses. For AC HTS cable, AC losses are contributed from the hysteresis loss, eddy current loss and coupling loss; for DC HTS cable, the AC ripple current with DC offset is the main source of the AC losses. But the characteristic resistance resulting from the AC losses is still much smaller than the ohmic loss from the copper cable. The inductance of the cable results from the enclosed magnetic energy of the cable. The inductance of the superconducting cable is much smaller than the conventional copper cable thanks to the opposite winding direction of each HTS layer, such that the cable axial magnetic flux resulting from each HTS layer is minimized. The capacitance of the HTS cable is similar to the conventional XLPE underground power cable because of the similar structure of the insulation layer. Table 6.3 summarizes the comparison among the HTS cable, the XLPE cable and the overhead line [114, 126].

Table 6.3: Comparison between the three transmission cable techniques.

Cable type	Resistance (Ω/km)	Inductance (mH/km)	Capacitance (nF/km)
HTS cable	0.0001	0.006	200
XLPE cable	0.03	0.36	257
Overhead lines	0.08	1.26	8.8

Compared with the conventional transmission cable techniques, the impedance of the HTS cable is very low. This has the benefit of easing the transmission congestion. With an HTS cable placed in parallel with a congestion conventional cable, the power will naturally flow into the HTS cable and ease the power congestion. However, due to the high capacity of the HTS cable, the HTS cable may cause power flow re-routing in the system. Hence, before applying the HTS cable to the meshed grids, detailed power system analysis is necessary to foresee potential problems in order to maximize the power transmission efficiency of the grid. The power system analysis

considering the HTS cable integrated into the power grid is discussed in this section, including the power flow, grid losses and voltage profile comparisons among the HTS cable and the XLPE underground cable.

6.3.2 The analysis of HTS cable integrated into a simple meshed grid using PSCAD/EMTDC

In order to install a new transmission cable into the system, it is necessary to analyse all the parameters of the system, including bus voltages, branch currents, real power flow and reactive power flow. The complex power equation containing real and reactive power entering into the i^{th} bus is shown in Eq. 6.12 [127]:

$$P_i + jQ_i = V_i \sum_{j=1}^{N} Y_{ij} V_j^* \qquad \text{Eq. 6.12}$$

where the P_i and Q_i are the real and reactive powers that are entered into the i^{th} bus, respectively. V_i and V_j are the voltage of the i^{th} bus. Y_{ij} is the admittance of the branch between the i^{th} bus and the j^{th} bus and the admittance matrix can be constructed by Y_{ij} containing the impedance of all the branches. N is the number of total buses in the meshed system. The Newton–Raphson iterative is one effective method for obtaining the solution [128]. With several iterative steps, the system can be linearized using the Tyler series with the higher order ignored, and the linearized system can be expressed in Eq. 6.13:

$$\begin{bmatrix} \Delta\delta \\ \Delta|V| \end{bmatrix} = -J^{-1} \begin{bmatrix} \Delta P \\ \Delta Q \end{bmatrix} \qquad \text{Eq. 6.13}$$

where ΔP and ΔQ are the mismatched equations and J is the partial derivative known as the Jacobian matrix, which is shown in Eq. 6.14 to Eq. 6.16, respectively:

$$\Delta P_i = -P_i + \sum_{k=1}^{N} |V_i||V_k|(G_{ik}\, cos\, \delta_{ik} + B_{ik}\, sin\, \delta_{ik}) \qquad \text{Eq. 6.14}$$

$$\Delta Q_i = -Q_i + \sum_{k=1}^{N} |V_i||V_k|(G_{ik}\, cos\, \delta_{ik} - B_{ik}\, sin\, \delta_{ik}) \quad \text{Eq. 6.15}$$

$$J = \begin{bmatrix} \frac{\partial \Delta P}{\partial \delta} & \frac{\partial \Delta P}{\partial |V|} \\ \frac{\partial \Delta Q}{\partial \delta} & \frac{\partial \delta}{\partial |V|} \end{bmatrix} \quad \text{Eq. 6.16}$$

Figure 6.8 shows an original meshed electrical power system with 3 generators and 9 notes. All the parameters of the system are shown in Table 6.4. The power flow problem can be solved using MATLAB by calculating a set of non-linear Eq. 6.12 to Eq. 6.16 [129]. In this section, a new method based on PSCAD/EMTDC is used to solve the power flow of the system shown in Figure 6.8 [130]. PSCAD/EMTDC can provide a user-friendly interface to simulate the power flow program with high accuracy. In the PSCAD simulation, the real and reactive power flow, voltage magnitude and phase angle are calculated with the base of 100 MVA and 230 kV at 50 Hz. The results of the original system are plotted in Figure 6.9. In the grid, the type of transmission cable is XLPE underground cable, and the series impedance and shunt capacitance are shown in Table 6.4. The lengths of all the transmission cables are assumed to be unit length. Based on the results shown in Figure 6.9, it can be seen that the voltage profiles at all the load buses (Bus 5, Bus 6 and Bus 8) are generally low in magnitude; in particular, the magnitude of the voltage at Bus 5 is only 0.9488 p.u. This is due to the significant losses dissipated from the transmission cable from Bus 5 to Bus 7, where the transmission cable is highly congested with a transmission load of 89%. And the transmission cable between Bus 4 and Bus 5 is close to the congestion level with a transmission load of 73%, which will likely be congested with an increased load at Bus 5 in the future. The overload of power cable will severely reduce the cable's life cycle and increase its risk of breaking down. In order to solve this problem, one solution is to install a new transmission line into the system. Assuming that the load at Bus 5 will increase in the near future and the generators from a power plant at Bus 3 is scheduled to produce more power, a new transmission line will be install between the Bus 5 and Bus 9. There are two techniques available to the utilities to use: one is conventional XLPE power cable and another is HTS cable. Detailed comparisons are necessary in terms of the transmission efficiency, voltage

profile improvement and the grid losses between the installation of the XLPE cable and the HTS cable.

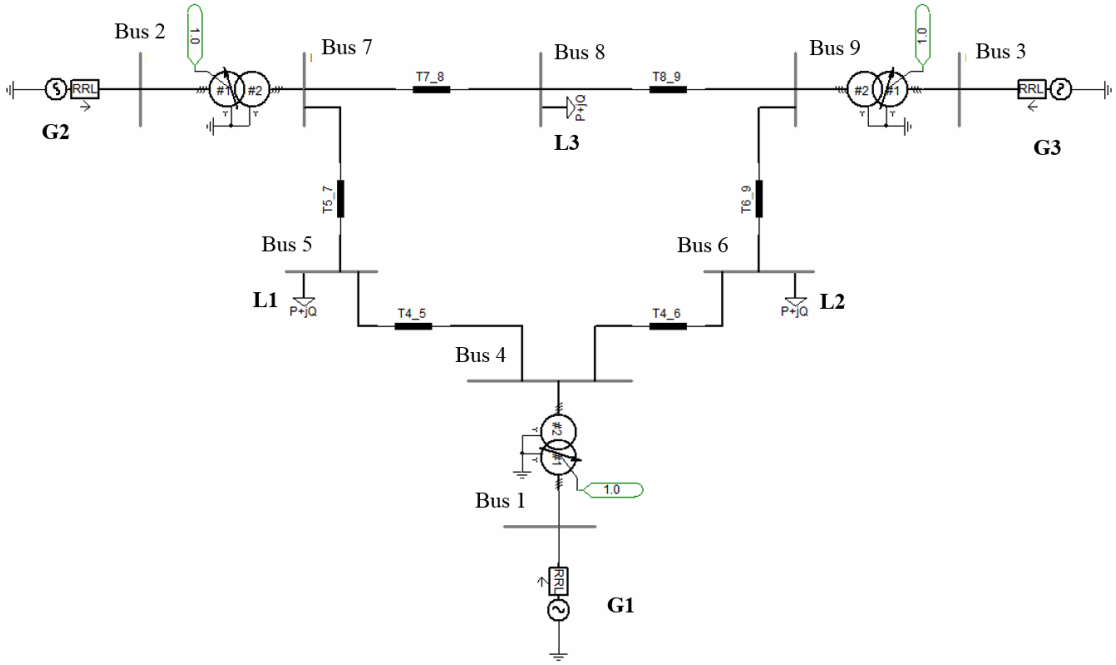

Figure 6.8: IEEE 9 bus, 3 generator system.

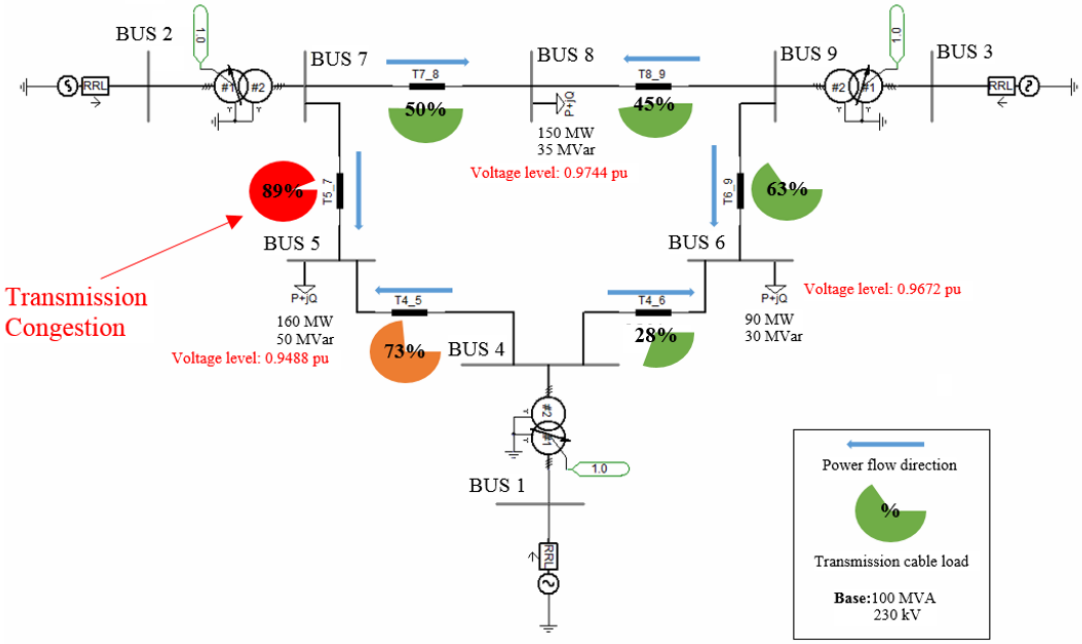

Figure 6.9: The power flow results of the original meshed system.

Table 6.4: Parameters of the IEEE 9 bus system.

Generator parameters			
Generator no.	No.1	No. 2	No. 3
Bus no.	Bus 1	Bus 2	Bus 3
Rating Power (MVA)	247.5	192	128
Rating voltage (kV)	16.5	18	13.8
Power factor	1.0	0.85	0.85

Branch parameters

From	To	Type	R (p.u.)	X (p.u.)	B/2 (p.u.)	Capacity (MW)
Bus 1	Bus 4	Transformer	0	0.0576	0	300
Bus 2	Bus 7	Transformer	0	0.0625	0	300
Bus 3	Bus 9	Transformer	0	0.0586	0	300
Bus 4	Bus 5	Transmission line	0.01	0.068	0.088	100
Bus 4	Bus 6	Transmission line	0.017	0.092	0.079	100
Bus 5	Bus 7	Transmission line	0.032	0.161	0.153	100
Bus 6	Bus 9	Transmission line	0.039	0.17	0.179	100
Bus 7	Bus 8	Transmission line	0.0085	0.0576	0.0745	200
Bus 8	Bus 9	Transmission line	0.0119	0.1008	0.1045	100

Load parameters

Load no.	Bus no.	Real power (MW)	Reactive power (MVar)
L1	Bus 5	160	50
L2	Bus 6	90	30
L3	Bus 8	150	35

An XLPE cable rated at 100 MW is installed between Bus 5 and Bus 9 as shown in Figure 6.10. The parameters of this XLPE cable is listed in Table 6.5 and the power flow results are also plotted in Figure 6.10. With additional transmission cable transferring power from the generator at Bus 3, the power transmission congestion between Bus 5 and Bus 7 is eased, and the transmission load reduces down to 65%. The magnitude of the voltage at Bus 5 is improved to 0.9734. However, the transmission load of the newly installed XLPE cable is 64%, so it does not have enough extra transmission capacity to handle the likely increase in power load at Bus 5 in the future. Therefore, installation of a new XLPE power cable with a higher transmission capacity is required for future load growth. In this case, extra underground space may be required to fit a larger electrical conduit, which could mean extremely expensive construction work in some urban areas.

An HTS cable rated at 300 MW is installed between Bus 5 and Bus 9 as an alternative solution. The parameters of this HTS cable is listed in Table 6.5 and the power flow results are plotted in Figure 6.11. It can be seen that the power transmission load of the cable between Bus 5 and Bus 7 has been further eased, with the transmission load reduced down to 48%. The magnitude of the voltage profile at Bus 5 has been significantly improved to 0.9903. More importantly, due to the high power capacity of HTS cable, the transmission load of the newly installed HTS cable is only 36%, with enough extra capacity to handle future increases in power load, and it can easily be installed in the existing underground electrical conduit due to the compact size. Figure 6.12 summarizes the improvements of the new cable installed between Bus 5 and Bus 7.

Table 6.5: Parameters of new cable installed between Bus 5 and Bus 7

Parameters	R (p.u.)	X (p.u.)	B/2 (p.u.)
XLPE cable	0.0279	0.096	0.0745
HTS cable	0.000093	0.016	0.08

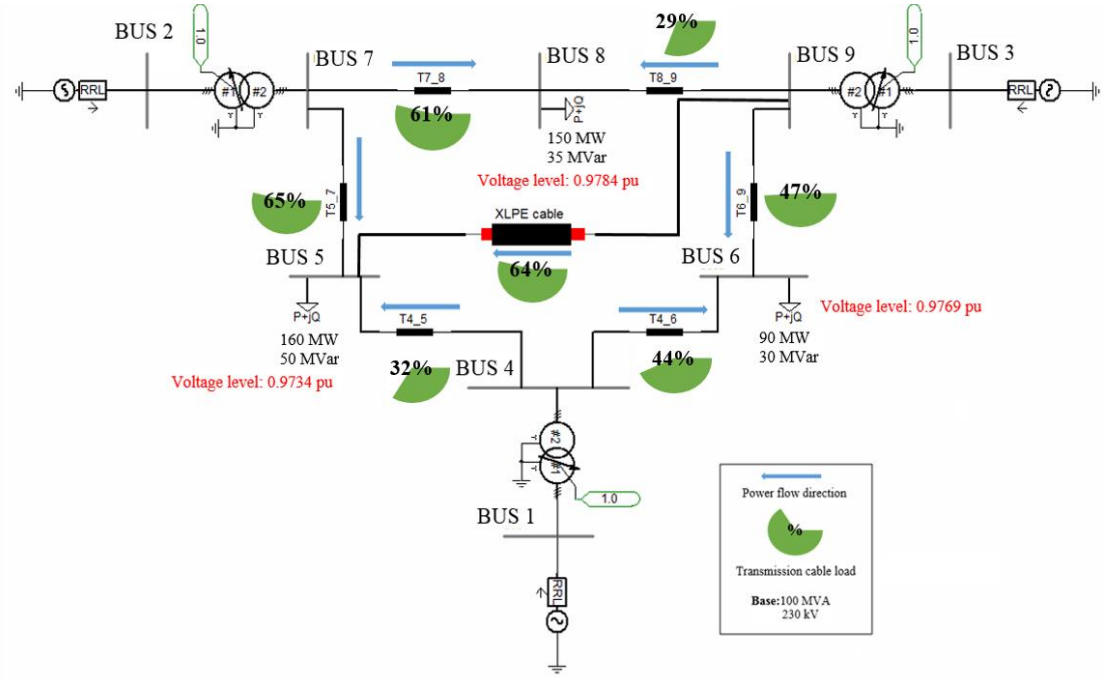

Figure 6.10: The power flow results with the new XLPE cable installed into the system.

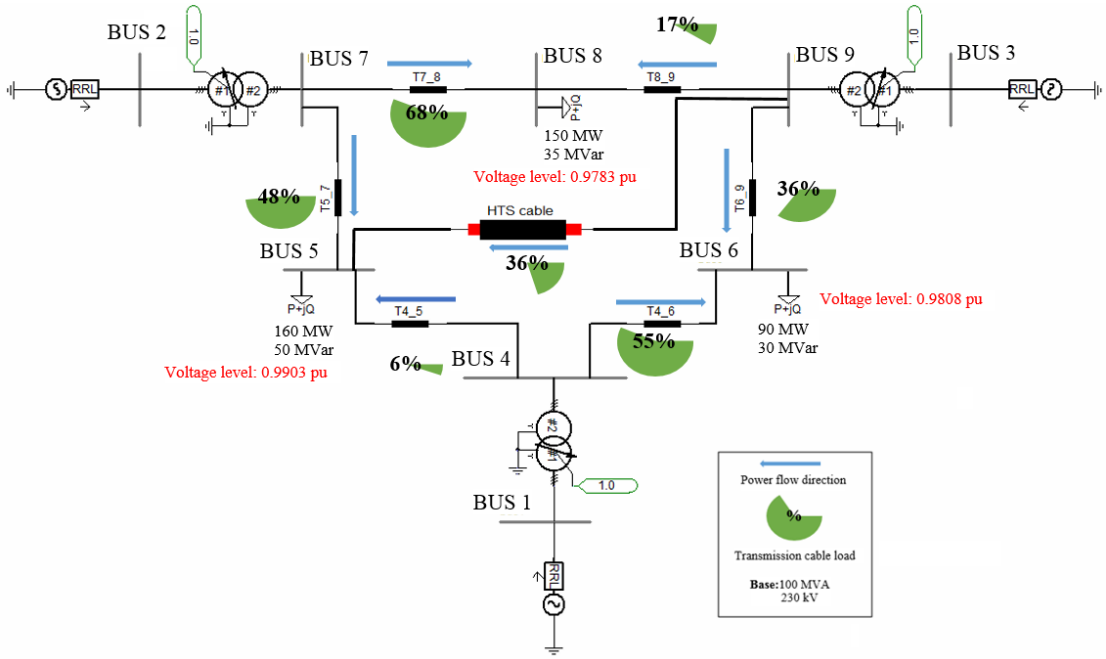

Figure 6.11: The power flow results with the new HTS cable installed into the system.

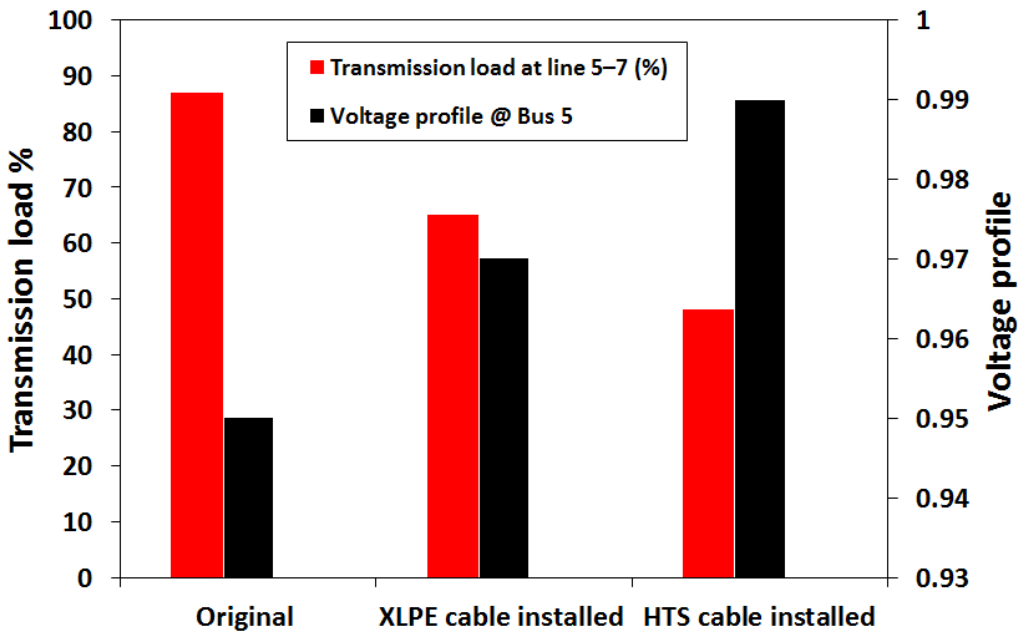

Figure 6.12: Improvements of the new cable installed between Bus 5 and Bus 7.

The total grid losses are considered in the comparison in terms of the conduction losses, which are directly proportional to the transmission line impedance and the square of the current. The total grid losses are calculated in Eq. 6.17, and only the ohmic losses of all the branches and the total power from all the generators in the system are considered.

$$P_{loss} = \sum_{k=1}^{N} P_{cable} \Big/ \sum_{k=1}^{m} P_G \qquad \text{Eq. 6.17}$$

where k is an integer, N is the number of total branches and m is the number of total generators. In Figure 6.13, the results are compared among the new installation of the XLPE cable, the HTS cable from Bus 5 to Bus 9, and the original meshed grid. It turns out that the grid losses of the XLPE installation are 2% while the grid losses of the HTS cable installation is 0.87%. This is reasonable because the HTS cable is able to transfer a large amount of power into the system with much smaller conduction losses. Overall, it can be concluded that the HTS cable has better performance on easing the power transmission congestion, improving the voltage profile and reducing the total grid losses compared with the XLPE cable.

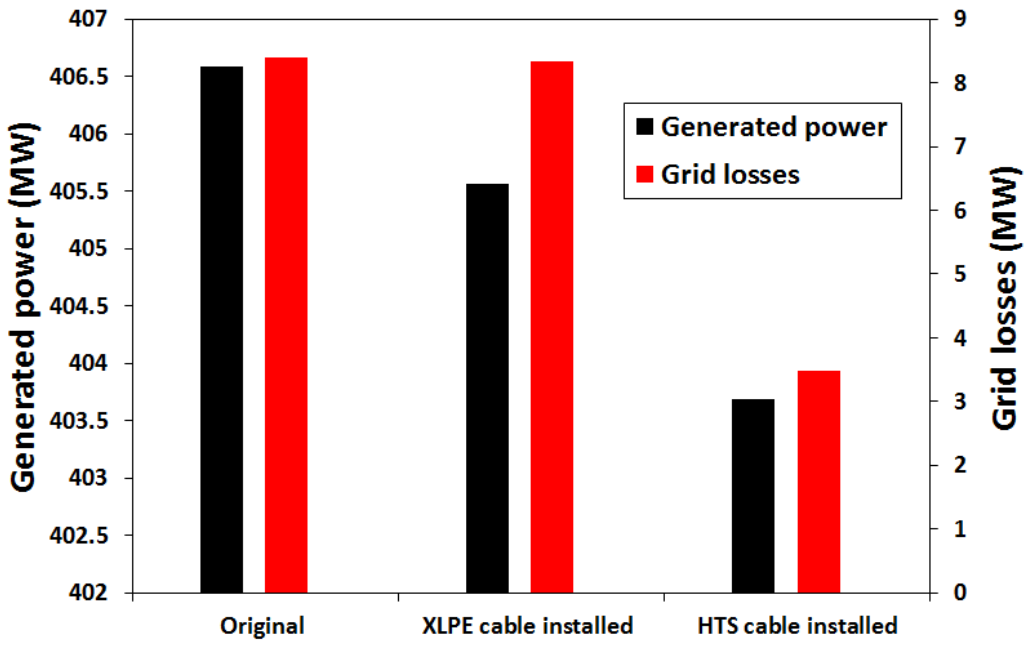

Figure 6.13: The grid losses comparison between new XLPE and HTS cable.

In the case of a fault occurring in the power system, it is necessary to study the fault current level of the HTS cable. In order to analyse the fault current impact on the HTS cable in the meshed grid, a three phase to ground fault is applied at Bus 5 for the duration of 0.2 s. Considering the comparison of the HTS cable and the XLPE cable, the fault currents are calculated based on PSCAD/EMTDC and the results are shown in Figure 6.14. It is shown that the fault current level of the HTS cable is three times higher than that for the XLPE cable. Within the thermally permissible margin, the HTS cable has a higher fault current capacity which is beneficial for enhancing the power system stability. However, the fault current will raise the temperature of the superconductor drastically. To prevent permanent damage to the HTS cable, the circuit breaker must take the HTS cable off the grid before the temperature of the HTS cable exceeds the maximum allowable temperature. Since the conventional circuit breakers have limited minimum reaction time, a proper protection strategy needs to be considered. In the case of the magnitude of fault current level is too high, which will cause the temperature of the superconductor to rise over the maximum allowable temperature in a few milliseconds, superconducting protection devices, such as SFCLs, are needed to limit the fault current level down to the protection region of the conventional circuit breaker [115, 131].

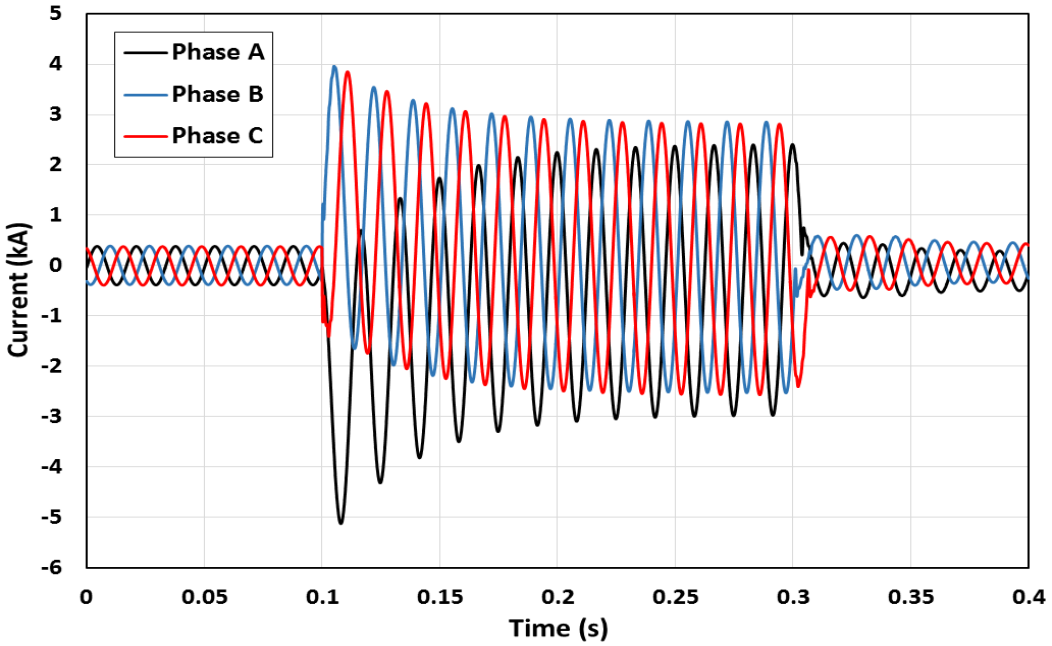

(a)

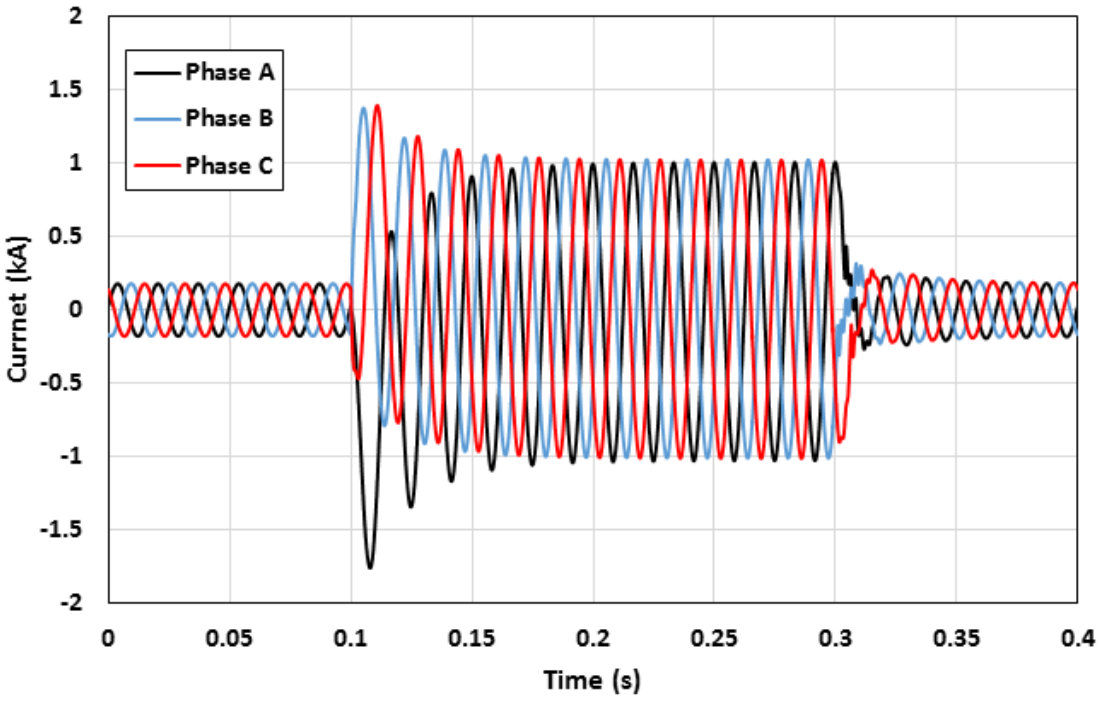

(b)

Figure 6.14: The three phase to ground fault current at Bus 5 of the installation of (a) HTS cable and (b) XLPE cable.

6.3.3 Feasibility analysis of HTS cable installed into the power grid considering the total cable transmission losses

In this section, the total losses of the HTS cable and the XLPE cable are compared in terms of the AC current load considering two main types of losses [132]:

1) The load dependent losses, which include the conduction loss and shielding loss. For the XLPE underground cable, the conducting losses result from the resistivity of the material in the form of heat dissipation. The shielding losses are proportional to the current that is induced by the AC magnetic field in and around the cable. For the HTS cable, AC losses result in conduction losses and shielding losses. There is currently no standard analytical formula or model to accurately quantify the HTS cable AC losses. Some analytical formulas exist to estimate the AC losses: the mono-block prediction model [98] and the Majoros model [133]. But these methods do not consider the pitch length of the cable in the 3D geometry. Nevertheless, the experimental AC loss measurement results in Chapter 5 can be used for reference: 0.42 W/kA*m. Although the AC losses are very small, only one-third of the resistive losses of the conventional cable [116], the heat dissipation has to be removed by a liquid nitrogen cryogenic path, where the refrigeration penalty is considered. The cooling penalty factor is dependent on the cooling technology. For the cooling system of the transmission cable, the cooling penalty factor of the open loop system, where liquid nitrogen is cooled down by an external bulky LN_2 container, is lower than the closed loop system, where the liquid nitrogen is cooled down by a cryocooler. Ideally, the cooling penalty factor is estimated as being within 10 and 18 at 77 K [134, 135].

2) The load independent losses, which include the dielectric losses in the insulation. The dielectric losses occur in the transmission cable insulation. Since the insulation material is non-ideal, the movement of charges in the AC electromagnetic field dissipates energy in the form of heat. The dielectric losses can be calculated in Eq. 6.18:

$$P_d = \omega C U_0 \tan \delta \qquad \text{Eq. 6.18}$$

where $\omega = 2\pi f$, $C = \frac{2\varepsilon_r \varepsilon_0}{Ln(D_o/D_i)}$ and D_o and D_i are the inner and outer diameters of the insulation layer. U_o is the operating voltage level and $tan\,\delta$ is the loss factor. It can be seen from Eq. 6.18 that only the voltage level and the type of material determine the dielectric factor, hence it is a load current independence losses. For the conventional cable, extruded dielectric materials are used as insulation, such as XLPE with the relative dielectric of $\varepsilon_r = 2.3$ [136]. For the HTS cable, polypropylene laminated paper (PPLP) is used as the insulation layer, of which the relative dielectric ε_r is 2.2 [137, 138]. The liquid nitrogen with the relative dielectric of $\varepsilon_r = 1.4$ fills the gaps between the PPLP layers. The liquid nitrogen is pressurized in order to prevent gas bubbles. Hence, with the same voltage level, the dielectric losses between the XLPE cable and the HTS cable are similar.

The HTS cable requires an additional cooling system to remove the dissipated heat into the liquid nitrogen path, which is unique to the HTS cable. Thermal leaking losses exist due to non-ideal thermal insulation. In order to reduce the thermal leaking, there is a vacuum thermal insulation layer between the inner wall and the outer wall cable cryostat to intercept heat from outside the cable. Based on the temperature difference ΔT between the cryogenic path (77 K) and the room temperature environment (300 K), the diameter of the inner wall d_i and the outer wall d_o, the thermal leaking can be calculated by equation 6.19:

$$P_{leak} = \frac{2\pi\gamma\Delta T}{Ln(d_o/d_i)} \tag{6.19}$$

where γ is the thermal conductive of the vacuum insulation, which is 0.1–0.2 mW/m*K dependent on the pressure of the vacuum [139]. The cable terminal resistive losses and joint losses need to be considered for both the HTS cable and the XLPE cable. Table 6.6 summarizes all types of losses of the HTS cable and XLPE cable. Considering the cooling penalty factor for the HTS cable, the total loss comparison between the HTS cable and the XLPE cable is shown in Figure 6.15. It can be seen that at lower current levels, the total losses of the HTS cable are higher than for the XLPE cable, because the cooling system still needs to operate in order to maintain a

temperature of 77 K for the HTS cable. Only at higher currents can the losses of HTS cable outperform that of the XLPE cable.

Table 6.6: The total loss comparison of 132 kV HTS cable and XLPE cable.

Loss type	HTS cable	XLPE cable
Conduction losses[140]	0.42 W/kA*m	20 W/kA*m
Thermal leaking losses[141]	1.5 W/m	0
Induced losses in the shield[140]	0.4 W/kA*m	0.77 W/kA*m
Dielectric losses[141]	0.9 W/m	0.7 W/m
Cable joints and termination losses[139]	0.7 W/kA	0.7 W/kA

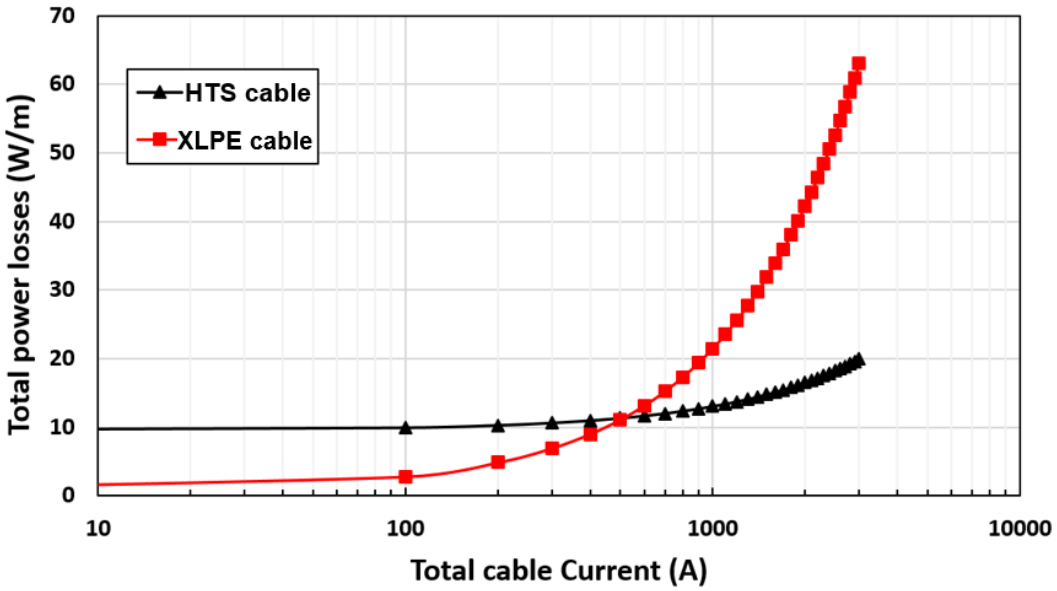

Figure 6.15: The total losses of comparison between the 132 kV HTS cable and the XLPE cable based on the current load.

6.4 Summary of the investigation

In this chapter, the simulation of the HTS cable in the power grid using PSCAD/EMTDC was described in detail. The superconductor component was developed based on a variable resistor coupled with MATLAB. A three phase HTS cable system was configured. A number of different impacts of the HTS cable installation in the power grid were investigated in order to maximize the benefits of using the HTS cable. A summary of the HTS cable model and comments on the impacts on the power grid are outlined below:

- Superconductor component improvement

  In PSCAD/EMTDC, a superconductor component was developed in order to couple the resistivity with the temperature and the current density. The thermal exchange between the HTS cable and the cryogenic path was also considered in the model, which could be used to design cooling systems for HTS cable and analyse the tolerance time in the case of a fault.

- Power grid planning

  In the near future, HTS cable will be used in conjunction with conventional cables in power grids. The low impedance HTS cable with large power transmission capacity could be a potential threat to the stability of the power system. Implementation of HTS cable into the power grid is a 'double-edged sword'. HTS cables are capable of easing the power congestion without auxiliary devices, but can also alter the power flow direction in some power transmission lines, causing power system instability. Nevertheless, the HTS cable could be beneficial to the power grid only if their impacts on the power grid are properly assessed.

- HTS cable location

  Since the HTS cable still requires cooling power at a rated capacity even if there is only little current load, installing HTS cable in the distribution network, such as in residential areas, is not economical at off-peak times. Hence, in order to make the most use of the benefits of HTS cable, it should be installed at paths where the

heavy current load is required at all times, such as substations, power plants and data centres.

Chapter 7

Conclusions

7.1 Summary

This dissertation has presented the physical background of the superconductivity and discussed the properties of state-of-the-art YBCO HTS wires. The configuration and the recent development of HTS cable projects have briefly been outlined. The accomplished results can be summarized as follows:

- The influence of anisotropy on critical current of YBCO HTS cable has been characterized. A completed experimental method for characterizing of anisotropic characteristics of the YBCO HTS tape was presented. By known the important parameters of anisotropy, the in-field properties of different YBCO HTS tapes can be compared regardless of the tape materials and structures. It can be of assistance in the design of HTS cable by choosing the right superconducting material. Due to the anisotropy of the HTS tape, the critical current of the HTS cable affected by gap distance was investigated by a cable circuit model consisted of parallel placed HTS tapes. The gap distance among the tapes can be adjusted freely and the tapes were electrically connected in series to eliminate the influence of contact resistances. The results show that considerable critical current improvement is possible if the gap distance is less than 1 mm.
- The current distribution of multi-HTS-layer cable is homogenized by optimizing the contact resistances and HTS layer inductances. It is found out that the contact resistances have a large influence on causing imbalanced current distribution for practical HTS cable and they could be the possible reason for the discrepancy between the experimental and modelling results. An HTS cable consisted of two HTS layers coaxial wound on the cable former was built. A novel measurement

technic was applied to obtain the contact resistances and current distribution between the two HTS layers. This current distribution measurement technique is easy to implement without complex auxiliary devices and altering the cable termination. The measured contact resistance can be used as input data of FEM modelling to accurately predict the performance of HTS cable as well as other HTS applications which have the issues of imbalance current distribution due to contact resistances. Apart from contact resistance, the HTS layer inductances also pose an important influence on current distribution if HTS cable carrying AC transporting current. An optimal algorithm was developed to achieve homogeneous current distribution by optimally designing the cable diameter, pitch angle and winding direction. The optimal results show that the algorithm is effective to achieve homogeneous current distribution for cable consisted of multi-HTS layers.

- A reliable AC loss measurement was carried out on the prototype HTS cable implementing electrical four probe method and symmetrical current return path. In order to improve the measurement accuracy, the copper cables in room temperature connected with HTS cable are arranged to form a symmetrical current return path from the HTS cable back to the AC power source in the measurement circuit in order to eliminate the electromagnetic field surrounding the HTS cable. The AC loss of the cable was firstly measured based on the DAQ technique. A compensating coil is adopted to cancel out the inductive component of measured voltage. But measurement errors exist in this method for low current (0.1-0.2I_c) due to inadequate sensitivity of phase angle detection. Alternatively, a lock-in amplifier is implemented to extract the in-phase component of the measured voltage. The compensating coil only needs to compensate the inductive component of measured voltage to the same order of magnitude of the resistive component and the real part of the signal extracted by the lock-in amplifier gives more accurate AC loss voltage. Hence, the measurement accuracy is improved for low current. For multi-HTS-layer cable, the potential probes are placed on the cable terminals. In this way, the issue of current distribution among the HTS layers is eliminated but it introduces additional ohmic losses contributed from the cable joints. In AC frequency, the terminal contact resistances are frequency dependent due to the skin effect. The terminal contact resistances obtained from the DC test are not applicable unless modified based on the various penetration

depths for each applied frequency. Then accurate AC loss results are obtained by subtracting the ohmic losses from the modified terminal contact resistance considering the skin effect.

- A new superconducting model was developed to predict the impact of HTS cable on power grids in PSCAD/EMTDC. The model takes into account the coated structure of the YBCO tape coupled with the heat exchange with the HTS cable cryogenic envelope in order to represent the real HTS cable application. The simulation results show that the HTS cable has superior performances on grid losses reduction, easing power transmission congestion compared with the conventional copper cable. However, the higher fault current level and possibility of varying power flow magnitude and direction may require additional planning before integrating the HTS cable into power grids. More importantly, this model is also applicable to other YBCO HTS applications, such as HTS transformer and superconducting fault current limiter.

7.2 Possible improvements

The work in the thesis can be potentially further improved as follows:

The discussions of the critical current of HTS cable in Chapter 3 simplify the real cable geometry to a cable circuit model consisted of parallel placed HTS tapes. It can be known that the small gap distance is beneficial to improve the HTS cable critical current due to anisotropic characteristics. But in practical HTS cable, the influence of the contact resistances makes it difficult to distinguish from the anisotropy effect. Unless the contact resistances can be equalized or totally eliminated, the further study should focus on whether the influence of anisotropy is important on HTS power cable.

The measurement technique presented in Chapter 4 is only capable of obtaining current distribution among each HTS layer in the cable. Although knowing the current of each HTS layer would be enough for engineering prospect of view, the properties of each HTS tape, especially the critical current, may be different, which results in the non-uniform current distribution among the HTS tapes. It is worth improving the

measurement technique which is capable of measuring the current of each HTS tape so that the weakest point of the cable can be detected to enhance the reliability of the HTS cable.

The optimal algorithm of current distribution homogenization considering the HTS layer inductance is difficult to be accurately verified by experimental measurement. The measurement of current distribution as shown in Chapter 4 is not homogeneous even the HTS cable is designed according to the optimal algorithm. For HTS cable of short length, the HTS layer inductance may not be large enough to dominate the current distribution compared with contact resistance. Further consideration of eliminating the influence of contact resistance is required in this experiment. It may be achieved by increasing the length of the HTS cable so that the value of HTS layer inductance is large enough to dominate the current distribution.

In Chapter 5, the voltage taps attached on the cable equalize the voltage potential of every individual tape in the layer. Hence, the AC loss measurement results are the average values. An alternative solution can be done by measured the separated AC loss of each HTS tape. A different structure of cable termination needs to be designed in order to obtain the current of each HTS tape. It should be interesting to compare these two methods with the numerical calculation.

In Chapter 6, the superconducting cable developed in PSCAD/EMTDC considers the cable with only one HTS layer. More accurate HTS cable model with detailed multi-layer structure and termination resistance may be included in the model. Each HTS layer of cable can be represented by an independent circuit and electrically coupled with a series mutual inductance. A more comprehensive thermal model may include the flow rate of the LN_2 and the thermal conductivity of the PPLP insulation layer.

7.3 Future of HTS cable

Although many HTS cable projects have carried out and the feasibility and reliability have been proven in the distribution network, there are still many works needed to be done before applying the superconducting cable in the long length transmission network.

The expensive superconducting material is the major disadvantage that will make utilities cautious to replace the conventional cable with superconducting cable completely in the power grid. If the market price of the superconductor price can be reduced to 10 to 50 $/kA·m, it will lead to the electrical power transmission revolution in the future.

The AC loss of the long superconducting cable requires considerable cooling power, which can be further improved by using striated multi-filamentary HTS tapes to fabricate the cable. The number of the filaments should be investigated due to the removal of superconducting material resulting in the compromise between the reduction of critical current and AC loss decrease.

To further explore the performance of the superconducting cable, development can be concentrated on the control of power flow based on the superconducting cables which are parallel with the existing conventional cables. Since the naturally low impedance of the HTS cable, it can act as the FACTS without complex power electronic devices, which is an additional benefit to implementing HTS cable in the grid.

Appendices

8.1 The Matlab code for triaxial cable impedance balance program

```
%================================Initial parameters=========================
clc
clear
format short e
global q;
global p;
global cp;
global k;
global t1
global T;
global radius;
global u;
global thickness;
global T_shield;
global Pa;
global Pb;
global Pc;
global Ps1;
global Ps2;


T_shield=77*ones(1,20);
u0=4e-7*pi;
cond_layer_num=3;
shield_layer_num=2;
radius_former=16/1000;
wide=4.4/1000;
thickness=0.4/1000;
DD=4000;

%================================optimazation algorithm====================


for aa=1:45
    Pa=aa;
    for bb=1:45
        Pb=bb;
        for cc=1:45
            Pc=cc;

     if (DD>20)

x=[Pa,Pb,Pc,40,42];
angle=(pi/180)*x;
angle_cond=angle(1:3);
angle_shield=angle(4:5);
Inormal=3000;
Ifault=25000;
Ic0=103;
winding_dir_cond=[1,-1,-1];
winding_dir_shield=[1,1];
```

```
radius=[radius_former+thickness,radius_former+thickness+5/1000,radi
us_former+thickness+10/1000,radius_former+thickness+15/1000,radius_
former+thickness+20/1000];%%%
radius_cond=radius(1:3);
radius_shield=radius(4:5);
number=floor(2*pi*(radius-
thickness).*cos(angle(1:5))/(wide+1/1000));
N=number;
D=radius_shield(shield_layer_num);
width=wide;
%--------------------------------

ind_cond=zeros(cond_layer_num,cond_layer_num);



for i=1:cond_layer_num
    for j=1:cond_layer_num
        if(i==j)

ind_cond(i,j)=u0/4/pi*((tan(angle_cond(i)))^2+2*log(D/radius_cond(i
)));
        end
        if(i<j)

ind_cond(i,j)=u0/4/pi*(winding_dir_cond(i)*winding_dir_cond(j)*radi
us_cond(i)/radius_cond(j)*tan(angle_cond(i))*tan(angle_cond(j))+2*l
og(D/radius_cond(j)));
           ind_cond(j,i)= ind_cond(i,j);
        end
   end
end

%=========================================================================
=======%

%--------------------------------

ind_shield=zeros(shield_layer_num,shield_layer_num);

for i=1:shield_layer_num
    for j=1:shield_layer_num
        if(i==j)

ind_shield(i,j)=u0/4/pi*((tan(angle_shield(i)))^2+2*log(D/radius_sh
ield(i)));
        end
        if(i<j)

ind_shield(i,j)=u0/4/pi*(winding_dir_shield(i)*winding_dir_shield(j
)*radius_shield(i)/radius_shield(j)*tan(angle_shield(i))*tan(angle_
shield(j))+2*log(D/radius_shield(j)));
          ind_shield(j,i)= ind_shield(i,j);
        end
    end
end
```

```
%------------------------

ind_cond_shield=zeros(cond_layer_num+shield_layer_num,cond_layer_num+sh
ield_layer_num);%
for i=1:cond_layer_num
    for j=1:shield_layer_num

ind_cond_shield(i,cond_layer_num+j)=u0/4/pi*(winding_dir_cond(i)*windin
g_dir_shield(j)*radius_cond(i)/radius_shield(j)*tan(angle_cond(i))*tan(
angle_shield(j))+2*log(D/radius_shield(j)));

ind_cond_shield(cond_layer_num+j,i)=ind_cond_shield(i,cond_layer_num+j)
;
     end
end


%=========================================================================
===%

%--------------------------------
for i=1:cond_layer_num
    for j=1:cond_layer_num
        ind_cond_shield(i,j)=ind_cond(i,j);
    end
end
for i=1:shield_layer_num
    for j=1:shield_layer_num

ind_cond_shield(cond_layer_num+i,cond_layer_num+j)=ind_shield(i,j);
    end
end

%============================transformation
matrix====================================


b=zeros(cond_layer_num+shield_layer_num,cond_layer_num+shield_layer_num
+2);
  for i=1:(cond_layer_num-1)
      b(i,i)=1;
      b(i,cond_layer_num)=-1;
  end
  for i=1:(shield_layer_num-1)
      b(cond_layer_num+i-1,cond_layer_num+i)=1;
      b(cond_layer_num+i-1,cond_layer_num+shield_layer_num)=-1;
  end
b(cond_layer_num-1+shield_layer_num-
1+1,cond_layer_num+shield_layer_num+1)=1;
b(cond_layer_num-1+shield_layer_num-
1+2,cond_layer_num+shield_layer_num+2)=1;
```

```
%=========================Current calulation and
plot=======================================

Q=ind_cond_shield;
M=[Q*314i;1 1 1 0 0;0 0 0 1 1];%%%%%%%%
R_L=M;%%%%%%%%%%%



W=b*R_L;
V=inv(W)*[0;0;0;-2828+4898.24i;-(0+0i)];


I=(abs(V)/1.414)'

II=[I(1) I(2) I(3)]

Imax=max(II);
Imin=min(II);
DD=Imax-Imin;
disp(DD);
disp(x);


            end
    end
end
        end

%=========================================================================
=======
```

References

[1] C. P. Poole, *Superconductivity*: Elsevier Ltd., 2007.

[2] http://www.superconductors.org/type1.htm.

[3] D. A. Cardwell, "Processing and properties of large grain (RE)BCO," *Materials Science and Engineering B-Solid State Materials for Advanced Technology*, vol. 53, no. 1-2, pp. 1-10, May 1, 1998.

[4] Wikipedia. "Type-II superconductor," https://en.wikipedia.org/wiki/Type-II_superconductor.

[5] A. A. Abrikosov, "On the Magnetic Properties of Superconductors of the Second Group," *Soviet Physics Jetp-Ussr*, vol. 5, no. 6, pp. 1174-1183, 1957.

[6] H. U. o. Technology. "High-Temperature Superconductivity," http://tfy.tkk.fi/aes/AES/projects/prlaser/supercond.htm.

[7] J. G. Bednorz, and K. A. Muller, "Possible High-Tc Superconductivity in the Ba-La-Cu-O System," *Zeitschrift Fur Physik B-Condensed Matter*, vol. 64, no. 2, pp. 189-193, 1986.

[8] "tdk-lambda programmable dc power supplies," 2014.

[9] B. Oswald, "Concise Encyclopedia of Magnetic and Superconducting Materials," *Elsevier*, 2005.

[10] S. Graser, P. J. Hirschfeld, T. Kopp *et al.*, "How grain boundaries limit supercurrents in high-temperature superconductors," *Nature Physics*, vol. 6, no. 8, pp. 609-614, Aug, 2010.

[11] J. C. Hernandez-Llambes, and D. Hazelton, "Advantages of Second-Generation High Temperature Superconductors for Pulsed Power Applications," *2009 IEEE Pulsed Power Conference, Vols 1 and 2*, pp. 221-226, 2009.

[12] D. T. Verebelyi, U. Schoop, C. Thieme *et al.*, "Uniform performance of continuously processed MOD-YBCO-coated conductors using a textured Ni-W substrate," *Superconductor Science & Technology*, vol. 16, no. 5, pp. L19-L22, May, 2003.

[13] A. Rimikis, R. Kimmich, and T. Schneider, "Investigation of n-values of composite superconductors," *IEEE Transactions on Applied Superconductivity*, vol. 10, no. 1, pp. 1239-1242, Mar, 2000.

[14] Y. X. V. Selvamanickam, & J. Reeves, "Progress in Scale-Up of 2G Conductor at SuperPowe," *FY2007 Superconductivity for Electric Systems Peer Review Project Summary Form* 2007.

[15] M. Zhang, J. H. Kim, S. Pamidi *et al.*, "Study of second generation, high-temperature superconducting coils: Determination of critical current," *Journal of Applied Physics*, vol. 111, no. 8, Apr 15, 2012.

[16] D. W. Hazelton, V. Selvamanickam, J. M. Duval *et al.*, "Recent Developments in 2G HTS Coil Technology," *IEEE Transactions on Applied Superconductivity,* vol. 19, no. 3, pp. 2218-2222, Jun, 2009.

[17] X. M. Xiong, K. P. Lenseth, J. L. Reeves *et al.*, "High throughput processing of long-length IBAD MgO and epi-buffer templates at SuperPower," *IEEE Transactions on Applied Superconductivity,* vol. 17, no. 2, pp. 3375-3378, Jun, 2007.

[18] M. W. Rupich, X. P. Li, S. Sathyamurthy *et al.*, "Second Generation Wire Development at AMSC," *IEEE Transactions on Applied Superconductivity,* vol. 23, no. 3, Jun, 2013.

[19] A. R. Kaul, S. V. Samoilenkov, V. A. Amelichev *et al.*, "Development of non-magnetic biaxially textured tape and MOCVD processes for coated conductor fabrication," *Superconductivity Centennial Conference 2011,* vol. 36, pp. 1434-1439, 2012.

[20] S. Lee, "Development and production of second generation high Tc superconducting tapes at SuperOx and first tests of model cables," *Supercond. Sci. Technol,* vol. 27, pp. 9, 2014.

[21] H.-S. Kim, "Ultra-High Performance, High-Temperature SuperconductingWires via Cost-effective, Scalable,Co-evaporation Process," *Scientific Reports* 2014.

[22] G. A. Levin, J. Murphy, T. J. Haugan *et al.*, "AC Losses of Copper Stabilized Multifilament YBCO Coated Conductors," *IEEE Transactions on Applied Superconductivity,* vol. 23, no. 3, Jun, 2013.

[23] K. Suzuki, J. Matsuda, M. Yoshizumi *et al.*, "Development of a laser scribing process of coated conductors for the reduction of AC losses," *Superconductor Science & Technology,* vol. 20, no. 8, pp. 822-826, Aug, 2007.

[24] I. Kesgin, G. Majkic, and V. Selvamanickam, "Fully filamentized HTS coated conductor via striation and selective electroplating," *Physica C-Superconductivity and Its Applications,* vol. 486, pp. 43-50, Mar, 2013.

[25] I. Kesgin, G. A. Levin, T. J. Haugan *et al.*, "Multifilament, copper-stabilized superconductor tapes with low alternating current loss," *Applied Physics Letters,* vol. 103, no. 25, Dec 16, 2013.

[26] C. P. Bean, "Magnetization of High-Field Superconductors," *Reviews of Modern Physics,* vol. 36, no. 1p1, pp. 31-&, 1964.

[27] Y. Wang, *Fundamental Elements of Applied Superconductivity in Electrical Engineering*: Wiley, 2013.

[28] D. Larbalestier, "Handbook of applied superconductivity," *Nature,* vol. 395, no. 6703, pp. 657-658, Oct 15, 1998.

[29] J. Rhyner, "Magnetic-Properties and AC-Losses of Superconductors with Power-Law Current-Voltage Characteristics," *Physica C-Superconductivity and Its Applications,* vol. 212, no. 3-4, pp. 292-300, Jul 15, 1993.

[30] S. S. Kalsi, *Applications of high temperature superconductors to electric power equipment*: Wiley, 2011.

[31] D. Willén, "The application of triaxial high-temperature superconducting power cables in distribution networks " *18th International Conference on Electricity Distribution,* 2005.

[32] Y. W. Zhang, J. Lewiner, C. Alquie *et al.*, "Evidence of strong correlation between space-charge buildup and breakdown in cable insulation," *IEEE Transactions on Dielectrics and Electrical Insulation,* vol. 3, no. 6, pp. 778-783, Dec, 1996.

[33] J. H. Lim, "Cryogenic System for 80 kV DC HTS Cable in the KEPCO Power Grid," *IEEE Transactions on Applied Superconductivity,* vol. 25, no. 3, 2015.

[34] M. Stemmle, F. Merschel, M. Noe *et al.*, "AmpaCity - Installation of Advanced Superconducting 10 kV System in City Center Replaces Conventional 110 kV Cables," *2013 IEEE International Conference on Applied Superconductivity and Electromagnetic Devices (ASEMD)*, pp. 323-326, 2013.

[35] M. OHYA, "Japan's First Live Power Transmission Using 3-in-One Superconducting Cable (High-Temperature Superconducting Cable Demonstration Project)," *SEI technical review,* vol. Special Issue, 2013.

[36] T. Shibata, M. Watanabe, C. Suzawa *et al.*, "Development of high temperature superconducting power cable prototype system," *IEEE Transactions on Power Delivery,* vol. 14, no. 1, pp. 182-187, Jan, 1999.

[37] Y. Xin, "China's 30m, 35kV/2kA ac HTS Power Cable Project " *EUCAS 2003* 2004.

[38] C. S. Weber, C. T. Reis, A. Dada *et al.*, "Overview of the underground 34.5 kV HTS power cable program in Albany, NY," *IEEE Transactions on Applied Superconductivity,* vol. 15, no. 2, pp. 1793-1797, Jun, 2005.

[39] F. M. Mark STEMMLE, Mathias NOE,Achim HOBL, "Ampacity project – worldwide first superconducting cable and fault current limiter installation in a german city center," in 22nd International Conference on Electricity Distribution, Stockholm, 10-13 June 2013.

[40] D. Politano, M. Sjostrom, G. Schnyder *et al.*, "Technical and economical assessment of HTS cables," *IEEE Transactions on Applied Superconductivity,* vol. 11, no. 1, pp. 2477-2480, Mar, 2001.

[41] J. Oestergaard, "Superconducting power cables in Denmark - A case study," *IEEE Transactions on Applied Superconductivity,* vol. 7, no. 2, pp. 719-722, Jun, 1997.

[42] L. Ren, Y. J. Tang, J. Shi *et al.*, "Techno-Economic Feasibility Study on HTS Power Cables," *IEEE Transactions on Applied Superconductivity,* vol. 19, no. 3, pp. 1774-1777, Jun, 2009.

[43] C. Révillon. "Very Low Impedance (VLI) superconductor cables: concepts, operational implications and financial benefits "; http://www.nexans.co.uk/UK/2011/Superconductivity%20White%20Paper_1.pdf.

[44] T. L. Baldwin, M. Steurer, and Y. Z. Liu, "A novel method of controlling the effective impedance of a cold-dielectric, very low impedance, superconducting cable," *IEEE Transactions on Applied Superconductivity,* vol. 15, no. 2, pp. 1783-1786, Jun, 2005.

[45] M. Zhang, J. Kvitkovic, C. H. Kim *et al.*, "Study of 2G high temperature superconducting coils: Influence of anisotropic characteristics," *Journal of Applied Physics,* vol. 114, no. 4, Jul 28, 2013.

[46] E. Pardo, M. Vojenciak, F. Gomory *et al.*, "Low-magnetic-field dependence and anisotropy of the critical current density in coated conductors," *Superconductor Science & Technology,* vol. 24, no. 6, Jun, 2011.

[47] Y. B. Kim, C. F. Hempstead, and A. R. Strnad, "Magnetization and Critical Supercurrents," *Physical Review,* vol. 129, no. 2, pp. 528-&, 1963.

[48] Y. B. Kim, C. F. Hempstead, and A. R. Strnad, "Critical Persistent Currents in Hard Superconductors," *Physical Review Letters,* vol. 9, no. 7, pp. 306-&, 1962.

[49] M. Zhang, J. Kvitkovic, S. V. Pamidi *et al.*, "Experimental and numerical study of a YBCO pancake coil with a magnetic substrate," *Superconductor Science & Technology*, vol. 25, no. 12, Dec, 2012.

[50] Z. N. Jiang, K. P. Thakur, M. Staines *et al.*, "The dependence of AC loss characteristics on the spacing between strands in YBCO Roebel cables," *Superconductor Science & Technology*, vol. 24, no. 6, Jun, 2011.

[51] L. Rostila, J. Lehtonen, R. Mikkonen *et al.*, "How to determine critical current density in YBCO tapes from voltage-current measurements at low magnetic fields," *Superconductor Science & Technology*, vol. 20, no. 12, pp. 1097-1100, Dec, 2007.

[52] W. J. Yuan, A. M. Campbell, Z. Hong *et al.*, "Comparison of AC losses, magnetic field/current distributions and critical currents of superconducting circular pancake coils and infinitely long stacks using coated conductors," *Superconductor Science & Technology*, vol. 23, no. 8, Aug, 2010.

[53] J. H. Zhu, Z. Y. Zhang, H. M. Zhang *et al.*, "Electric Measurement of the Critical Current, AC Loss, and Current Distribution of a Prototype HTS Cable," *Ieee Transactions on Applied Superconductivity*, vol. 24, no. 3, Jun, 2014.

[54] F. Grilli, F. Sirois, V. M. R. Zerme *et al.*, "Self-Consistent Modeling of the of HTS Devices: How Accurate do Models Really Need to Be?," *IEEE Transactions on Applied Superconductivity*, vol. 24, no. 6, pp. 1-8, 2014.

[55] F. Grilli, F. Sirois, V. M. R. Zermeno *et al.*, "Self-Consistent Modeling of the I-c of HTS Devices: How Accurate do Models Really Need to Be?," *IEEE Transactions on Applied Superconductivity*, vol. 24, no. 6, Dec, 2014.

[56] F. Gomory, and B. Klincok, "Self-field critical current of a conductor with an elliptical cross-section," *Superconductor Science & Technology*, vol. 19, no. 8, pp. 732-737, Aug, 2006.

[57] J. C. Lagarias, J. A. Reeds, M. H. Wright *et al.*, "Convergence properties of the Nelder-Mead simplex method in low dimensions," *Siam Journal on Optimization*, vol. 9, no. 1, pp. 112-147, Dec 21, 1998.

[58] http://people.chem.ucsb.edu/laverman/leroy/Chem116/PDF116CL/Solver.pdf.

[59] S. Stavrev, F. Grilli, B. Dutoit *et al.*, "Comparison of numerical methods for modeling of superconductors," *IEEE Transactions on Magnetics*, vol. 38, no. 2, pp. 849-852, Mar, 2002.

[60] S. Pratap, and C. S. Hearn, "3-D Transient Modeling of Bulk High-Temperature Superconducting Material in Passive Magnetic Bearing Applications," *IEEE Transactions on Applied Superconductivity*, vol. 25, no. 5, Oct, 2015.

[61] Z. Hong, A. M. Campbell, and T. A. Coombs, "Numerical solution of critical state in superconductivity by finite element software," *Superconductor Science & Technology*, vol. 19, no. 12, pp. 1246-1252, Dec, 2006.

[62] B. Klincok, and F. Gomory, "Influence of gaps in monolayer superconducting cable on AC losses.," *7th European Conference on Applied Superconductivity (Eucas'05)*, vol. 43, pp. 897-900, 2006.

[63] J. Sun, H. Watanabe, M. Hamabe *et al.*, "Effects of HTS Tape Arrangements to Increase Critical Current for the DC Power Cable," *IEEE Transactions on Applied Superconductivity*, vol. 23, no. 3, Jun, 2013.

[64] J. Sun, S. Yamauchi, M. Sugino *et al.*, "Critical current measurements for design of superconducting DC transmission power cable," *Physica C-Superconductivity and Its Applications*, vol. 471, no. 21-22, pp. 1313-1316, Nov, 2011.

[65] L. Rostila, L. Soderlund, R. Mikkonen *et al.*, "Modelling method for critical current of YBCO tapes in cable use," *Physica C-Superconductivity and Its Applications,* vol. 467, no. 1-2, pp. 91-95, Dec 1, 2007.

[66] D. C. van der Laan, "YBa2Cu3O7-delta coated conductor cabling for low ac-loss and high-field magnet applications," *Superconductor Science & Technology,* vol. 22, no. 6, Jun, 2009.

[67] V. Pothavajhala, L. Graber, C. H. Kim *et al.*, "Experimental and Model Based Studies on Current Distribution in Superconducting DC Cables," *IEEE Transactions on Applied Superconductivity,* vol. 24, no. 3, Jun, 2014.

[68] J. G. Kim, S. K. Kim, D. M. Chau *et al.*, "A Novel Multi-Terminal Based Evaluation Method for an HTS DC Power Cable," *IEEE Transactions on Applied Superconductivity,* vol. 23, no. 3, Jun, 2013.

[69] J. H. Kim, C. H. Kim, V. Pothavajhala *et al.*, "Current Sharing and Redistribution in Superconducting DC Cable," *IEEE Transactions on Applied Superconductivity,* vol. 23, no. 3, Jun, 2013.

[70] K. Sim, S. Kim, S. Lee *et al.*, "The Estimation of the Current Distribution on the HTS Cable by Measuring the Circumferential Magnetic Field," *IEEE Transactions on Applied Superconductivity,* vol. 20, no. 3, pp. 1981-1984, Jun, 2010.

[71] M. Takayasu, L. Chiesa, L. Bromberg *et al.*, "HTS twisted stacked-tape cable conductor," *Superconductor Science & Technology,* vol. 25, no. 1, Jan, 2012.

[72] D. C. van der Laan, P. D. Noyes, G. E. Miller *et al.*, "Characterization of a high-temperature superconducting conductor on round core cables in magnetic fields up to 20 T," *Superconductor Science & Technology,* vol. 26, no. 4, Apr, 2013.

[73] V. Zermeno, P. Kruger, M. Takayasu *et al.*, "Modeling and simulation of termination resistances in superconducting cables," *Superconductor Science & Technology,* vol. 27, no. 12, Dec, 2014.

[74] Z. Y. Zhang, M. Zhang, J. H. Zhu *et al.*, "An Experimental Investigation of Critical Current and Current Distribution Behavior of Parallel Placed HTS Tapes," *IEEE Transactions on Applied Superconductivity,* vol. 25, no. 3, Jun, 2015.

[75] J. H. Zhu, Z. Y. Zhang, H. M. Zhang *et al.*, "Inductance and Current Distribution Analysis of a Prototype HTS Cable," *11th European Conference on Applied Superconductivity (Eucas2013), Pts 1-4,* vol. 507, 2014.

[76] D. C. van der Laan, X. F. Lu, and L. F. Goodrich, "Compact GdBa2Cu3O7-delta coated conductor cables for electric power transmission and magnet applications," *Superconductor Science & Technology,* vol. 24, no. 4, Apr, 2011.

[77] Y. Kim, S. Kim, T. H. A. Harano *et al.*, "Layer-current waveform of coaxial multi-layer HTS cable considering the flux flow state," *Cryogenics,* vol. 44, no. 1, pp. 37-43, Jan, 2004.

[78] S. M. Blair, C. D. Booth, and G. M. Burt, "Current-Time Characteristics of Resistive Superconducting Fault Current Limiters," *IEEE Transactions on Applied Superconductivity,* vol. 22, no. 2, Apr, 2012.

[79] S. K. Olsen, C. Traeholt, A. Kuhle *et al.*, "Loss and inductance investigations in a 4-layer superconducting prototype cable conductor," *IEEE Transactions on Applied Superconductivity,* vol. 9, no. 2, pp. 833-836, Jun, 1999.

[80] S.-K. Kim, "Tri-axial Core Design of a Distribution System Class HTS Power Cable," *International Journal of Control and Automation,* vol. 5, no. 3, 2012.

[81] M. P. Oomen, "AC LOSS IN SUPERCONDUCTING TAPES AND CABLES," *Universiteit Twente*, pp. 9-25, 1972.
[82] M. P. Paranthaman, and T. Izumi, "High-performance YBCO-coated superconductor wires," *Mrs Bulletin*, vol. 29, no. 8, pp. 533-536, Aug, 2004.
[83] F. Grilli, E. Pardo, A. Stenvall *et al.*, "Computation of Losses in HTS Under the Action of Varying Magnetic Fields and Currents," *IEEE Transactions on Applied Superconductivity*, vol. 24, no. 1, Feb, 2014.
[84] A. Kameari, "Calculation of Transient 3d-Eddy Current Using Edge-Elements," *Ieee Transactions on Magnetics*, vol. 26, no. 2, pp. 466-469, Mar, 1990.
[85] J. P. Webb, and B. Forghani, "A Scalar-Vector Method for 3d Eddy-Current Problems Using Edge Elements," *IEEE Transactions on Magnetics*, vol. 26, no. 5, pp. 2367-2369, Sep, 1990.
[86] D. A. Bein, J. Zbasnik, S. Graham *et al.*, "Eddy-Current Inspection of Superconducting Cable during Manufacturing," *Supercollider 4*, pp. 677-684, 1992.
[87] K. H. Muller, "AC power losses in flexible thick-film superconducting tapes," *Physica C*, vol. 281, no. 1, pp. 1-10, Jul 21, 1997.
[88] Y. Fukumoto, "Alternating current losses in mono and multicored silver sheathed (Bi,Pb)2Sr2Ca2Cu3O10 tapes at T=27 K in direct current magnetic fields," *Journal of Applied Physics*, vol. 78, no. 4584, 1995.
[89] D. Miyagi, M. Umabuchi, N. Takahashi *et al.*, "Study of AC transport current loss of assembled HTS coated-conductors with ferromagnetic substrate using FEM," *Physica C-Superconductivity and Its Applications*, vol. 463, pp. 785-789, Oct 1, 2007.
[90] H. Moriwake, T. Kato, A. Kuwabara *et al.*, "Magnetic Properties of Ni Alloys for Superconducting Wire Substrates: A First-Principles Study," *Japanese Journal of Applied Physics*, vol. 48, no. 8, Aug, 2009.
[91] A. A. Akhmetov, "Long current loops as regular solutions of the equation for coupling currents in a flat two-layer superconducting cable," *Cryogenics*, vol. 43, no. 3-5, pp. 317-322, Mar-May, 2003.
[92] M. Baert, V. V. Metlushko, R. Jonckheere *et al.*, "Flux Phases and Quantized Pinning Force in Superconductor with a Periodic Lattice of Pinning Centers," *Europhysics Letters*, vol. 29, no. 2, pp. 157-162, Jan 10, 1995.
[93] T. Matsushita, "Flux Pinning in Superconductors," *Springer.*, 2006.
[94] M. Ashkin, "Flux Distribution and Hysteresis Loss in a Round Superconducting Wire for the Complete Range of Flux-Penetration," *Journal of Applied Physics*, vol. 50, no. 11, pp. 7060-7066, 1979.
[95] C. P. Bean, "Magnetization of Hard Superconductors," *Physical Review Letters*, vol. 8, no. 6, pp. 250-&, 1962.
[96] M. D. Ainslie, T. J. Flack, Z. Y. Hong *et al.*, "Comparison of first- and second-order 2D finite element models for calculating AC loss in high temperature superconductor coated conductors," *Compel-the International Journal for Computation and Mathematics in Electrical and Electronic Engineering*, vol. 30, no. 2, pp. 762-774, 2011.
[97] M. J. Gouge, D. T. Lindsay, J. A. Demko *et al.*, "Tests of tri-axial HTS cables," *Ieee Transactions on Applied Superconductivity*, vol. 15, no. 2, pp. 1827-1830, Jun, 2005.
[98] G. Vellego, and P. Metra, "An Analysis of the Transport Losses Measured on Htsc Single-Phase Conductor Prototypes," *Superconductor Science & Technology*, vol. 8, no. 6, pp. 476-483, Jun, 1995.

[99] W. T. Norris, "Calculation of Hysteresis Losses in Hard Superconductors Carrying AC - Isolated Conductors and Edges of Thin Sheets," *Journal of Physics D-Applied Physics*, vol. 3, no. 4, pp. 489-&, 1970.

[100] F. Gomory, M. Vojenciak, E. Pardo *et al.*, "AC losses in coated conductors (vol 23, 034012, 2010)," *Superconductor Science & Technology*, vol. 26, no. 4, Apr, 2013.

[101] S. Elschner, E. Demencik, B. Douine *et al.*, "New Experimental Method for Investigating AC Losses in Concentric HTS Power Cables," *IEEE Transactions on Applied Superconductivity*, vol. 25, no. 3, pp. 1-5, 2015.

[102] M. P. Oomen, J. Rieger, V. Hussennether *et al.*, "AC loss in high-temperature superconducting conductors, cables and windings for power devices," *Superconductor Science & Technology*, vol. 17, no. 5, pp. S394-S399, May, 2004.

[103] H. Noji, "AC loss of a high-Tc superconducting power-cable conductor," *Superconductor Science & Technology*, vol. 10, no. 8, pp. 552-556, Aug, 1997.

[104] H. Noji, K. Ikeda, K. Uto *et al.*, "Numerical analysis of the AC loss in a high-T-C superconducting cable measured by calorimetric method," *Physica C-Superconductivity and Its Applications*, vol. 425, no. 3-4, pp. 97-100, Sep 15, 2005.

[105] O. Tsukamoto, J. Ogawa, M. Ciszek *et al.*, "Origins of errors in AC transport current loss measurements of HTS tapes and methods to suppress errors," *IEEE Transactions on Applied Superconductivity*, vol. 11, no. 1, pp. 2208-2211, Mar, 2001.

[106] S. A. Awan, and S. Sali, "Self-field AC power dissipation in high-Tc superconducting tapes and a prototype cable," *IEE Proceedings-Science Measurement and Technology*, vol. 149, no. 1, pp. 2-8, Jan, 2002.

[107] "MODEL DR830 DSP Lock-In Amplifier," *Standford Researcg Systems*, 2011.

[108] "Fluke i2000 Flex AC Current Clamp "; http://en-us.fluke.com/products/all-accessories/fluke-i2000-flex.html#techspecs.

[109] M. Solovyov, E. Pardo, J. Souc *et al.*, "Non-uniformity of coated conductor tapes," *Superconductor Science & Technology*, vol. 26, no. 11, Nov, 2013.

[110] H. Noji, "Reduction of Alternating-Current Losses in (RE)Ba2Cu3Ox Monolayer and Double-Layer Superconducting Power Cables," *International Journal of Energy Engineering*, vol. 5, no. 5, 2015.

[111] M. Yagi, S. Tanaka, S. Mukoyama *et al.*, "Measurement of AC losses of superconducting cable by calorimetric method and development of HTS conductor with low AC losses," *IEEE Transactions on Applied Superconductivity*, vol. 13, no. 2, pp. 1902-1905, Jun, 2003.

[112] S. Elschner, E. Demencik, B. Douine *et al.*, "New Experimental Method for Investigating AC Losses in Concentric HTS Power Cables," *Applied Superconductivity, IEEE Transactions on*, vol. 25, no. 3, pp. 1-5, 2015.

[113] B. N. Anguan Wu, *Line Loss Analysis and Calculation of Electric Power Systems*, Singapore: John Wiley & Sons Singapore Pte Ltd., 2015.

[114] J. Jipping, A. Mansoldo, and C. Wakefield, "The impact of HTS cables on power flow distribution and short-circuit currents within a meshed network," *2001 IEEE/PES Transmission and Distribution Conference and Exposition, Vols 1 and 2*, pp. 736-741, 2001.

[115] Z. Jiahui, Q. Ming, L. Xiaokang *et al.*, "Modeling and analysis of the power transmission with an 110kV/3kA HTS cable in a meshed grid." pp. 1-5.

[116] C. H. Gu, Y. Zhang, F. R. Li *et al.*, "Economic Analysis of Interconnecting Distribution Substations via Superconducting Cables," *2012 IEEE Power and Energy Society General Meeting*, 2012.

[117] J. G. Kim, A. R. Kim, D. Kim *et al.*, "Development of a PSCAD/EMTDC Model Component for AC Loss Characteristic Analysis of HTS Power Cable," *IEEE Transactions on Applied Superconductivity,* vol. 20, no. 3, pp. 1280-1283, Jun, 2010.

[118] S. K. Ha, S. K. Kim, J. G. Kim *et al.*, "Transient Characteristic Analysis of a Tri-Axial HTS Power Cable Using PSCAD/EMTDC," *IEEE Transactions on Applied Superconductivity,* vol. 23, no. 3, Jun, 2013.

[119] J. H. Bang, H. H. Je, J. H. Kim *et al.*, "Critical current, critical temperature and magnetic field based EMTDC model component for HTS power cable," *IEEE Transactions on Applied Superconductivity,* vol. 17, no. 2, pp. 1726-1729, Jun, 2007.

[120] S. Lee, J. Yoon, B. Lee *et al.*, "Modeling of a 22.9 kV 50 MVA superconducting power cable based on PSCAD/EMTDC for application to the Icheon substation in Korea," *Physica C-Superconductivity and Its Applications,* vol. 471, no. 21-22, pp. 1283-1289, Nov, 2011.

[121] S. R. Curras, J. Vina, M. Ruibal *et al.*, "Normal-state resistivity versus critical current in YBa2Cu3O7-delta thin films at high current densities," *Physica C-Superconductivity and Its Applications,* vol. 372, pp. 1095-1098, Aug 1, 2002.

[122] D. Giancoli, *Electric Currents and Resistance*, New Jersey: Physics for Scientists and Engineers with Modern Physics 2009.

[123] J. H. Lim, H. S. Yang, S. H. Sohn *et al.*, "Cryogenic System for 80-kV DC HTS Cable in the KEPCO Power Grid," *IEEE Transactions on Applied Superconductivity,* vol. 25, no. 3, pp. 1-4, 2015.

[124] Y. G. Zhou, G. M. Zhang, X. H. Li *et al.*, "Performance of YBa2Cu3Ox Tapes With Different Structures Under AC Overcurrent Conditions," *IEEE Transactions on Applied Superconductivity,* vol. 19, no. 4, pp. 3665-3669, Aug, 2009.

[125] J. Duron, F. Grilli, L. Antognazza *et al.*, "Finite-element modelling of YBCO fault current limiter with temperature dependent parameters," *Superconductor Science & Technology*, vol. 20, no. 4, pp. 338-344, Apr, 2007.

[126] R. Zuijderduin, O. Chevtchenko, J. J. Smit *et al.*, "AC HTS transmission cable for integration into the future EHV grid of the Netherlands," *Superconductivity Centennial Conference 2011,* vol. 36, pp. 1149-1152, 2012.

[127] K. W. Louie, A. Wang, P. Wilson *et al.*, "A newly built power flow program in PSCAD/EMTDC for electric power system studies," *2004 International Conference on Power System Technology - POWERCON, Vols 1 and 2*, pp. 1502-1507, 2004.

[128] B. M. Weedy, *Electric power systems*, Chichester : Wiley, 2012.

[129] M. F. Akorede, and H. Hizam, "Teaching power system analysis courses using MATPOWER." pp. 45-51.

[130] I. Nurul Huda, I. Iza Sazanita, S. Abdullah *et al.*, "Performance comparison of electric power flow solutions using PSCAD." pp. 542-547.

[131] G. J. Lee, J. P. Lee, S. D. Hwang *et al.*, "The feasibility study of high temperature superconducting cable for congestion relaxation regarding quench effect." pp. 1285-1292 Vol. 2.

[132] M. Leghissa, J. Rieger, H. W. Neumuller *et al.*, "Development of HTS power transmission cables," *IEEE Transactions on Applied Superconductivity,* vol. 9, no. 2, pp. 406-411, Jun, 1999.
[133] M. Majoros, "Hysteretic losses at a gap in a thin sheet of hard superconductor carrying alternating transport current," *Physica C,* vol. 272, no. 1-2, pp. 62-64, Nov 20, 1996.
[134] T. J. Leszek JAROSZYŃSKI, "YBCO coated conductors for superconducting transformer windings," *Przegląd Elektrotechniczny*, 2014.
[135] O. Tonnesen, M. Daumling, K. H. Jensen *et al.*, "Operation experiences with a 30 kV/100 MVA high temperature superconducting cable system," *Superconductor Science & Technology,* vol. 17, no. 5, pp. S101-S105, May, 2004.
[136] "XLPE insulated power cables up to 1000 V (IEC 60502-1)."
[137] C. Rey, *Superconductors in the Power Grid: Materials and Applications*, p.^pp. 197: Woodhead Publishing Ltd, 2014.
[138] W. J. Kim, S. H. Kim, H. J. Kim *et al.*, "The Fundamental Characteristics of PPLP as Insulating Material for HTS DC Cable," *IEEE Transactions on Applied Superconductivity,* vol. 23, no. 3, Jun, 2013.
[139] J. Oestergaard, J. Okholm, K. Lomholt *et al.*, "Energy losses of superconducting power transmission cables in the grid," *IEEE Transactions on Applied Superconductivity,* vol. 11, no. 1, pp. 2375-2378, Mar, 2001.
[140] C. Bayliss, *Transmission and Distribution Electrical Engineering*, Third Edition ed., p.^pp. 439.
[141] O. Tonnesen, S. Hansen, P. Jorgensen *et al.*, "Power applications for superconducting cables," *Superconductor Science & Technology,* vol. 13, no. 5, pp. 506-509, May, 2000.